T.C.
DOKUZ EYLUL UNIVERSITY
IZMIR INTERNATIONAL
BIOMEDICINE AND GENOME
INSTITUTE

FUNCTIONAL VALIDATION OF CANDIDATE GENES ASSOCIATED WITH INHERITED NEURODEVELOPMENTAL DISEASES

SEVAL KILIÇ

MOLECULAR BIOLOGY AND GENETICS Ph.D. PROGRAM

Ph.D. THESIS

Thesis Code: DEU.IBG.PhD-2017850002

FUNCTIONAL VALIDATION OF CANDIDATE GENES ASSOCIATED WITH INHERITED NEURODEVELOPMENTAL DISEASES

MOLECULAR BIOLOGY AND GENETICS Ph.D. PROGRAM
Ph.D. THESIS

SEVAL KILIÇ

Ph.D. Advisor: Assoc. Prof. M. Kasım Diril

(This thesis was supported by The Scientific and Technological Research Council of Turkey (TUBITAK) with grant numbers 120S396, 121S347, 122Z025)

Thesis Code: DEU.IBG.PhD-2017850002

T.C.
DOKUZ EYLÜL ÜNİVERSİTESİ

İZMİR ULUSLARARASI BİYOTIP VE GENOM ENSTİTÜSÜ

Ph.D. THESIS DEFENSE EXAM REPORT

Seval Kılıç, who is a student at the Department of Molecular Biology and Genetics Ph.D. program of the Dokuz Eylul University's Izmir International Biomedicine and Genome Institute, with the student ID 2017850002, succeeded her Ph.D. thesis titled "Functional Validation of Candidate Genes Associated with Inherited Neurodevelopmental Diseases" as a result of her thesis defense on 29.11.2023.

CHAIR

Assoc. Prof. M. Kasım Diril

JURY MEMBER

Prof. Dr. Abdullah Yalçın

JURY MEMBER

Assoc. Prof. Dr. Şerif Şentürk

JURY MEMBER

Prof. Dr. Mehmet Öztürk

JURY MEMBER

Dr. Yavuz Oktay

JURY MEMBER

Prof. Dr. S. Neşe Atabey

JURY MEMBER

Prof. Dr. Şermin Genç

T.C.
DOKUZ EYLÜL ÜNİVERSİTESİ

İZMİR ULUSLARARASI BİYOTIP VE GENOM ENSTİTÜSÜ

DOKTORA TEZ SAVUNMA SINAVI TUTANAĞI

Dokuz Eylül Üniversitesi, İzmir Uluslararası Biyotıp ve Genom Enstitüsü, Genom Bilimleri ve Moleküler Biyoteknoloji Anabilim Dalı, Moleküler Biyoloji ve Genetik Doktora Programı 2017850002 numaralı öğrencisi Seval Kılıç, "Functional Validation of Candidate Genes Associated with Inherited Neurodevelopmental Diseases" konulu Doktora tezini 29.11.2023 tarihinde yapılan savunma sınavı sonucunda başarılı olarak tamamlamıştır.

BAŞKAN

Doç. Dr. M. Kasım Diril

JÜRİ ÜYESİ

Prof. Dr. Abdullah Yalçın

JÜRİ ÜYESİ

Doç. Dr. Şerif Şentürk

JÜRİ ÜYESİ

Prof. Dr. Mehmet Öztürk

JÜRİ ÜYESİ

Dr. Öğr. Üyesi Yavuz Oktay

YEDEK JÜRİ ÜYESİ

Prof. Dr. S. Neşe Atabey

YEDEK JÜRİ ÜYESİ

Prof. Dr. Şermin Genç

TABLE OF CONTENTS

TABLE OF CONTENTS ..... **I**

LIST OF TABLES ..... **III**

LIST OF FIGURES ..... **IV**

ABBREVIATIONS ..... **VIII**

ACKNOWLEDGEMENT ..... **X**

ABSTRACT **1**

ÖZET **2**

1. AIM AND OBJECTIVES **3**

2. INTRODUCTION **6**

2.1. WDR62 ..... **7**

2.2. VARS1 ..... **12**

2.3. ATG9B **17**

2.3.1. Mechanism of Autophagy 17

2.3.2. The Role of ATG9 Proteins in Mammalian Autophagy 21

2.3.3. The Function of ATG9B 25

2.3.4. Involvement of Autophagy in Embryonic Development and Mouse Models 29

2.3.5. The Role of Autophagy in Placental Development 30

2.3.6. Involvement of ATG9B in diseases 32

3. MATERIALS AND METHODS **34**

3.1. Type of the Research **34**

3.2. Location and Time of the Research **34**

3.3. Universe of the Study, Sample of the Study/Study Groups **34**

3.4. Materials of the Study **34**

3.5. Variables of the Study **37**

3.6. Data Collection Tools **37**

3.6.1. Sample preparation for WES and Sanger Sequencing. 37

3.6.2. Identification and Validation of Candidate Pathologic Variants 38

3.6.3. ATG9B gene synthesis 38

3.6.4. Cell Lines, Media, Culture, Transfection 38
3.6.5. Lentivirus production and infection 39
3.6.6. Development of stable clonal cell lines 40
3.6.7. Protein Expression and Localization assays 40
3.6.8. RNA Expression Assays 42
3.6.9. Rabbit Polyclonal ATG9B Antibody Production 43
3.6.10. Generation of Transgenic Mouse Models and Functional Studies 45
3.7. Plan of the Research 48
3.8. Evaluation of the Study 48
3.9. Limitations of the Study 48
3.10. Ethics Committee Approval 49
4. RESULTS 50
4.1. Blue Gene Project and identification of candidate genes mutations 50
4.2. WDR62 51
4.3. VARS1 52
4.4. ATG9B 57
4.4.1. Determination of ATG9B Expression in Human Cell Lines 60
4.4.2. Functional Characterization of ATG9B Truncation Mutation in Cellular Models 62
4.4.3. Production of ATG9B Polyclonal Antibody 83
4.4.4. Development and Genetic Characterization of Transgenic Mouse Models 91
4.4.5. Molecular and Histologic Characterization of Knock-in Mice 108
4.4.6. Expressional and Histological Studies in Transgenic Mouse Tissues 119
5. DISCUSSION 126
6. CONCLUSION AND FUTURE PERSPECTIVES 132
7. REFERENCES 133
8. ATTACHMENTS 147

LIST OF TABLES

Table 1. Domain-specific pathogenic mutation number of aminoacyl-tRNA synthetases. 15

Table 2. Phenotypes observed in systemic autophagy specific gene knockouts 30

Table 3. The recipes for protein extraction buffers. 35

Table 4. Antibodies that were used in this study. 35

Table 5. Oligonucleotides used in this thesis. 36

Table 6. The timeline for rabbit immunization. 45

Table 7. The timeline of the thesis work. 48

Table 8. The effects of the *VARS1* mutations in protein stability. 57

Table 9. The effect of *VARS1* mutations in hydrophobic interactions. 57

Table 10. Plasmid constructs used in human cell line studies. 66

Table 11. The pattern of inheritance of Atg9b genetic disease knock-in model. 109

Table 12. The timeline of mouse placental development. 109

LIST OF FIGURES

Figure 1. The conservation of *WDR62* gene.....8

Figure 2. The map of mutations reported for *WDR62* gene in ClinVar (29).....10

Figure 3. The amino-acylation reaction.....13

Figure 4. The crystal structure of ValRS of *Thermus thermophilus*. 14

Figure 5. Pathogenic variants in identified in *VARS1* gene.....17

Figure 6. The structure of yeast Atg9.....21

Figure 7. The dynamic intracellular traffic of ATG9A. 22

Figure 8. The lipid scramblase activity of ATG9A.....23

Figure 9. Nondegradable ubiquitination of ATG9A in Golgi stress. 25

Figure 10. The expression of ATG9B in human tissue organs, cell types, and cell lines. 26

Figure 11. The structure and localization of ATG9B.....27

Figure 12. The involvement of ATG9B in focal adhesion assembly. 28

Figure 13. The role of trophoblasts in the development of the human placenta. 31

Figure 14. Pathogenic variants identified in *ATG9B* gene. 33

Figure 15. Identification and validation of the novel *WDR62* frameshift mutation. 52

Figure 16. Identification and validation of the novel *VARS1* missense mutation. 54

Figure 17. The conservation of amino acids in the mutational hotspot in *VARS1* gene.....55

Figure 18. The effect of p.T1068M substitution in VARS1 protein. 56

Figure 19. Identification and validation of the novel *ATG9B* frameshift mutation.....59

Figure 20. The domain organization of ATG9B protein. 59

Figure 21. The expression of ATG9B in placental cell lines. 61

Figure 22. ATG9B and ATG9A protein expression in human cell lines. 62

Figure 23. The ATG9B protein, and locations of the epitope tags.....65

Figure 24. The ectopic expression of pCS2 hATG9B-GFP WT and TR constructs.....67

Figure 25. The ectopic expression of pcDNA3.1 hATG9B WT and TR constructs. 68

Figure 26. The ectopic expression and localization of FLAG-ATG9B WT and TR. 69

Figure 27. The ectopic expression studies with FLAG-hATG9B clones. 70

Figure 28. The ectopic expression of 4xFLAG-hATG9B constructs. 71

Figure 29. 4xFLAG-ATG9B WT and TR expression in different time points post-transfection and upon proteasomal inhibition. 72

Figure 30. The inefficiency of ATG9B TR protein expression at different time points post-transfection. 74

Figure 31. Lentiviral infection of various cell lines indicating the inefficiency of ATG9B TR protein expression. 75

Figure 32. Production of monoclonal HeLa FLAG-hATG9B WT expressing cells 76

Figure 33. Co-localization of ATG9B WT and ATG9A in cells expressing ATG9B stably... 77

Figure 34. Co-localization of ATG9B WT with TGN. 78

Figure 35. Co-localization of ATG9B WT and LC3. 79

Figure 36. Localization of WT and TR ATG9B in various cell lines. 80

Figure 37. Co localization of FLAG WT with WT-myc and TR-myc. 81

Figure 38. The localization of WT and TR ATG9B in TGN compartments. 82

Figure 39. Autophagy assessment upon ATG9A knockdown conditions. 83

Figure 40. The schematic representation of the antigen sites on the *ATG9B* DNA map. 84

Figure 41. The alignment of mouse and human ATG9B protein sequences. 85

Figure 42. The antigenicity predictions of selected peptides. 86

Figure 43. The plasmid map and sequence for Antigen 1 cloned to pGEX-6P-1 vector. 87

Figure 44. The production and isolation of Antigen 1. 87

Figure 45. The large scale production and purification of Antigen 1. 88

Figure 46. The antibody tests in transfected and stable Hela cells. 89

Figure 47. The determination of anti-ATG9B serum in immunoblotting. 91

Figure 48. Conservation of C-terminal ATG9B sequence between human and mouse. 93

Figure 49. The strategy for editing and screening of Atg9b knock-in disease model. 94

Figure 50. The efficiency of the HDR-mediated knock-in strategy in embryos. 95

Figure 51. The generation of HDR mediated CRISPR/Cas9 HDR mediated knock-in mice model. 96

Figure 52. The genotyping and confirmation of founder mice of the Atg9b knock-in rare genetic disease model. 97

Figure 53. The genotyping and confirmation of heterozygous knock-in mice. 98

Figure 54 The sequence confirmations of the nucleotide deletions for DEL-1 and DEL-2 mice. 98

Figure 55. The design and screening strategy of FLAG-Atg9b mouse model development. 100

Figure 56. The schematic representation of asymmetrical homology arms in the HDR template. 100

Figure 57. Sequence validation of the FLAG-Atg9b knockin allele. 102

Figure 58. The editing and genotyping strategy for 3xFLAG Atg9b. 103

Figure 59. FLOX Editing Strategy. 104

Figure 60. Sanger sequencing of double LoxP embryo. 105

Figure 61. Double Flox screening. 106

Figure 62. The genotyping of heterozygous and homozygous Atg9b knock-out mice. 107

Figure 63. Atg9b Knock-out model confirmation by DEL-3 and DEL-4 sequencing. 107

Figure 64. The method of placenta isolation. 110

Figure 65. The morphology of 13.5 dpc homozygote and heterozygote embryos. 110

Figure 66. Atg9b expression in heterozygote and homozygote knock-in placenta tissues at 13.5 and 17.5 dpc. 111

Figure 67. The histology of WT and knock-in placenta. 112

Figure 68. Histomorphometric analysis of the placenta in *Atg9b* knockin mice. 113

Figure 69. The locomotor activity test. 114

Figure 70. The ball embedding test. 115

Figure 71. The open field test. 115

Figure 72. The social preference test. 116

Figure 73. The novel object recognition test. 117

Figure 74. The spatial object recognition test. 118

Figure 75. The passive avoidance test. 119

Figure 76. Immunofluorescence staining of mouse placenta sections with anti-FLAG antibody. 120

Figure 77. Atg9b expression during placental development in RNA level. 122

Figure 78. Atg9b expression in protein level for WT, knock-out and knock-in mouse tissues. 123

Figure 79. Immunohistochemistry staining employing anti-ATG9B serum developed in our laboratory. 124

Figure 80. Atg9b protein expression in trophectoderm cells. 125

ABBREVIATIONS

ARS: Aminoacyl-tRNA synthetase

ASD: Autism spectrum disorder

ATG9B: Autophagy related 9B

AURKA: Aurora A kinase

BSA: Bovine serum albumin

C: Cytosine

CHD: Congenital heart disease

cKO: Conditional knockout

CP1: Connective peptide 1

CRC: Colorectal cancer cells

dpc days post coitum

EEG: Electroencephalography

ER: Endoplasmic Reticulum

ERK1: Extracellular signal-regulated kinase 1

FA: Focal adhesion

FBS: Fetal bovine serum

GPCR: G protein coupled receptor

hCGβ: Human chorionic gonadotrophin β

HDR: Homology directed repair

IARS1: Isoleucyl-tRNA synthetase 1

IF: Immunofluorescence

JNK: c-Jun N-terminal kinase

KIN: Knock-in

LAMC2: Laminin subunit gamma-2

MAPK: Mitogen-activating protein kinase

MCPH: Autosomal recessive primary microcephaly

MHY: Myosin 9

MKK7β1: MAP kinase kinase 7β1

MLCK: Myosin light chain kinase

MMR: Motormental retardation

MRI: Brain magnetic resonance imaging

mTORC1: Mammallian target of rapamycin 1

NEAA: Non-essential amino acids

NHEJ: Non homologous end joining

NHEJ: Non-homologous end joining

P/S: Penicillin/Streptomycin

PAS: Phagophore assembly sites

PDB: Protein Data Bank

PP_i: Pyrophosphate

RF: Rossman fold

RMSD: Root Mean Square Deviation

SNARE: Soluble N-Ethylmaleimide-Sensitive Factor Attachment Protein Receptors

snRNP: Small nuclear ribonucleoprotein

SVZ: Subventricular zone

TGN: Trans-Golgi network

TPX2: Targeting protein for Xklp2

TR: Truncated

ULK: Unc-51-like kinase

UPS: Ubiquitin proteosome system

USP25: Ubiquitin carboxyl-terminal hydrolase 24

VARS1: Valyl-tRNA synthetase 1

VZ: Ventricular zone

WDR62: WD Repeat Domain 62

WES: Whole Exome Sequencing

WT: Wild Type

ZO-1: Zona occludens-1

ACKNOWLEDGEMENT

I would like to thank my thesis advisor Assoc. Prof. Kasım Diril for his mentorship, academic contributions, and guidance throughout the Ph.D. program. His contribution to my education is immensely appreciated. I would like to thank Prof. Dr. Mehmet Öztürk for his guidance during the early years of the program which was essential. He provided an environment composed of not only co-workers but friends.

I would like to thank Kerem Esmen who with his excellent skills and technique performed embryonic manipulations and generated founder mice, also helped with colony management and in the process taught me patiently how to work with mouse models.

I would like to thank all my interns, especially Liubovi Sopcovi and Ayşe Miray Oto for never hesitating to learn and apply with their all to contribute to the research.

I would like to thank our project partners from Hacettepe University, especially Bilge Köse for carrying out neurobehavioral experiments. I also thank Şeyda Demir and Prof. Dr. Alper Bağrıyanık for their contributions in histological analyses. I would like to thank Assoc. Prof. Şerif Şentürk who has never turned me down in my request for help.

I would like to thank Assoc. Prof. Gökhan Karakülah for his work in the interpretation of the Whole Exome Sequencing data.

I thank my father and my mother who were always supportive and patient with my struggles during my PhD. They always loved, cared, took care of me, and made sure I had nothing but my work in my mind.

I would like to thank my best friend Esra Katkat who was always by my side and who was the first person I went to whenever I had a problem or needed a friend. I am extremely grateful for her friendship.

I would like to thank past and present members of the Öztürk Lab for their support and friendship. I would like to especially thank Aybike Erdoğan for her work in the Blue Gene project before my arrival, Erhan Bal and Sıla Kahyaoğlu who were always helpful.

I would like to thank IBG Core Facilities, Serhat Özgenç from Vivarium, Ece Uzun from Histology and Aslı Seren from Optical Imaging for their attentiveness to my work.

I received financial support from YOK100/2000, TUBITAK BIDEB 2211/A and 2250 programs during my Ph.D. education. My projects were supported by TUBITAK with 1005, 1002 and 1001 grants.

FUNCTIONAL VALIDATION OF CANDIDATE GENES ASSOCIATED WITH INHERITED NEURODEVELOPMENTAL DISEASES

Seval Kılıç

Izmir International Biomedicine and Genome Institute

Dokuz Eylul University, 35430, Izmir, TÜRKİYE

ABSTRACT

This study aims to elucidate genetic diseases through the validation and characterization of novel mutations identified in a group of children born of consanguineous marriages. Three such pediatric patients were selected for further investigation. They were all clinically suspected of genetic diseases but were unable to be diagnosed with known genetic mutations. Clinical findings included microcephaly, motor-mental retardation, neuro-developmental disorders, and epilepsy. Whole exome sequencing identified previously unreported candidate mutations: nucleotide deletions in *WDR62* and *ATG9B* genes resulting in frameshift and premature termination of translation, and a missense mutation in *VARS1* gene resulting in single amino acid alteration. In the literature, *WDR62* mutations were extensively reported as causative factor for microcephaly. Therefore, the *WDR62* mutation was only validated by Sanger sequencing. The effects of the *VARS1* mutation were studied by structural modeling and shown to have destabilizing effects on the VARS1 protein.

The focus of this thesis was the *ATG9B* mutation. *ATG9B* has not been associated with any genetic disease and its function is poorly characterized in literature. The eleven-nucleotide deletion identified in the *ATG9B* gene causes a frameshift resulting in protein truncation. We characterized WT and mutant ATG9B by ectopic expression in cells and developed several mouse models for *in vivo* studies. We showed that truncated protein is not stable when expressed in cells. Using *in vivo* models, we demonstrated that Atg9b is expressed in the placenta and testis, but not essential for viability or fertility. We didn't observe any major histological differences between WT and mutant placenta. On the other hand, behavioral assays revealed reduced fear memory in the homozygous knockin animals. We additionally developed knockout and FLAG knockin mouse models of ATG9B, and generated antisera to study its functions *in vivo* and *in vitro*.

Keywords: Rare genetic disease, Neurodevelopmental disorders, Genetically modified mouse models, ATG9B

NÖROGELIŞIMSEL HASTALIKLARLARLA ILIŞKILENDIRILEN ADAY GENLERIN IŞLEVSEL VALIDASYONU

Seval Kılıç

Izmir International Biomedicine and Genome Institute

Dokuz Eylul University, 35430, Izmir, TÜRKİYE

ÖZET

Bu çalışma, akraba evliliklerinden doğan bir grup çocukta tanımlanan yeni mutasyonların doğrulanması ve karakterizasyonu yoluyla genetik hastalıkların aydınlatılmasını amaçlamaktadır. Üç pediatrik hasta daha ileri araştırmalar için seçilmiştir. Hastaların tümünde klinik olarak genetik hastalıklardan şüphelenilmesine rağmen bilinen genetik mutasyonlarla tanıları konulamamıştır. Klinik bulgular mikrosefali, motor-mental gerilik, nörogelişimsel bozukluklar ve epilepsiyi içermektedir. Tüm ekzom dizilimiyle, daha önce raporlanmamış aday mutasyonlar tanımlanmıştır: *WDR62* ve *ATG9B* genlerindeki nükleotid delesyonları, çerçeve kaymasına ve translasyonun erken sonlanmasına ve *VARS1* genindeki missense mutasyon bir amino asit değişikliğine sebep olmaktadır. Literatürde *WDR62* mutasyonlarının mikrosefaliye yol açtığı yaygın olarak raporlanmıştır. Bu nedenle WDR62 mutasyonu yalnızca Sanger dizilimi ile valide edilmiştir. *VARS1* mutasyonunun etkileri yapısal modelleme ile incelenmiş ve VARS1 proteini üzerinde destabilize edici etkilere sahip olduğu gösterilmiştir.

Bu tezin odak noktası *ATG9B* mutasyonudur. *ATG9B* herhangi bir genetik hastalıkla ilişkilendirilmemiş ve işlevi literatürde yeterince tanımlanmamıştır. ATG9B geninde tanımlanan on bir nükleotid delesyonu, proteinin kısalmasıyla sonuçlanan bir çerçeve kaymasına neden olmaktadır. WT ve mutant ATG9B hücrelerde ektopik ekspresyonla karakterize edilmiş ve *in vivo* çalışmalar için birkaç fare modeli geliştirilmiştir. Kısalan proteinin hücrelerde ifade edildiğinde stabil olmadığı gösterilmiştir. *In vivo* modelleri kullanarak Atg9b'nin plasenta ve testislerde ifade edildiğini ancak hayatta kalım veya üreme için gerekli olmadığı gösterilmiştir. WT ve mutant plasenta arasında büyük bir histolojik farklılık gözlemlenmemiştir. Öte yandan davranışsal analizler, homozigot knockin hayvanlarda korku hafızasının azaldığını ortaya çıkarmıştır. Ayrıca knockout ve FLAG knockin Atg9b fare modelleri geliştirilmiş ve işlevlerini *in vivo* ve *in vitro* olarak incelemek için antiserumlar üretilmiştir.

Anahtar kelimeler: Nadir genetik hastalıklar, Nörogelişimsel bozukluklar, Genetiği değiştirilmiş fare modelleri, ATG9B

1. AIM AND OBJECTIVES

The aim of this study is to identify, validate, and functionally characterize novel mutations that have not been linked to any disease in the literature. We studied three consanguineous families with children showing microcephaly, epilepsy, motor-mental disorders, and mental retardation. Due to consanguineous marriage, a genetic disease was suspected by clinicians but known genetic diseases were not diagnosed. Therefore, whole exome sequencing was performed, and three candidate gene variants were identified from each family on *WD-repeat protein 62* (*WDR62*), *Valyl-tRNA synthetase* (*VARS1*), and *Autophagy-related 9B* (*ATG9B*) genes. These variants were validated by Sanger sequencing characterized by an extensive literature review for *WDR62*, *in silico* structural modeling for *VARS1*, and ectopic expression studies in cells and genetically modified mouse models for *ATG9B*.

The first patient was presented with microcephaly and motor-mental retardation clinical findings. A novel mutation identified in the *WDR62* gene was a single-nucleotide deletion mutation on exon 1 of the gene causing a frameshift on the protein sequence. WDR62 functions in cell division localize to centrosomes and promote centriole duplication (1). Additionally, it is involved in spindle organization and stability during the cell cycle and is essential for normal brain development due to its function in neurogenesis (2). Mutations in the *WDR62* gene have been reported as causative for primary microcephaly, a condition described with a small head and abnormal brain development (3). The objective of *WDR62* research was to describe a novel frameshift mutation with autosomal recessive inheritance, causing microcephaly, lissencephaly, and motor-mental retardation and define the effect by taking advantage of the existing literature.

The second patient was presented with microcephaly and developmental delay. A novel mutation identified in the *VARS1* gene was a missense mutation due to single-nucleotide alteration. VARS1 is an aminoacyl-tRNA synthetase that attaches valine to its tRNA via anticodon recognition, by catalytic reaction (4). In the literature, mutations in aminoacyl-tRNA synthetases have been associated with neurodevelopmental disorders (5). In the *VARS1* gene, we saw that the mutation alters an amino acid in the anticodon binding domain. There were three other mutations reported in the literature in close proximity to the novel mutation that we have identified (6–8). The majority of aminoacyl-tRNA synthetase mutations causing neurodevelopmental disorders are located in the catalytic domain, despite the four mutations that are located in the anticodon binding domain within a 15-amino acid stretch. Therefore, our objective for this study was to apply *in silico* structural modeling approaches to ascertain the

effects of this cluster of mutations comprehensively, in order to identify the importance of the anticodon binding domain and the mutations.

The mutation that we were most interested in was in the *ATG9B* gene, causing mental retardation in children of consanguineously married couple. ATG9A and ATG9B proteins are the only transmembrane proteins in the autophagy pathway, ATG9B is a vertebrate and tissue-specific paralog of ATG9A (9,10). These two proteins are involved in autophagy, a core cellular degradation mechanism responsible for the catabolism of large, aggregated proteins, old or dysfunctional organelles, and pathogens (11). ATG9A is ubiquitously expressed therefore, its function is more verified. ATG9A functions as a lipid scramblase, elongating phagophore membranes for autophagosome formation (12,13). On the other hand, ATG9B is expressed in the pituitary gland, in reproductive organs, especially in the placenta (Protein Atlas). Additionally, functional characterization of ATG9B is very limited, it was suggested that ATG9B can rescue autophagy phenotype in the absence of ATG9A (10). ATG9B mutations are linked with a variety of diseases such as cardiovascular diseases and cancers yet, *ATG9B* variants are not linked with genetic diseases (14,15). Considering the lack of functional characterization of ATG9B and the novel mutation we have identified, we focused our objectives on ATG9B in cell and mouse models.

Characterization by cell culture model: We produced WT and mutated (truncated) ATG9B protein coding overexpression vectors to study the localization and expression of the protein by transient and stable cell models.

Characterization by mouse models:

Atg9b Knock-in Model of the novel genetic disease: To understand the effect of the mutation on the nervous system and placental morphology, we generated an *ATG9B* knock-in rare genetic disease mouse model mimicking the human mutation. Through this model, we focused on morphological abnormalities of the placenta, also the effect of the mutation on the nervous system by performing a series of cognitive tests.

FLAG-Atg9b Model: To study ATG9B protein expression in mammalian tissues we focused on developing FLAG tagged WT Atg9b mouse model to address which tissues express Atg9b by immunoblotting and histology assays.

Atg9b Knock-out model: Our initial objective was to create a conditional knock-out model for Atg9b, specific to the placenta. We hypothesized that the knock-out of Atg9b should have an effect on placental and fetal development. In the process, we obtained exon-2 deletion

mutations, since they were viable and can reach adulthood, we shifted our objective to study function of Atg9b in knock-out mice.

2. INTRODUCTION

Rare diseases are defined as diseases that affect a small number of people in the population (16). The definition of rare disease is complicated because of the lack of a global definition. The American Orphan Drug Act (1983) defined rare disorders with a prevalence of 86 per 100 000 people, the European Union defined with no more than 50 per 100 000 while other national definitions range from 5-76 per 100 000 (17). The Orphanet database contains descriptions of 6172 unique rare disorders including prevalence in geographic regions. 71.9% of the rare diseases are genetic and 69.9% affect pediatric patients. Rare diseases affect 263-446 million people in the world at any given time which constitutes 3.5-5.9% of the population worldwide (17). In Türkiye, nearly 7 million people are estimated to be affected by rare diseases with a prevalence of 38 per 100 000 (18). While affecting a small percentage of the human population, rare diseases are often life-threatening, complex, and chronic. Drugs to treat rare diseases are named as "orphan drugs" which are crucial for a small number of people and, therefore financially very unfavorable for drug companies to make investments (16). A survey with 498 individuals revealed recently that the majority of the rare disease patients were children, % 91 of them had a precise diagnosis, and almost 10% were undiagnosed. The rate of diagnosis was 69% for patients within their first six months of life. Access to physicians with relevant specialties was the main obstacle for % 81 of the patients, and reaching to orphan drugs was the obstacle for % 73 of them (19).

Diagnosis of a genetic disease can be dependent on single gene tests or gene panels when a small number of genes are suspected of the disease. Yet, whole exome sequencing (WES) is increasingly used as a diagnostic tool for disorders with genetic heterogeneity, complex neurologic symptoms, and multiple congenital abnormalities. Another valuable contribution of WES is leading to novel pathogenic variants of genes which have never been linked to any diseases. WES has been utilized for gene discovery for patients with autism, epilepsy, brain malformations, and neurodevelopmental disabilities. WES was able to give predictions analyzed and grouped(20):

- Definitive result (Category 1) pathogenic or likely pathogenic variants in a gene associated with disease phenotype.
- Possible/probable diagnosis (Category 2) variants in a gene possibly associated with disease phenotype.

- Novel candidate gene (Category 3) variants are predicted to be pathogenic in a novel candidate gene that has not been linked to any reported disease.
- Negative result (category 4) no variants in genes associated with the phenotype.(20)

While WES has immensely changed the diagnosis and discovery of rare genetic diseases, it has limitations. WES has non-uniform coverage and is challenged in first exons, high GC sequences, and low complexity regions. Therefore, it is crucial to confirm the variants with orthogonal methods such as microarray, qPCR, or Sanger sequencing (20,21).

Variants that are the subject of this thesis are in the genes:

- Category 1: *WD-Repeat Domain 62 (WDR62), Valyl-tRNA synthetase 1 (VARS1)*
- Category 3: *Autophagy related-9B (ATG9B)*

The subjects of this thesis are pediatric patients of consanguineous marriages with epilepsy, microcephaly, motor-mental retardation, and mental retardation. Patients were unable to be diagnosed with known pathogenic gene variants. Therefore, WES was performed with the peripheral blood of the pediatric patients and their immediate family. WES identified candidate gene variations, I will give brief information about their function and their link with genetic diseases.

WES studies have been interpreted utilizing Ensembl75, available in 2014 therefore the annotation will be used accordingly (22).

2.1.WDR62

WD-repeat domain 62 *(WDR62)* gene is localized at chromosome 19 with the genomic: GRCh37:CM000681.1:36545783:36596008:1. Human *WDR62* contains 32 exons encodes protein with 1523 amino acids. *WDR62* gene is evolutionarily conserved from *Drosophila* to humans (Figure 1).

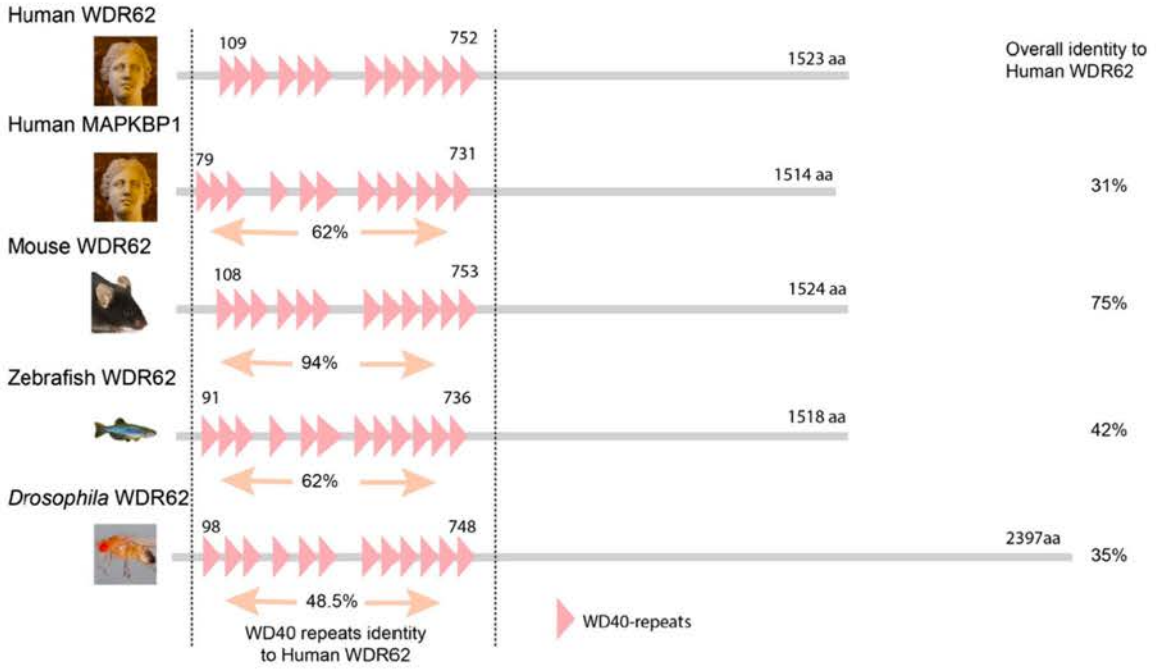

Figure 1. The conservation of *WDR62* gene. WD40 repeats are conserved from Drosophila to human (23).

WDR62 is a ubiquitously expressed scaffold protein. N terminal domain of WDR62 contains 12 repeats of WD40, C terminal loop contains MAP kinase kinase 7β1 (MKK7β1) and c-Jun N-terminal kinase (JNK) binding and dimerization domains (24). It is involved in mitogen-activating protein kinase (MAPK) pathway. MAPK pathway regulates cell proliferation, differentiation, and death depending on the signal stimulus.

Upon stress, G protein-coupled receptor (GPCR) agonists stimulus, JNK, and p38 MAPK proteins are activated for inflammation, apoptosis, growth, and differentiation responses (25). WDR62 binds and activates JNK through JNK binding domain but doesn't bind to other MAPK proteins such as p38 or ERK1. Upon stress stimuli, WDR62 expression increases by JNK and the protein localizes in stress granules (26). A mitotic Aurora A kinase (AURKA) also colocalizes with WDR62 specifically in the spindle poles and spindle microtubules. N terminal region of WDR62 is phosphorylated by AURKA mediating WDR62 localization in microtubules. During mitosis JNK phosphorylates WDR62 but this phosphorylation is not essential for spindle localization. (1). Targeting protein for Xklp2 (TPX2) is a spindle assembly factor, an upstream activator of AURKA, TPX2 binding to WDR62 causes recruitment of katanin and regulates spindle minus-end depolymerization (27,28).

Variations of *WDR62* have been identified as causative for autosomal recessive primary microcephaly (MCPH), category 1 pathogenic mutations (29). Microcephaly is described as significantly reduced head/brain size without structural abnormalities, mild/moderate cognitive impairment, and additional neurologic symptoms in patients with normal height and body weight. Primary microcephaly genes have been *MCPH1* at the first locus in chromosome 8, *MCPH2* (*WDR62*) at the second locus on chromosome 19 has been identified in multiple members of the consanguineous Pakistani family corresponding to the *WDR62* gene (30). MPCH is diagnosed during gestation and at birth, as a result of developmental abnormalities. For primary microcephaly, 17 causative genes have been identified including *WDR62* (MCPH2). Thirty-five pathogenic mutations have been associated with *WDR62* making it the most frequently mutated MCPH gene. Pathogenic and likely pathogenic variants are accessible through ClinVar database. Sixty-three pathogenic, and 35 likely pathogenic variants have been identified for *WDR62* presented as gene map (Figure 2) (29).

The clinical presentations associated with *WDR62* gene mutations are not limited to microcephaly and reduced brain size. The mutations cause diverse severe cerebral cortical malformations such as pachygyria (incomplete lissencephaly), and cortical thickening. Some patients exhibit schizencephaly (cerebral hemisphere clefts), cerebellar hypoplasia, and polymicrogyria due to *WDR62* mutations. While these were previously regarded as separate diseases, *WDR62* mutations were shown to be causative, by studying patients from eastern Turkey. It was also shown that WDR62 is expressed in developing mouse brains by the same authors (31). Pathogenic variants detected in *WDR62* are autosomal recessive nonsense, frameshift, base pair duplications, splice-site site alterations, compound heterozygous deletions which likely result in non-functional protein, severe truncation or nonsense-mediated decay.

Naturally, children of consanguineous marriages not only provided with the identification of novel pathogenic variants with autosomal recessive inhertance, but also led to the discoveries of the protein function by phenotype to genotype approach (23,32).

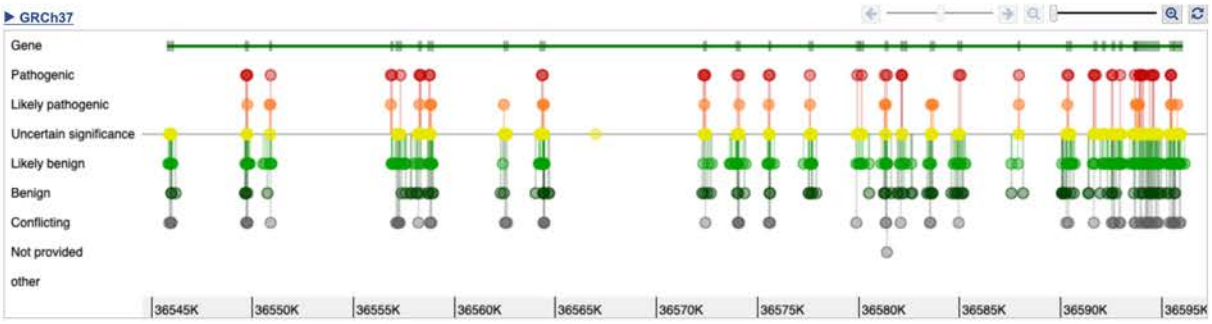

Figure 2. The map of mutations reported for *WDR62* gene in ClinVar (29).

One family from Mexico with distantly related parents had 3 children with severe microcephaly, developmental delay, and seizures and one healthy child. A second family from Türkiye were identified with similar symptoms (33). Interestingly, this family had a prenatal death of a male fetus previously described and identified for Norman—Roberts syndrome (34). These children had small brains, small Gyra, corpus callosal abnormalities, polymicrogyria, schizencephaly, and subcortical heterotopia with brain asymmetry. These families were both identified for novel *WDR62* pathogenic variants by insertion or deletion, causing frameshift. The expression of *WDR62* mRNA in developing mouse embryos was studied in 14.5 dpc by *in situ* hybridization and showed that *WDR62* localized in the cortical plate (33). In addition, it was also shown that WDR62 protein localizes at Golgi, and colocalizes with centrosome protein CEP170 and dynein at spindle poles in mitotic cells (33). In interphase, WDR62 localized at nucleoli (35). In light of these studies, the function of WDR62 was postulated to be in cell division and the brain abnormalities arising from mutations in the WDR62 gene may be attributed to disruptions in this cellular process. (33).

Studies exploring WDR62 mutations have enhanced our understanding of its functional role. The discovery of 7 new pathogenic variants in Pakistani and Caucasian families led to the comparative functional studies of WT and mutants in cells. The authors confirmed previous literature on WDR62 localization at spindle poles during mitosis. One missense mutation and one frameshift mutation were introduced into WDR62-GFP constructs and mutants failed to localize at spindle poles during mitosis. Therefore, it was hypothesized that the disease mechanism is due to mitotic deficiency in neural progenitor cells. They performed studies with embryo brains at 11, 13, and 15 dpc, which showed endogenous WDR62 is localized in the cytoplasm of mitotic apical and basal neural precursor cells, newborn neurons, and newly migrated cortical neurons. Neuroepithelium expression of WDR62 is only detected in apical

mitotic precursors which are the only mitotic cells in neuroepithelium. Intermediate neural precursors also express WDR62 exclusively during mitosis. In the human embryonic brain corresponding to 13 dpc of the mouse in terms of neurogenesis, WDR62 was expressed expression in neural precursor cells (36).

Another group studied WDR62 in rat brains and showed that WDR62 is expressed in the ventricular zone (VZ) and subventricular zone (SVZ). Knockdown of WDR62 resulted with the limited influx of neural progenitor cells to the cerebral cortex which could only be rescued by WT WDR62, as opposed to mutant WDR62. WDR62 knockdown also resulted with a decreased number of apical progenitor and radial glial cells. In contrast, WDR62 knockdown caused an increased number of intermediate and basal progenitor cells in VZ/SVZ in the first couple of days, then the number decreased in days 3-4. These observations suggested premature differentiation and then depletion of basal intermediate progenitor cells. The mechanism was hypothesized as WDR62 knockdown decreased mitotic cells resulting in their premature differentiation. Upon mitotic induction, the knockdown of WDR62 in HeLa cells resulted in increased multipolar spindles suggesting compromised spindle organization. Knockdown of JNK has similar defects as WDR62, a known binding partner of WDR62. Upon mitotic induction, WDR62 and JNK colocalize near nuclei at centrosomes suggesting WDR62 may control neurogenesis through JNK (2).

Taken together, the mechanism of action of the MHPC phenotype resulting from *WDR62* mutations was proposed to be due to a deficiency of neurogenesis due to its integral role in mitosis, especially in neural progenitor cells (2).

In recent years, a variety of diseases have been linked to *WDR62* such as autism (37), and congenital heart diseases (CHD) (38). CHD is the most common birth defect worldwide. Four heterozygous point mutations have been identified in CHD patients. The mutations were modeled in zebrafish, the phenotype showed heart looping and chamber growth. By generating *Wdr62* knockout mice they showed *Wdr62* regulates cell proliferation by spindle assembly by interacting with AURKA and the knockout mice showed heart defects et 14.5 dpc (38). Autism spectrum disorder (ASD) has genetic and clinical heterogeneity. Patients often have impairment of reciprocal social interactions, repetitive behaviors, and restricted interests. WES identified point mutations in *WDR62* in Chinese sporadic ASD patients (39). In another study, *Wdr62* knockout mice had reduced brain size, impaired learning and memory, microcephaly, also ASD-like behavior in mice. A conditional differentiated neuron specific *Wdr62* knockout

mouse model was also generated, while these mice had normal brain size they showed ASD-like behavior. Morphological analysis of mouse brains revealed that the secondary dendritic branching is reduced, and dendritic spine development is compromised in pyramidal neurons, indicating lower complexity in the brain. Oral gavage retinoic acid treated the ASD-like behavior in mice, possibly by increasing the expression of synapse-related genes (37).

The role of WDR62 has been elucidated more effectively in recent years and the pathogenic variants that are discovered provided substantial insights for its function. *WDR62* was first discovered as a disease-causing gene, pathogenic variants of microcephaly helped the discovery of WDR62 function *in vitro* and *in vivo*. It is important to state that the identification and study of rare genetic diseases often lead to characterizing the function of proteins and a better understanding of cell biology and mammalian biology.

2.2. VARS1

Valine-tRNA synthetase (ligase) 1 *(VARS1)* gene is localized at chromosome 6 with the genomic coordinates of: GRCh37:CM000668.1:31745295:31763730:1(22). It is a member of cytoplasmic aminoacyl class I tRNA synthetases having 30 exons coding for VARS1 protein with 1264 amino acids (22).

Aminoacyl-tRNA synthetases (ARSs) are ubiquitously expressed housekeeping genes. They catalyze the esterification reaction of amino acids to their target tRNA, the product of the reaction being aminoacyl-tRNA. Aminoacyl tRNA synthetases are named after the product of their reaction such as Valyl-tRNA synthetase ValRS or MARS. In humans, there are 37 aminoacyl tRNA synthetases. The cytoplasmic and mitochondrial aminoacyl tRNA synthetases are designated with numbers. For example, example MARS1 for cytoplasmic, and MARS2 for mitochondrial aminoacyl tRNA synthetase. Bifunctional glycyl (GARS), lysyl (KARS), and glutaminyl-tRNA synthetases (QARS) work both in the cytoplasm and mitochondria (5).

Aminoacylation is a two-step, ATP-dependent anabolic reaction. In the first step, aminoacyl-tRNA synthetase binds to the amino acid and ATP forming an aminoacyl-AMP intermediate, releasing pyrophosphate (PP_i). In the second step, tRNA binds to an amino acid by anticodon binding domain, releasing AMP. Then, the free aminoacyl-tRNA synthetase can catalyze another amino acylation reaction (Figure 3) (40).

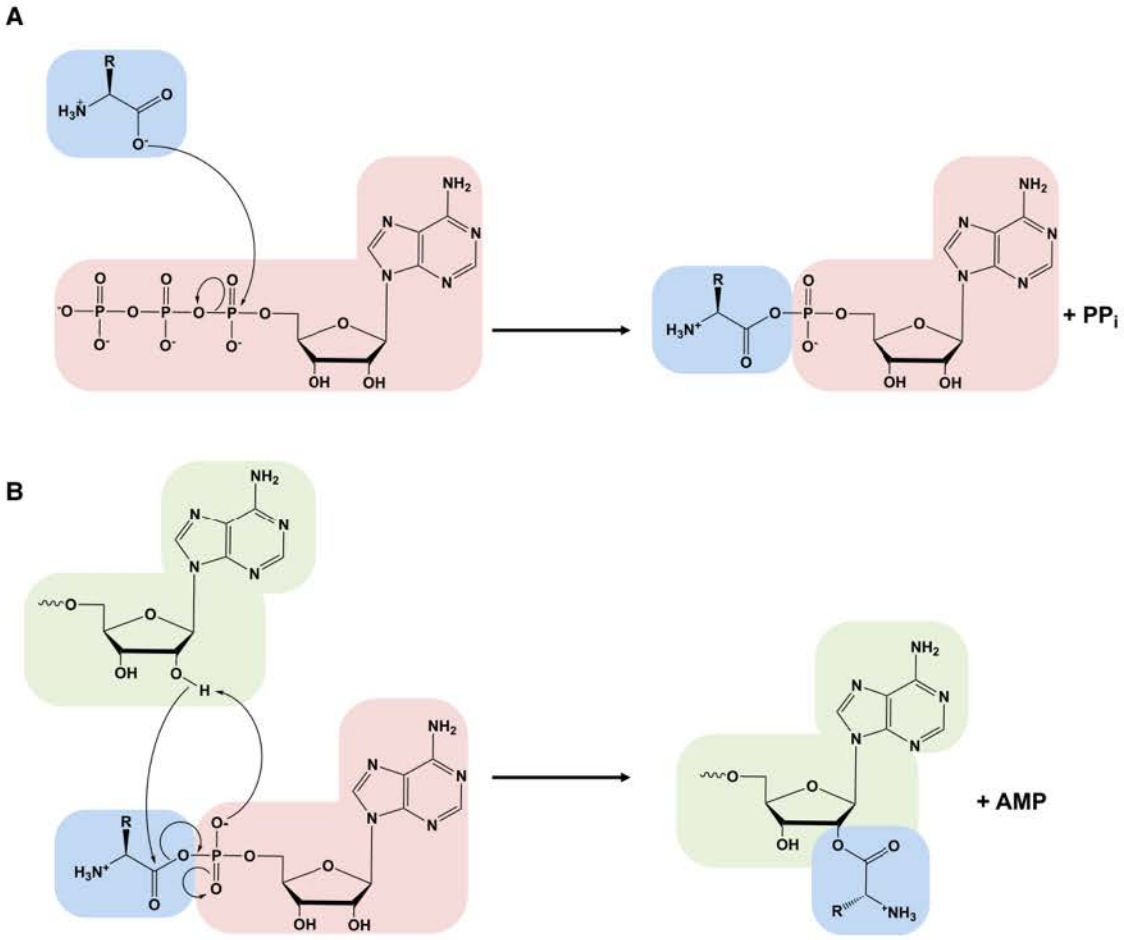

Figure 3. The amino-acylation reaction. This is a 2-step reaction that first, aminoacyl tRNA synthetase binds to the amino acid forming an aminoacyl-AMP intermediate while in the second step, tRNA binds to an amino acid by anticodon binding domain releasing the aminoacyl tRNA synthetase and AMP. (40).

There are 2 classes of aminoacyl-tRNA synthetases based on their active sites. Class I ARS are usually monomeric, the catalytic domain has a dinucleotide or Rossman fold (RF) with five stranded parallel β-sheets connected by α helices. RF contains conserved motifs HIGH and KMSKS separated by connective peptide 1 (CP1). The anticodon binding domain is usually located downstream of the catalytic domain. Class II ARS are homodimeric, the catalytic site has 7 β-sheets flanked by α helices less conserved than Class I. Class I has 3 motifs: motif 1 contains a long α-helix connected to β-strand, terminated by conserved prolines involved in the dimer interface. Motif 2 and motif 3 make up ATP and amino acid binding sites. Anticodon binding domain approaches tRNA through the major groove (4,5) (Figure 4). Class I aminoacyl synthetases are further divided into 3 subgroups according to their sequence and structural

similarity. Valyl-tRNA synthetase (VARS1), together with LARS1, MARS1, CARS1, RARS1 belong to ClassIa subgroup. VARS1, IARS1, and LARS1 are evolutionarily related, CP1 has a proofreading and editing role to distinguish and select against near-cognate amino acids (double sieve mechanism). The crystal structure of *Thermus thermophilus* valyl-tRNA synthetase (ValRS) helped the understanding of VARS1-tRNA^{Val} and provided a template to model human VARS1 to be modeled based on its conservation with human VARS1 (41).

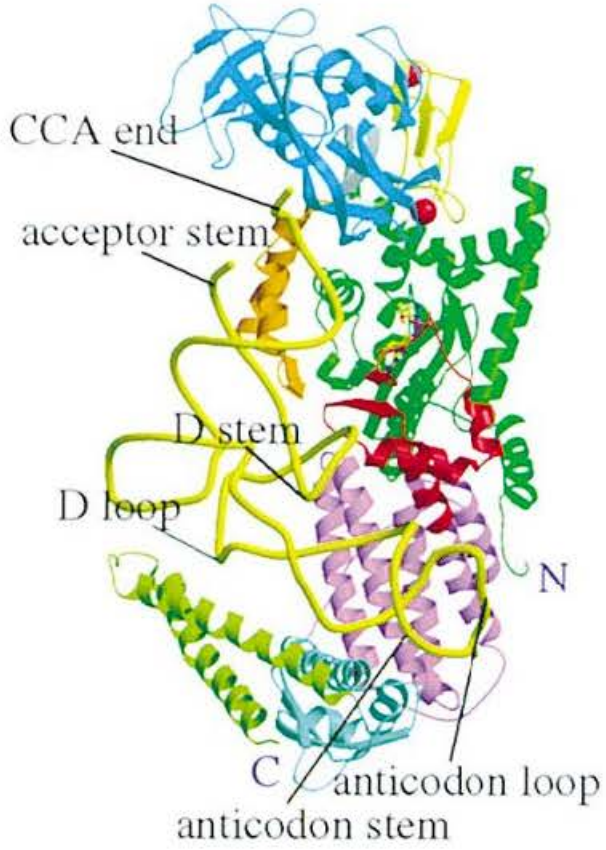

Figure 4. The crystal structure of ValRS of *Thermus thermophilus*. This protein has 6 major domains: Rossman fold domain – green, connective peptide CP-1, CP-2, CP-3 – cyan-orange-yellow, stem-contact domain (SC) – red, anticodon binding domain – magenta, anticodon-stem binding junction domain – light blue, C-terminal coiled-coil domain – light green. Zinc ions – red spheres (42).

Since aminoacyl-tRNA synthetase function is critical for protein synthesis, mutations of these genes have been associated with genetic diseases in the literature. These diseases are often related to encephalopathy, cerebellar ataxia, peripheral neuropathy, and diseases that are

related to the development and function of neurons. Isoleucyl-tRNA synthetase 1 (*IARS1*) is a class I ARS recessive or biallelic missense mutation implicated with growth retardation, impaired intellectual development, hypotonia, and hepatopathy (43–46). Heterozygous missense mutations in Alanyl-tRNA synthetase 1 (*AARS*) have been linked with leukoencephalopathy, developmental and epileptic encephalopathy, axonal Charcot-Marie-Tooth disease type 2N which is a mild type of the disease with slow progression and peripheral sensorimotor neuropathy phenotype (47–49). Autosomal dominant mutations in *GARS* and *YARS* genes, also have been linked with different types of Charcot-Marie-Tooth disease (5).

Among 20 cytoplasmic and bifunctional tRNA synthetases, 96 missense mutations have been associated with genetic diseases. The majority of these mutations, of 61% are identified in the tRNA synthetase (catalytic) domain, 9% in the anticodon binding domain, and 28% in other domains of the proteins (29) (Table 1).

Table 1. Domain-specific pathogenic mutation number of aminoacyl-tRNA synthetases.

	tRNA synthetase	Anticodon	Other	Total
VARS1 (VALINE)	8	4	5	17
LARS1 (LEUCINE)	2	0	0	2
IARS1 (ISOLEUCINE)	5	1	2	8
AARS1 (ALANINE)	4	0	1	5
RARS1 (ARGININE)	2	1	3	6
QARS (GLUTAMINE)	2	0	2	4
NARS1 (ASPARAGINE)	0	0	0	0
DARS1 (ASPARTIC ACID)	6	0	0	6
KARS (LYSINE)	1	2	0	3
EPRS (GLUTAMIC ACID, PROLINE)	5	0	0	5
CARS1 (CYSTEINE)	0	0	0	0
TARS1 (THERIONINE)	0	0	0	0
MARS1 (METHIONINE)	7	0	3	10
HARS1 (HYSTIDINE)	5	1	0	6
FARSA (PHENYLALANINE)	0	0	0	0
FARSB (PHENYLALANINE)	4	0	2	6
YARS1 (TYROSINE)	5	0	1	6
WARS1 (THERIONINE)	0	0	1	1
GARS (GLYCINE)	2	0	8	10
SARS1 (SERINE)	1	0	0	1
TOTAL	**59**	**9**	**28**	**96**
Percentage	**61**	**9**	**29**	**100**

In the literature a variety of *VARS1* mutations were identified leading to a rare neurodevelopmental disorder. In one study, pediatric patients were two daughters born of a consanguineous marriage of a Turkish family clinically presented with microcephaly, seizures, and cortical atrophy. One of the missense mutations causing p.L885F change located at catalytic tRNA-synthetase domain while the other causing p.R1058Q located in the anticodon binding domain. Later, p.L885F substitution was modeled in yeasts and was showed that yeast sustained growth in complementation assay (7,8).

A boy of Indian origin and unrelated parents was presented with similar clinical findings and compound heterozygous mutations have been identified in the *VARS1* gene. The missense mutation was causing p.M1064I alteration, located in the anticodon binding domain, predicted to have a destabilizing effect on the protein. Functional studies with cells derived from the patient suggested that VARS1 mRNA expression is reduced by 50%, a 4-fold reduction of aminoacylation activity, and decreased VARS1 protein level. There was also a frameshift mutation causing splice site alteration which causes exon 13 deletion. This mutation was predicted to affect both catalytic and anticodon binding domains, yet studies with patient cells showed nonsense-mediated decay in mRNA. The older brother of the proband unfortunately had died 12 months after birth (6).

In another report, a 5-year-old Egyptian girl of consanguineous marriage presented with similar symptoms. A p.R947H alteration located on the catalytic domain of the VARS1 protein due to a homozygous missense mutation in the *VARS1* gene was detected. Experimental studies with patient cells demonstrated similar levels of expression with the WT VARS1 protein but the enzymatic activity was reduced. Additionally, 3 patients from 2 unrelated consanguineous families from Egypt were reported with similar symptoms, and a *VARS1* missense mutation causing p.R1119C was reported to result in reduced enzymatic activity and similar levels of protein with WT (50).

p.L434V and p.G822S substitutions were detected in 2 brothers of German descendants causing lower enzymatic activity due to compound heterozygous missense mutations (7).

For the exploration of the VARS1 function, a zebrafish CRISPR/Cas9-based *vars1* knockdown model was generated. The knockdown of *vars1* resulted in phenotypes of increased death, loss of posture and behavioral abnormality, progressive microcephaly, and increased apoptosis in zebrafish (7). The reported mutations in the literature was presented as gene map(29) (Figure 5).

In the scope of this thesis, it is important to recognize the detrimental effects of pathogenic missense mutations in aminoacyl-tRNA synthetases and *VARS1*. Most of the mutations that are reported in the *VARS1* are located in the catalytic domain or near, but in the anticodon binding domain, while the mutations are less frequent, they are closely clustered.

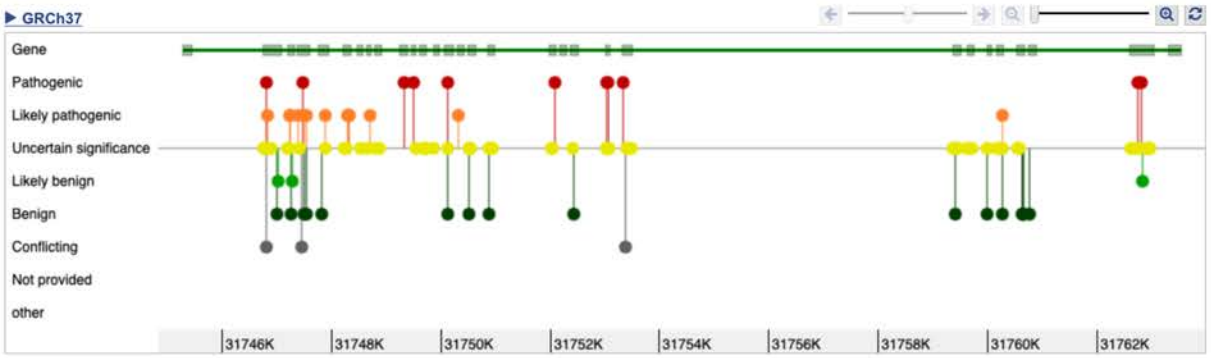

Figure 5. Pathogenic variants in identified in *VARS1* gene. Red spheres are indicated in red and likely pathogenic variants are indicated in orange (29).

2.3.ATG9B

ATG9B located at chromosome 7 with the coordinates of GRCh37:CM000669.1:150709297:150721586:1 (22). ATG9B protein has 19 exons coding for a 924 amino acid protein and is involved autophagy mechanism.

Forty autophagy-related genes (ATG) have been identified in yeast, and their mammalian homologs have been discovered (51). Autophagy is a core cellular degradation mechanism for large cytoplasmic cargo, the conservation of autophagy mechanism underscores its significance in cellular homeostasis and survival. The process of autophagy can be divided into three key stages: nucleation, membrane elongation, and fusion/degradation within lysosomes.

2.3.1. Mechanism of Autophagy

The fundamental autophagy mechanism has been conserved from yeasts to mammals in all eukaryotic organisms. This process comprises three mean stages:

Nucleation: The initiation of autophagy involves the ULK1-ATG13-FIP200 complex, which maintains stability irrespective of the nutritional state of the cell. In nutrient-rich conditions, Mammalian target of rapamycin complex 1 (mTORC1) suppresses autophagy by phosphorylating Atg13 and ULK1. Upon starvation, mTOR inhibition activates ULK1, leading to its autophosphorylation. This event induces trans-phosphorylation of ATG13 and FIP200.

Activated ULK1 also stimulates PI3K, initiating PI3P synthesis at sites of autophagosome formation initiating the formation of isolation membrane (phagophore). The PI3K complex, comprising VPS34, VPS15, ATG14, and Beclin1, plays a pivotal role in this process, with particular emphasis on Beclin1's contribution to VPS34 activity (52).

Membrane Elongation: Membrane elongation of phagophores involves two ubiquitin-like proteins, ATG12 and LC3. ATG12 is activated by the E1-like enzyme ATG7 and transferred to an E2-like enzyme ATG10. ATG12 then binds to ATG16L1. LC3, present as LC3-I in the cytoplasm, is cleaved at its C terminus by ATG4B and activated by ATG7, allowing it to bind with ATG3. LC3 is covalently conjugated with phosphatidylethanolamine (PE), forming LC3-II, which localizes to phagophores and autophagosomes. This lipidized form of LC3 is essential for autophagy and is commonly used as an autophagy marker. LC3-II within autophagosomes participates in binding autophagy-targeted cargoes such as SQSTM1/p62 and facilitates their sequestration (53).

Fusion and Degradation: Autophagosome-lysosome fusion is essential for autophagy progression involving various steps and proteins. The V-ATPase complex binds with RAB GTPases such as RAB7, RAB22, and RAB24. Dynein proteins transport autophagosomes to lysosomes along microtubules. SNARE proteins facilitate the fusion of autophagosome and lysosome membranes. Syntaxin17 is involved in autophagosome recognition, while cytoplasmic SNAP29 and lysosomal membrane SNAREs (VAMP7 or VAMP8) control fusion. The result of this fusion is the autolysosome, where the cargo is degraded by lytic enzymes (54).

2.3.1.1. The Role of Atg9 in Autophagy in Yeasts

Atg9 is a pivotal autophagy-related protein initially discovered in yeast, having a critical role in functional autophagy. This transmembrane protein is unique in its involvement in autophagy processes. It resides in perivacuolar puncta structures and cycles between mitochondria and phagophore assembly sites (PAS) (55,56). Atg1, an essential autophagy regulator, activates myosin light chain kinase (MLCK), resulting in myosin activation. This activated myosin II drives the movement of Atg9 vesicles from the trans-Golgi network (TGN) to phagophore assembly sites, which are crucial for autophagy (57).

Atg9 relies on the Atg1-Atg13 complex and Atg18 during PAS cycling. The recycling of Atg9 is facilitated by Atg2 and the PtdIns 3-Kinase complex I. Atg9's trafficking involves anterograde transport to PAS through Atg23 and the actin cytoskeleton while the retrograde movement of Atg9 to mitochondria is regulated by, Atg13, Atg2, Atg18, and PtdIns3-Kinase Vps34 (58). Another transmembrane protein Atg27, essential for specific and bulk autophagy Atg27 facilitates Atg9 cycling between PAS, mitochondria, and the Golgi complex, contributing to autophagy efficiency (59). The majority of Atg9 puncta exhibit high mobility, with only a fraction of Atg9 residing in Golgi, endosomes, and mitochondria are immobile. Knockouts of Atg23 and Atg27 lead to a reduction of mobile Atg9 vesicles, affecting their localization. Atg9 overexpression leads to Golgi-associated accumulation, suggesting a need for regulated expression. The assembly of Atg9 vesicles at PAS is required for the formation of autophagosomes (60). Atg9 particle mobility occurs through free diffusion, with vesicles averaging at a certain diameter. Each vesicle contains a specific number of Atg9 molecules, which increases under autophagy-inducing conditions (61). Atg9 is a self-interacting protein through its C-terminal cytosolic domain, demonstrated by mutation models targeting different domains of the Atg9 in yeast. In both nutrient-rich and starvation conditions, Atg9 self-multimerization is essential for its function in autophagy (62).

SNARE proteins, responsible for vesicle fusion, play a role in phagophore biogenesis. The Golgi apparatus acts as a membrane reservoir for autophagy, facilitated by proteins like Rab GTPase Sec5 and its GEF counterpart Sec2. Coordinating with SNARE proteins such as Sso1/2, Sec9, Snc1/2, and Sec22/Ykt6, Rab GTPases promote vesicle fusion in autophagy (54). Trs85, a subunit of the TRAPIII complex involved in vesicle trafficking, interacts with Atg9 and assists in recruiting autophagy proteins. Trs85 has a role in the recruitment of Atg9 vesicles to PAS, along. Activated by Trs85, Yeast Rab GTPase 1 (Ypt1) is involved in the delivery of Atg9 vesicles to PAS by tethering and fusion of the vesicles (61). Phosphoinositides, including PtdIns3P and PtdIns(3,5)P2, regulate cellular membranes and are involved in autophagy. Vps34, Atg14, Vps30, and Vps15 form a complex crucial for autophagy regulation. PtdIns4P, generated by Pik1, influences Atg9 movement and localization, affecting autophagy processes (63).

Additionally, cellular organelles are important in Atg9 sorting. Mitochondrial impairment disrupts Atg9 sorting, as observed when the ER-mitochondria network is targeted by *sed5* and *sec12* gene mutations. The absence of the Vps fifty-three (VFT) tethering complex affects

autophagy and the CVT pathway, essential for Golgi-mediated protein transport. The mutants that are defective for Endoplasmic Reticulum (ER) and Golgi demonstrated disruptions in Atg9 transportation to PAS (59).

In the process of autophagy activation, Atg1 directly phosphorylates Atg9 and Atg2 in autophagy activation. Six Atg1 consensus-matching phosphorylation sites were identified. Two of these S657 and S948 were phosphorylated *in vitro*. 4 of the 6 phosphorylation sites (S802, S831, S948, S969) was phosphorylated by Atg1 located at C-termini. Mutations of these sites disturbed Atg9's was also shown to recruit Atg2 and Atg18 (64).

The mechanism of action of Atg9 in phagophore expansion has recently been elucidated. Atg9 functions as lipid scramblase in phagophore assembly sites translocating phospholipids between outer and inner leaflets of liposomes. Lipid scramblases are responsible for the bi-directional transport of lipids independent of ATP. Atg2 is a phospholipid transfer protein, receiving membrane from Endoplasmic Reticulum and deliver to phagophores where it is translocated from cytoplasmic to the luminal leaflets by Atg9. Atg9 thereby elongates the phagophore membranes by transporting phospholipids bi-directionally. Atg9 forms a homo-trimer with two connected pores. The pores form a path between the membrane leaflets one protomer opens laterally to the cytoplasmic leaflet while the one located at the trimer center passes through the membrane vertically. Atg9 protomer structure has six membrane-buried regions, and cytosolic HINGE and ARCH domains composed of N-terminal, Middle, and C-terminal cytosolic portions. ARCH domain forms the lateral pore by extensive hydrophobic interactions. The HINGE domain connects protomers to form trimer and forms large vertical pore. These pores are essential for phagophore expansion and mutations affecting the regions involved result in defective autophagy. The study uncovered Atg9 structure and function for both yeast Atg9 and its mammalian ortholog ATG9A (Figure 6) (65).

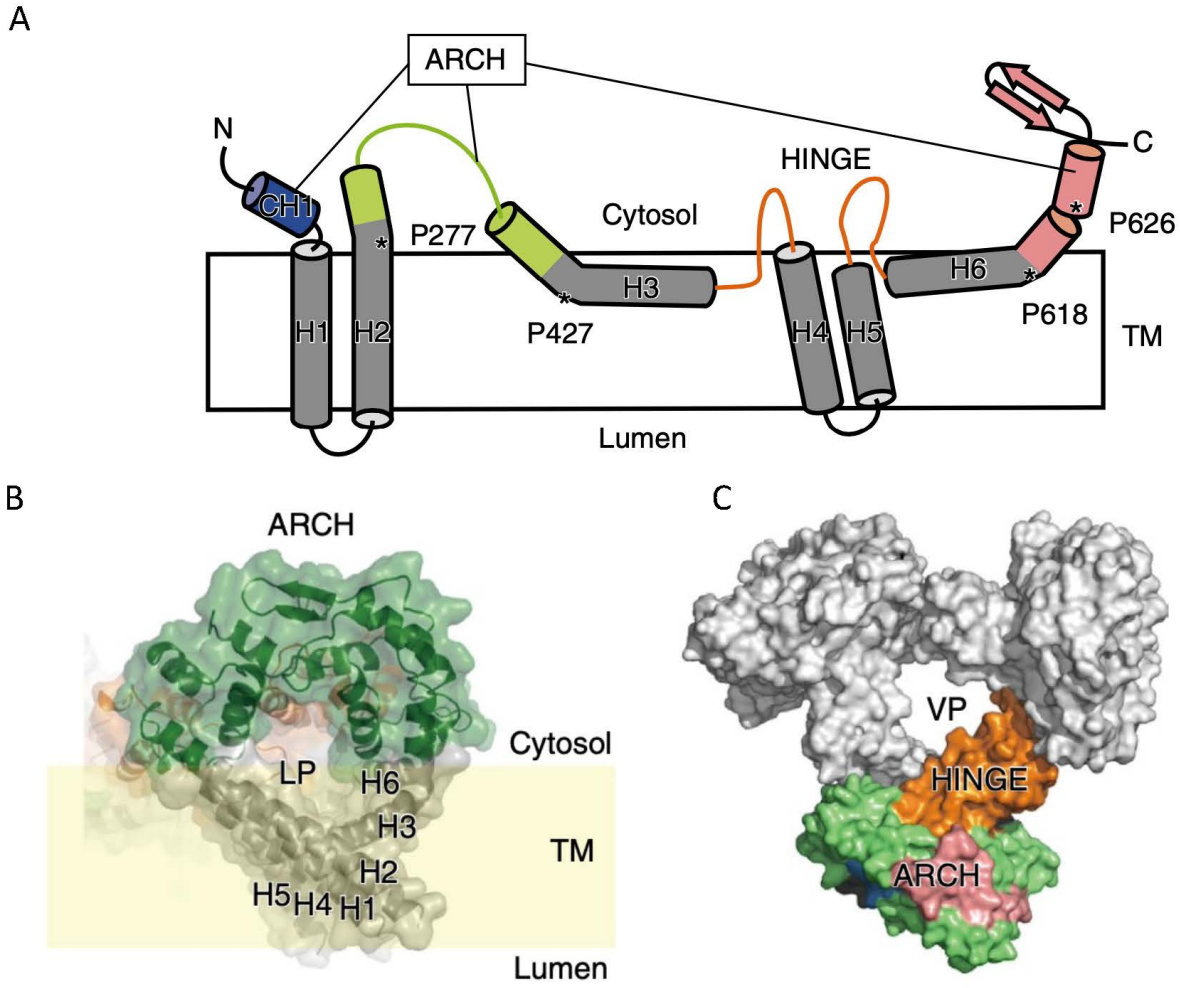

Figure 6. The structure of yeast Atg9. A) Schematic representation of Atg9 demonstrating topology, with a particular focus on the ARCH and HINGE domain contributors (colored). B) Structural model representing ARCH domain and lateral pore. C) Structural model representing ARCH and HINGE domains with vertical pore.

2.3.2. The Role of ATG9 Proteins in Mammalian Autophagy

The ATG9 protein is involved in the earliest stages of autophagy, providing membrane transport from cellular membrane sources to phagophores during the autophagosome formation process. The protein found in yeast as Atg9 has two orthologs in humans, ATG9A and ATG9B. They are the only trans-membrane protein in the autophagy pathway. In mammals, ATG9A cycles between the Trans-Golgi Network (TGN), recycling endosomes, and endosomal compartments (66). Upon starvation and other autophagy-inducing conditions, it disperses as puncta in the cytoplasm and goes to phagophore formation sites.

ATG9A trafficking is regulated by the proteins involved in the Golgi-endosome-ER trafficking. Initially, the Unc-51 like autophagy activating kinase (ULK) complex (Homolog of yeast Atg1) is critical in the ATG9A trafficking from TGN to the ATG9A. In addition, p38IP induces ATG9A upon amino acid starvation. When p38IP was reduced, ATG9A trafficking is disturbed and ATG9A remained in endosomes (67). Adapter protein complexes AP1 and AP4, BAR-domain-containing proteins such as Bif-1, SNX18, and Arfaptin proteins are involved in the movement of ATG9A from the TGN and endosomal compartments to phagophores (Figure 7) (68,69).

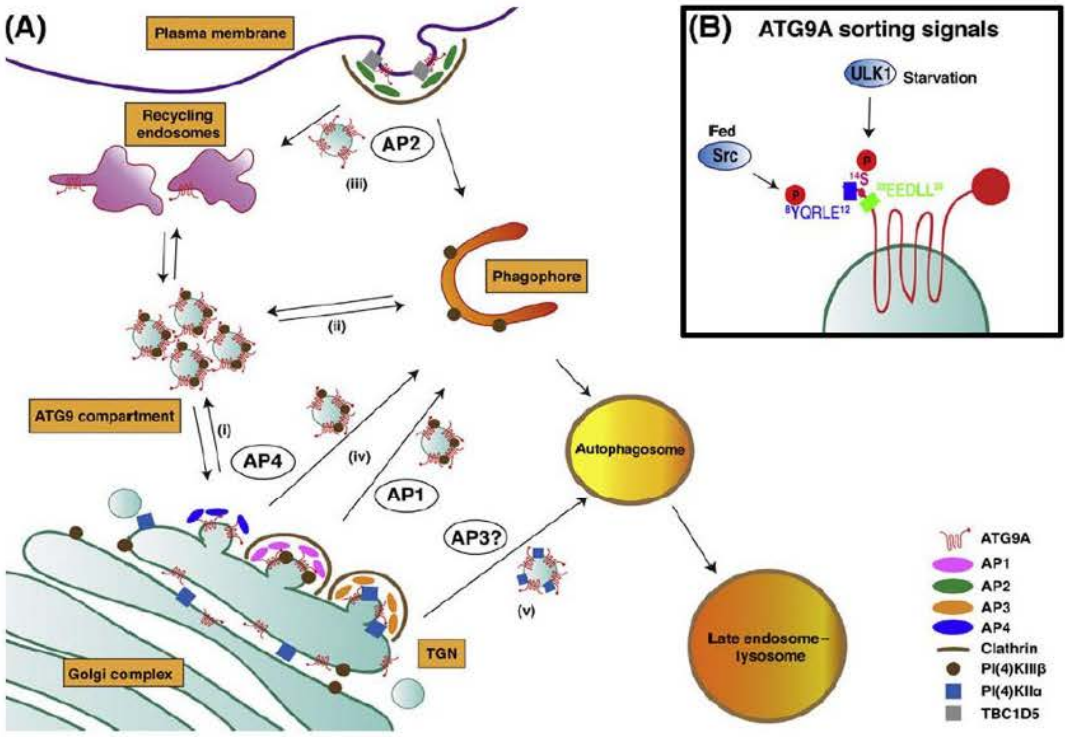

Figure 7. The dynamic intracellular traffic of ATG9A. A) ATG9A trafficking from the TGN to PAS is regulated by AP1 and AP4 complexes. Vesicles containing AP2 are transported from the plasma membrane and endosomes to autophagosome formation sites via TBC1D5. B: The traffic of ATG9A vesicles is possible during starvation conditions through phosphorylation of the cytoplasmic N and C termini of ATG9A by ULK1 (70).

ATG9A is involved in phagophore biogenesis, in the initiation of autophagy. Studies in yeast and humans have shown that there are phosphorylated sites in the cytoplasmic N-terminal region and C-terminal region of the protein, excluding the transmembrane regions for ULK1. ULK1 phosphorylates serine residues, one at the N-terminal and the other four at the C-terminal

cytoplasmic sites in ATG9A. These phosphorylations are critical for the proper functioning of ATG9A and functional autophagy. Serine 761 is phosphorylated by ULK1 at a low level under basal conditions. This phosphorylation forms a docking site for the 14-3-3ζ protein to an RXXpS/TXP binding motif. 14-3-3ζ is involved in the stress response in cells, modulating cell survival (71).

ATG9A transiently interacts with ULK1 partner, ATG13, and the autophagosome marker LC3 (72). Although there are proteins involved in ATG9A trafficking, the interaction of ATG9A with these proteins are transient. However, ATG9A colocalized with phagophore markers (example: DFCP1-23%) (73).

Recently, ATG9A has been shown to take a role in phagophore expansion through lipid scramblase activity independent of ATP energy. ATG9A and yeast Atg9 have been shown to trimerize in a lipid scramblase fold with cryo-electron microscopy. The central pore of the trimer is hydrophilic which spans the bilayer (74). Structurally yeast Atg9 and human ATG9A are similar. ATG9A trimer is shown to be able to bend lipid bilayers, bind with ATG2A which carries to the donor membrane through the ATG9 core domain, and exert scramblase activity in phagophore expansion (75) (Figure 8).

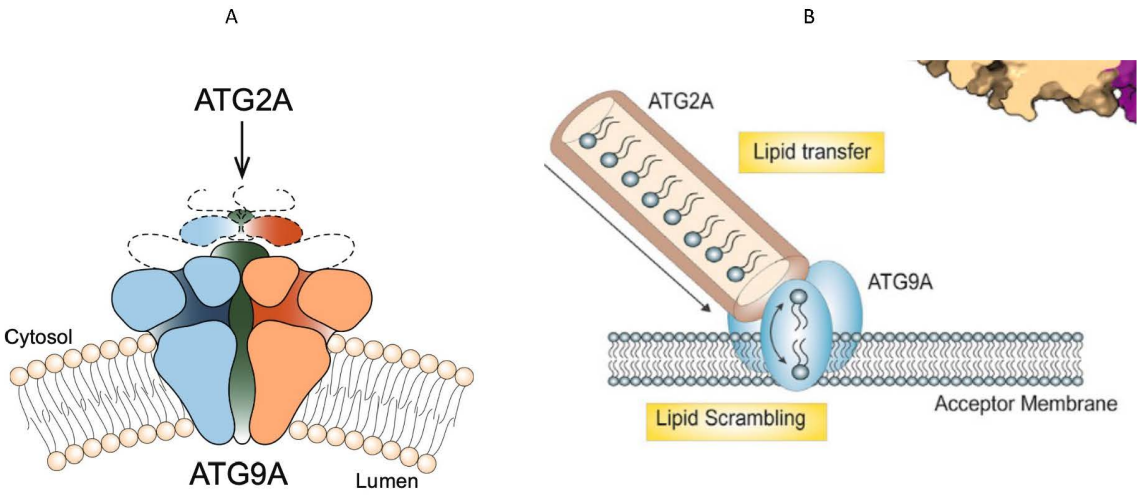

Figure 8. The lipid scramblase activity of ATG9A.Heterotetrameric structure of ATG9A-ATG2A complex B) The localization and lipid scramblase activity of ATG9A-ATG2A complex on the acceptor membrane. ATG9A itself is a homotrimeric protein. By ATG2A binding heterotetrameric complex functions as lipid scramblase in membrane mechanism (74,76).

ATG9A involvement in intracellular lipid regulation began to reveal ATG9A roles beyond autophagy involvement. ATG9A is shown to protect against plasma membrane damage (77). Moreover, ATG9A can exert the scramblase activity from intracellular lipid droplets for phagophore expansion (78).

Recent evidence has emerged indicating that ATG9A undergoes N-linked glycosylation at Asparagine 99 in the endoplasmic reticulum (ER) prior to its translocation to the Golgi, where it encounters complex glycans associated with N-linked glycosylation. This maturation process results in the appearance of two distinct bands when analyzing ATG9A via immunoblotting. When ATG9A is ectopically overexpressed, during the early hours, the dominant band is enriched in the ER, whereas after 24 hours or longer, the dominant band is enriched in the Golgi (79).

Furthermore, a non-canonical role for ATG9A in organizing Golgi structure and function has been identified. Upon heat stress, which leads to Golgi fragmentation, ATG9A undergoes K63 non-degradable ubiquitination mediated by Membrane-Associated RING-CH 9 (MARCH9) E3-ubiquitin ligase for Golgi-associated proteins. This ubiquitination is through K63 and non-degradable, which affects both N-terminal and C-terminal lysine residues of ATG9A, and results in the inhibition of Golgi reassembly and stacking protein of 55kDa (GRASP55) oligomerization. Consequently, GRASP55 inhibition leads to Golgi fragmentation in stress response (80) (Figure 10).

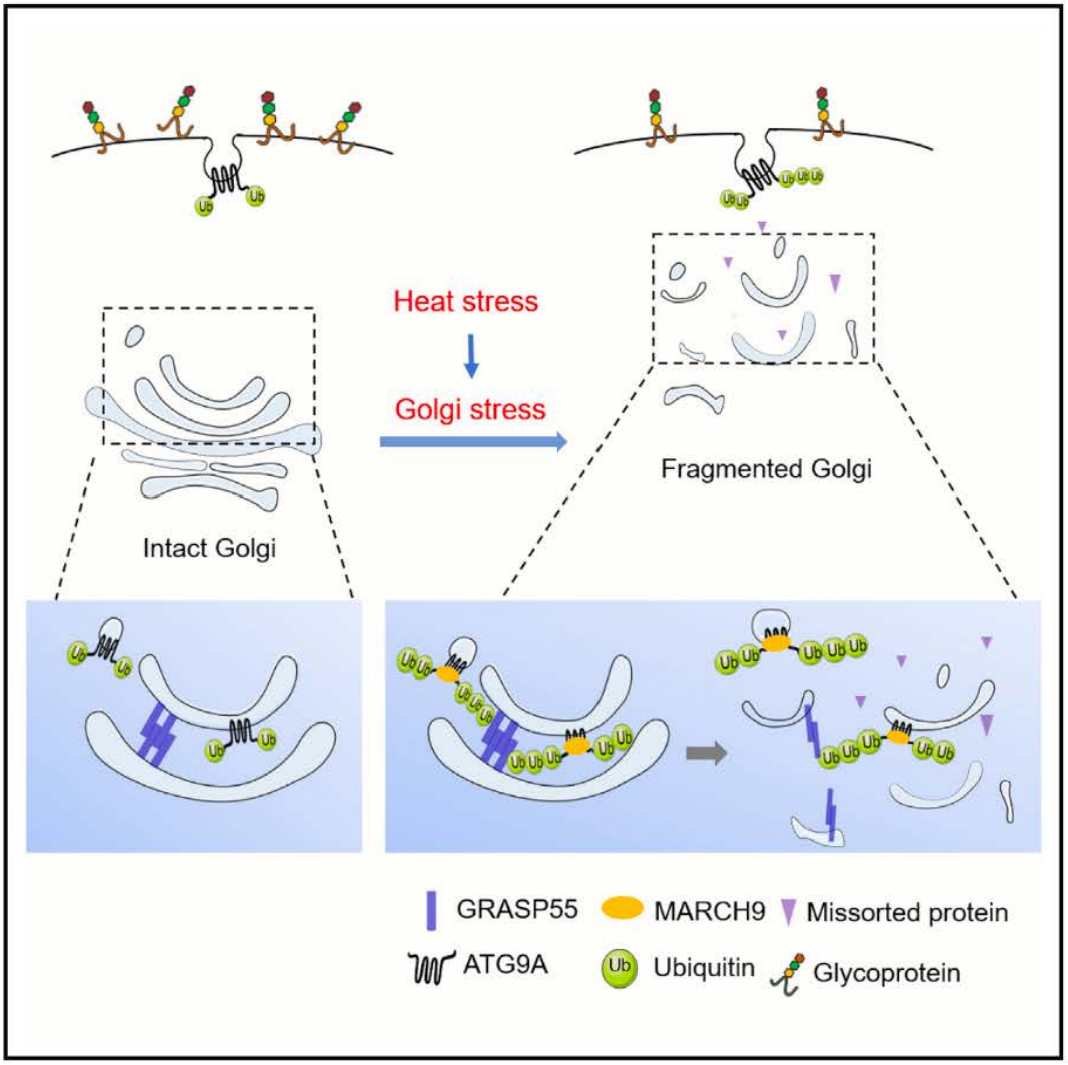

Figure 9. Nondegradable ubiquitination of ATG9A in Golgi stress. ATG9A ubiquitination by K63 linkage is mediated by MARCH9. Ubiquitinated ATG9A works in concert with GRASP55 mediating Golgi fragmentation which is a vital pathway for Golgi stress response (80).

2.3.3. The Function of ATG9B

The focus of the mammalian ATG9 has been on ATG9A so far in this section. Although this thesis is mainly about ATG9B, there is limited information in the literature on ATG9B According to Protein Atlas, placenta syncytiotrophoblast cells and placenta-derived BeWo cell linefrom a patient with choriocarcinoma cells express ATG9B the highest (Figure 10). Syncytiotrophoblasts are multinucleated epithelial cells covering fetal capillary networks, directly involved in maternal-fetal nutrient transfer. Syncytiotrophoblasts are formed by the

fusion of cytotrophoblasts by the fusion of the cell membranes. It is also frequently used as *in vitro* model for the placenta.

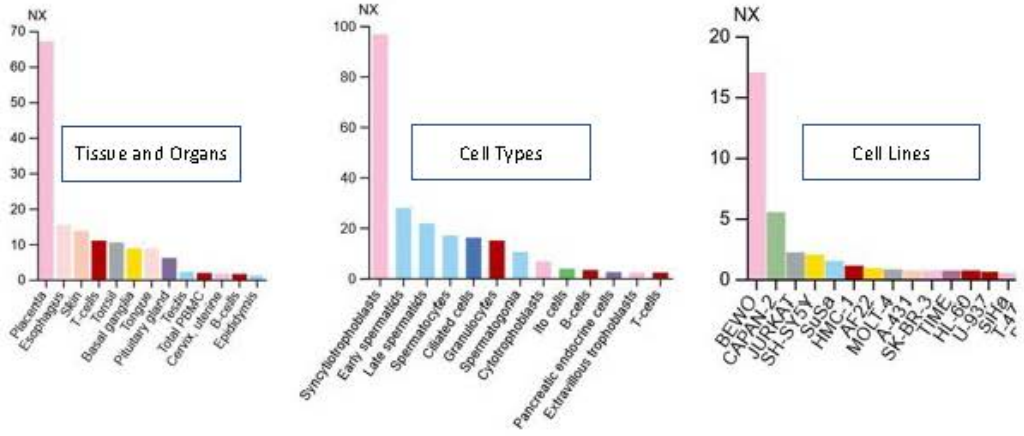

Figure 10. The expression of ATG9B in human tissue organs, cell types, and cell lines. (Protein Atlas)

Recently, the evolutionary conservation, structure, and function of ATG9B have been elucidated. Firstly, ATG9B is a vertebrate-specific paralog of ATG9B. By Cryo-EM and structural modeling, it was shown that structurally the two proteins are similar. The C terminal regions fold back and form a C-terminal platform above the HINGE domain similar to the ARCH domain shown in yeast Atg9A. ATG9B also forms a homotrimer. ATG9B also is a functional lipid scramblase and can compensate for ATG9A in starvation-induced autophagy, and physically interact with ATG2A. ATG9B trafficking is also similar to ATG9A residing predominantly in Golgi, in early and recycling endosomes to a lesser extent, during nutrient-rich conditions and translocates to cytosol in starvation conditions as cytoplasmic puncta. While ATG9A and ATG9B partially colocalize the colocalization is not absolute, suggesting that they

are localized in different membranous structures as well, suggesting that they may have different biological functions as well (Figure 11) (9).

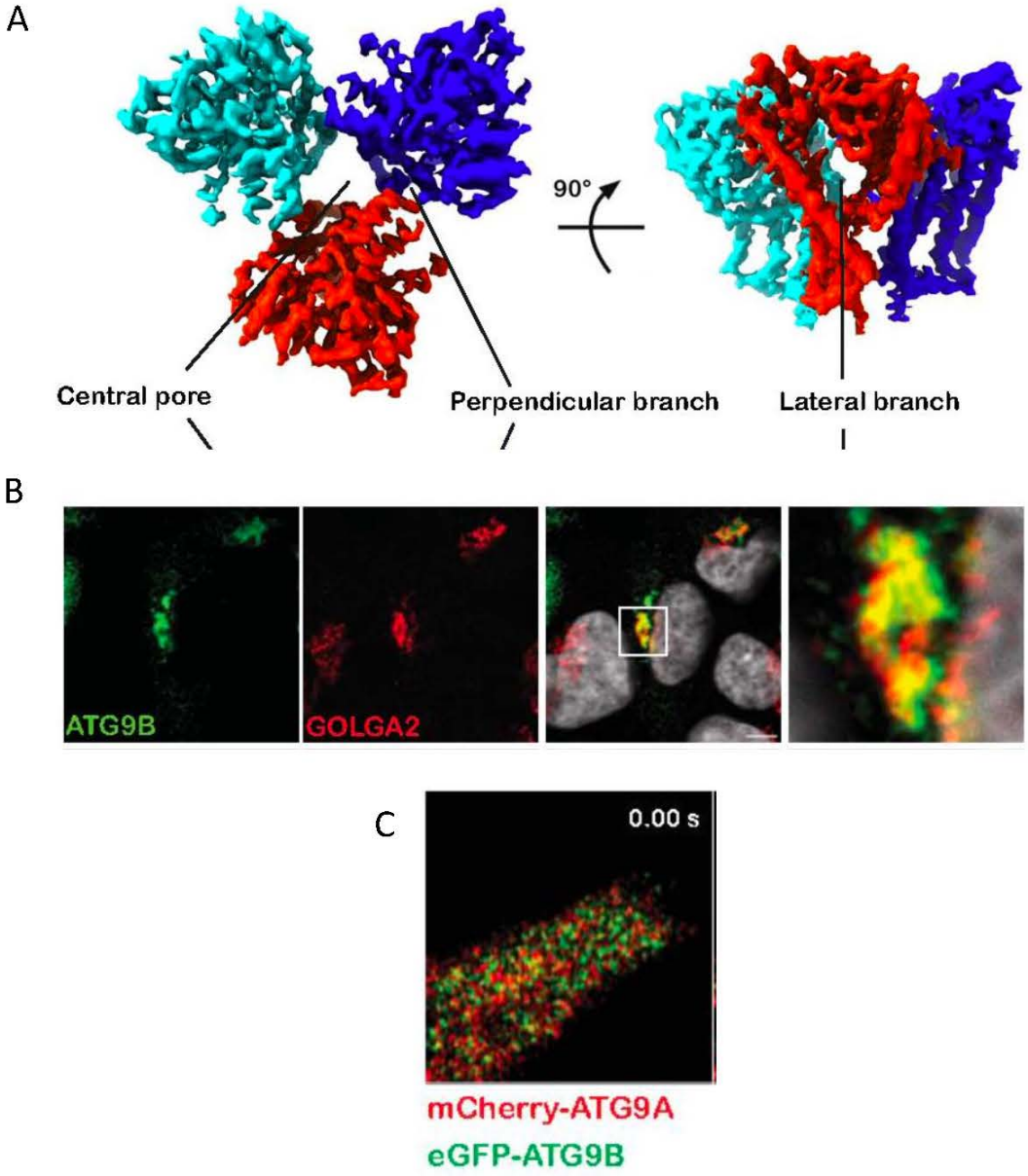

Figure 11. The structure and localization of ATG9B. A) ATG9B protomer structure is similar with ATG9A and yeast Atg9. The central pore and lateral pores are shown in the structure. B) ATG9B colocalizes with Golgi. C) ATG9A and ATG9B colocalizes to some extent.

While the majority of the information in the literature on ATG9B involvement in diseases which will be explained in the following section, there is a recent literature illuminating ATG9B function in colorectal cancer cells (CRC). In CRC ATG9B expression is increased,

influencing metastatic recurrence of CRC. ATG9B is shown to interact with myosin-9 (MHY9) by immunoprecipitation assay. ATG9B-MHY9 physically interacts through amino acids 368-411, corresponding to the first cytosolic stretch between transmembrane sites. This interaction increases the stability of each protein and protects against ubiquitin-mediated degradation and STUB1-mediated ubiquitination. Upon overexpression, ATG9B translocates from the perinuclear site to the cell's leading-edge dependent on MHY9. ATG9B overexpression increased focal adhesions (FAs) formation and translocation to the cell's leading edge. ATG9B promotes FA assembly through MHY9. FA assembly is the mechanism of cells of interacting with the extracellular matrix. ATG9B is involved in FA assembly by mediating integrinβ1 polarization towards the cell edge. ATG9B may be involved in the invasion and metastasis of CRC (81) (Figure 12).

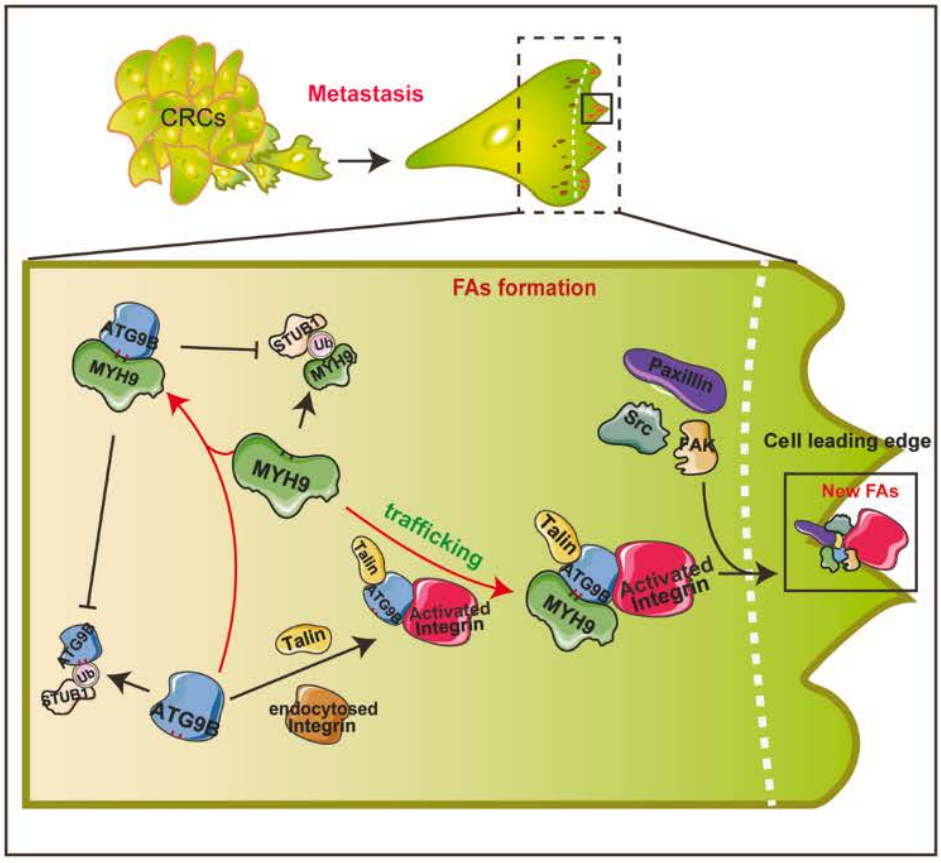

Figure 12. The involvement of ATG9B in focal adhesion assembly. In colorectal cancer cells ATG9B directly interacts with MHY9, promotes integrin β1 activation, blocking ubiquitination sites of MYH9. In concert, MYH9 dependent translocation of activated integrin through polarized cell leading edge forming focal adhesions. This is involved in CRC invasion mechanism in metastasis.

Beyond CRC scope, ATG9B involvement in cell motility and focal adhesion together with recent developments in ATG9A in lipid metabolism suggest that ATG9 proteins may involve in many cellular pathways beyond autophagy.

2.3.4. Involvement of Autophagy in Embryonic Development and Mouse Models

Autophagy begins as early as in fertilized eggs. Initial autophagy appears during early preimplantation, Atg5 is essential for the process. Autophagy stays low in unfertilized oocytes but surges 4 hours post-fertilization due to calcium oscillation, marking the first autophagic wave. During late one-cell to middle two-cell stages and mitosis, autophagy decreases, in line with cultured mammalian cells. *Atg5* knockout mice survive early embryogenesis due to maternal *Atg5*. Maternal *Atg5* knockout leads to embryonic lethality at 4-cell or 8-cell stages. Early embryonic autophagy might generate a sufficient level of amino acids for protein synthesis. Protein synthesis is reduced in autophagy-deficient embryos. In the placenta, initial nutrient production turns into extreme post-birth starvation. The second autophagy wave occurs during embryo-to-neonate transition of the mouse, in all tissues except in the brain. In the brain, autophagy increases 1-2 days after birth. Knockouts of autophagy genes resulted in diminished protein levels in neonatal plasma and tissues, underscoring autophagy's importance in providing an amino acid reservoir for neonates (82).

Knockouts of autophagy genes result in neonatal death within a day (Table 2). Knockouts of autophagy genes resulted in reduced protein levels in neonatal plasma and tissues, indicating autophagy's role in neonatal amino acid supply. While how these amino acids are utilized remains uncertain, one possibility is meeting heightened tissue energy demands. In the heart and diaphragm post-birth, autophagy is active; *Atg5* knockout hearts show lowered AMPK activation, an energy-sensing kinase. Whether amino acid decline solely causes neonatal death is uncertain. Though neuronal autophagy isn't enhanced, lacking basal autophagy might contribute to suckling issues. Suckling alone can't explain early death, as *Atg5* and *Atg7* knockout neonates die sooner than wild types even without suckling. Autophagy might also target macromolecules beyond proteins. *Atg5* knockout mice have less adipose tissue due to adipogenesis defects. *Atg5* knockout's faulty apoptotic corpse clearance may lead to developmental issues. After birth, autophagy-mediated degradation could be vital for cellular reprogramming during environmental changes. Embryos completely deficient in autophagy due to oocyte-specific *Atg5* knockout die before implantation. However, *Atg3*, *Atg5*, *Atg7*, *Atg9*,

and *Atg16L1* knockout embryos survive embryonic stages and are born at typical frequencies, suggesting that autophagy may be non-essential for embryogenesis but potentially important for embryonic development *Beclin 1*, *Ambra 1*, and *FIP200* knockouts lead to embryonic demise. *Beclin1* knockouts result in embryonic death at 7.5 dpc due to cell death, and failure in proamniotic canal closure. *Ambra1* knockout, an interacting partner of Beclin1, causes embryonic death 10-14. *FIP200* and *ULK1* knockout results in embryonic lethality between 13.5-16.5 dpc due to impaired heart and liver development. *FIP200*, *Beclin1*, *Ambra1*, and *ULK1* engage early in autophagy, contrasting *Atg3*, *Atg16L*, *Atg5*, and *Atg7*'s later roles. *ATG9A* knockout, an early autophagy protein, exhibits a milder phenotype: mouse embryo survives embryonic stages but dies in the neonatal period. This suggests potential compensatory interactions among distinct Atg proteins (82,83).

Autophagy is a central mechanism for eukaryotes therefore knockouts of core autophagy genes often lead to lethality.

Table 2. Phenotypes observed in systemic autophagy specific gene knockouts (83).

***Atg* gene**	**Survival time**	**Phenotypes**
Becn1	E8.5	Defects in proamniotic canal closure, (spontaneous tumors in heterozygotes)
Pik3c3/Vps34	E8.5	Fail to form mesoderm, reduced cell proliferation
Atg9a	Embryonic lethal	Growth retardation
Rb1cc1	E14.5-E16.5	Defective heart and liver development
Atg13	E17.5	Growth retardation defective heart development
Ulk1/2	Neonatal lethal	Impaired lung function
Atg3	Neonatal lethal	Die within one d after birth,
Atg5	Neonatal lethal	morphologically normal, reduced amino acids levels, suckling defect
Atg7	Neonatal lethal	
Atg12	Neonatal lethal	
Atg16l1	Neonatal lethal	
Atg4b	Viable	Balance dysfunction
Atg4c	Viable	Increased susceptibility to carcinogen-induced fibrosarcomas
Map1lc3b	Viable	No obvious abnormality
Gabarap	Viable	No obvious abnormality
Ulk1	Viable	Increased reticulocyte number, delayed mitochondrial clearance
Ulk2	Viable	No obvious abnormality

2.3.5. The Role of Autophagy in Placental Development

The placenta is a fetomaternal organ located between the fetus and the mother, providing gas, nutrient, and waste exchange during fetal development. It derives from the trophectoderm layer of blastocysts in the early stages of pregnancy. Trophoblasts are the main cell type that in the placenta. When cytotrophoblast cells meet the maternal endometrium, they transform into

multinucleated syncytiotrophoblasts by fusion and infiltrate into the extracellular matrix of the endometrium and ensure implantation (Figure 13). Placental development requires the coordination of dynamic cellular processes such as proliferation, differentiation, and apoptosis. Dysfunction of trophoblasts can cause gynecological diseases and malformation of the fetus (84,85).

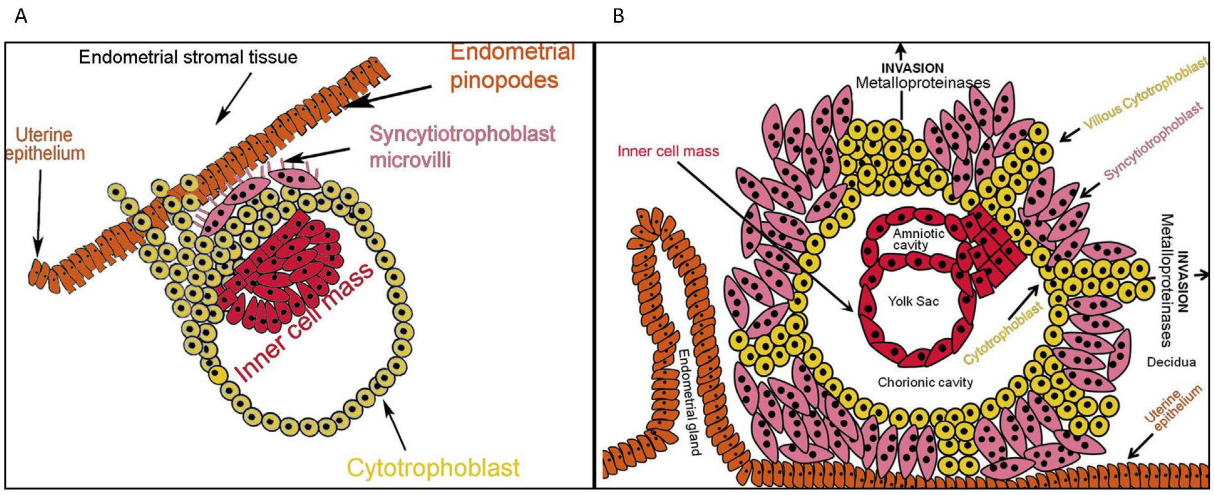

Figure 13. The role of trophoblasts in the development of the human placenta. A) Implantation: The blastocyst is attached to the endometrium with microvilli on the syncytiotrophoblasts. B) Infiltration: Syncytiotrophoblasts settle into the endometrial stroma by infiltration of cytotrophoblasts by degrading the extracellular matrix (86).

Fetal growth restriction (FGK) is a clinical condition that can affect 5-10% of pregnancies, in which the intrauterine development of the fetus is retarded. FGK can lead to perinatal death as well as neurological and cognitive developmental delay, cardiovascular and endocrine diseases. The most important cause of FGK is placental dysfunction (87,88).

Under normal conditions, autophagy is stimulated by the formation of a hypoxic environment during the development of the placenta. Autophagy is required for trophoblasts to infiltrate and migrate into the endometrium by degrading the extracellular matrix. In addition, it is a cellular process needed for the development of the placenta and remodeling of the endometrium, clearance of damaged organelles, maintenance of cell homeostasis, and differentiation of trophoblasts. Abnormalities in the autophagy process negatively affect the development of the fetus and placenta and are observed in gynecological diseases such as preeclampsia. On the other hand, there are studies suggesting that autophagy is suppressed in

extra villous trophoblasts in preeclampsia, and this negatively affects the pathology of the disease (89).

Placental development in autophagy mouse models: Various genetically modified mouse models have been produced to examine the functions of Atg genes involved in the autophagy process. Among them, deletion of *Atg7* inhibits starvation-induced autophagy (90). Due to Atg7 knockout being fatal to mice, A placenta trophoblast-specific conditional knockout of Atg7 was generated to yield significant consequences, including gestational hypertension and various placental abnormalities. These abnormalities encompass the failure of trophoblast invasion and vascular remodeling, a reduction in the area of the spongiotrophoblast layer, the accumulation of SQSTM1/p62 protein in the placenta, an increase in apoptotic cell numbers, and, ultimately, impaired placentation. Despite these notable effects on placental function, fetal growth restriction was not observed in this experimental context (91).

2.3.6. Involvement of ATG9B in diseases

The above-mentioned studies indicate that the ATG9 human homologue, ATG9A, may be essential, particularly important in embryonic development. However, there is not enough information about ATG9B in the literature. Interestingly, associations of ATG9B deficiency with diseases have been found in the literature. For example, ATG9B deficiency in hepatocellular carcinoma has been shown to reduce autophagy and cause endoplasmic reticulum stress-induced hepatocyte apoptosis in hepato-carcinogenesis (92). It has been observed that human papillomavirus 16E6/E7 activates autophagy via ATG9B and LAMP1 in cervical cancer cells (93). A correlation was found between ATG9B expression level and TNM level, distant tissue metastasis and survival time in clear cell renal cell carcinoma (94). It has been observed that ATG9B is more methylated and expressed at a lower level in invasive ductal carcinoma compared to normal tissue, and this methylation adversely affects the TNM level (95). It has been shown that a polymorphism in ATG9B can be used as a marker in coronary artery disease (14). In addition, it has been suggested that ATG9B frameshift mutations may be effective in 13 cancer types such as breast cancer, hepatocellular carcinoma, gastric cancer malignancy, and colorectal cancer (15). Interestingly, silencing ATG9B expression in hepatocarcinogenesis has been shown to reduce colocalization of LC3 and p62 autophagy markers and negatively regulate autophagy (92).

ATG9B is shown to be involved in variety of diseases, yet there is not a genetic disease has been linked with *ATG9B* variants (Figure 14) (29).

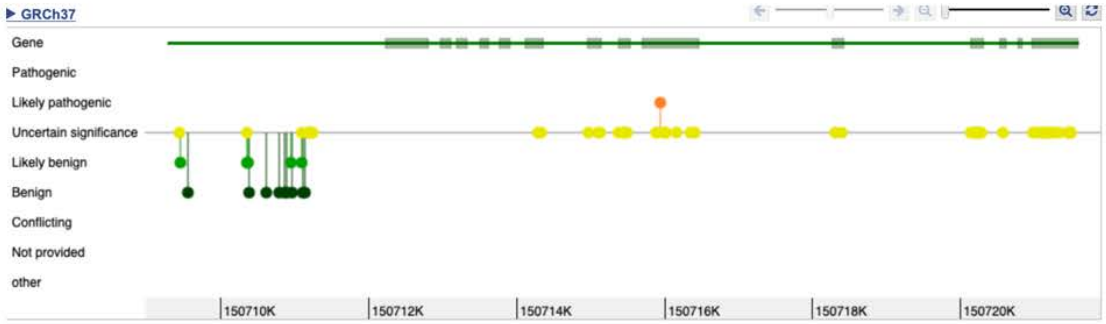

Figure 14. Pathogenic variants identified in *ATG9B* gene. One likely pathogenic missense mutation was linked to premature ovarian failure no pathogenic variant has been linked to ATG9B gene (29).

3. MATERIALS AND METHODS

3.1. Type of the Research

This research is experimental.

3.2. Location and Time of the Research

This study was performed in Gene Targeting and Transgenic Models Platform between 2019 September and November 2023 in IBG.

3.3. Universe of the Study, Sample of the Study/Study Groups

The patients that are introduced in this study are volunteers for Blue Gene project. Pediatric patients born to consanguineous marriage that are suspected of an undiagnosed genetic disease were chosen for the study with their immediate family.

3.4. Materials of the Study

Cell lines that are used for this study were present in our laboratory. BeWo (ATCC CCL-98), JAR (ATCC HTB-144) cells obtained specifically for this study. C57BL6/J micewere from Jackson Laboratories and were provided by IBG. New Zealand White rabbit is provided by IBG.

Table 3. The recipes for protein extraction buffers.

RIPA:	**TNTE**:
50 mM Tris-HCl (pH:7.6)	1% Triton
150mM NaCl	150 mM NaCl
1% NP40	20 mM Tris-HCl, pH 7.4
0.5% Sodium deoxycholate	0.5 mM EDTA
0.1% SDS	

Table 4. Antibodies that were used in this study. NA stands for "not applied".

Antibody	**Catalog #**	**IB**	**IF**
Anti-ATG9B	Novus NBP1-77169	1:1000	1:200
Anti-ATG9B	StressMark SPC-646D	1:1000	1:200
Anti-ATG9A	Cell Signaling #13509	1:1000	NA
Anti-LC3B	Cell Signaling 2778S	1:2000	1:200
Anti-FLAG M2	Sigma F1804	1:1000	1:1000
Anti-FLAG	Sigma F7425	1:1000	1:200
Anti-Golgin-97	A-21270	NA	1:200
Anti-Actin	Abcam ab6276	1:2000	NA
Anti-ZO-1	Invitrogen 40-2200	NA	1:200
Anti-Mouse-HRP	Cell signaling 7076S	1:5000	NA
Anti-Rabbit-HRP	Cell signaling 7074S	1:5000	NA
Anti -Mouse Alexa 594	Cell signaling 8890S	NA	1:500
Anti-rabbit Alexa 488	Cell signaling 4412S	NA	1:500

Table 5. Oligonucleotides used in this thesis.

Oligo Code	Sequence 5' to 3'	Bases	Notes
WDR62_FWD	CCCATTGGTTCTAAGCGCC	19	Sequencing human
WDR62_REV	GTTAGGGGACGAGGCATGG	21	Sequencing human
VARS1_FWD	ATCCGGGTGAGGTTGTAGTC	21	Sequencing human
VARS1_REV	AGTTGGCCTTGAGACCTAAGC	22	Sequencing human
ATG9B_FWD	CCCATTGGTTCTAAGCGCC	20	Sequencing human
ATG9B_REV	GTTAGGGGACGAGGCATGG	21	Sequencing human
RT-ATG9B-1_FWD	CCCCTCATACAAGAAGCTCCC	21	Primerbank ID: 239582719c1
RT-ATG9B-1_REV	TGCAGGTTGAGCCTGTGTTG	20	Primerbank ID: 239582719c1
RT-ATG9B-2_FWD	CTGGGGCCGAGTACAACAAG	20	Primerbank ID: 239582719c3
RT-ATG9B-2_REV	CTGGGCAATTCGGGAAATGGA	21	Primerbank ID: 239582719c3
SK_001	CCCCTCATACAAGAAGCTCCC	21	Human FWD N terminal RT-PCR
SK_002	TGCAGGTTGAGCCTGTGTTG	20	Human REV N terminal RT-PCR
SK_003	CTGGGGCCGAGTACAACAAG	20	Human FWD C terminal RT-PCR
SK_004	CTGGGCAATTCGGGAAATGGA	21	Human REV C terminal RT-PCR
SK_005	CCATCCCACAATGATACACACC	22	Mouse FWD N terminal RT-PCR
SK_006	CCTCTAGCCGTTCATAGTCCT	21	Mouse REV N terminal RT-PCR
SK_015	TATGGGGCAGTATTTTTCATCC	22	Mouse FWD CRISPR screening
SK_016	AAGGAACTTAGAGCTGTGCCCT	22	Mouse REV CRISPR screening
SK_019	AAAGACGATGACGACAAGGTGAGCCGAATGGGC	33	pcDNA 3.1 FLAG-hATG9B WT FWD
SK_020	GATCAAGCTTATGGACTACAAAGACGATGACGAC	34	pcDNA 3.1 FLAG-hATG9B WT FWD Cloning
SK_022	GATCCTCGAGTCAGTCAGTGCAAGAGG	27	pcDNA 3.1 FLAG-hATG9B WT REV Cloning
SK_023	TTGCCGTCCTCCGCACGAGGCCTCAGTCTG	30	pcDNA 3.1 FLAG-hATG9B TR REV Cloning
SK_024	GATCCTCGAGTCAGTCTTGCCGTCCTCCGCA	31	pcDNA 3.1 FLAG-hATG9B TR REV Cloning
KD_089	TGTACGGTGGGAGGTCTATATA	22	pcDNA 3.1 FLAG-hATG9B WT FWD Colony I
SK_039	CCCCTTGACCTGTGATGACC	21	Human FWD hCGβ RT-PCR
SK_040	TATTGTGGGAGGATCGGGGT	21	Human REV hCGβ RT-PCR
SK_041	GATCGGATCCATGGACTACAAAGACGATGACGAC	34	pBOBI FLAG-hATG9B WT FWD Cloning
SK_042	GGGCATCCTCAGGTTAGAGC	20	Mouse FWD CRISPR screening
SK_043	ATCCAGACTCCCCTGCATCT	20	Mouse REV CRISPR screening
SK_044	CCCATCGCAGCCTTCATCTA	20	Mouse FWD CRISPR screening
SK_045	AACTTAGAGCTGTGCCCTGG	20	Mouse REV CRISPR screening
SK_062	GATCAAGCTTATGGTGAGCCGAATGGGCTGGGG	33	pcDNA3.1 hATG9B WT myc his A FWD Clonii
SK_054	gatcCTCGAGGTCAGTGCAAGAGGCCC	27	pcDNA3.1 hATG9B WT myc his A REV Clonin
SK_055	gatcCTCGAGGTCTTGCCGTCCTCCGCACG	30	pcDNA3.1 hATG9B TR myc his A REV Clonin
SK_058	gatcGAATTCATGGTGAGCCGAATGGGCTG	30	pGEX-6P-1 AG0 FWD Cloning
SK_059	gatcCTCGAGTTAGTAGATCTTGGTGAAGAAACTG	36	pGEX-6P-1 AG0 REV Cloning
SK_060	GATCCTCGAGGGGGCAGTATTTTTCATCCTGC	32	pBlueScript SKII mouse Atg9b FWD Cloning
SK_061	GATCAAGCTTCTTAGAGCTGTGCCCTGGTGG	31	pBlueScript SKII mouse Atg9b FWD Cloning
KD_446	GATCATAACTTCGTATAATGTATGCTATACGAAGTTAT	38	FWD LoxP oligo FWD annealing
KD_447	GATCATAACTTCGTATAGCATACATTATACGAAGTTAT	38	Rev.complement LoxP oligo FWD annealing
KD_473	AACCCTTGCTTCATGTACCCG	21	Genotyping ATG9B FLOX editing
KD_478	TGCCTAAGCCTACGGACTCT	20	Genotyping ATG9B FLOX editing
KD_510	GGTGGTGGAAGAGTGGAGTG	20	ATG9B KIN genotyping, FWD
KD_512	GATGGAGGGTGGCAAGAACA	20	ATG9B KIN genotyping, REV
KD_536	AAGTCTCCGCTCAGCTTCAC	20	FLAG-ATG9B Genotyping FWD
KD_557	GAGATCCTCCTTCCCCCAGT	20	FLAG-ATG9B Genotyping REV
KD_542	gatcGAATTCCCCCAGGACTCTCCTGGG	28	pGEX-6P-1 AG1 FWD Cloning
KD_543	gatcTAACTCGAGGCCATTCCGCTGGTGGTA	31	pGEX-6P-1 AG1 REV Cloning
KD_544	gatcGAATTCCGCTCAGTCTGCAACCTCT	29	pGEX-6P-1 AG2 FWD Cloning
KD_545	gatcTAACTCGAGGTCGCTGCGCTTGTAGGCG	32	pGEX-6P-1 AG2 REV Cloning
KD_599	CTGAGCAGGACTATGAACGG	20	Mouse Atg9b RT-PCR FWD
KD_600	AGGCAAAGCCATTCCGCT	18	Mouse Atg9b RT-PCR REV
SD-348	TTCACCACCATGGAGAAGGC	20	Mouse Gapdh RT-PCR FWD
SD-349	GGCATGGACTGTGGTCATGA	20	Mouse Gapdh RT-PCR REV
KDCr_04	GGATCCTAATACGACTCACTATAGGCTTTCAGAGGGACAGACAGGTTTTA GAGCTAGAA	59	Atg9B sgRNA1
KDCr_05	GGATCCTAATACGACTCACTATAGGCTCTGCACGCTGAGAGAGTGGTTTTA GAGCTAGAA	60	Atg9B sgRNA4
KDCr_06	ATACCAGAAGGACTCCCTTCCTTGCAGTGGCTTTCAGAGGGACAGACAGAa ttCTgACTCTCTCAGCGTGCAGAGGATGGAAAGACCGAACTCTCCTTAATGC GGTTCTC	110	Atg9B HDR
KDCr_11	gtcgaggcaggtttgggtttgatagagaaattaatcacaaatgggacaatgccaagtATAACTTCGTATAATGT ATGCTATACGAAGTTATcttgacactgtttctctgtgcccaggttcctggcat	127	Atg9B 5'LoxP HDR
KDCr_12	caggttcctggcatcacatccagaacctggacagtttttcaccaagatatcctttgATAACTTCGTATAATGTA TGCTATACGAAGTTATtgcccagcatgcagagggggcatggtgggggactgt	127	Atg9B 3'LoxP HDR
KDCr_28	aaatgggacaatgccaagtcttgacactgATAACTTCGTATAATGTATGCTATACGAAGTT ATttctctgtgcccaggttcctggcatcacatccagaacctggacagtttttcaccaagatatcctttgATAACTTCGTA TAATGTATGCTATACGAAGTTATgcccagcatgcagagggggcatggtgggggactgt	200	Atg9b FLOX HDR
KDCr_33	GGATCCTAATACGACTCACTATAGGaccccgttcgtctcaccatcGTTTTAGAGCTAGA A	60	FLAG-ATG sgRNA
KDCr_34	actgacctctgtggaaacaacagcagtccagtcccttcaacctctcaagagaagctgcggcctgatgGATTACAAGGA CGACGATGACAAGgtgagacgaacggggtgggggggggagcaggaggcaa	127	FLAG-ATG asyHDR
KDCr_47	ccagtcccttcaacctctcaagagaagctgcggcctgatgGACTACAAAGACCATGACGGTGATTAT AAAGATCATGACATCGATTACAAGGATGACGATGACAAGgtgagacgaacggggtg gggggggagcaggaggcaa	142	3xFLAG-ATG asyHDR

Buffer Recipes

Blocking Buffer for Immunofluorescence:

10% FBS

1X PBS

0.2% TritonX-100

Binding Buffer for GST-Antigen 1 Purification

50 mM TrisCl pH 8

100 mM NaCl

0.5 mM PMSF

2 mM DTT

3.5.Variables of the Study

Variables of the study are described as independent, dependent and control variables. These categorizations are not applicable for our studies due to experimental approaches that were employed in this study.

3.6.Data Collection Tools

3.6.1. Sample preparation for WES and Sanger Sequencing.

During our study, routine blood collection was carried out with the voluntary consent of participating family members. Each collection involved the extraction of 4 mL of blood, which was carefully preserved in EDTA tubes.

Following blood collection, the blood samples were aliquoted and stored at -80°C to ensure their integrity and stability.

To isolate genomic DNA from some of these archived blood samples, we used isolation kits: the QuiaAmp DNA isolation kit and the Invitrogen Purelink Genomic DNA isolation kit (K182000) according to manifacturer's protocol.

Identity Protection:

Sample owners' identity information was not utilized during any stage of the process.

A unique code was assigned to each patient by the physician at the time of blood collection.

Subsequently, samples were identified solely by these code numbers and not by donor names.

3.6.2. Identification and Validation of Candidate Pathologic Variants

In the Blue Gene Project, whole exome sequencing was conducted to identify candidate gene mutations with genomic DNA isolated from patient blood. The data interpretations for the identification of candidate are presented in the results section appropriately.

To validate the detected genomic alterations in candidate genes, I prepared the samples for Sanger sequencing in complement with other bioengineering methods. Initially, a draft DNA sequence was acquired via the Ensembl Genome Browser (Ensembl 75: Feb 2014 (GRCh37), I designed primers for amplicons ranging in size from 500-600 bp. Following the primer design, the oligonucleotides were synthesized by a service provider. Patient DNA samples were then subjected to amplification using these designed primers and the Thermo Scientific High Fidelity DNA Polymerase kit, employing the polymerase chain reaction (PCR) method. Subsequently, the sequenced products were dispatched to a service provider for sequencing, employing the Sanger sequencing method.

The sequences obtained by Sanger sequencing, densiometric quality was determined and aligned with the genomic sequence of candidate genes obtained from Ensembl database by tools such as Clustal Omega Pairwise Alignment or NCBI Blast. Sequences were analyzed to determine whether the detected modifications in patient DNA were confirmed using the Sanger sequencing method.

3.6.3. ATG9B gene synthesis

Human ATG9B-WT and ATG9B-TR coding sequences were synthesized and was cloned to pUC57 plasmid by service provider GeneWiz. We placed common restriction sites BamHI and EcoRI at 5' and 3' of the coding sequences to digest for subcloning into most mammalian expression vectors. The details on plasmids cloned with ATG9B were presented in results section with the purpose, usage and data obtained for the study.

3.6.4. Cell Lines, Media, Culture, Transfection

The appropriate media compositions of the cells were checked from (https://www.atcc.org). DMEM F12 media (Gibco™ 11330032) was used for culturing BeWo, RPMI-1640 (Gibco™ 11875-093) for JAR and DMEM (Gibco™

41965039) for the other cells were used. Complete media prepared by addition 10% FBS (Gibco™ 10270106), 1% Penicillin Streptomycin (Thermo 15140122) and sodium pyruvate 100 μM (PAN Biotech P04-43100).

The cell lines used in this thesis were adherent, cells were seeded onto suitable 24-well plates on 12-mm cover glasses for immunofluorescence, 6-well or 12-well plates for ectopic expression assays, and 100-mm dishes for expansion. Cells were passaged in every 24-72 hours after seeded depending on their duplication time.

3.6.4.1. Cell Passaging

Cell culture media were aspirated from the cells. The cells were washed with PBS and subsequently treated with 0.25% Trypsin-EDTA (#T4049) at 37°C for 1-3 minutes. Following the incubation trypsin was inactivated with complete media. Detached cells were further disengaged by pipetting until they are monocellular stage in media suspension and were inoculated into appropriate plates at a ratio of 1-5:10 to promote their growth and propagation.

3.6.4.2. Cell Cryopreservation

Cell cryopreservation followed a process similar to cell passaging until cell suspension was obtained. For cryopreservation, cells were centrifuged at 200 g for 5 minutes. The pellets were subsequently resuspended in a solution consisting of 40% DMEM, 50% FBS, and 10% DMSO. The cell suspension in freezing media were frozen at -80°C in a freezing container containing isopropanol to ensure their viability during storage.

3.6.4.3. Transfection

Transient transfection was performed using Promega Fugene HD (#E2311) transfection reagent, according to manufacturer's protocol. All plasmids that are used for he transfection process were isolated using the PureLink™ HiPure Plasmid Miniprep Kit (K210002) or the MN Macherey-Nagel™ Nucleospin™ Plasmid Transfection-grade (#740490) kits to ensure their cell culture purity was achieved for the experiment.

3.6.5. Lentivirus production and infection

HEK293T cells were transfection using the lentivirus 2nd Generation system, introducing pBOBI FLAG-hATG9B WT and Truncated. After 48-hour incubation period produced virus are collected within the cell culture media off the cells. The collected virus was prepared for

infection by diluting with fresh growth media appropriate for the cells. Infection media is aspirated after 24-hour and cells were washed and replenished with normal growth medium. BeWo, HeLa, Hep3B, and HepG2 were transduced with WT and TR viruses by utilizing this protocol.

3.6.6. Development of stable clonal cell lines

The attempt of stable clonal cells with transient transfection was performed by cell sorting after pCS2 transfection because this plasmid does not have antibiotic resistance gene.

To achieve stable transient transfection pcDNA3.1 plasmid was used due to the geneticin resistance gene. For transiently transfected cells geneticin selection was performed until the untransfected cells were eliminated.

pBOBI lentiviral infected cells were cultured in normal culture media until they reached confluency. Then, for generating stable monoclonal HeLa cells cells were counted with hemacytometer. By limited dilution, 1 cell/well cell was seeded to 96-well plates. Single-cell colonies were confirmed after several days of growth and then expanded. The expression of single-cell clones was confirmed by seeding the cells on coverslips and screened with immunofluorescence with FLAG-M2 antibody.

3.6.7. Protein Expression and Localization assays

3.6.7.1. Protein extraction

For immunoblotting and RNA isolation, cells were detached by trypsin and collected in media. Afterward, they were centrifuged at 200 g for 5 minutes. The resulting cell pellets were resuspended in PBS and then briefly centrifuged at +4°C, then the PBS was aspirated. These pellets were stored at -80°C until lysate preparation.

Mouse tissues were rapidly frozen in liquid nitrogen following scarification and tissue harvesting, and were stored at -80°C. Before lysate preparation or RNA extraction, the frozen tissues were handled in liquid nitrogen until they are mechanically pulverized without thawing.

For both cells and tissues, the lysis buffer (RIPA or TNTE) was supplemented with 1x PI (Roche 04693116001), 1 mM PMSF (protease inhibitors), 1 mM NaF, and 1 mM NaOV3. Upon thawing, the cell/tissue pellets were resuspended in the respective lysis buffer. The lysates were vortexed in 3 sets of 5-minute intervals, and then they were centrifuged at 17,000 g for 15 minutes at 4°C.

In the case of mouse tissues, they were pulverized using pestles immediately after removal from liquid nitrogen. Subsequently, the tissues were homogenized in the lysis buffer through sonication for 15 seconds, followed by resting on ice for 30 seconds, for a total of 3 cycles.

At this stage, the cell and tissue lysates were centrifuged at 17,000 g at +4°C for 30 minutes. The supernatants were collected into clean tubes. The concentrations of these lysates were determined by measuring absorbance at a wavelength of 595 nM in a 96-well plate using Bradford reagent. To generate standard curves, BSA at concentrations of 0.25, 0.5, 1, and 2 mg/ml was used. Following the determination of concentration, the lysates were prepared for loading onto SDS-PAGE gels.

3.6.7.2. Immunoblotting

For gel loading, lysates were prepared by adding 5X SDS sample buffer and then boiled at 95 °C for 5 minutes, or they were loaded onto the gel directly without boiling. We employed an 8% Tris/Glycine SDS polyacrylamide gel for Atg9b immunoblotting. Samples, along with the PageRuler plus molecular weight marker (#26619), were loaded onto the gel.

The samples were initially run at 80 V in the stacking gel and subsequently at 200 V in the resolving gel. The gel was then transferred to a methanol-activated protein membrane (Pierce PVDF #85518) using a wet sandwich system at a constant current of 400 mA for 2 hours. Following the transfer, the membrane was blocked in 5% non-fat dry milk (BioShop SKI400.250) in TBS-T for 1 hour.

The primary antibody was incubated in 5% BSA supplemented with sodium azide in TBS-T overnight at 4°C. Then, the membrane was washed three times for 5 minutes with TBS-T. Subsequently, the membrane was incubated in the secondary antibody at a 1:5000 dilution in 5% non-fat dry milk in TBS-T for one hour at room temperature. The membranes were washed again, three times for 5 minutes each.

For obtaining the chemiluminescence images, Biorad Clarity Western ECL Substrate (#170-5061) was mixed at a 1:1 ratio and applied to the membrane. The image was captured using the Bio-Rad Chemidoc Touch system.

3.6.7.3. Immunofluorescence

The cells adhered to coverslips were fixed using a 4% paraformaldehyde in PBS for 20 minutes at room temperature, followed by three PBS washes. Subsequently, permeabilization and blocking were carried out for 45 minutes at room temperature with a blocking/permeabilization buffer. Coverslips were then incubated with 10-20 µl of primary antibody for 1.5 hours at room temperature or overnight at 4°C and subjected to three 5-minute PBS washes.

Secondary antibody incubation was carried out in a humidified chamber for 1 hour in the dark, followed by another round of three 5-minute PBS washes. DAPI was applied (diluted at 1:1000 in water) for 1 minute at room temperature for nuclear staining and then washed with water. The coverslips were mounted for visualization on slides using mounting media.

The antibodies used for immunoblotting and immunofluorescence, along with their respective dilutions, are listed in Table 4. Notably, prior to seeding HEK293T cells on glass, a Poly-L-Lysine coating was applied, and all solutions used were filtered through a 0.45 µm filter.

The same protocol was employed for placental tissue sections embedded in OCT, with slight alterations, primary antibody incubation period of 2 hours, and secondary antibody incubation lasting 1.5 hours. Tissues subjected to hematoxylin and eosin staining were prepared with the support of the IBG histopathology unit.

3.6.8. RNA Expression Assays

3.6.8.1. RNA Isolation and cDNA Synthesis

Cell pellets or mouse tissue were initially treated with resuspension buffer immediately after pulverization in liquid nitrogen. RNA isolation was performed by the Qiagen RNeasy kit (#74104), following the provided manufacturer's protocol. The concentration and purity of the isolated total RNA were assessed using nanodrop measurements.

Subsequently, cDNA was synthesized from 1µg of total RNA using the RevertAid First Strand cDNA Synthesis Kit (#K1621). The cDNA was then diluted in a 1:5 ratio with ultrapure water, with 5 µl of it was used as a template in RT-PCR.

3.6.8.2. PCR, RT-PCR

The list of primers used in semi-quantitative RT-PCR and cloning can be found in Table 5. In semi-quantitative PCR, the cycling process was interrupted once the desired cycle number was reached, and PCR cycles were then resumed for more amplification (AMPLIQON Taq DNA polymerase A111103).

For the cloning procedure, pUC57 hATG9B WT and truncated plasmids were used that are obtained from the gene synthesis vendor. The addition of a FLAG tag to hATG9B was accomplished using primers with nucleotide sequences encoding FLAG. To minimize the error rate during the insert generation, a high-fidelity polymerase (Amplicon APQ-A457401) was used. Subsequently, the inserts were cloned into mammalian expression vectors or lentiviral vectors, depending on the specific experiments conducted. The detail in the plasmids and their employment in the experiments will be provided in the results section.

3.6.9. Rabbit Polyclonal ATG9B Antibody Production

3.6.9.1. Production, Isolation, and Dialysis of Antigen 1

Initially, a 200 ml starter culture was prepared from glycerol stocks of both pGEX-6P-1 (empty) and pGEX-6P-1 GST-AG1, which were cultured overnight at 37°C with 225 rpm agitation. Subsequently, 40 ml of the starter culture was used to inoculate three cultures of 1 L LB medium. These cultures were grown at 37°C with 200 rpm agitation until an OD of 0.6-0.8 absorbance was obtained, and a pre-induction sample was taken. The cultures were then induced by adding IPTG to a final concentration of 100 µM and continued to grow for an additional 4 hours at 30°C with 160 rpm agitation.

Following growth, the cultures were centrifuged at 4°C and 3164 g for 30 minutes, and the resulting pellets were stored at -80°C overnight. The next day, the pellets were resuspended in 20 ml of binding buffer and treated with lysozyme (Sigma L6876-1G) with 100 µg/ml final concentration, on ice, for 20 minutes. Subsequently, 1.5 ms 50% amplitude sonication was performed, with 15-second intervals on ice for 3 minutes. Then, MgCl2 with 1 mM final concentration and 30 units/20 ml Pierce universal nuclease (Thermo Scientific 88700) were added, and the mixture was centrifuged at 12500 g for 60 minutes.

After clarification of the lysate, 200 µl bed volume of GST beads were added, and the mixture was incubated on a rotator at 4°C for 2 hours. Subsequently, washing and centrifugation steps were performed with binding buffer containing 1% TritonX-100, repeating the process

three times with centrifugations at 1000 rpm. Finally, the beads were washed with binding buffer, then water, and the antigen was eluted with 200 µl elution buffer containing excess GST.

Following elution, dialysis was performed at 4°C with mild stirring in 1 L PBS using a at 4°C in 1 L PBS (CelluSept T2-10-15).

3.6.9.2. Rabbit Immunization with Antigen 1 for Production of ATG9B Antibody

The antibody generation and serum preparation process involved a series of steps. Initially, a pre-immune bleed from the rabbit was obtained by collecting 5 ml of blood from the marginal ear vein. The serum obtained from the blood was stored at -80°C.

For the first immunization, 85 µg of the antigen in PBS was mixed with complete Freund's adjuvant, creating an emulsion. This emulsion was injected subcutaneously to the rabbit with four 50 µl injections at different sites.

On day 14, the second immunization, the first booster, was administered, 85 µg of antigen mixed with incomplete Freund's adjuvant.

On day 25, 500 µl of blood was taken from the marginal vein to assess the titer.

On day 43, the third immunization was performed in the same way with 30 µg of antigen mixed with incomplete Freund's adjuvant.

On day 53, the rabbit was sacrificed, and a final bleed was collected.

To obtain serum, the collected blood was allowed to clot by incubating at 37°C for 30 minutes and then at 4°C for 1 hour. Subsequently, it was centrifuged at 10,000 g at 4°C for 10 minutes, yielding the serum. The serum was collected, aliquoted, and stored at -80°C for future use. Before utilization in experiments, the serum was diluted in blocking buffer, with a 1:1000 dilution for immunofluorescence and immunoblotting, and sodium azide was added to a final concentration of 0.02% for preservation. The timeline of the study is presented in Table 6.

Table 6. The timeline for rabbit immunization.

	Day 0	Day 14	Day 24	Day 28	Day 38	Day 43	Day 53
1st Immunization CFA	X						
2nd Immunization IFA		X					
3rd Immunization IFA				X			
4th Immunization IFA						X	
Test bleed			X		X		
Final Bleed							X

3.6.10. Generation of Transgenic Mouse Models and Functional Studies

3.6.10.1. Design of sgRNA and ssODN Oligonucleotides for Transgenic Mouse Models

In selecting sgRNAs targeting the mouse locus to which the mutation was introduced, the most commonly used methods currently include:

- https://chopchop.cbu.uib.no/
- https://portals.broadinstitute.org/gpp/public/analysis-tools

To select suitable sgRNAs for targeting the mouse locus with sgRNA's, web-based sgRNA tools were used as listed. The selection of sgRNA were considerations of the proximity to the mutation site, on-target efficacy score, and off-target activity.

The single-stranded oligonucleotide (ssODN) donor is used as template for repairing the locus that is targeted by the Cas9/sgRNA complex. This template works in the homology-directed repair (HDR) to obtain the precise alteration within the locus. The ssODN molecules used in this study were synthesized by the service provider Eurofins in examer quality standards.

3.6.10.2. Expression of sgRNAs through in vitro transcription (IVT) method

The assembly of the DNA template for *in vitro* transcription (IVT) was carried out through polymerase chain reaction (PCR). The oligonucleotide template and primers as listed in Table 5 (96). sgRNA molecules were synthesized utilizing the NEB HiScribe T7 High Yield RNA Synthesis Kit (NEB E2040S), according to the manufacturer's protocol. TheDNA

template, nucleotides, T7 RNA polymerase, and buffer solution were mixed and the mixture was then incubated at 37°C for a duration of 18-24 hours within the PCR machine. Subsequently, DNase was added to degrade the DNA. The sgRNA molecules were isolated by the Monarch RNA purification kit.

The quality of the RNA was assessed nanodrop spectrophotometry and by running it on a pre-cast polyacrylamide gel. sgRNA1 and sgRNA4 were obtained targeting the ATG9B locus, by this method. The mixture of sgRNAs, single-stranded oligonucleotide (ssODN), and Cas9 protein were pre-mixed and stored at -80°C in preparation for the electroporation studies.

3.6.10.3. Superovulation, embryo isolation and culture

For the generation of transgenic mice strains, we selected the C57BL6/J WT mice. To induce superovulation, 4-week-old female mice were intraperitoneally injected with PMSG hormone (5 IU in 100 µl). After 48-hour, a second injection with hCG hormone (5 IU in 100 µl) was administered. Then the females were mated with WT males. These mated females were sacrificed and then embryo harvesting was performed from the ovaries and reproductive tract under a stereomicroscope (Group A). Subsequently, these females were sacrificed, and embryos were collected. The embryos were separated from cumulus cells using hyaluronidase/M2 media and treated with Tyrode solution for 30 seconds to thin the zona pellucida. Zona thinning was then halted using M2/BSA media. Subsequently, the embryos were gently mixed with snRNP in OPTIMEM RPMI media, transferred into electroporation cuvettes, and electroporated for 3 milliseconds at 80 V with 100 ms intervals, totaling 4-6 cycles.

Concurrently, CD1 females were mated with vasectomized males to induce pseudopregnancy (Group B). On 0.5 days post coitum (dpc) for the transfer of electroporated embryos.

3.6.10.4. Preparation of Tail Samples HotShot Lysates for Genotyping

The embryos that were electroporated with ssODN-sgRNA-Cas9 protein mixture were cultured in an incubator until they reached the blastocyst stage for genotyping. For the mice genotyping, tail biopsies were obtained. The samples were treated according to the hotshot lysis protocol, HotShot buffer (25 mM NaOH and 0.2 mM EDTA) was added to the samples incubated at 95°C for 1.30 hours with gentle agitation. Subsequently, the lysis buffer was

neutralized in 1:1 ratio, using a neutralization buffer (40 mM Tris-HCl). The resulting lysates were used directly in PCR reactions (97).

3.6.10.5. Screening Strategies of Transgenic Mouse Models

PCR and subsequent restriction digestion for Atg9b knock-in mouse model of the disease was adopted for the analysis of HDR mediated precise alteration. WT Atg9b gene has StuI restriction site that is localized at the position of alteration. By changing this StuI site with EcoRI with ssODN template we created a seamless genotyping strategy FLAG-Atg9b and the Atg9b exon 9 deletions (DEL1, DEL2), and Atg9b exon 2 deletions (DEL3, DEL4) strains, the agarose gel electrophoresis was used by taking advantage of the nucleotide number differences between alleles. The primers that are used are detailed in Table 5.

3.6.10.6. Histology

For immunofluorescence experiments with mouse placenta sections embedded in OCT directly after isolation, placenta sections were fixed with 4% PFA for 20 minutes at room temperature. Permeabilization was achieved using blocking and permeabilization buffer (PBS containing 10% serum, and 0.5% TritonX-100) at room temperature for one hour. Antibodies were diluted in the blocking buffer and were left to incubate at +4°C overnight. The secondary antibodies with fluorophores were incubated in dark at room temperature for 1 hour. Imaging was conducted using a fluorescent microscope (Olympus BX61) or a confocal microscope (Zeiss LSM880). Appropriate secondary antibodies were utilized for each primary antibody.

The antibodies that are used for the study are commercial anti-ATG9B antibodies (NBP1-77169, SPC-646D), anti-FLAG polyclonal antibody produced in rabbits (Sigma 7425) and anti-ATG9B serum that was generated in our laboratory.

IHC experiments are ongoing in the present with our project partners in the Dokuz Eylul University (DEU) Histology and Embryology department.

3.6.10.7. Cognitive and Behavioral Evaluation of Knock-in Mice

Learning and memory evaluation tests were performed for Atg9b knock-in genetic disease model. These experiments were performed by our project partners in Hacettepe University. We bred 15 ATG9B homozygous and 15 WT male littermate mice (20-25 gr) for behavioral experiments and send them to the facility. The experiments began after a 1–2-week adaptation period in the laboratory. Behavioral assessments structured to start with least stressful and

conclude with most stressful test. Then they isolated and preserved brain tissues of the mice for potential histology experiments.

3.7.Plan of the Research

Table 7. The timeline of the thesis work.

Plan of the study	Timeline
Molecular Cloning Studies	September 2019-September 2020
Cell culture Studies	September 2020- September 2022
Design of CRISPR ODN's	September 2021-December 2021
Generation of Knock-in Founder Mice	January 2022-March 2022
Generation of Heterozygous Knock-in Mice	April 2022-August 2022
Generation of Homozygous Knock-in Mice	September 2022- January 2023
Expansion of Heterozygous Knock-in Mice	January 2023-March 2023
Generation of FLAG-Atg9b mice	January 2023-June 2023
Generation of Knock-out mice	September 2022- June 2023
Behavior experiments	March 2023-May 2023
Histology experiments	September 2022-August 2023
Gene Expression Studies with Mouse Models	August 2022-August 2023

3.8.Evaluation of the Study

Immunoblotting studies are evaluated comparatively to loading controls, housekeeping genes. In immunofluorescence and immunohistochemistry experiments, histology the experiments were evaluated according to suitable negative controls: no first antibody or non-specific first antibody, non-immune serum, with nuclear counter-staining. Histology samples of human placentas are also being evaluated by histomorphometry studies with Student's T-Test. Behavioral studies were statistically evaluated by our project partners in Hacettepe.

3.9.Limitations of the Study

The human patients had an addition of six amino acids that differed from the WT sequence prior to the stop codon. There is a possibility that these six modified amino acids may have the presentation of the disease. However, we did not explore this possibility by introducing nucleotide changes through homology-directed repair (HDR). Instead, we modified the sequence by inserting a stop codon at the beginning of the frameshift assuming that the C-terminal deletion was the primary factor for clinical presentation. Additionally, human and mouse species display high genetic conservation and mouse models are frequently used as a

model organism for genetic diseases. However, mouse models are essentially different species. Mouse nervous system is not as complex as humans and while both species have hemochorial placenta (direct contact with maternal blood) there are differences between their placenta.

3.10. Ethics Committee Approval

The blood samples were obtained in the Blue Gene project, study was approved for functional characterization studies with 446-SBKAEK code. The sample for the informed consent form is provided in the attachments. Genetically modified mouse model studies were approved with 2020-017, 2021-013 IBG HADYEK approval code for TUBITAK 120S396 and TUBITAK 121S347 projects respectively. 2022-005 HADYEK approval code for TUBITAK 122Z025 project including rabbit immunization and transgenic mice studies. The generation of FLAG-Atg9b transgenic mouse was approved by 2022-031 code. Behavioral experiments are approved with 2023/01-02 code by Hacettepe University.

4. RESULTS

4.1.Blue Gene Project and identification of candidate genes mutations

The subjects of this thesis have originated from a large genetic screen project in which pediatric patients with neurodevelopmental diseases were suspected of having a genetic disease because of the consanguineous marriage of their parents but no genetic disease was identified with known genetic markers. Patients and their immediate families donated blood and consented to participation in the study. By Whole Exome Sequencing, candidate genetic variants were determined.

For the interpretation of the WES data first, the quality of the sequencing data was assessed, and low-quality readings were removed. Then, high-quality readings were aligned to the human reference genome using the Burrows-Wheeler Aligner (BWA), and duplicate data were removed. The Genome Analysis Tool Kit (GATK) was used for indel realignment and base recalibration, followed by the identification of variants shorter than 50 nucleotides. For the assessment of the likelihood of identified variants in the general population, the allele frequencies from the 1000 Genomes Project were merged with the dataset obtained in the Blue Gene Project. The variants with less than 1% frequency were annotated using Annovar software, with the details on associated gene locations, exons, and any associations to the known phenotypes or diseases. The effects of these mutations at the gene locations at the transcript level (e.g., nonsense, missense, frameshift) were also assessed. All annotations were stored in Variant Calling Format (VCF) files. The compatibility of observed variants with specified inheritance patterns was assessed using the GEMINI software, and analysis code in the R programming language facilitated the necessary analyses. Additionally, the relevance of genes matching the determined inheritance pattern to the specific phenotype based on disease-gene relationship data from the GeneCards database was evaluated.

3 different variants for three different consanguineously married families we studied after obtaining the candidate gene variants: A single nucleotide deletion in the *WDR62* gene causing frameshift mutation, a single nucleotide alteration for the *VARS1* gene causing missense mutation, and an eleven-nucleotide deletion in *ATG9B* gene causing frameshift mutation. *WDR62* variant was confirmed by Sanger sequencing and subsequent pairwise alignment for proband, her sister, and their parents. The Proband of *VARS1* mutation was also confirmed by Sanger sequencing. The variation destroys a Tsp45I restriction site therefore proband and family members were confirmed by restriction digestion as well. Eleven-nucleotide deletion of

ATG9B was creating nucleotide shift therefore the variation was confirmed by Sanger sequencing for proband and agarose gel electrophoresis for the other members of the family.

By this, we were able to identify and confirm novel category 1 pathogenic variants *WDR62* and *VARS1*, and category 3 likely novel pathogenic variant *ATG9B* as stated in the introduction section. Detailed data are presented in the following sections.

4.2.WDR62

The proband, a child born of consanguineous marriage, presented with microcephaly and suspected motor-mental retardation (MMR). Her parents, who shared the same great-grandparents and were third cousins, were healthy, but her sister also exhibited microcephaly, lissencephaly, and MMR (Figure 15-A). The first cousin of the mother had mental retardation and the first cousin of the father had microcephaly and MMR. Considering the clinical presentation, family history and consanguineous marriage clinicians suspected a genetic disease, but genetic tests failed to identify any known genetic disorder. Consequently, with the consent of the patient and her immediate family, blood samples were obtained for their participation in the Blue Gene study.

Genomic DNA isolation from the peripheral blood was, and subsequent WES analysis revealed the variant as a single cytosine (C) deletion, located at chromosome: 19:36,545,976, in the first exon of the WDR62 gene. This deletion occurred in the 103rd position of the coding sequence, leading to a frameshift mutation. Notably, both sisters were homozygous for this deletion, while their parents were heterozygous. This variant had not been previously identified in the dbSNP database or in the ClinVar database in NCBI.

To validate this genetic variation, Sanger sequencing was employed. Specifically designed primers were used to generate PCR products, which were subsequently subjected to Sanger sequencing. This analysis confirmed that the variant was indeed homozygous in the proband and her sister, while it was heterozygous in their parents (Figure 15-B).

To confirm the genetic variation by Sanger sequencing, primers were designed, and PCR product was sequenced with Sanger sequencing. The single nucleotide deletion occurred in exon 1 of the WDR62 gene, which have 32 exons in total, resulted in a frameshift mutation. The deletion occurred in 103rd nucleotide, the Proline amino acid at this position remained unchanged due to the of adjacent cytosine residues. The downstream amino acid sequence

completely changed due to the frameshift, and the introduction of a stop codon after the 75th amino acid resulting in a complete loss of the protein. (Figure 15-C).

In this project, we identified a novel, autosomal recessive frameshift mutation in *WDR62* gene causing microcephaly, lissencephaly, motor-mental retardation phenotype.

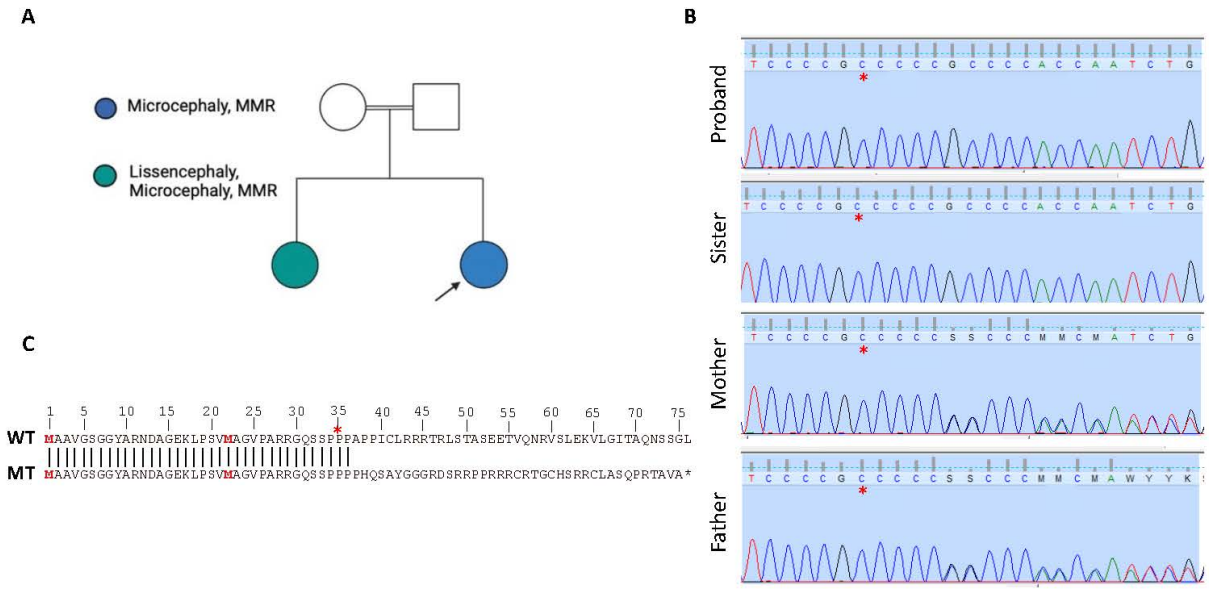

Figure 15. Identification and validation of the novel *WDR62* frameshift mutation. A) Family tree of the proband. Healthy consanguineously married couple and their two daughters with microcephaly, lissencephaly, motor-mental retardation. B) Sanger sequencing densitometry of the family. C) Deletion in the first coding exon of *WDR62* gene causing a frameshift mutation, alteration of the polypeptide sequence.

4.3.VARS1

The pediatric patient was born of a 39-year-old mother with gestational diabetes at 38 weeks of pregnancy without complication via cesarean section. She was 3300 g at birth, the third child of a consanguineously married couple who are the first cousins. Parents were asymptomatic so were their two older daughters.

The patient was admitted to the hospital three days after birth with dehydration and hyperthermia. At 15 days old, she had urinary tract infection and was admitted to the hospital again. She had, bifrontal narrowing and high palate, indications of microcephaly, and left renal

agenesis, patent foramen ovale, the syndrome that occurs when the valve between the left and right atriums of the heart does not close as it does spontaneously after birth in healthy newborns.

She was admitted to the hospital at 45-days of age with migrating myoclonic seizures that are active in sleeping, and awake states, lasting for 3 days. She had mild axial hypotonia (low muscle tone affecting the trunk of the body), mild upper limb spasticity, increased deep tendon reflexes, bilateral clonus (involuntary and rhythmic muscle contractions), no Babinski sign (reflex of thumbs bend when the skin of the base of the foot is stimulated). Her biochemical tests were normal. Electroencephalography (EEG) revealed multifocal epileptic activity, and Brain magnetic resonance imaging (MRI) revealed T2 hyperintensity in cerebral white matter indicating abnormalities in white matter composed of axons of the nerve cells. MR spectroscopy revealed slightly higher lactate in the brain, which may indicate metabolic or cellular alterations.

During the 3-month follow-up visit to the hospital, it was seen that the patient's condition worsened. She had axial hypotonia, increased deep tendon reflexes, clonus, and spasticity with severe developmental delay, she could not control her head, and maintain eye contact or eye tracking. She had epileptic encephalopathy and experienced drug-resistant seizures. She died at the age of 11 months because of complications due to an upper respiratory infection.

Whole-exome sequencing (WES) identified a homozygous missense variant (rsID: rs777665186) on chromosome 6:31747470, leading to a G>A change and resulting in p. T1068M alteration (Figure 16-A). This variant had a global frequency of 0.0002. WES also revealed two other variants in the Laminin subunit gamma-2 (LAMC2) and Ubiquitin carboxyl-terminal hydrolase 24 (USP24) genes. All three variants were located in conserved regions. Previously reported mutations related to the symptoms of the patient suggested that the VARS1 variant as the causative mutation for the disease. It's important to note that this specific variant had not been previously associated with any clinical disease in the ClinVar database.

The candidate variant was subsequently confirmed for the proband through Sanger sequencing. Additionally, it was discovered that the wild-type (WT) gene possessed a Tsp45I enzymatic restriction site that was disrupted by the G>A change in the mutant allele (Figure 16-B). Therefore, the mutation was confirmed for the family members through PCR and restriction digestion. The mutation followed an autosomal recessive inheritance pattern. The

proband was homozygous for the mutation, the parents and one sister were heterozygous and asymptomatic, and one sister did not inherit the mutated allele (Figure 16 C-D).

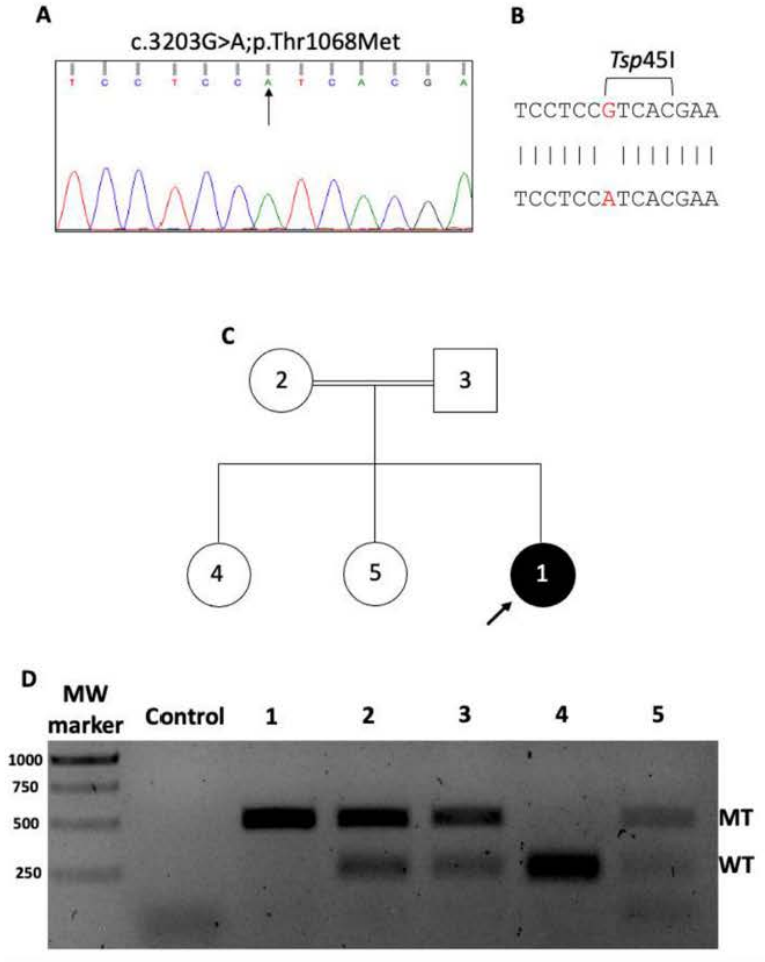

Figure 16. Identification and validation of the novel *VARS1* missense mutation. A) The confirmation of the nucleotide alteration by Sanger sequencing for the proband. B) Tsp45I enzyme site of on WT *VARS1* and destruction in mutated sequence. C) Family tree indicating autosomal recessive inheritance for the mutation. D) Genotypic confirmation of the family for the variant by digestion with Tsp45I enzyme.

Upon a more detailed examination of the p.T1068M missense mutation, the amino acid was located in the anticodon binding domain of the VARS1 protein. Notably, mutations of aminoacyl-tRNA synthetases (ARS) are typically identified within the enzymatic domains. In the literature, there were three other mutations (p.R1058Q, p.F1072L, p.M1064I) identified in very close proximity to p.T1068M, forming a cluster of mutations within a 15-amino acid stretch in the anticodon binding domain (Figure 18-A) (6–8). All four amino acids were

conserved among the mammalian species (Figure 17). This mutation hotspot captured our attention and motivated us to comprehensively study these mutations identify their detrimental effects on the protein, by structural biology.

The crystal structure of *Thermus thermophilus ValRS*, as deposited in the Protein Data Bank (PDB) under the code 1GAX. This crystal structure served as a template to model the human VARS1 protein (Figure 1-B) (42). Through this structural analysis, we aimed to elucidate the consequences of the clustered mutations on the VARS1.

Figure 17. The conservation of amino acids in the mutational hotspot in *VARS1* gene. A) Multiple sequence alignment of human VARS1 and close mammalian relatives show that the anticodon binding domain region the mutation p.T1068M was detected is highly conserved. B) Mutfunc webserver predicted the mutations in the cluster to be impactful due to its conservation.

The mutations p.R1058Q, p.M1064I, p.T1068M, and p.F1072L are all localized within the 15-amino acid stretch of the anticodon binding domain, from Q1047 to L1075 (Figure 18-A). This segment corresponds to a helix-turn-helix (HTH) motif commonly found in proteins that are involved in DNA binding and other molecular interactions (Figure 18-B, C) (98).

The mutations have destabilizing effects on the protein according to MaestroWEB server (Table 8).

For p.M1064I and p.F1072L, the mutations disturb the interhelical hydrophobic interactions within the HTH motif. Hydrophobic interactions are crucial for stabilizing protein

structures. The disruption of these interactions is likely to have a destabilizing effect on the protein (99).

In the cases of p.T1068M, p.R1058Q and p.T1068M, the mutations lead to a reduction in hydrophobic interactions within the HTH motif. Electrostatic interactions play a significant role in protein structure and function by the attraction or repulsion of charged groups in the protein. Therefore the reduction in the electrostatic interactions may have a destabilizing effect on the protein (100) (Table 9).

Moreover, the p.T1068M mutation results in the loss of a stabilizing hydrogen bond with p.S1061 located on the reciprocal helix within the HTH motif (Figure 18-D). Hydrogen bonds are known to be among the strongest non-covalent interactions and are critical for both intra-molecular stability and inter-molecular interactions. The loss of this hydrogen bond may significantly impact the stability of the protein (101).

Taken together, the mutations within the p.Q1047-L1075 stretch of the HTH motif, including p.T1068M potentially disrupt the structural integrity and stability of the protein ultimately contributing to the observed disease presentation.

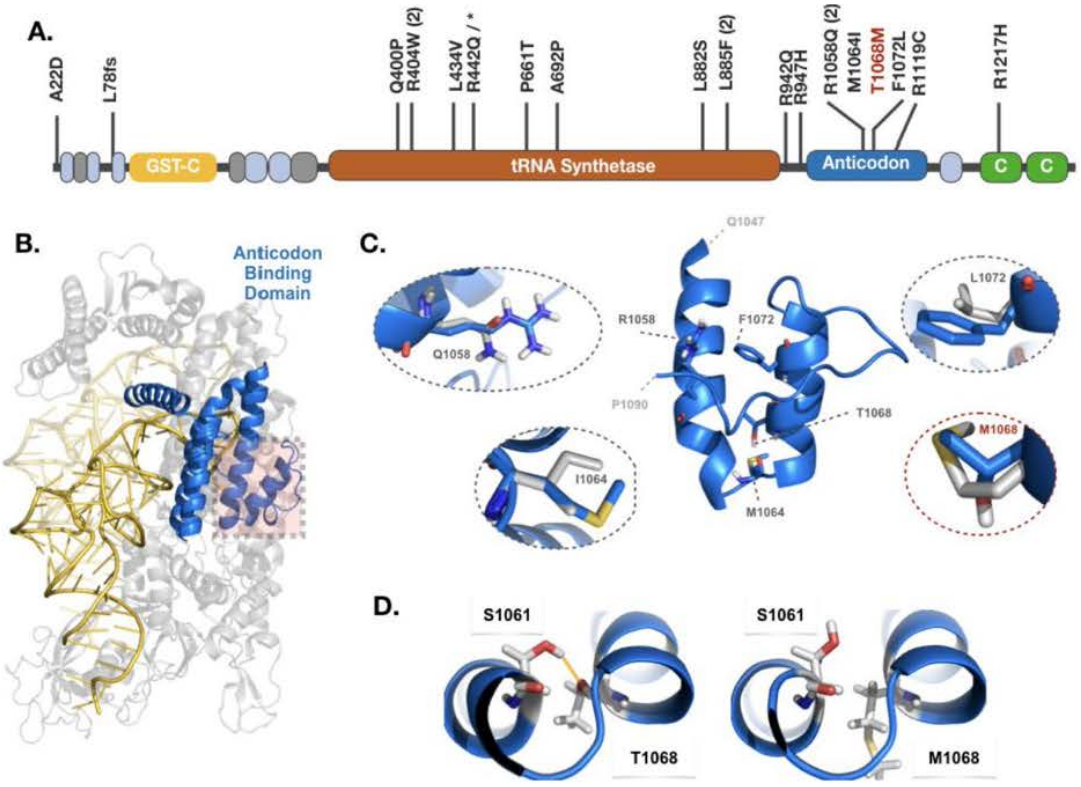

Figure 18. The effect of p.T1068M substitution in VARS1 protein. A) Domain structure and mutations reported in the literature were presented as a diagram. B) The human VARS1 model based on *Thermus thermophilus* ValRS crystal structure on PDB (1GAX) C) The structural

motif harboring the mutation sites. D) The loss of hydrogen bond between reciprocal alpha-helices due to p.T1068M.

Table 8. The effects of the *VARS1* mutations in protein stability. (Predicted by MaestroWeb server.)

Mutation	MaestroWeb (arbitrary units)
p.T1068M	0.49 (Destabilizing)
p.R1058Q	1.83 (Destabilizing)
p.M1064I	0.84 (Destabilizing)
p.F1072L	1.76 (Destabilizing)

Table 9. The effect of *VARS1* mutations in hydrophobic interactions. Number of anticodon binding domain and tRNA synthetase domain interactions are reduced in total compared to WT.

Contact types	WT	p.R1058Q	p.M1064I	p.T1068M	p.F1072L
charged-charged:	4	3	4	3	3
charged-polar:	13	12	12	12	12
charged-apolar:	48	46	47	47	44
polar-polar:	2	2	2	2	2
polar-apolar:	28	29	23	29	24
apolar-apolar:	75	73	70	74	78
Total	170	165	158	167	163

4.4.ATG9B

The pediatric patient, a 13-year-old male came to Dokuz Eylul University Hospital with a complaint of intellectual disability. The patient was born to a consanguineously married healthy couple. The medical history of the patient involved mental retardation, having trouble with literacy, communicating with a limited number of words, and attending a special education program abroad where the family lives. The patient did not have motor complaints but walked late, no history of seizures was reported. The patient was undiagnosed with a known genetic disease even though a genetic disease was clinically suspected. The physical examination of

the patient confirmed the limited communication with short one-word answers, displayed attention deficit, and was unable to concentrate during the examination. The patient was obese, his eyes were deeply located on his face suggesting facial dysmorphia and had a simian line on his right hand. The patient's MRI and his biochemical tests were normal. The patient had a 9-year-old with milder mental retardation, who was also receiving special education and had a high appetite and obesity. The oldest child of the family, a 16.5-year-old older brother, had more severe motor-mental retardations, unable to talk, walk, and had hearing loss. Additionally, he had epileptic seizures. The physical state of the older brother being bed-bound abroad where the family lives made it impossible to have him included in the study (Figure 19-A).

The family participated in the Blue Gene project and WES identified a deletion at chromosome: 7:150714319-150714329 DEL (x2). The candidate variant was in the *ATG9B* gene (rsID: rs747858674) with a global 0.01 frequency. Deleted nucleotides, 5'-CGCTGAGACAG-3' composed of 11-nucleotide located in exon 9 of 13 exon protein, therefore it was predicted to cause frameshift mutation and C-terminal deletion in the protein sequence. Sanger sequencing confirmed the deletion (Figure 19-B). Additionally, the 11-nucleotide size difference was taken advantage of for the genotyping of the proband and the other family members by agarose gel electrophoresis (Figure 19-C). The deletion caused the protein sequence to change starting with amino acid 695 and after six altered amino acids a premature stop codon caused the truncation of the C-terminal cytosolic site of the protein (Figure 19-D).

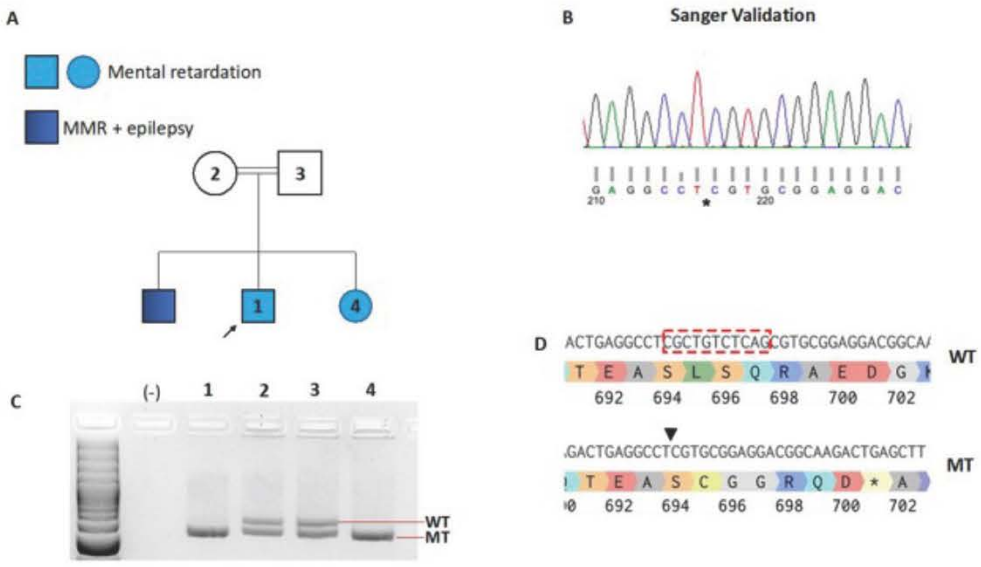

Figure 19. Identification and validation of the novel *ATG9B* frameshift mutation. A) The family tree of the consanguineously married couple and their affected children. B) Sanger sequencing confirmation of the deletion in the *ATG9B* gene the proband. D) Alteration of the amino acids sequence due to the deletion.

Human ATG9B is 924 amino acids long and is composed of six membrane-embedded domains with cytosolic N-terminal and C-terminal disordered regions. Four of the membrane-embedded domains are in the APG9 core domain. The C-terminal cytosolic site of the protein is altered due to the frameshift, starting at the 695th amino acid and resulting in a premature stop codon gain after the 700th amino acid. Due to the frameshift, 224 amino acid is deleted at the C terminal, truncating the ATG9B protein (Figure 20).

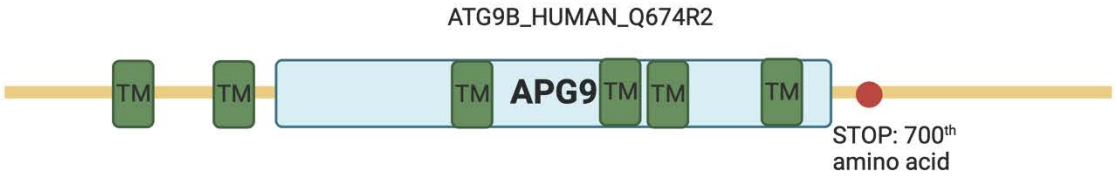

Figure 20. The domain organization of ATG9B protein. (Prepared in Biorender, adapted from UniProt PFAM)

The literature on ATG9B is very limited but it was suggested that it could rescue autophagy defects due to ATG9A knockdown. The alterations of ATG9B expression were reported to have effects on a variety of diseases as detailed in the introduction section. Most importantly, ATG9B is expressed mainly in the placenta, and pituitary gland, and moderately

in the esophagus and testis according to Protein Atlas. Additionally, C terminal deletion of the protein may disrupt the protein folding, structure, trimerization, trafficking, or localization. Additionally, disordered regions are known for maintaining protein-protein, and protein-lipid interactions (102). ATG9B expression profile suggests that the disease phenotype may have originated in placental development. Neurobehavioral disorders such as autism spectrum disorder are linked back to placental development referred to as the placenta-brain axis. Brain development is prone to be affected by placental disturbances *in utero* (103).

In this study, we have identified a novel *ATG9B* frameshift mutation causing a novel neurodevelopmental disease. To study the function of ATG9B and the truncation we studied its expression in cell lines, we modeled cells ectopically express WT and truncated forms of the ATG9B. To study the expression of ATG9B in human cell lines and in mice tissues we generated N terminal ATG9B.

We generated a genetically modified mouse model of the genetic disease by CRISPR-EZ technique. We inserted a stop codon by homology-directed repair (HDR) template on the mouse Atg9b gene to the position of frameshift mutation seen in patients. Since mouse and human ATG9B sequences were conserved we were able to model the genetic disorder as close to as seen in human pediatric patients. We performed histology, immunofluorescence, and immunoblot experiments to visualize the expression of ATG9B and potential placental abnormalities due to truncation. We performed behavioral studies to better understand the disease phenotype. We also generated ATG9B knock-out, FLAG-Atg9B mouse lines for histology and expressional studies to better understand ATG9B function *in vivo*.

4.4.1. Determination of ATG9B Expression in Human Cell Lines

The expression data obtained from Protein Atlas is derived from RNA datasets lacking protein-level data on ATG9B expression in tissues or cell lines. Hence, our objective was to investigate ATG9B expression in various human cell lines at both transcriptional and translational levels. We designed two primer sets targeting the N-terminal and C-terminal cytosolic regions. Subsequently, we performed semiquantitative RT-PCR with these primers for 30-35 cycles. In line with the literature, BeWo cells exhibited higher ATG9B expression compared to HeLa and HEK293T cells (Figure 21-A).

To confirm this data, we repeated the RT-PCR for 30 cycles using primers for the GAPDH housekeeping gene, obtaining similar GAPDH expression for all three cell lines

(Figure 21-B). Notably, in human cells, while cytotrophoblasts expressed ATG9B syncytiotrophoblasts expressed ATG9B significantly higher. BeWo cells, treated with forskolin, were used to model *in vitro* syncytiotrophoblast formation (104). Successful induction of syncytiotrophoblasts resulted in membrane fusion, confirmed with immunofluorescence experiment with anti-Zona occludens-1 (ZO-1) antibody expressed in plasmas membrane tight junctions. (Figure 21-C). Furthermore, syncytiotrophoblasts specifically express human chorionic gonadotrophin β (hCGβ) (104). The significant increase in hCGβ suggests the model was successful and ATG9 expression in BeWo and JAR cells is increased upon syncytialization (Figure 21-D). This study presents the first documentation of ATG9B upregulation resulting from forskolin-induced cellular syncytialization.

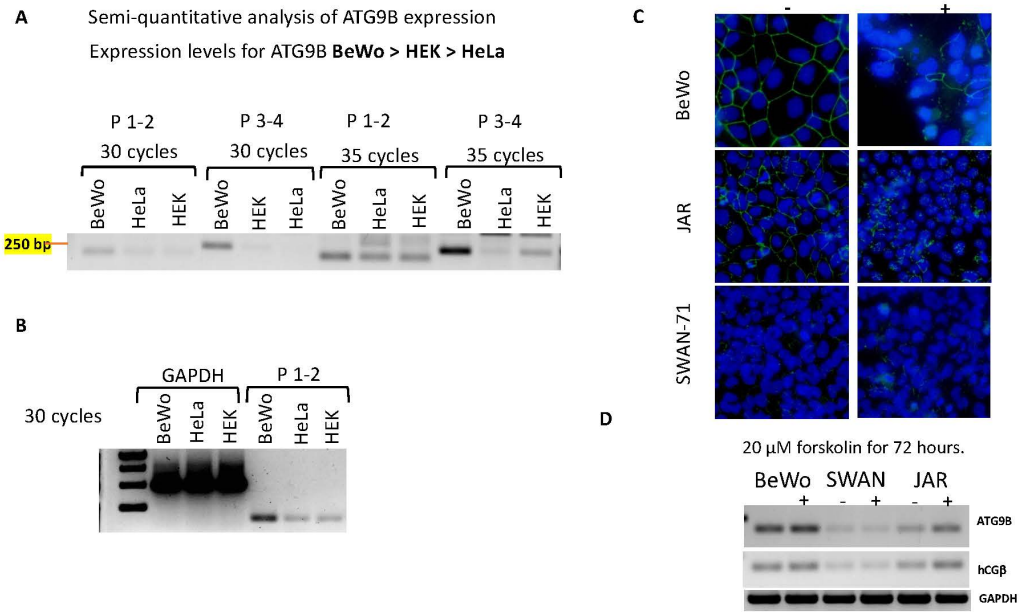

Figure 21. The expression of ATG9B in placental cell lines. A) Semi-quantitative RT-PCR showing ATG9B expression is elevated in BeWo cells. B) The confirmation of data in A with housekeeping GAPDH control in RT-PCR. C) The demonstration of cell membrane fusion upon forskolin treatment in BeWo and JAR cells D) RT-PCR upon forskolin treatment with ATG9B and hCGβ and ATG9B.

For assessing ATG9B expression at the protein level, we performed immunoblot screening across various human cell lines with placental trophoblast and choriocarcinoma origin in parallel with a variety of liver cancer, neuroblastoma, embryonic kidney, and cervical cancer cell lines. The commercial antibodies recognizing epitopes in both the N-terminal (Stressmark SPC-646D) and C-terminal (Novus NBP1-77169) cytosolic domains of ATG9B

were used for the assessment. In the literature ATG9B exhibits tissue-specific expression while ATG9A is ubiquitously expressed in most tissues, we investigated ATG9A expression concurrently (Cell Signaling D4090). As a positive control, we took advantage of HeLa monoclonal B3 which stably expresses ATG9B. ATG9B expression in the B3 clone was clear, albeit endogenous level expression was not detected in any of the cells including BeWo despite the RNA level expression data from the Protein Atlas (Figure 22-A). Furthermore, ATG9A expression was evident in HeLa, HEK293, SNU449, SWAN-71, and HEP3B, in decreasing order (Figure 22-B).

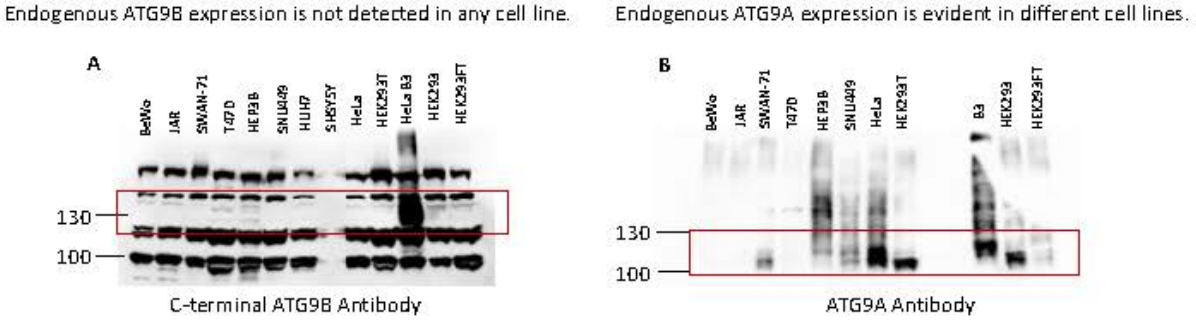

Figure 22. ATG9B and ATG9A protein expression in human cell lines. A) Endogenous ATG9B expression is not detected in cells, HeLa B3 positive control ATG9B expression was detected. B) ATG9A expression was detected in the majority of the cell lines.

4.4.2. Functional Characterization of ATG9B Truncation Mutation in Cellular Models

4.4.2.1. Molecular Cloning of ATG9B Ectopic Expression Constructs

In the previous section, we could not detect endogenous ATG9B expression at protein level in any of the cell lines we studied (Figure 22). Therefore, we decided to study wild-type (WT) and truncated ATG9B by mammalian ectopic expression vectors. The mutation in the patient results in a premature stop codon and subsequent C-terminal deletion of ATG9B protein, a truncation.

Firstly, we obtained coding sequences of WT and truncated ATG9B from a gene synthesis vendor (GeneWiz) to avoid experiment-driven point mutations. The truncation was modeled by synthesis of the ATG9B coding sequence until the beginning of the altered amino acids due to the frameshift. Neither of the constructs had a STOP codon to be able to directly subclone to plasmids with GFP 3' site of the multiple cloning site. We included 5'-BamHI and 3'-EcoRI restriction sites for subcloning. The synthesized WT and truncated ATG9B were cloned to pUC57 plasmid and then sequenced for confirmation by the vendor. Then using the

mentioned restriction sites, WT and truncated ATG9B were subcloned to pCS2 mammalian/zebrafish expression plasmid to the 5' site of the GFP tag. We were unable to see the expression of the truncated ATG9B by pCS2 clones on the protein level upon transfection (Figure 24). Moreover, the pCS2 plasmid does not possess an antibiotic resistance gene, and even with cell sorting by GFP signal, twice, did not retain the expression for more than one week. Therefore, we decided to take advantage of mammalian expression vectors with antibiotic resistance genes.

We subcloned ATG9B-GFP constructs into a mammalian expression vector, pcDNA3.1 having a geneticin resistance gene to generate stable clones of human cell lines expressing hATG9B WT-GFP and hATG9B TR-GFP (Figure 25). We could not maintain stable WT or TR ATG9B expression for the long term upon geneticin selection (data not shown).

We also decided to use a smaller well-established tag at the N-terminal site of ATG9B WT and truncated constructs. The purpose was to avoid any hindrance that can be caused by the large GFP protein at the C-terminal site of ATG9B or any problems with folding on the region we were most interested in. We decided on the FLAG tag for this purpose since it is well-established and experimental protocols, antibodies were abundant for this tag. We used the pUC57-ATG9B WT plasmid from the synthesis vendor for both FLAG-WT and TR ATG9B generation. We decided to add six altered amino acids to the C terminal site of truncated ATG9B to model the truncation seen in the patient genotype completely (Figure 19). By PCR, we were able to add the FLAG tag at the 5' and a stop codon at the 3' of ATG9B for both constructs. We also added the six altered amino acids 5' to the stop codon of ATG9B-TR (Figure 26). We were unable to generate the stable cells we planned for WT or TR ATG9B by transfection and geneticin selection (Data not shown).

To address stable cell generation more efficiently, we decided to follow a lentiviral transduction method for both constructs. We subcloned FLAG-hATG9B WT and TR to pBOBI lentiviral vector. Although this plasmid does not benefit from antibiotic resistance it made it possible to generate monoclonal FLAG-ATG9B WT expressing stable cell line for HeLa B3 (Figure 31). Yet, stable cell generation expressing ATG9B truncated expression was unable to be obtained even with genomic integration (Figure 32).

3xFLAG tag is an improvement of a single FLAG tag developed by Sigma-Aldrich. It promises 200 times more detection upon utilization. In single FLAG constructs we were unable to detect ectopic expression through anti-FLAG antibody (F1804) but we observed significant

expression with 3xFLAG-FAM134B protein that is used as a positive control (Figure 27). We decided to amplify the detection by taking advantage of the mammalian expression vectors with 3xFLAG tags for transient transfection studies. We used p3x-FLAG-CMV-10 vector and subcloned FLAG-hATG9B WT and TR, obtaining 4xFLAG-hATG9B WT and 4xFLAG-hATG9B TR constructs (Figure 28).

We wanted to obtain hATG9B WT and TR constructs with a different tag for co-localization studies. The aim of this was after generating FLAG-hATG9B WT expressing stable monoclonal HeLa B3 cells we wanted to address the similarities and differences between WT and TR ATG9B proteins in co-localization. We cloned hATG9B WT and TR, to pcDNA3.1-myc-his A vector and generated hATG9B WT-myc and hATG9B TR-myc constructs, tag located at the 3' end of the coding sequence, without FLAG tags at the 5' to the coding sequence (Figure 37).

The experimental necessities of these clones were stated in this section briefly, detailed information will be provided in the following sections in terms of experimental results and subsequent actions.

The protein products are represented in Figure 23 schematically and the complete list of the cloned vectors is presented in Table 10. Primer designs, frame confirmations were performed on SnapGene program.

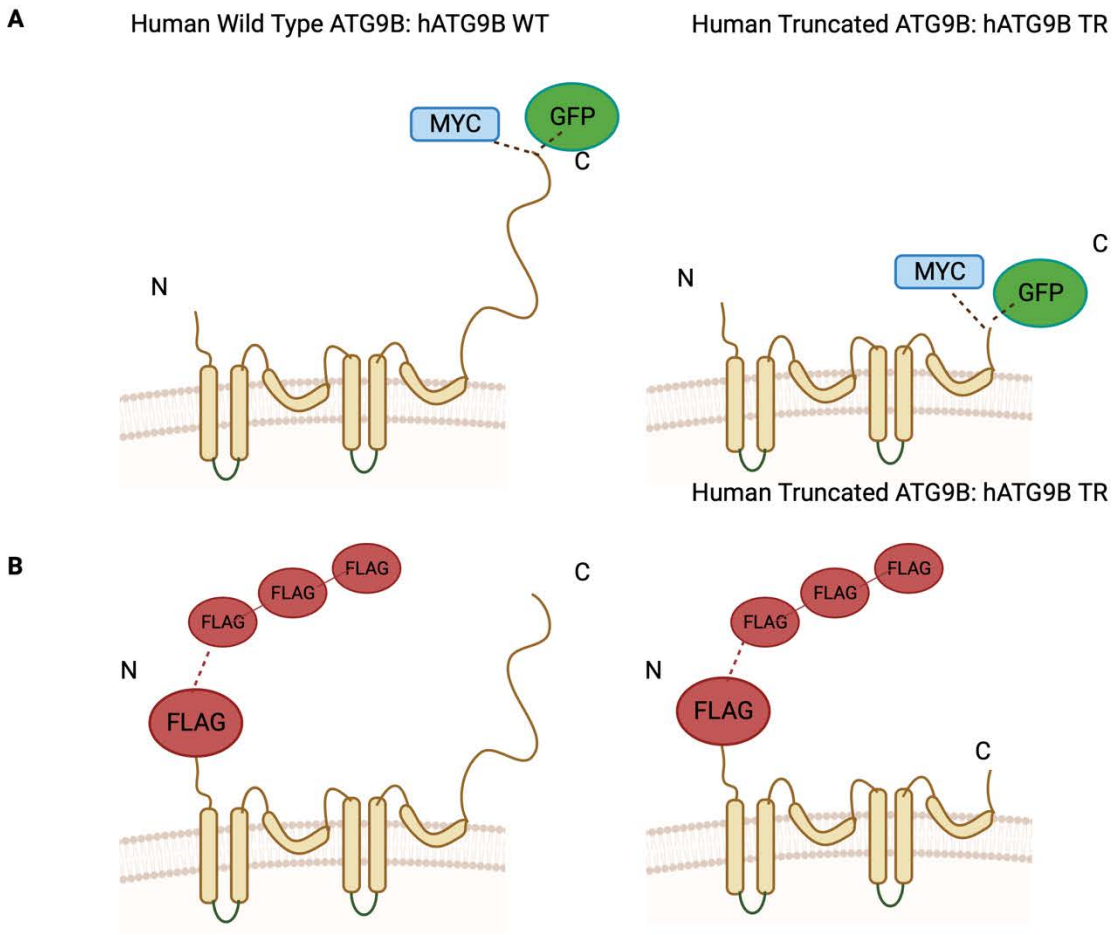

Figure 23. The ATG9B protein, and locations of the epitope tags. A) For direct fluorescent imaging I inserted hATG9B before GFP or MYC tag, in frame. B) FLAG tag was inserted before hATG9B-WT and TR. (Prepared in BioRender, adaptation from reference (78)).

Table 10. Plasmid constructs used in human cell line studies.

	PLASMID CONSTRUCTS	PURPOSE
1	pUC57-hATG9B WT	From gene synthesis vendor
2	pUC57-hATG9B TR	From gene synthesis vendor
3	pCS2-hATG9B WT-GFP	GFP fusion construct
4	pCS2-hATG9B TR-GFP	GFP fusion construct
5	pcDNA3.1-hATG9B WT-GFP	GFP fusion construct with geneticin
6	pcDNA3.1-hATG9B TR-GFP	GFP fusion construct with geneticin
7	pcDNA3 FLAG-hATG9B WT	FLAG fusion construct with geneticin
8	pcDNA3 FLAG-hATG9B TR	FLAG fusion construct with geneticin
9	pBOBi FLAG-hATG9B WT	Lentiviral transduction
10	pBOBi FLAG-hATG9B TR	Lentiviral transduction
11	pcdna3.1 hATG9B WT myc his A	myc construct for colocalization
12	pcdna3.1 hATG9B TR myc his A	myc construct for colocalization
13	p3xFLAG-FLAG hATG9B WT	Improved detection
14	p3xFLAG-FLAG hATG9B TR	Improved detection

4.4.2.2. Characterization of hATG9B WT and hATG9B TR by Transfection/Ectopic Expression Studies

To investigate the expression and localization patterns, we transfected pCS2-hATG9B WT-GFP and TR-GFP constructs into HEK293 cells. The transfection efficiency was visualized by the GFP signal on culture plates. After 48 hours, we collected the cells and prepared lysates for immunoblotting. One membrane was blotted with Anti-ATG9B (targeting the C-terminal epitope), and the other with Anti-GFP (Santa Cruz SC9996) antibodies. hATG9B WT and TR GFP fusion proteins should be visualized at molecular weight bands of 129 kDa and 103 kDa, respectively.

Upon initial observation, the expression of hATG9B-TR was lower compared to WT and GFP-only plasmid, and the transfected cells displayed rounder and less healthy morphology, despite identical experimental conditions for all samples (Figure 24-A). We successfully visualized the expression of ATG9B WT using both GFP and ATG9B antibodies. However, the truncated form (TR) was not expressed. Notably, it was expected that the C-terminal antibody not being able to detect the truncated form due to the deletion of the

antibody's epitope. Nevertheless, GFP antibody should have been able to reveal its expression (Figure 24-B).

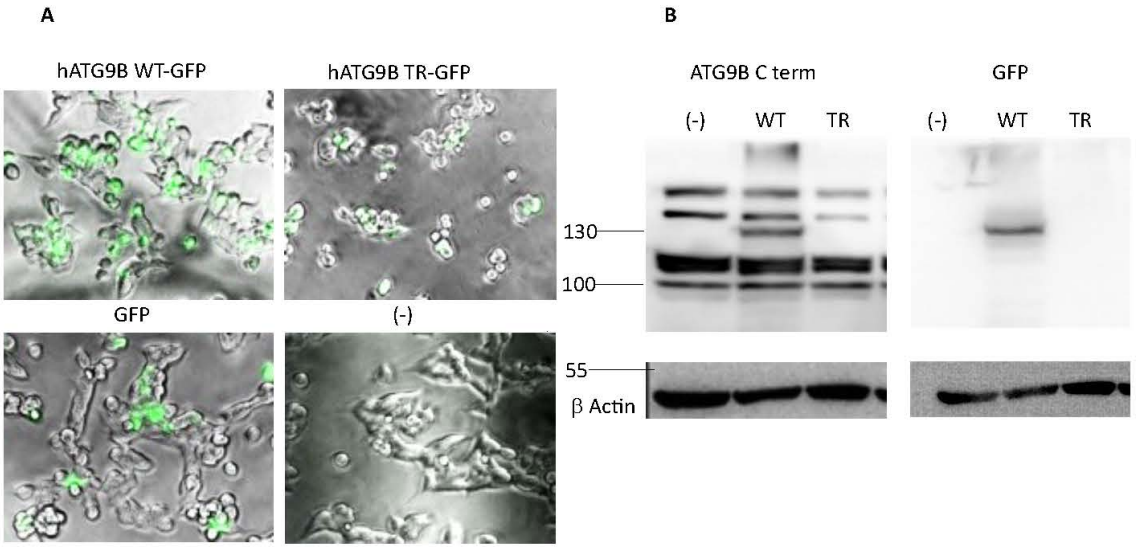

Figure 24. The ectopic expression of pCS2 hATG9B-GFP WT and TR constructs. A) ATG9B-GFP proteins are visualized post-transfection. B) The expression of the ATG9B-GFP proteins blotted with Anti-ATG9B antibody (C terminal epitope) and anti-GFP antibodies.

Under normal nutrient conditions, we failed to detect the expression ATG9B-GFP truncated (TR) by immunoblotting. To investigate whether the expression of TR is induced upon starvation condition that is known to stimulate autophagy, we designed an experiment using pCS2 constructs. Before cell collection, we subjected HEK293, HeLa, and HUH7 cells to a 4-hour period of starvation treatment with EBSS. In a separate experiment, we extended the post-transfection incubation time to 48 hours to maximize protein expression. Despite these efforts, we were unable to observe the TR expression (Results not shown). We started to explore the generation of stable cells expressing these fusion proteins. The pCS2 vector lacks an antibiotic resistance gene. Therefore, we utilized the BD FACSAria cell sorter to selectively collect GFP-expressing cells. The GFP signal gradually reduce over time, and the colonies could not maintain the GFP signal continuously (Results not shown).

For the generation of cell lines stably expressing hATG9B WT-GFP and hATG9B TR-GFP, we cloned these constructs to pcDNA3.1 mammalian expression vector containing an antibiotic resistance gene geneticin (Data not shown). To confirm their expression, we conducted an immunofluorescence experiment with HeLa cells using a GFP antibody. In this

experiment, the green fluorescent signal should overlap with the red indirect GFP signal (Figure 25).

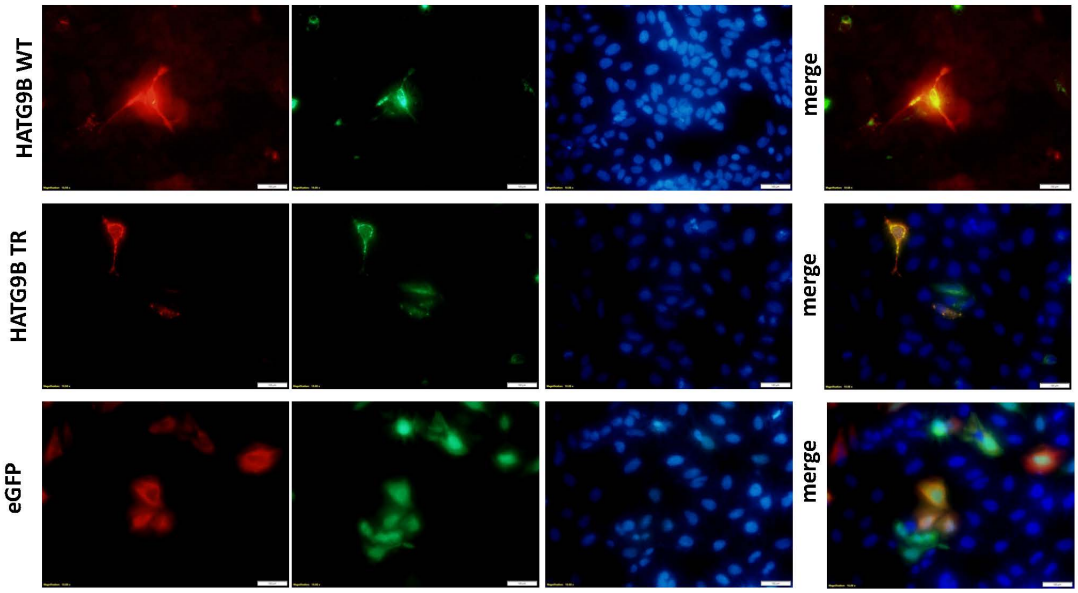

Figure 25. The ectopic expression of pcDNA3.1 hATG9B WT and TR constructs. GFP: Indirect signal is red and direct signal is GFP.

I initiated the generation of stable cell lines expressing hATG9B-WT and hATG9B-TR using HeLa, HEK293, due to their transfection suitability and HEP3B, SNU449 relevance in tumorigenesis studies of liver cancer linked to ATG9B mutations (92). Except for HEK293 WT construct we could not obtain stable expression by geneticin selection.

The TR form possibly was not stable and cannot be expressed due to the absence of the C-terminal cytosolic site. However, we first wanted to eliminate the possible effect of 27 kDa GFP tag at the C-terminus on the protein folding. Therefore, we generated FLAG-hATG9B WT and FLAG-hATG9B TR constructs, utilizing pUC57-hATG9B WT plasmid from the vendor. We added the altered amino acids prior to stop codon from as seen in patients by PCR. Consequently, we generated a more precise model and of the truncation. Additionally, the tag was cloned to the 5' of the coding sequence thereby freeing the C-terminal region of the protein.

By using N-terminal and C-terminal ATG9B and FLAG antibodies, we conducted immunofluorescence experiments WT and TR ATG9B expression and cellular localization (Figure 26).

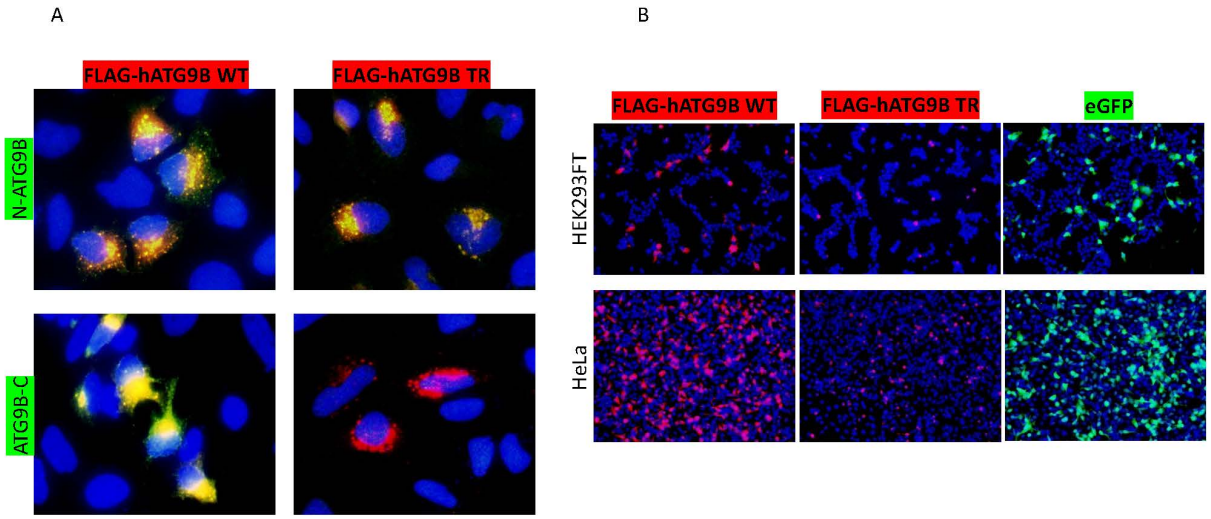

Figure 26. The ectopic expression and localization of FLAG-ATG9B WT and TR. A) Co-localization of FLAG, ATG9B N-terminal and C-terminal commercial antibodies. FLAG-hATG9B WT localization in near the nucleus and cytosol as puncta, FLAG-hATG9B-TR is aggregated and restricted to perinuclear compartments. B) Lower magnification shows that the expression of TR is significantly lower than WT.

Two observations were noteworthy from these experiments. Firstly, FLAG-hATG9B WT localization was mainly perinuclear as well as puncta distributed around the cytoplasm. On the other hand, ATG9B-TR localization was strictly restricted in perinuclear large vesicles (larger puncta). Secondly, as observed with ATG9B-GFP fusion proteins (Figure 24), FLAG hATG9B-TR expression was lower than WT in both HEK293 and HeLa cells (Figure 26).

Subsequently, we performed immunoblots using HEK293FT and HeLa cells transfected with FLAG hATG9B-WT and TR constructs. Although we could detect FLAG-ATG9B by microscopy, we were not able to observe ATG9B WT or TR expression by immunoblotting.

Notably, we observed a dramatic band in the lysate of 3X-FLAG FAM134B control. (Figure 27).

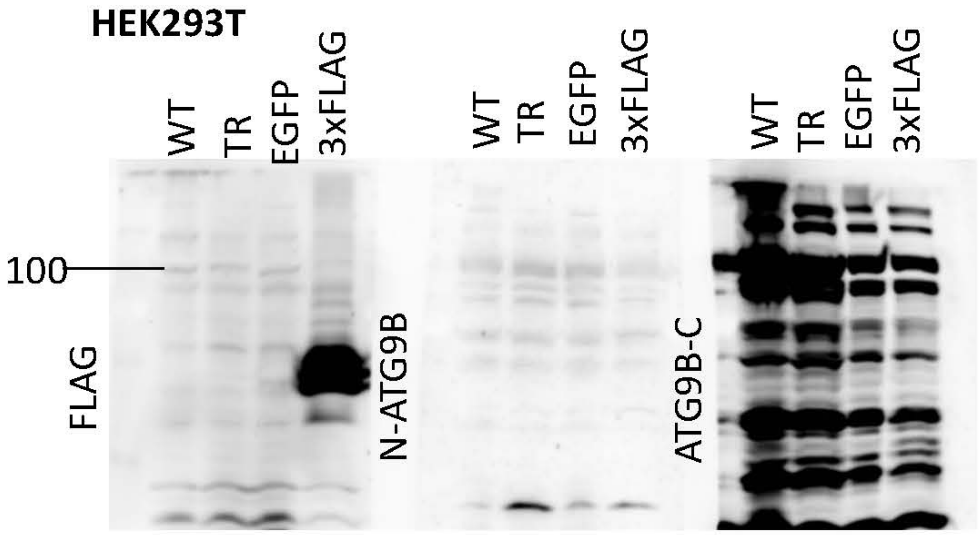

Figure 27. The ectopic expression studies with FLAG-hATG9B clones.

Ultimately, our objective was to establish easily detectable hATG9B WT and hATG9B TR protein expression. To achieve this, we subcloned FLAG-ATG9B constructs to 3xFLAG-CMV-10 vector generating 4xFLAG hATG9B WT and TR plasmids to boost the signal of the expression. We studied the effectiveness of these 4xFLAG constructs in comparison to 1xFLAG constructs by transient transfection subsequent immunoblotting. Notably, the 4xFLAG signal significantly enhanced the detection of the WT and TR signals. Remarkably, we successfully observed the hATG9B-TR signal via immunoblotting for the first time, confirming our initial observations that TR is not expressed well and the present expression is significantly lower than that of the WT (Figure 28).

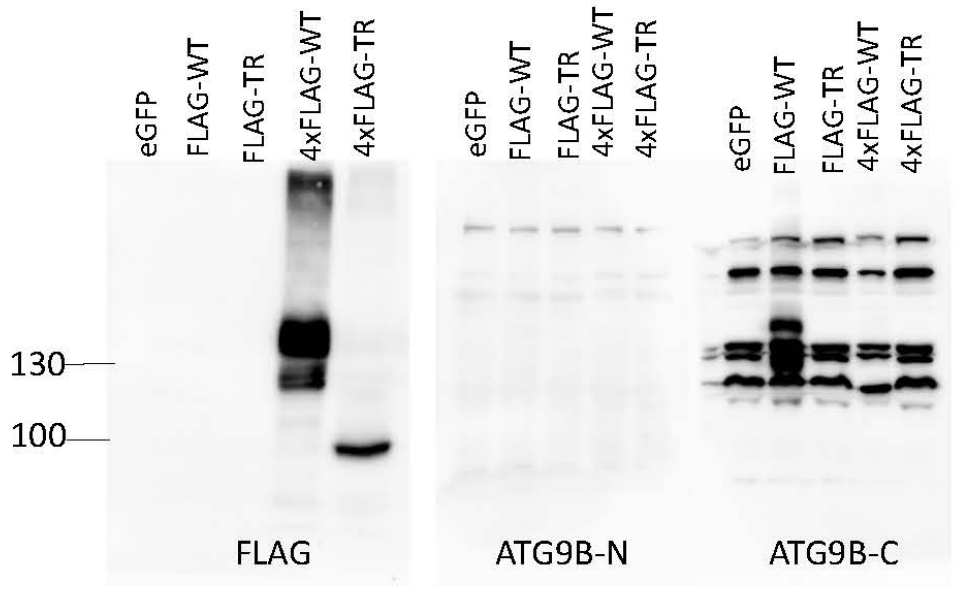

Figure 28. The ectopic expression of 4xFLAG-hATG9B constructs. Immunoblotting of HeLa cells transiently transfected with hATG9B WT and TR constructs. 4xFLAG tag made it possible to detect hATG9B-TR expression albeit very lower than WT. Anti-ATG9B against N-terminal epitope failed to detect the expression C terminal only works with overexpressed ATG9B-WT and does not recognize hATG9B-TR as expected.

I must emphasize that the N-terminal ATG9B antibody proved ineffective, while the C-terminal antibody worked as expected, but only when transfection efficiency was high (Figure 26). However, 4x-FLAG has a remarkable detection. The detection of WT while present in the C-terminal antibody was enhanced significantly upon the 4xFLAG detection with Anti-FLAG antibody. These experiments also underlined that due to ineffective N-terminal antibody, a need for a new antibody with specific N-terminal epitopes became evident for our genetically modified mouse model of the disease. However, the majority of the commercial ATG9B antibodies are designed for C-terminal epitopes, and the ones with N-terminal epitopes lacked convincing evidence of their efficiency or specificity. Hence, we decided to produce an N-terminal ATG9B antibody through rabbit immunization, a topic that will be discussed in the following chapter.

Having successfully shown hATG9B-TR expression, albeit at a lower level, we aimed to test our hypothesis that the truncated protein is either not expressed or exhibits poor stability and rapid degradation. We conducted time-course experiments to explore the effects of post-transfection incubation time on the expression of TR. Initially, we tested 1-day and 6-day post-

transfection timepoints using HEK293T and HeLa cells with 4xFLAG WT, TR, and eGFP-only constructs.

On day 1 WT expression was substantially higher than TR expression in both cell lines, as evident in both immunoblotting and immunofluorescence. On Day 6, WT expression was only minimally detectable in the IF and immunoblot, while TR expression was entirely lost (Figure 29-A, B). Then we wanted to investigate the hypothesis that TR might undergo proteasomal degradation, potentially due to truncated ATG9B being a non-functional protein. After transfection, MG-132 proteasome inhibitor was performed for up to 72 hours at a concentration of 5 μM. Although hATG9B WT expression was more pronounced in cells treated with MG-132, there was no increase in TR expression (Figure 29-C).

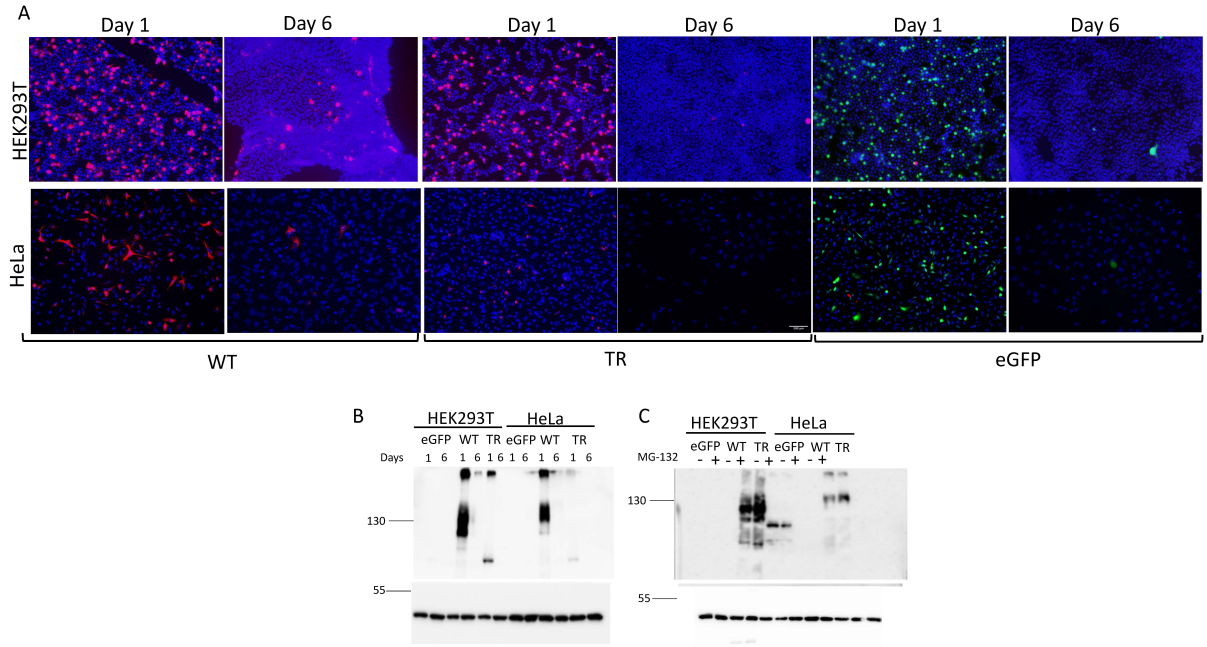

Figure 29. 4xFLAG-ATG9B WT and TR expression in different time points post-transfection and upon proteasomal inhibition. A) Immunofluorescence of HEK293T and HeLa cells show TR expression is lower in day 1 than WT. In day 6 the expression of hATG9B-TR is completely lost while WT retained some expression. C) Proteasomal inhibition resulted in the accumulation of WT while having no effect on TR.

We performed another time course experiment, 3-day period to enhance the observation of hATG9B-TR expression. Our primary objective was to identify the peak expression of hATG9B-TR using both immunofluorescence and immunoblotting. Notably, 4xFLAG hATG9B-WT expression was detectable on day 1, reached its apex on day 2, and remained

visible on day 3 albeit at a lower level. A similar expression pattern was observed for TR however, the expression levels were lower than WT. On day 3, cell samples were collected to perform semi-quantitative RT-PCR using primers specific to the N-terminal and C-terminal cytosolic sites. The expectation was that C-terminal primers should not amplify any product, serving as a negative control for TR. The mRNA levels were found to be similar for hATG9B-WT and hATG9B-TR, indicating that the lack the protein expression of TR was not due to transfection or experimental variations (Figure 30).

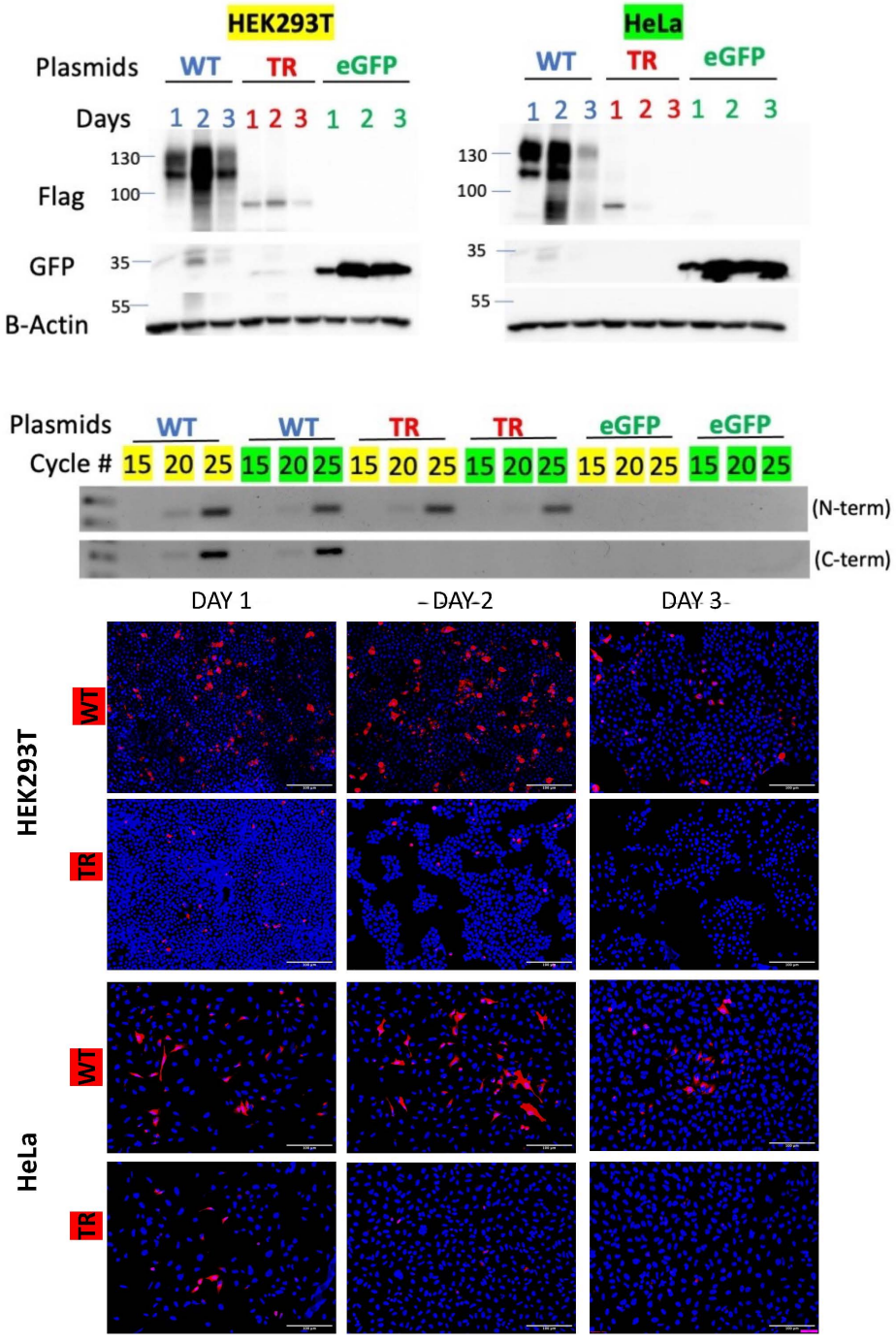

Figure 30. The inefficiency of ATG9B TR protein expression at different time points post-transfection. HEK293T cells and HeLa cells were transfected with 4xFLAG hATG9B-WT and truncated constructs. On day 1, day 2 and day 3 cell pellets were collected for immunoblotting and cells were fixed for IF. On day 3, cell pellets were collected for RNA expression.

4.4.2.3. Development of Monoclonal Cell Lines Expressing hATG9B WT

Initially, our attempts with transient transfection and geneticin selection were unsuccessful, as the cells were unable to sustain the plasmids over the long term. Consequently, we decided to adopt lentiviral transduction. We subcloned FLAG hATG9B-WT and TR constructs into the pBOBI lentiviral vector. Our aim was to employ lentiviral infection for the generation of stable cell lines expressing both FLAG ATG9B-WT and TR.

Efforts to observe FLAG- hATG9B TR expression in HeLa, BeWo, HEP3B, and HEPG2 cells through lentiviral transduction proved unsuccessful, despite conducting the experiment twice. This outcome mirrors our previous experiences, the inability to sustain expression for TR, despite initial success. Even when genome integration through lentiviral transduction was attempted, TR expression remained elusive. Therefore, we discontinued our pursuit of maintaining stable ATG9B-TR expression and concluded that this protein could not be expressed stably over long time periods (Figure 31).

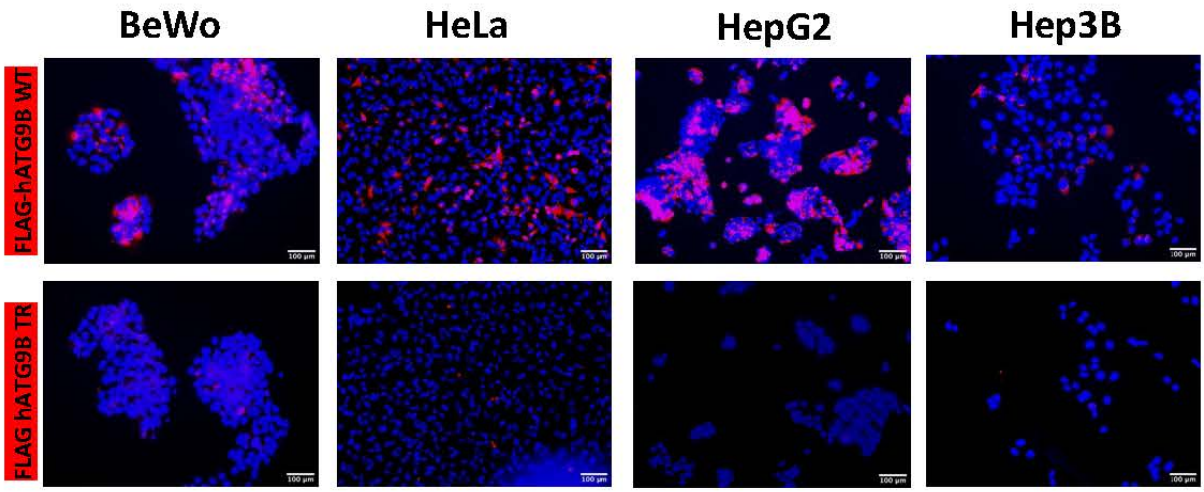

Figure 31. Lentiviral infection of various cell lines indicating the inefficiency of ATG9B TR protein expression.

Simultaneously, we generated monoclonal HeLa cells to investigate the function of ATG9B-WT. The infected HeLa cells expressing FLAG ATG9B-WT were seeded in 96-well plates, with one cell per well. We selected and expanded the monoclonal cells, to be analyzed with immunofluorescence and immunoblotting. HeLa B3 clone displayed the highest

expression. The cellular localization was consistent with previous experiments and the clone was suitable for microscopy studies (Figure 32).

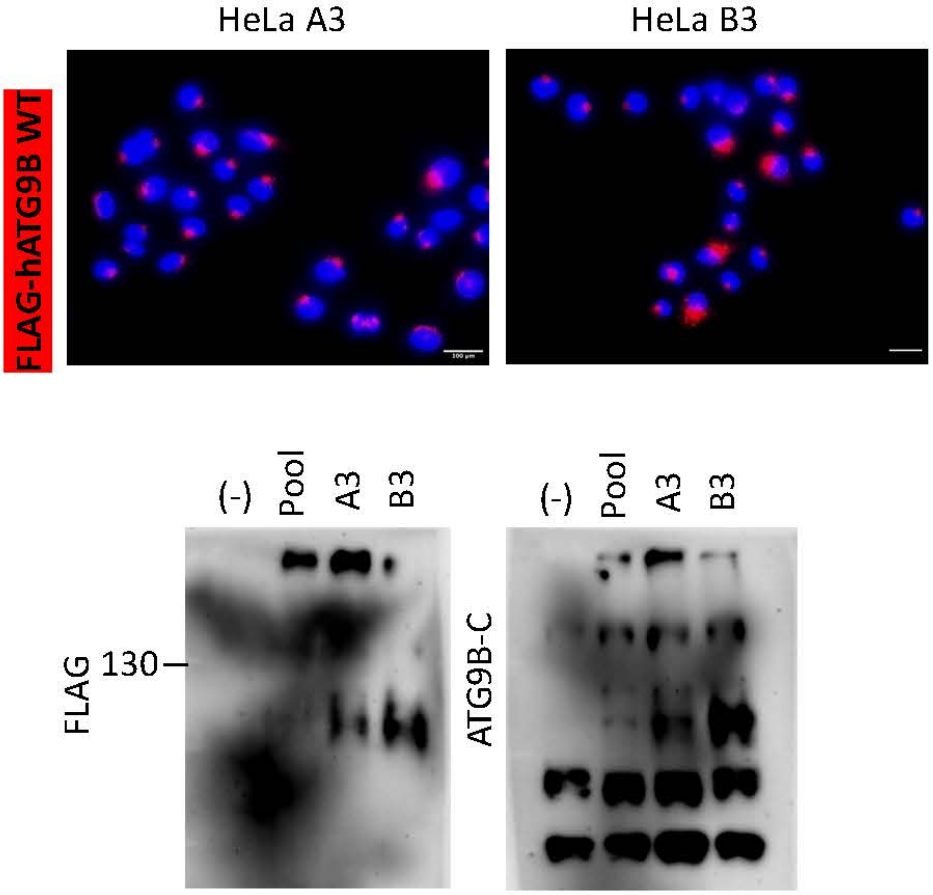

Figure 32. Production of monoclonal HeLa FLAG-hATG9B WT expressing cells A3 and B3 clones were inspected by FLAG IF and immunoblotting. The highest expression was seen in B3 cells.

4.4.2.4. Analysis of ATG9B Localization and Trafficking, and Involvement in Autophagy

We aimed to characterize ATG9B WT since there was limited information in the literature on ATG9B. To address whether ATG9B and ATG9A are functionally similar as suggested in the literature we performed immunofluorescence of ATG9B-WT and ATG9A in normal nutrient conditions to address their localization. We used the monoclonal HeLa B3 cell line and the polyclonal Hep3B cell line expressing FLAG-hATG9B-WT obtained by lentiviral

transduction. While these proteins co-localize, it's important to note that co-localization is not absolute, and they also are present in different vesicular compartments (Figure 33).

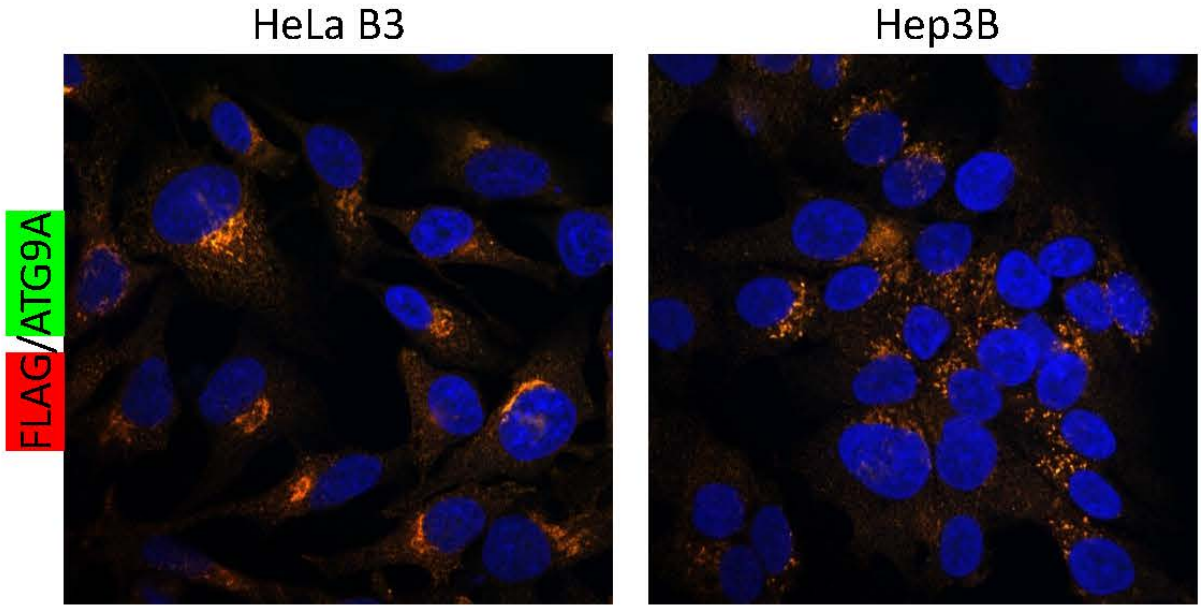

Figure 33. Co-localization of ATG9B WT and ATG9A in cells expressing ATG9B stably.

ATG9A predominantly localizes within the Trans-Golgi Network (TGN) under nutrient-rich conditions and translocates to the Pre-Autophagosomal Structure (PAS), appearing as cytoplasmic puncta in upon starvation. Thus, we aimed to investigate the subcellular distribution of ATG9B in HeLa B3 cells upon starvation for varying time intervals. To adress ATG9B trafficking we used Golgin 97 as a marker for the TGN. We conducted a time-course Co-Immunofluorescence (Co-IF) experiment using anti-ATG9B serum that we produced together with anti-Golgin-97 antibody.

ATG9B puncta localized within the TGN and the cytoplasm. Cytoplasmic puncta increased up to 4 hours of starvation but decreased at 6 and 8 hours, with ATG9B re-localizing to perinuclear sites. The reduced TGN colocalization at 6 and 8 hours may suggest possible localization at ER omegasomes, phagophore assembly sites. This experiment did not definitively identify the specific membrane-containing organelles associated with ATG9B in this context (Figure 34).

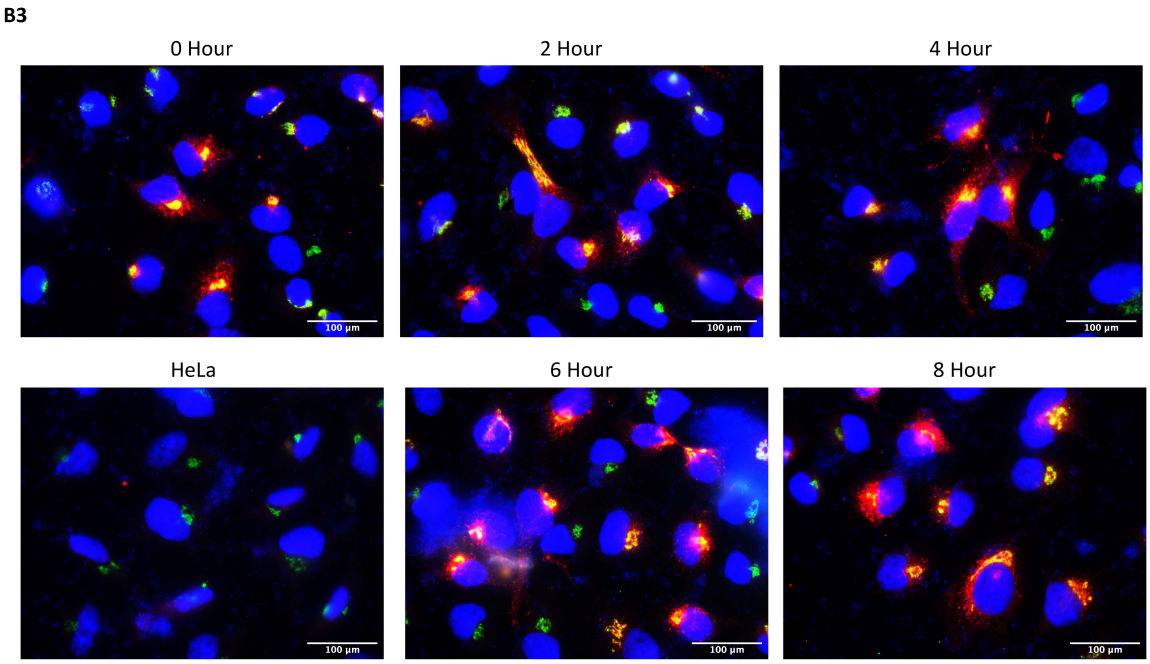

Figure 34. Co-localization of ATG9B WT with TGN. HeLa B3 clones were subjected to time-course starvation treatment. Red fluorescence shows anti-ATG9B-serum (Rabbit) that we generated and green fluorescence shows the Golgin97 (mouse) antibody. Colocalization is indicated as yellow.

ATG9B was first identified as an autophagy protein and can rescue autophagy upon ATG9A knockdown. While ATG9A is localized on phagophores, it does not localize at autophagosomes once they are maturated, closed (72). We hypothesized that ATG9B functions similarly to ATG9A, facilitating membrane translocation from donor membranes to the Pre-Autophagosomal Structure (PAS) and serving as a membrane scramblase.

LC3, a widely acknowledged isolation membrane autophagosome marker, undergoes degradation upon autophagosome-lysosome fusion. LC3 puncta number increases upon autophagy induction. Our objective was to investigate whether ATG9B colocalizes with LC3

at different stages of starvation treatment, and our observations revealed no colocalization between ATG9B and LC3 for different durations of the starvation treatment (Figure 35).

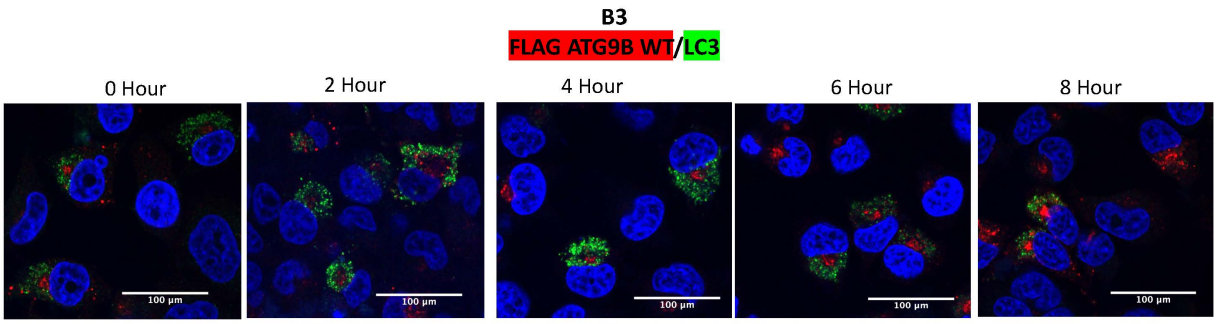

Figure 35. Co-localization of ATG9B WT and LC3. ATG9B does not localize on fully formed closed autophagosomes where LC3 localizes.

We used transient transfection to investigate the distinctions in the cellular localization and trafficking of ATG9B TR in comparison to WT. The purpose was to illuminate the localization and trafficking disturbances of hATG9B TR and provide. Since the expression of TR cannot be maintained for a period, we adopted the transient transfection method to study TR protein.

To comprehensively address this, we extended our experiments beyond HEK293T and HeLa cells in which the phenotype was initially observed (Figure 24). The primary objective was to validate our observations that WT localizes to perinuclear sites and cytosol as puncta, whereas TR forms larger puncta, strictly at perinuclear sites. By utilizing various cell lines suitable for transfection, we explored the applicability of our findings to different cell types such as breast cancer (Mcf-7) and liver cancer cell lines (Hep3B, HepG2). The localization patterns were in line with HEK293T and HeLa cells, WT localized as puncta in perinuclear sites and in cytosol while TR was aggregated and restricted in perinuclear sites (Figure 36).

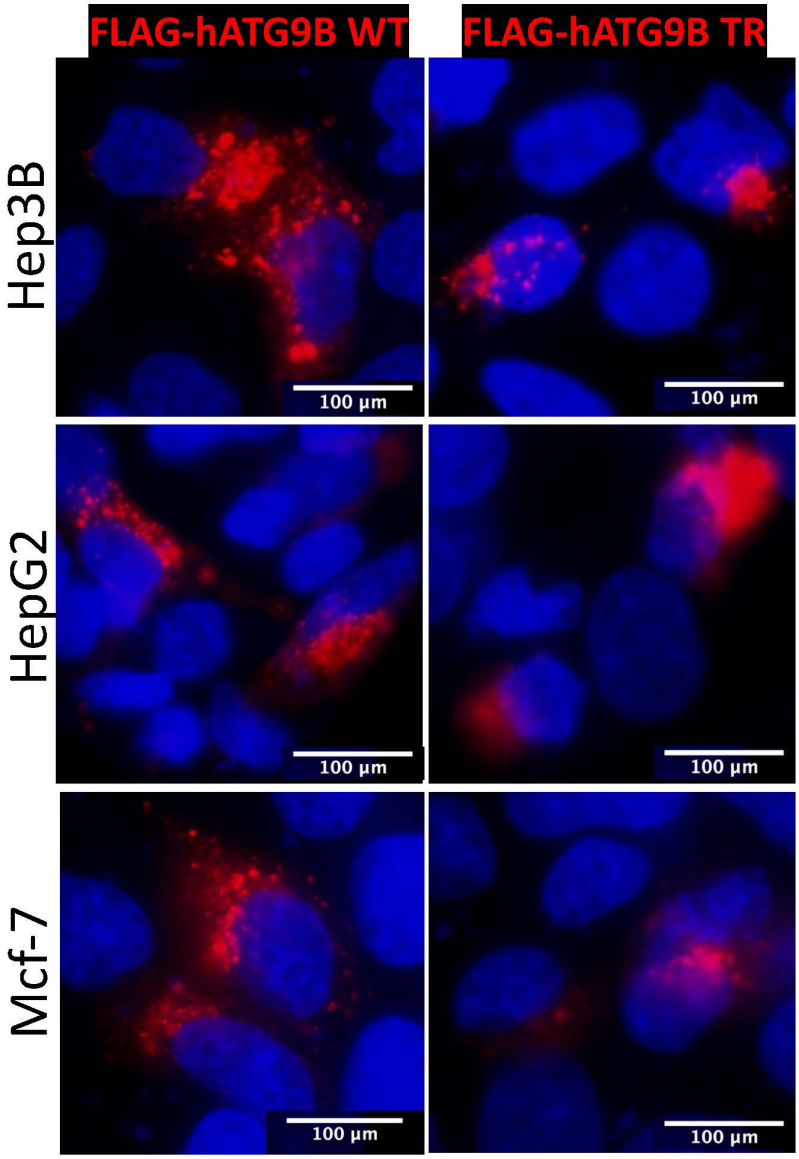

Figure 36. Localization of WT and TR ATG9B in various cell lines. WT is localized at perinuclei and in cytosol as puncta while TR is aggregated at perinuclear compartments.

Following these observations regarding the distribution of WT and TR we wanted to elucidate WT and TR colocalization, to assess whether the localization of TR differed from of WT. For this purpose, we utilized a HeLa B3 clone expressing FLAG hATG9B-WT and performed a Co-Immunofluorescence experiment after transfection with WT-myc and TR-myc constructs, with analysis performed at the 24-hour time post-transfection.

The signal patterns for WT and TR exhibited partial colocalization. In our previous experiments, both WT and TR were observed in perinuclear vicinity in line with this observation. While TR colocalized with the WT this colocalization was not absolute.

Furthermore, WT displayed also localized in the cytosol as discrete puncta structures, aligning with our previous observations. Additionally, vesicular structures WT and TR colocalized showed abnormality (Figure 37).

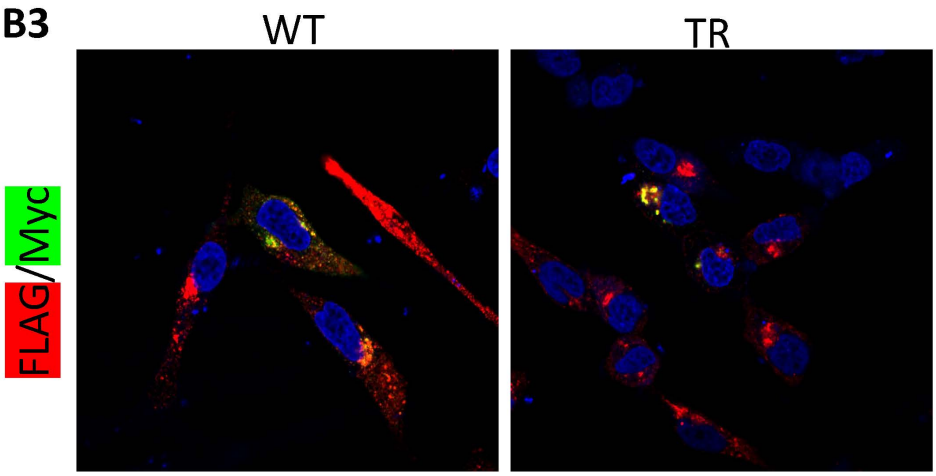

Figure 37. Co localization of FLAG WT with WT-myc and TR-myc. HeLa B3 cells stably expressing FLAG-hATG9B WT were transiently transfected with myc constructs for subsequent colocalization experiment.

Subsequently, we aimed to determine whether WT and TR localize to distinct cellular compartments, especially focusing on the possibility of TR being exclusively confined to a particular peri-nuclear organelle such as the Golgi. We relied on transient transfection, focusing particularly on the 8-hour starvation time point. In our previous experiments, we observed WT cytoplasmic puncta decreased and concentrated in the vicinity of the nucleus upon prolonged starvation in contrast to its initial cytoplasmic distribution. This concentration did not appear in the Trans-Golgi Network. Therefore, in this experiment, we performed immunofluorescence for WT and TR with Golgin-97. While WT trafficking exhibited similar behavior with previous experiments, the truncated expression strictly resided within the Golgi compartments, irrespective of the nutrient status. Moreover, the truncated form exhibited larger puncta. Additionally, in line with the observation in Figure 37, the TGN structure displayed abnormality suggesting TR expression may have disturbing effects in the vesicular systems in cells (Figure 38).

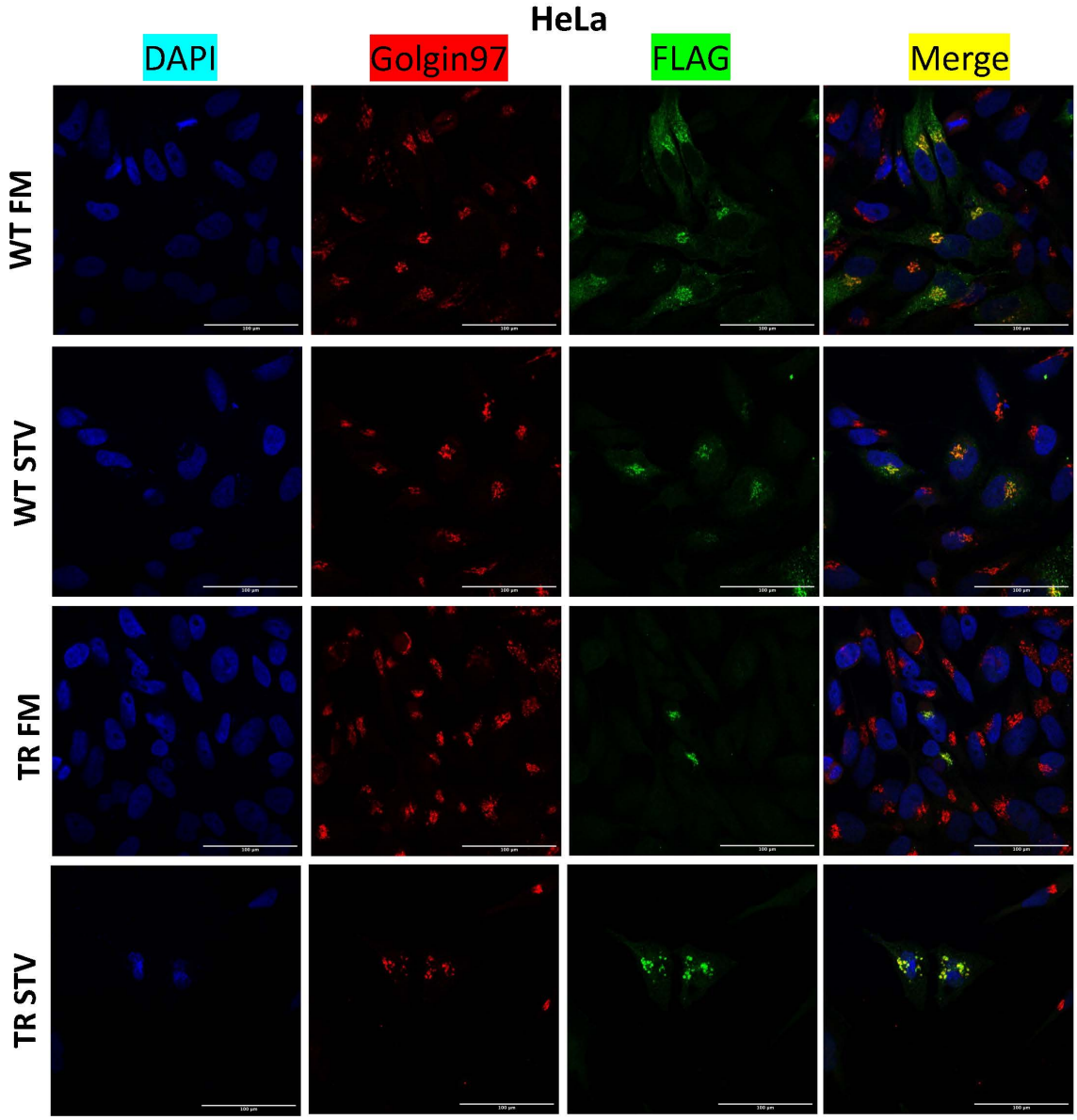

Figure 38. The localization of WT and TR ATG9B in TGN compartments. HeLa cells transiently transfected with FLAG-hATG9B WT and TR and CO-IF was performed in fed and starvation conditions to observe ATG9B trafficking divergences.

Following the characterizations for the cellular trafficking, we aimed to investigate the impact of ATG9A knockout on the autophagy and capacity of ATG9B WT and truncated rescuing the phenotype. Using CRISPR/Cas9 mediated ATG9A knockout virus, we generated ATG9A knockdown HEK293T and HeLa cells. Our objective was to transfect ATG9B-WT

and ATG9B-TR plasmids and assess whether the ectopic expression of ATG9B could replicate the rescue effect reported in the literature.

The ATG9A virus led to suppression of the expression, but a complete knockout phenotype was not observed (Figure 39-A). Initially, we used parental HeLa cells and ATG9A knockdown cells. ATG9A transfection is expected to rescue the autophagy completely so it was used as a positive control to compare with, WT and TR. However, no discernible disruption of autophagy was observed to begin with, rendering the results inconclusive (Figure 39-B).

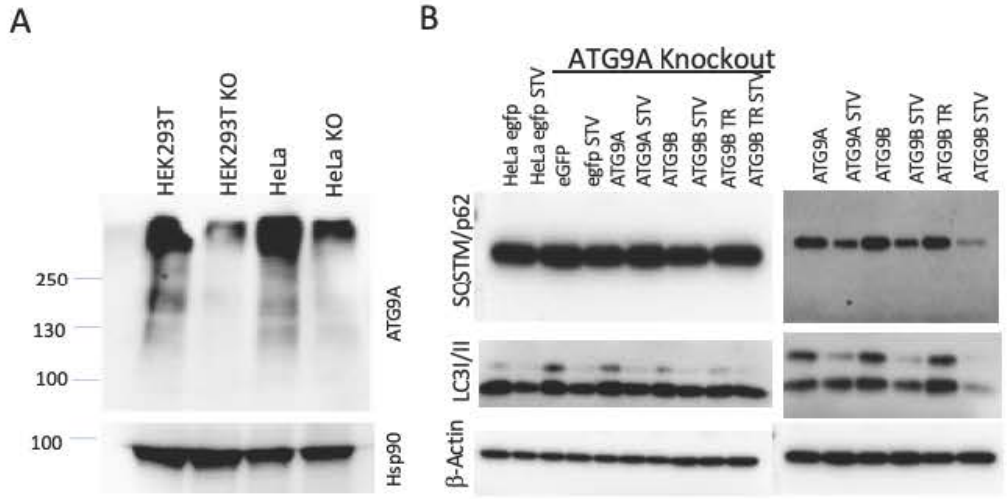

Figure 39. Autophagy assessment upon ATG9A knockdown conditions. A) ATG9A suppression was successful. B) HeLa parental and ATG9A knockdown cells upon 8-hour starvation treatment transfected with a WT or TR ATG9B.

4.4.3. Production of ATG9B Polyclonal Antibody

We performed our studies for the characterization of ATG9B WT and ATG9B TR in cells using ectopic expression for investigations related to expression and trafficking. However, we were still in need of an antibody for studying endogenous expression in mouse tissues and parental human cell lines. Notably, the antibody with a C-terminal epitope worked in ectopic expression studies while the antibody with a N-terminal did not, and neither antibody could detect endogenous ATG9B expression in BeWo, the highest ATG9B expressing cell line according to Protein Atlas.

Moreover, we were interested in generating genetically modified mouse models to identify ATG9B-expressing tissues and to model the neurodevelopmental disorder. It is important to remind that the ATG9B antibody with C-terminal epitope detected only ectopic

expression of ATG9B while the N-terminal did not, neither antibody could detect endogenous ATG9B expression in BeWo, nor the mouse placenta tissues the highest ATG9B expressing cell line and tissue respectively. Therefore, we needed an N-terminal antibody but commercial antibodies were mostly designed for the C-terminal cytosolic site and several antibodies with N-terminal epitopes did not provide evidence in the literature. We decided to generate an ATG9B antibody by rabbit immunizations.

The important consideration was to select conserved, antigenic, and cytosolic polypeptide sequences. ATG9B protein is a complex protein has six membrane domains which is considered to hinder productivity, halter purification of the antigen and have low antigenicity. Naturally we focused on cytoplasmic sites of the protein (Figure 40).

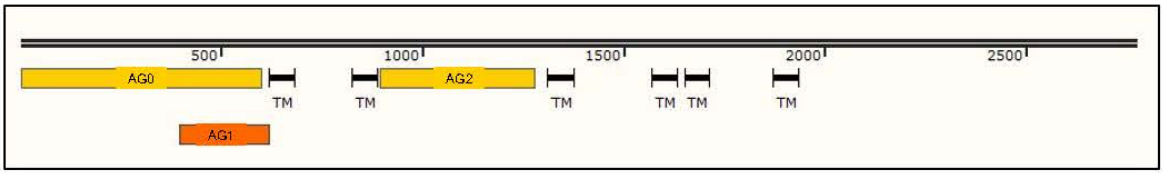

Figure 40. The schematic representation of the antigen sites on the *ATG9B* DNA map. Antigens are chosen in cytosolic sites for the protein for high antigenicity and solubility. Transmembrane regions are indicated on the map for clarification.

Subsequently, pairwise alignment for human and mouse ATG9B was performed by the Water algorithm. The proteins are conserved with the identity between two sequences is 87.3% while the similarity is 89.7%. Three antigen sites near the N-terminal site with high conservation were chosen for the study. The sequence with a yellow background is AG0, with red color is AG1 and the green background indicates AG2 (Figure 41).

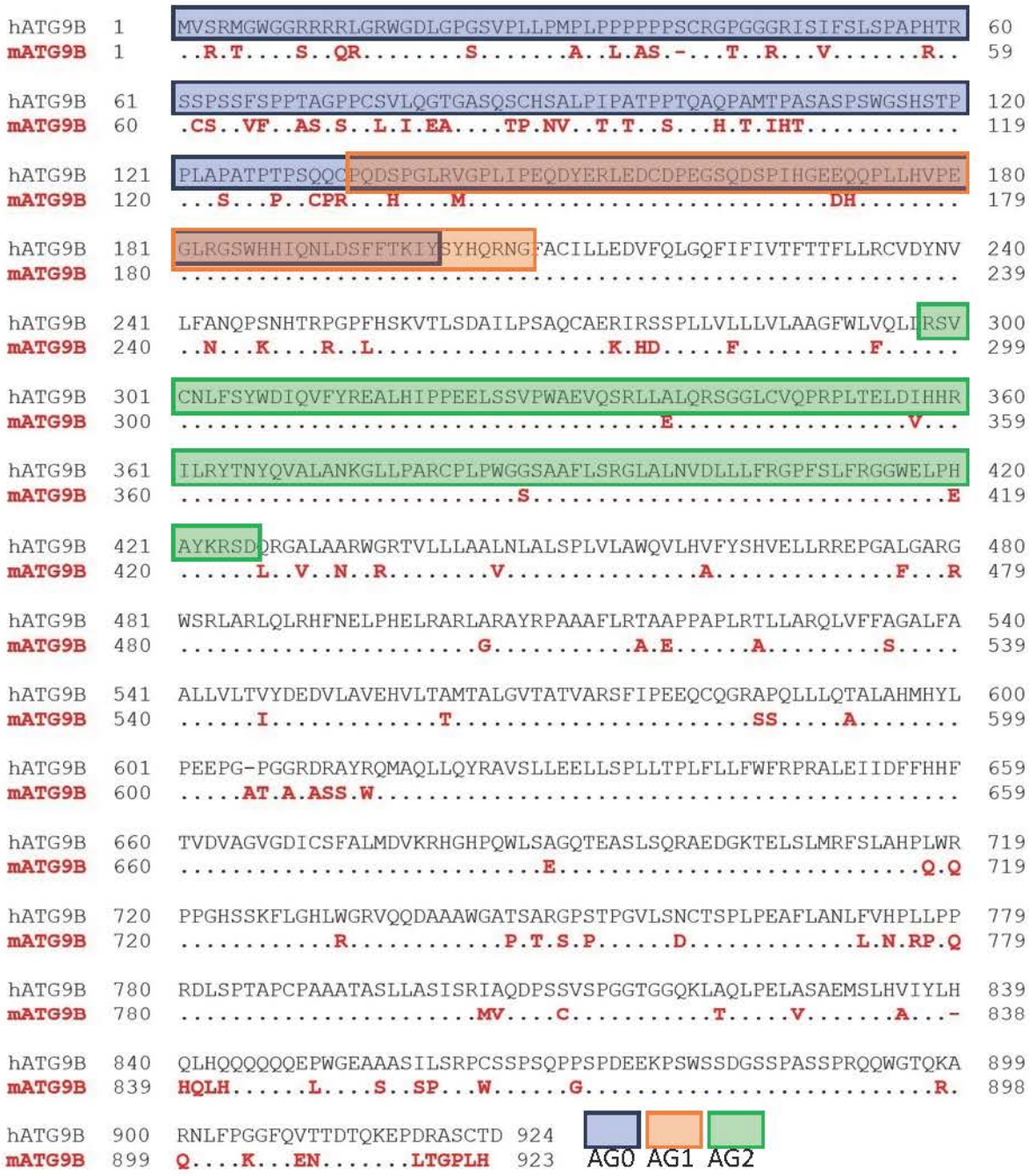

Figure 41. The alignment of mouse and human ATG9B protein sequences. Alignment shows that the proteins are conserved between the species. The antigen sites (AG0, AG1, AG2) are indicated in the sequence.

We evaluated the antigenicity of the selected peptides by an online prediction tool (http://imed.med.ucm.es/Tools/antigenic.pl). Peptides with an overall score >1 are considered to be

potentially antigenic. The prediction tool also provide the antigenic amino acids by graphical representation (Figure 42).

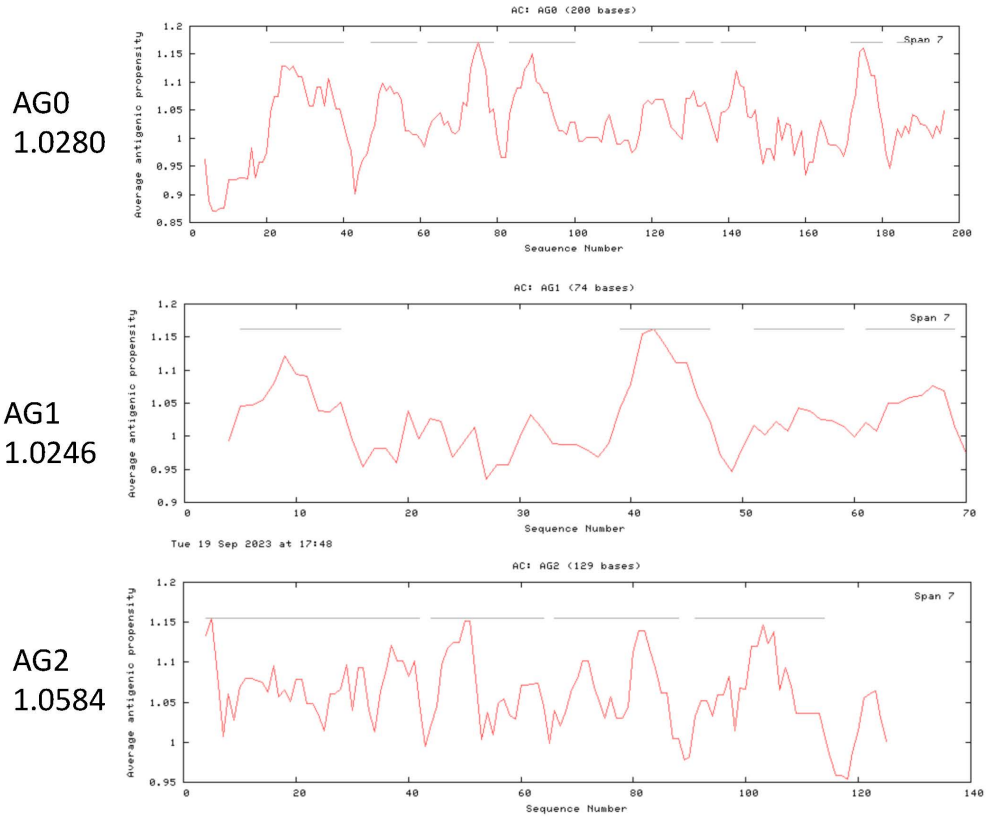

Figure 42. The antigenicity predictions of selected peptides. All peptides have high antigenicity sites with a score >1 predicting that they can induce high immune response.

Following the determination of the antigenic sites, we cloned the selected sequences into the pGEX-6P-1 vector 3' to the GST site (Figure 43). By this, we could use *E. Coli* BL21 strain for antigen expression and pull down the antigen by GST beads as detailed in methods section. Antigen 0 was not expressed by *E. coli* therefore we focused our efforts to Antigen 1 and Antigen 2 (Figure 44).

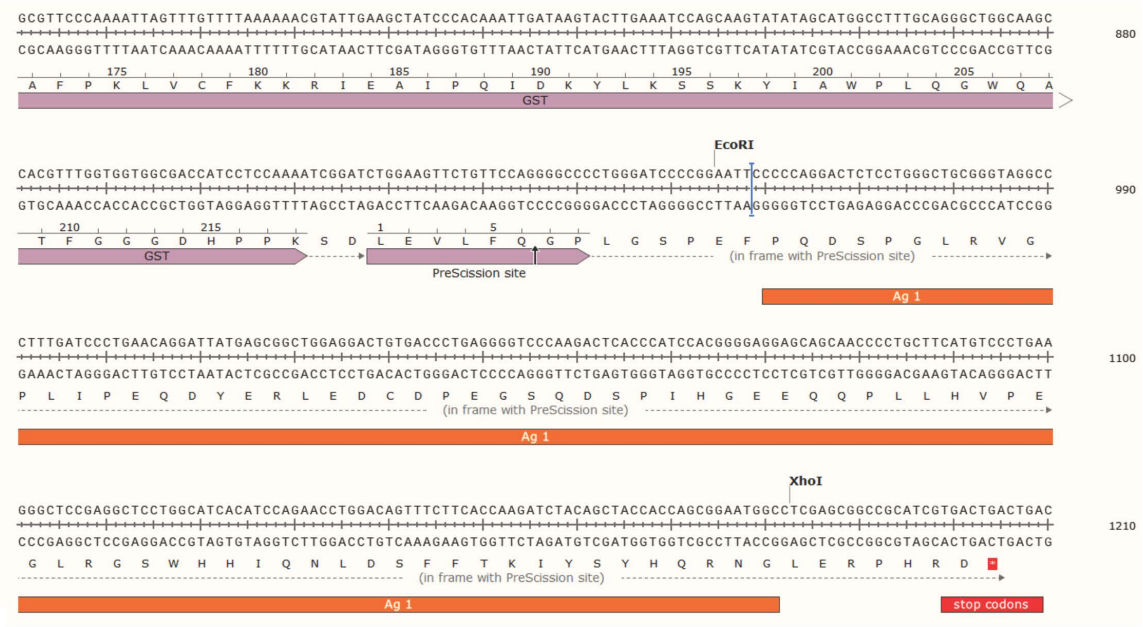

Figure 43. The plasmid map and sequence for Antigen 1 cloned to pGEX-6P-1 vector. Same cloning was performed for Antigen 0, 1 and 2. Sequences were in frame with GST producing a fusion protein that can be pulled down and purified by GST beads.

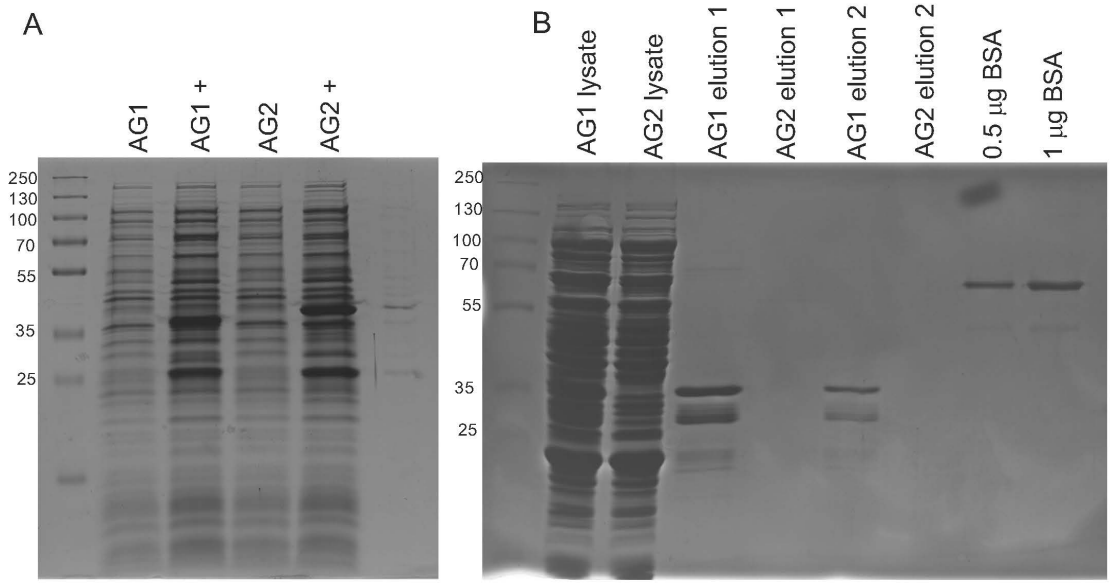

Figure 44. The production and isolation of Antigen 1. A) Antigen 1 and Antigen 2 were both produced in BL21 strain of E. Coli. Culture samples were taken before and after IPTG induction (+) indicating IPTG. B) Purification of Antigen 1 with GST pull down assay and the production of AG1.

After efficient production and purification were optimized, we upscaled the production to obtain high yield antigen purification for rabbit immunization. We were able to obtain antigen 1 after in a sufficient amount and concentration in PBS for immunization after production isolation, and dialysis (Figure 45).

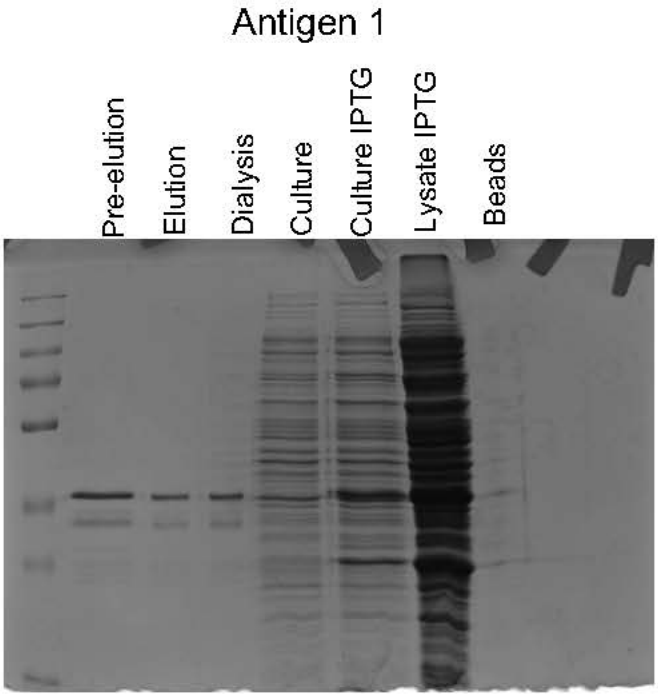

Figure 45. The large scale production and purification of Antigen 1. Antigen 1 production and isolation were optimized in sufficient quality for immunizations. We were able to elute the majority of the GST-Antigen 1 fusion protein and efficiently dialyzed without losing the product.

GST-Antigen 1 fusion protein was used directly for the immunizations. A male 3 months old 3025-gram New Zealand White rabbit was immunized for the study. Before first immunization 5 ml pre-immune bleed was obtained from the rabbit. First immunization was performed with 85 μg antigen administered by mixing with Freund's complete adjuvant in 1:1 ratio in a total 200 μl emulsion. On day 14, the first booster immunization was performed using incomplete Freund's adjuvant. The first test bleed was obtained on the 10th day following this booster. Subsequently, two more booster immunizations were administered at 14-day intervals, with test bleeds collected every 10 days thereafter.

Following the third booster, the rabbit was euthanized, and the final blood was collected from the cardiac vein.

Having possessed FLAG-hATG9B-WT and TR constructs, we were able to assess the specificity and effectivity of the serum. Additionally, HeLa B3 cell line expressing FLAG-hATG9B-WT stably was obtained and served as a good model for assessment of the serum.

We performed Co-Immunofluorescence with the FLAG-M2 antibody (mouse) to determine the specificity and the efficiency of the serum. In 1st bleed (10-days after booster) the antibody worked in 1:500 dilution and co-localized with FLAG on HeLa cells transfected with FLAG WT and TR (Figure 46-A). Subsequently, after the final bleed the serum that was efficient at a 1:1000 dilution (Figure 46-B).

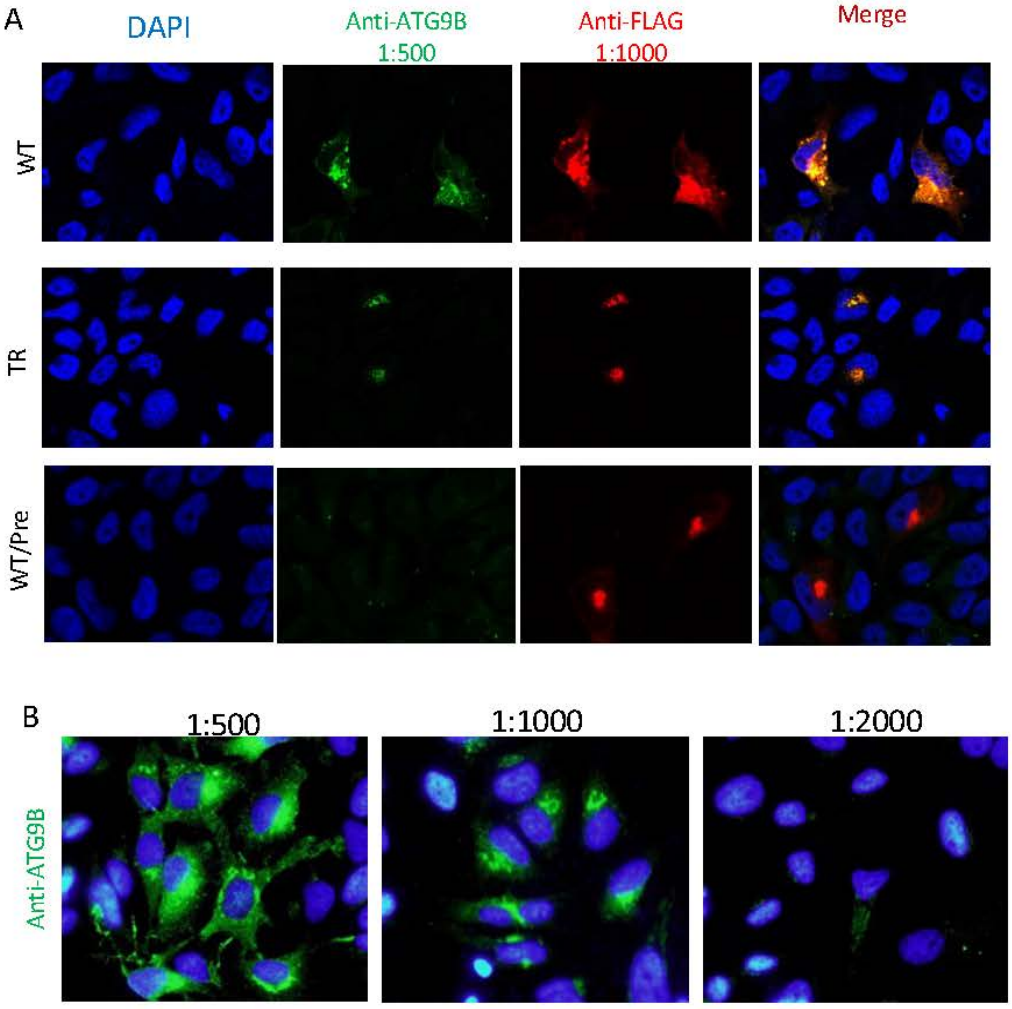

Figure 46. The antibody tests in transfected and stable Hela cells. A) Our home-made antibody worked in transiently transfected HeLa cells for both WT and TR constructs. The antibody was efficient and specifically colocalized with FLAG. Pre: pre-immune serum. B) The boosters resulted with a strong titer, 1:1000 dilution of the serum was sufficient to visualize the expression adequately ("Pre" indicates preimmune serum).

The following step involved the assessment of the antibody's efficiency in immunoblotting. We used HeLa B3 cell pellets and tested the antibody with different buffers and incubation conditions. Simultaneously, we investigated a recent literature, stating that incubating lysates prepared in TNTE buffer at 65°C for 5 minutes could prevent the aggregation of ATG9A, and we investigated whether this to ATG9B as well (79).

Interestingly, we showed that polyclonal ATG9B developed in our lab works more efficiently in the same dilution than anti-FLAG M2 antibody from Sigma (F1804). Although the monoclonal anti-FLAG M2 specificity was higher than anti-ATG9B serum the efficiency and specificity of the serum was sufficient. In parallel, we observed that ATG9B protein is best

preserved in TNTE buffer in 25°C and 37°C after mixing it with SDS loading buffer without heating (Figure 47).

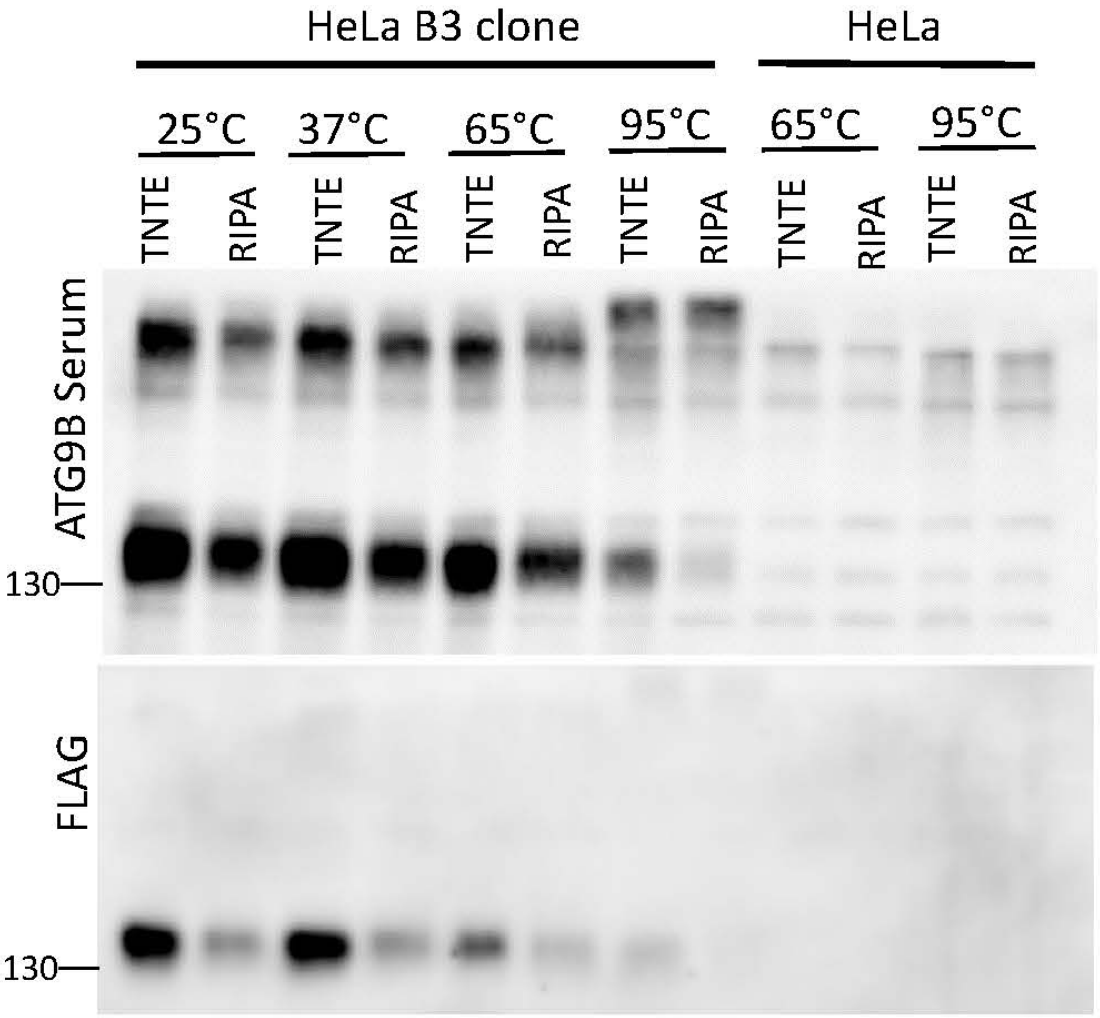

Figure 47. The determination of anti-ATG9B serum in immunoblotting. The dilution 1:1000 dilution worked more efficiently than FLAG M2 antibody with the same dilution. ATG9B protein detection in HeLa B3 stable cell line is best in TNTE buffer in 25°C and 37°C.

4.4.4. Development and Genetic Characterization of Transgenic Mouse Models

In this research, we decided to generate a mouse model of Atg9b knock-in genetic disease model. This genetic manipulation introduced STOP to exon 9, resulting in the C-terminal deletion of the Atg9b protein. Additionally, we generated FLAG-Atg9b mice that retained the WT wild-WT *Atg9b* gene. These mouse models were engineered using the homology-directed

repair (HDR) template, using single-stranded oligodeoxynucleotide (ssODN). Furthermore, we generated Atg9b knock-out mice by exon 2 deletions (44-bp and 230-bp) causing frameshift mutations.

For the generation of genetically modified mouse models, we adopted CRISPR/EZ technology, which was applied by our laboratory at IBG vivarium facility. CRISPR/EZ offers the transfer of small nuclear ribonucleoprotein (snRNP) molecules into a high number of embryos through electroporation efficiently, expediting the genetic engineering process and reducing the technical difficulty of microinjections.

To evaluate the efficiency of the genomic alterations, a subset of embryos was cultured to the blastocyst or morula stage within a controlled CO2 incubator *ex-vivo* and subsequently, was genotyped individually. After the success of genomic alterations in embryos generation of the transgenic strains was initiated by embryo transfer to pseudo-pregnant mice to obtain founder generation.

From the founder mice, tail biopsies were obtained, and hotshot lysates were subsequently prepared. As genotyping methods PCR and enzymatic digestions were performed appropriate to the strain that is generated specifically. When founders reached to adulthood, aged between four and six weeks, harboring the genetically modified allele were mated with WT mice to obtain the F1 heterozygote generation. Subsequently, heterozygote littermates were mated to obtain the homozygous F2 generation.

4.4.4.1. Atg9b Knock-in Model of Human Rare Genetic Disease

Considering ATG9B expression is marginally higher in the placenta than other tissues we hypothesized that the neurobehavioral symptoms that are observed in patients can have placental development origins. Placenta-brain axis was described as a variety of neurodevelopmental and neurobehavioral abnormalities are originated from abnormalities in brain development *in utero* due to placental disturbances (103).

Taken together, the generation of a mouse model with the precise human mutation was invaluable to further characterize the disease by histology, molecular biology, and behavioral studies. To this purpose, we generated a Knock-in model utilizing a CRISPR-Cas9 method and inserted a stop codon at the position of the frameshift by a homology-directed repair template.

It is important the remind that the human and mouse ATG9B genes share an 87% sequence identity. Additionally, the deleted segment of the gene is highly conserved (Figure 48).

```
ATG9B_HUMAN      650 LEIIDFFHHFTVDVAGVGDICSFALMDVKRHGHPQWLSAGQTEASLSQRA
                     |||||||||||||||||||||||||||||||||||||.||||||||||||
ATG9B_MOUSE      650 LEIIDFFHHFTVDVAGVGDICSFALMDVKRHGHPQWLSEGQTEASLSQRA

ATG9B_HUMAN      700 EDGKTELSLMRFSLAHPLWRPPGHSSKFLGHLWGRVQQDAAAWGATSARG
                     |||||||||||||||||.|:||||||||||||.||||||||||||.|.|.
ATG9B_MOUSE      700 EDGKTELSLMRFSLAHPQWQPPGHSSKFLGHLRGRVQQDAAAWGAPSTRS

ATG9B_HUMAN      750 PSTPGVLSNCTSPLPEAFLANLFVHPLLPPRDLSPTAPCPAAATASLLAS
                     |.||||||:||||||||||||||.|:|..|.||||||||||||||||||||
ATG9B_MOUSE      750 PPTPGVLSDCTSPLPEAFLANLLVNPRPPQRDLSPTAPCPAAATASLLAS

ATG9B_HUMAN      800 ISRIAQDPSSVSPGGTGGQKLAQLPELASAEMSLHVIYLHQLHQQQQQQE
                     |||:.||||.||||||||||||.|||||.|||||||.|||||||  ||||||
ATG9B_MOUSE      800 ISRMVQDPSCVSPGGTGGQKLTQLPELVSAEMSLHAIYLHQLH-QQQQQE

ATG9B_HUMAN      850 PWGEAAASILSRPCSSPSQPPSPDEEKPSWSSDGSSPASSPRQQWGTQKA
                     .||||:||..|||.||||||.|||||||||||||||||||||||||||:|
ATG9B_MOUSE      849 LWGEASASSPSRPWSSPSQPGSPDEEKPSWSSDGSSPASSPRQQWGTQRA
```

Figure 48. Conservation of C-terminal ATG9B sequence between human and mouse. Yellow highlight indicating the amino acids that are affected by the frameshift mutation and subsequent deletion.

Design of sgRNAs: In the human ATG9B gene, an 11-nucleotide-long deletion results in the addition of six different amino acids followed by the incorporation of a premature STOP code. However, making a similar deletion in the mouse gene causes the addition of nearly thirty different amino acids before the introduction of the STOP codon. Therefore, the deletion of the C-terminal sequences was planned to be interrupted by adding STOP codon to the beginning of the frameshift.

Design of ssODN Donor DNA: The ssODN donor DNA serves as a template for repairing the cleaved locus through homology-directed repair (HDR) directed by the Cas9/sgRNA complex, instead non-homologous end joining (NHEJ). The 110-nucleotide ssODN was designed, to introduce critical nucleotide modifications for the alteration. These alterations transfer the STOP codon, remove the StuI site from WT sequence, and add an EcoRI restriction site. The ssODN was also used for the elimination of PAM sequence for further recognition and cleavage by sgRNA/Cas9. (Figure 49). Symmetrical homology arms, consisting of 50-nucleotide sequences at both the 5' and 3' ends are identical to the

corresponding nucleotides in the mouse locus, ensuring the annealing and successful recombination.

Screening/Genotyping Strategy: A straightforward and reliable screening strategy has been developed to confirm that the mutation has been transferred correctly. According to our strategy, the region encompassing the site of the genetic alteration by PCR. Changing the nucleotides by ssODN-driven homologous recombination destroys the StuI restriction sequence and transfers EcoRI. HotShot lysates possessing genomic DNA from the embryo and mouse tail biopsies were amplified and subsequently digested with StuI and EcoRI Since the StuI site might also be disrupted through NHEJ after Cas9 nuclease cleavage, restriction by EcoRI efficiently confirmed the HDR-mediated recombination (Figure 49).

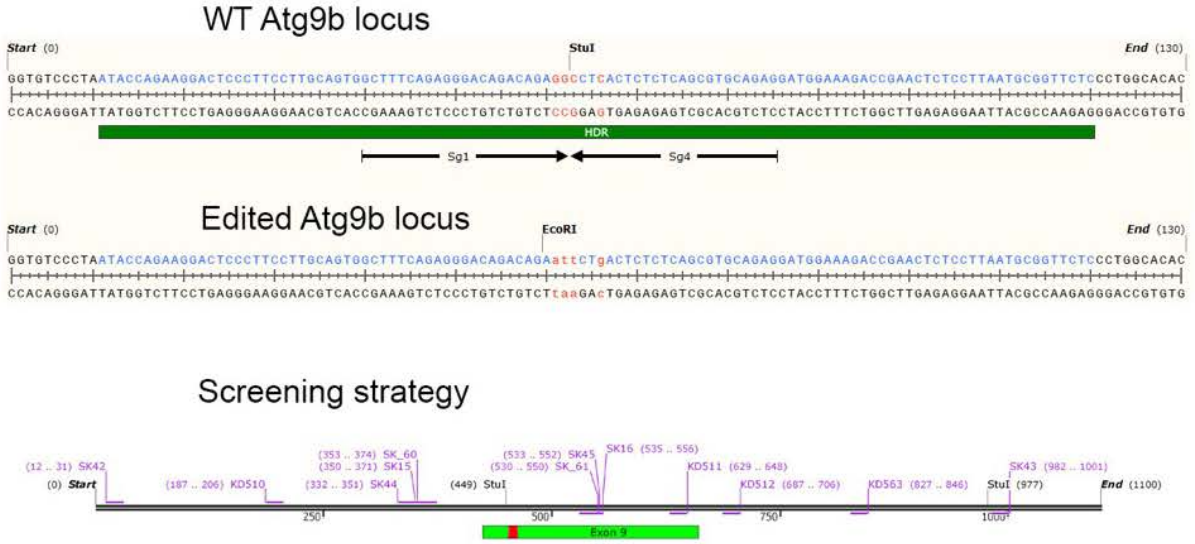

Figure 49. The strategy for editing and screening of Atg9b knock-in disease model. sgRNA's are designed for targeting the WT exon 9, HDR template changing WT StuI site to EcoRI site in knock-in, and screening primers.

The development of a transgenic model for studying human disease was important for elucidating histological and behavioral alterations of the related to placental development and the clinical manifestations observed in patients.

Ex-vivo Characterization

Following electroporation, the embryos can be cultured in growth media up to the blastocyst stage to evaluate the efficiency of the genomic alteration. We performed PCR and restriction digestion with StuI, digestion confirmed the presence of the WT allele, while EcoRI

digestion identified embryos of the altered transgenic allele. Remarkably, over 30% of the screened embryos harbored the knock-in mutation (Figure 50), and we proceeded with founder line generation by embryo transfer into pseudo-pregnant CD1 female specified in the methods section (50).

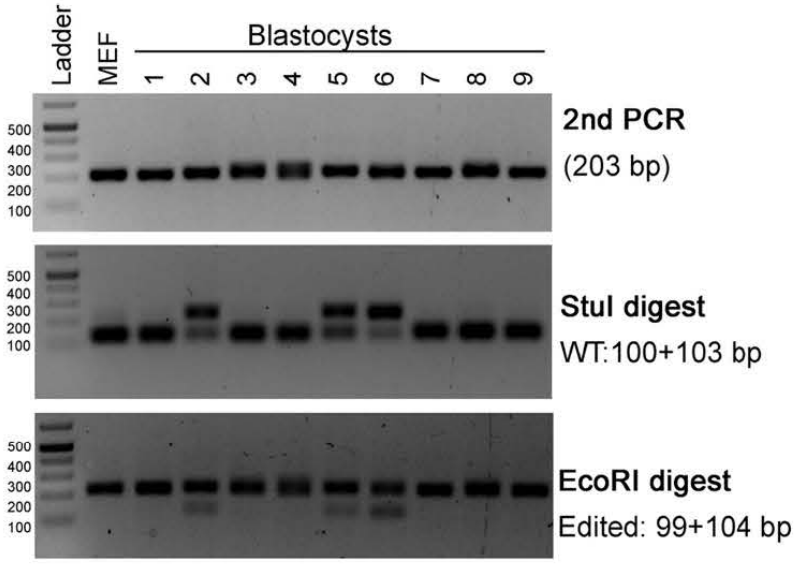

Figure 50. The efficiency of the HDR-mediated knock-in strategy in embryos. We were able to generate more than 30% efficiency in blastocysts for the precise HDR-mediated knock-in generation.

Generation of the Colony: After generation of founder mice and breeding with WT mice to obtain heterozygous knock-in mice we proceeded to Sanger sequencing confirmation of the precise editing. The nucleotide alteration is presented in Figure 51-A. Our sequencing data confirms the successful editing of the locus, as evidenced by double peaks of the WT and edited alleles from the heterozygous mouse for the knock-in mutation (Figure 51-B). Furthermore, these nucleotide alterations resulted in the successful addition of the STOP codon causing termination by deleting the C-terminal site of Atg9b modeling the patient mutation (Figure 51-C).

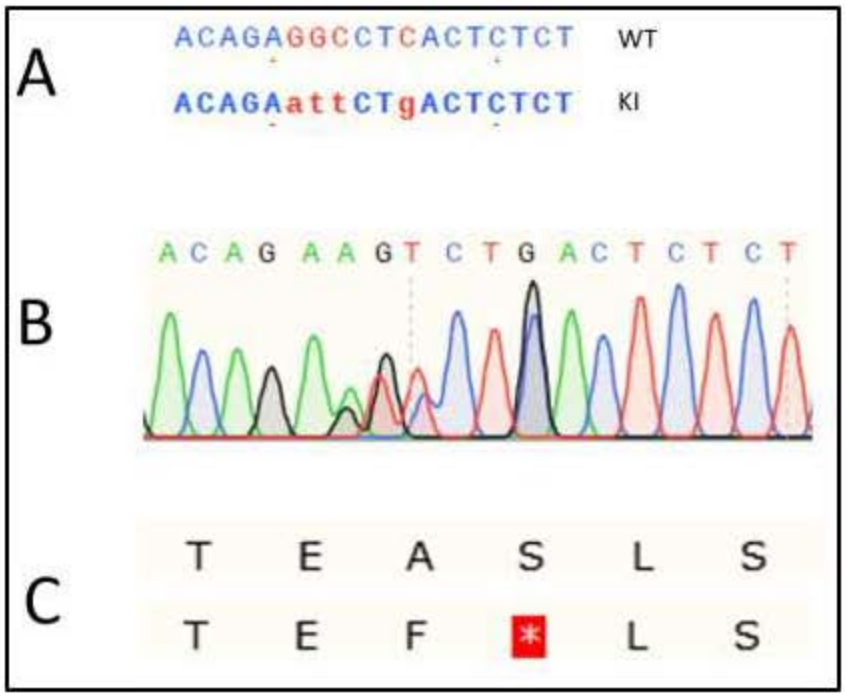

Figure 51. The generation of HDR mediated CRISPR/Cas9 HDR mediated knock-in mice model. A) The nucleotide alteration and comparison of WT and knock-in. B) The sequence confirmation of alteration. B) The addition of stop codon addition.

The founder mice were born of CD1 females 3-4 weeks after the embryo implantation. By the tailored method of StuI and EcoRI digestion, we performed genotyping from the HotShot lysates prepared from the tail samples of the founders. Our analyses revealed the presence of knock-in mutations in founder mice with the numbers 3, 5, and 6 (Figure 52-A).

Furthermore, in mouse 8 a deletion of around 40 nucleotides (DEL-1), and in 15 and 17 a deletion of around 200 nucleotides were observed (DEL-2) (Figure 52-A, B).

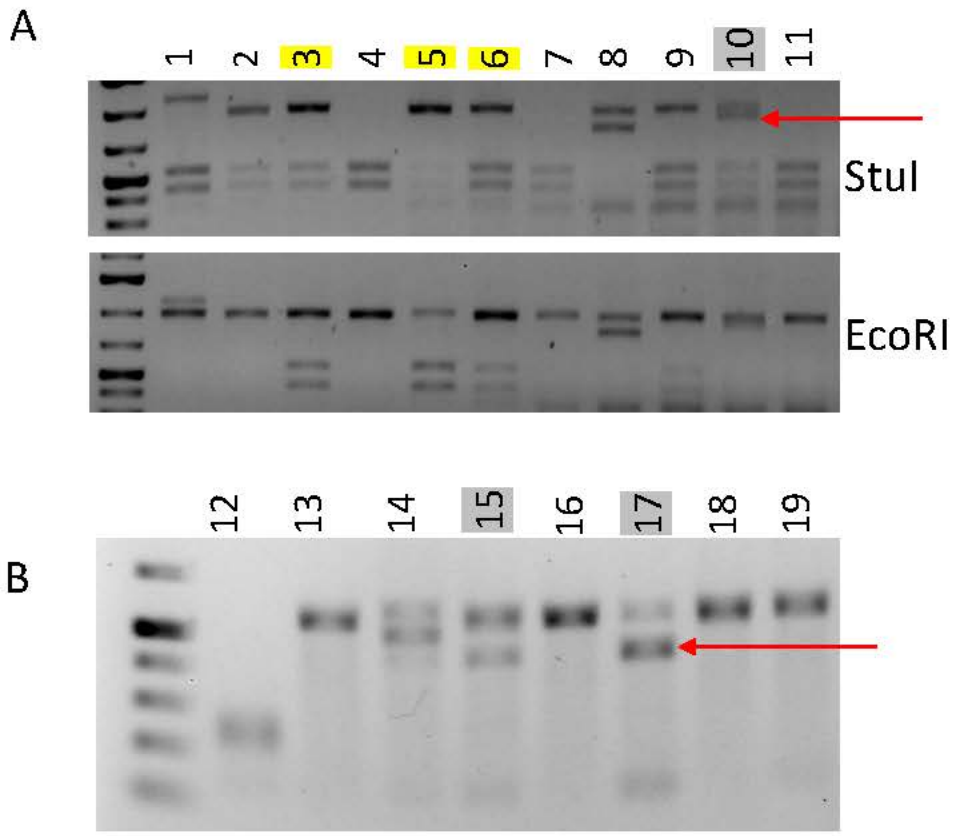

Figure 52. The genotyping and confirmation of founder mice of the Atg9b knock-in rare genetic disease model. A) Three founder mice harboring the knock-in mutation and one mouse with 40-nt deletion were detected. B) Two founder mice with 200-nt deletion were detected. The yellow color indicates the mice with the knock-in allele, and the gray indicates the mice with a deletion. Red arrows show the position of alleles with the deletion.

Subsequently, we proceeded with the heterozygous knock-in generation by breeding Founder 3 and 6 with WT mice. Additionally, we bred Founder 10 and 17 with each other and subsequently 10 with WT generating WT/DEL-1 and WT/DEL-2 and DEL-1/DEL-2 genotyped mice.

Generation and Confirmation of Heterozygous F1 Litters: The offsprings were designated as 30 to 41 born of the Founder 6 breeding and 42 to 54 from the Founder 3 breeding. Initially, genotyping was performed to identify heterozygous mice within litters. Subsequently, we validated the heterozygous EcoRI addition through Sanger sequencing (Figure 53).

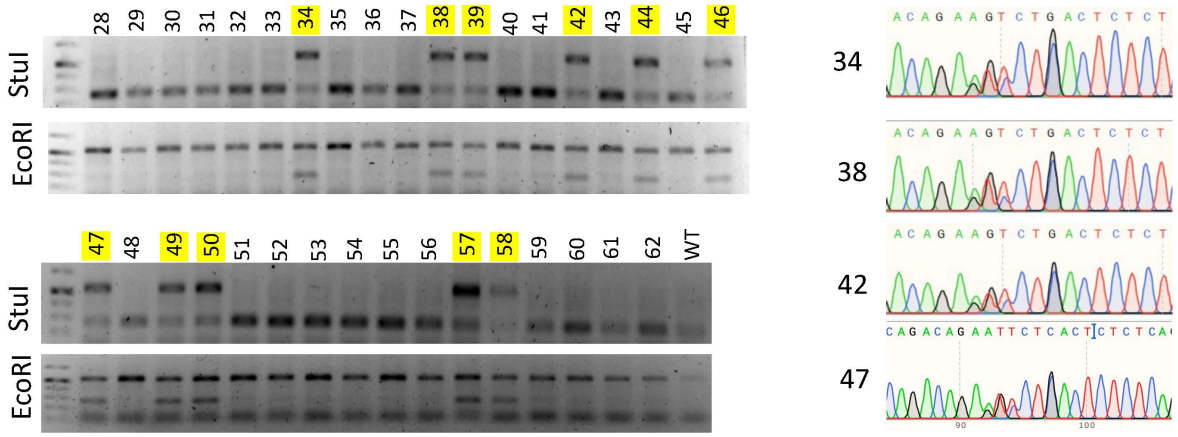

Figure 53. The genotyping and confirmation of heterozygous knock-in mice. F1 generation was generated by WT crossing of Founder 3 and 6 respectively. One male and female litter from each breeding were sequenced to confirm heterozygous EcoRI addition.

4.4.4.2. Atg9b Exon 9 Knock-out Model (DEL-1--- DEL-2)

The mice harboring exon 9 deletion alleles that were obtained during the development of Atg9b knock-in model bred as mentioned in the previous section (Founder 8 and 17). The mice bearing DEL-1/DEL-1 and DEL-1/DEL-2 deletions exhibited a healthy phenotype, reached adulthood, and were fertile. To identify the precise consequences of these deletions, we performed sequencing on the homozygous DEL-1 and DEL-2 mice (Figure 54). DEL-1 exhibited the destruction of exon 9 intron-exon boundary while DEL-2 completely deletes exon 9.

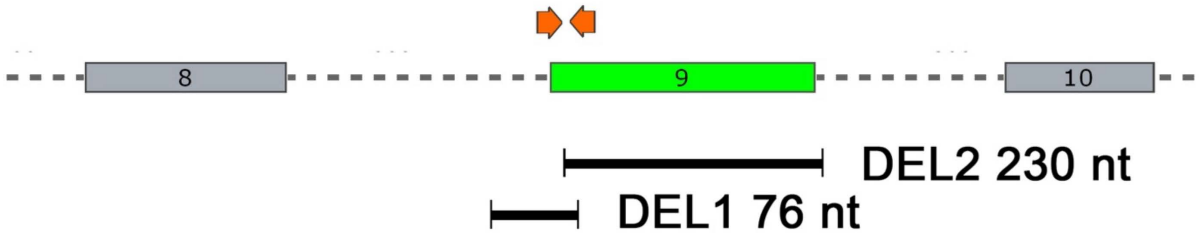

Figure 54 The sequence confirmations of the nucleotide deletions for DEL-1 and DEL-2 mice.

We explored the possibility that exon 9 deletions could potentially exhibit a similar phenotype with knock-in mutation or might have more detrimental effect on the placenta. To ensure the maintenance of exon 9 deletion alleles, we initiated breeding by crossing four female

DEL1/DEL2 mice with two male WT/DEL1 mice. Interestingly, we observed that two out of the four DEL1/DEL2 female mice died shortly after giving birth, with the newborns subsequently perishing. Following this, we continued the breeding with the two remaining pairs of mice. In this case, mothers remained alive and healthy after giving birth, but newborns died in the neonatal period when more than 6 offsprings were born and when the majority of them harbored deletion DEL-1/DEL-1 and DEL-1/DEL-2. This observation led us to consider that a high number of conceptuses predominantly of these genotypes might exert a detrimental, potentially toxic effect, contributing to neonatal deaths shortly after birth, and possibly impacting the adult mother. Subsequently, we performed breeding with WT, WT/DEL1, and DEL1/DEL1 female mice, which were mated with homozygous DEL1/DEL1 male mice. Mice were able to successfully give birth, and the offspring reached adulthood for all genotypes without any adverse outcome. This led us to speculate that the presence of both DEL1 and DEL2 alleles, particularly in abundance during pregnancy, could lead to a more unstable Atg9b protein, resulting in an additive toxicity within the uterus that subsequently led to maternal and newborn mortality. To explore this possibility further and obtain more definitive results, we wanted to investigate the possibility using full Atg9b knockout model that was currently under development.

4.4.4.3. FLAG-Atg9b WT Model

During our immunoblotting studies with commercial antibodies, we could not detect endogenous expression of Atg9b in mouse tissues, especially in the placenta where the highest expression was shown in RNA level. To address this issue, we developed an ATG9B antibody, in parallel we generated FLAG-Atg9b mice. Similar to our cell studies we wanted to use commercial FLAG antibodies in mouse tissues to determine the Atg9b profile in tissues by immunohistochemistry and immunoblotting.

Design of sgRNAs: We designed sgRNA's targeting exon 1 of the *Atg9b* gene with the same tools mentioned in knock-in strategy. We selected one sgRNA targeting and cleaving the prior the start codon of the Atg9b (Figure 55).

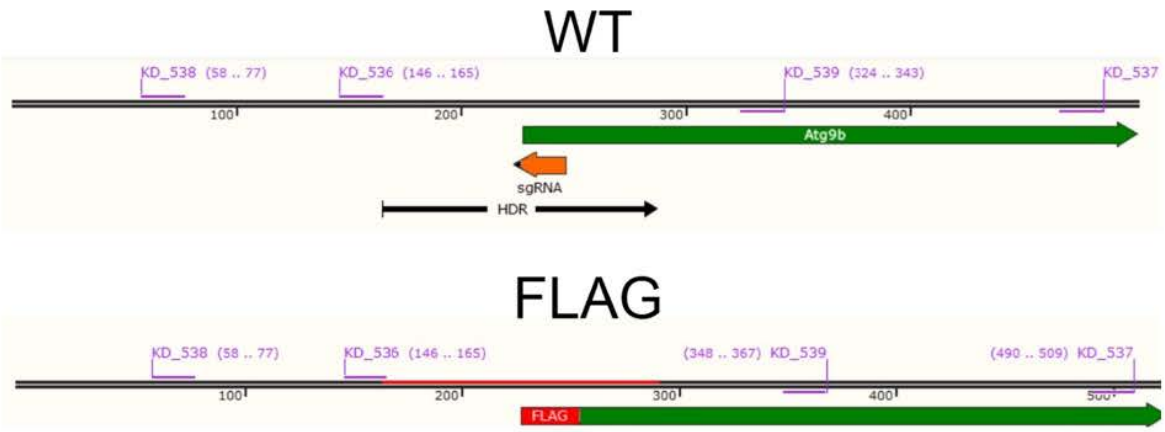

Figure 55. The design and screening strategy of FLAG-Atg9b mouse model development. We designed two sgRNA's targeting the transcription initiation site. By using the HDR template added FLAG tag after the first codon of Methionine.

ssODN to be used to add DYKDDDDK amino acids (FLAG amino acids) with the methionine start codon at the 5' to the FLAG sequence. This was the longest insertion we have attempted with HDR template. The successful FLAG addition would result in the addition of 24 nucleotides which can be separated from WT allele by high-concentration agarose gel electrophoresis (3%).

To increase the efficiency of the long insertion, we implemented an asymmetrical HDR template strategy. We adapted the asymmetrical HDR template strategy. The annealing site, 30% of the ssODN length, while donor site 70%, which was shown to improve the homology-directed repair by 60% in cells (105) (Figure 56).

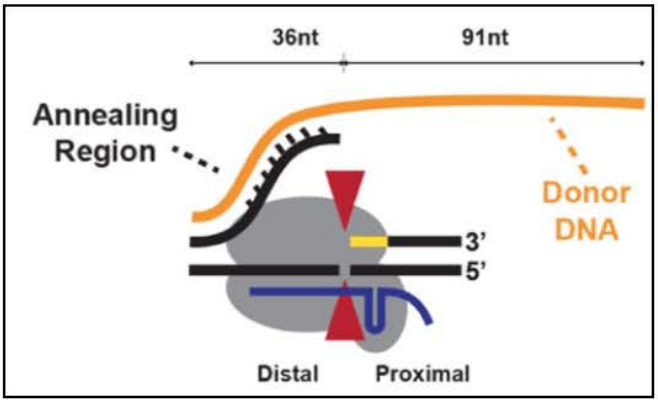

Figure 56. The schematic representation of asymmetrical homology arms in the HDR template. Annealing region corresponds to 30% of HDR and donor region to 70%. (105).

The creation of FLAG-Atg9b mice offers an alternative approach for detection of the Atg9b expression in mouse tissues that express Atg9b. In case of the generation of a rabbit ATG9B antibody may not be successful, FLAG tag can serve experimental advantage since the FLAG tag is associated with a variety of well-established commercial antibodies and assay protocols developed for it.

Considering we are not working with ectopic expression there was one potential problem that we foresaw: like in cells, one tag may not be sufficient and 3xFLAG editing could be a necessity. Regarding that we are attempting endogenous level Atg9b detection we also designed 3xFLAG strategy. However, we were attempting one FLAG addition the largest insertion we tried so far with HDR template, and we were unsure about its efficiency. We did not commence with 3xFLAG Atg9b strategy before characterizing FLAG Atg9b.

We took advantage of 21-nucleotide difference in length for resolving WT and FLAG alleles on 3% agarose gel. 4 founder mice harbored the FLAG allele. It is important to note that not identical, but highly similar DNA sequences such as CRISPR/Cas9 mediated alterations, the alleles can form heteroduplex and can migrate in an upper size. This allowed us to migrate WT, FLAG, and heteroduplex alleles on high-concentration agarose gel for genotyping (106). Therefore, we saw that the protocol worked efficiently, even with a longer insertion, and we confirmed the addition of FLAG tag through Sanger sequencing (Figure 57).

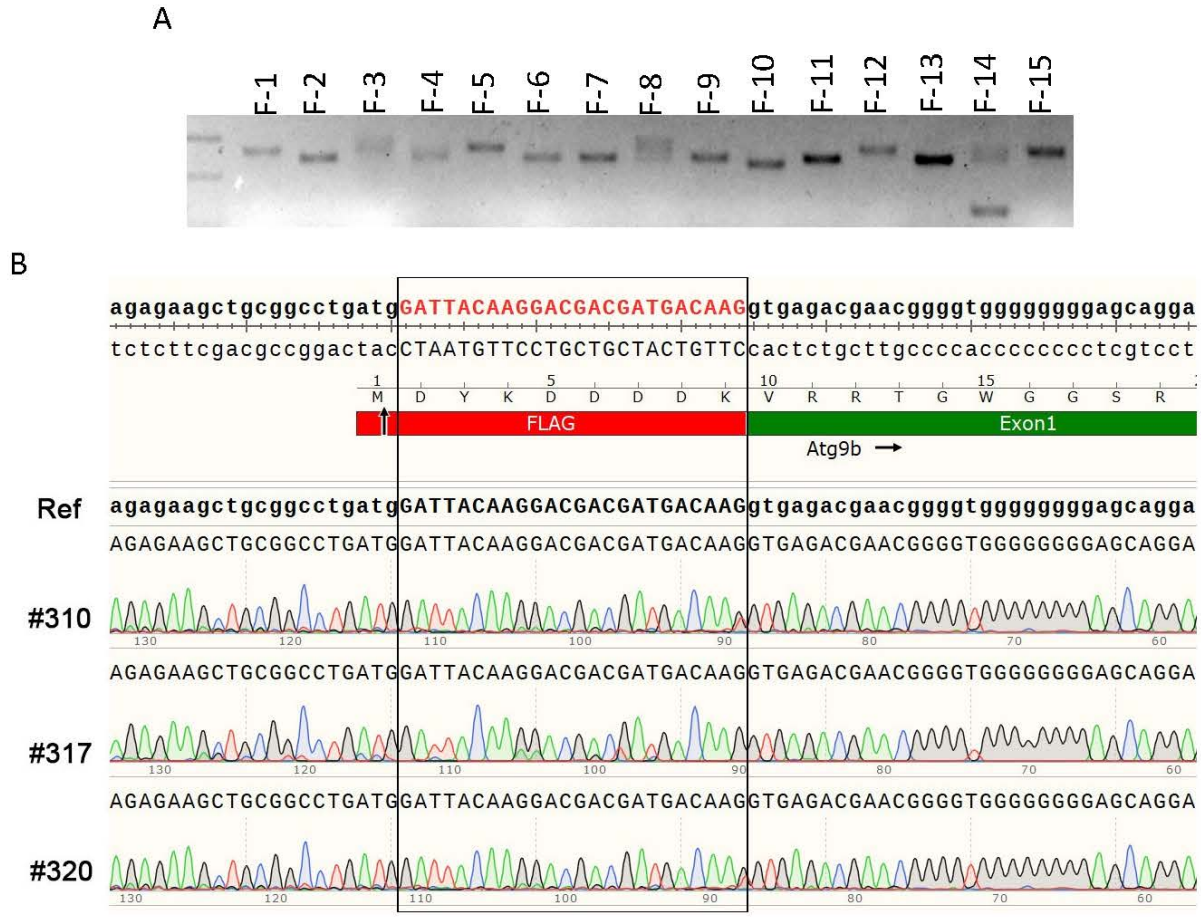

Figure 57. Sequence validation of the FLAG-Atg9b knockin allele. A) Agarose gel electrophoresis of founder mice indicating WT and FLAG alleles and FLAG/WT heteroduplex. B) Confirmation of FLAG addition by Sanger Sequencing.

4.4.4.4. 3xFLAG-Atg9b Strategy

3xFLAG tag polypeptide sequence is DYKDHDG-DYKDHDI-DYKDDDDK composed of 21 amino acids and 63 nucleotides in length. For this editing, we modified the HDR template while using the same sgRNA for targeting and cleaving with Cas9. The HDR template used was 142 bp and the nucleotides were inserted after the start codon (Figure 58-A). For the screening strategy, similar to the single FLAG addition, the nucleotide difference was taken advantage of, and the alleles amplified by PCR resolved in high-concentration agarose gel. Unfortunately, the 3xFLAG addition was unsuccessful in the two founders that were born.

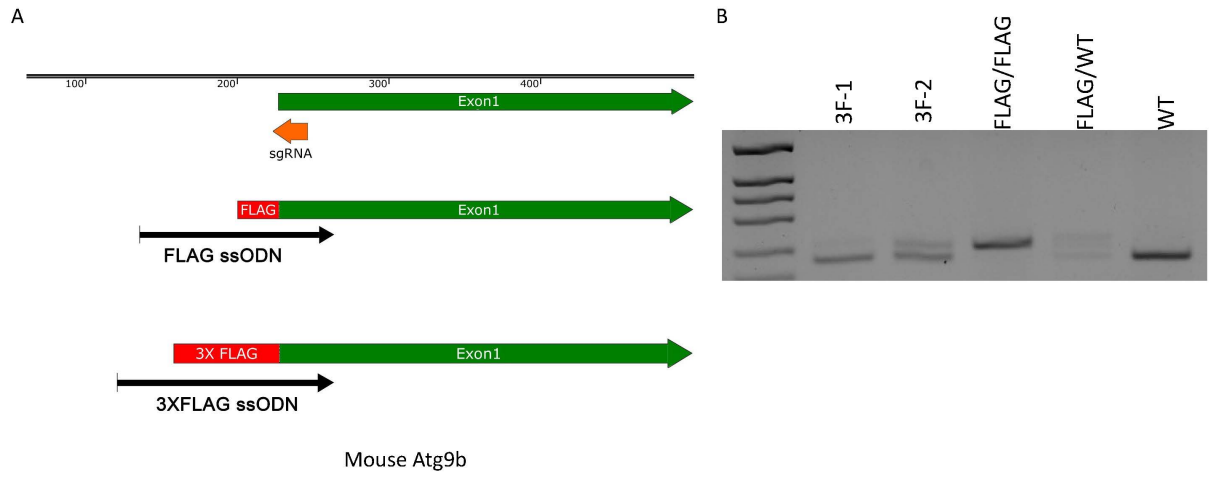

Figure 58. The editing and genotyping strategy for 3xFLAG Atg9b.The locus was targeted with the same sgRNA in FLAG-Atg9b strategy and modified HDR template. The ssODN was altered to harbor additional FLAG sequences. B) Genetic screening of founder mice born (3F-1 and 2).

4.4.4.5. Atg9b Conditional Knock-out Model

In the early phases of our transgenic mouse development strategies, we considered the possibility that Atg9b knock-in to be lethal. In this case, to understand the role of Atg9b in placenta morphology and histology, and in trophoblast cells, having a conditional Atg9b knockout would have been an asset.

We initiated our strategy by the alignment of the mouse and human ATG9B loci. Exon 2 was almost completely conserved, as well as its flanking intronic regions. We designed sgRNA's to the flanking introns of mouse exon 2 (Figure 58). The Cre-Lox system is the most common strategy to generate cKO mice. In the first step, 2 LoxP sites are inserted in the genome, in our case to the 5' and 3' flanking sequences of exon 2 of the *Atg9b* gene. The LoxP sites can be inserted with CRISPR/Cas9 HDR system which we aimed to accomplish. In case of double LoxP addition, the next step would be trophoblast-specific Cre^{+}/Cre^{+} WT of mating of double LoxP mice. It is important to state that exon 2 deletions can lead to frameshift mutations and subsequently, a complete knockout when HDR editing is inefficient.

In our initial approach, which involved the use of two sgRNAs and two donors, the yield was low. To address this, we decided to conduct additional experiments using an extended donor DNA. However, due to the low electroporation efficiency associated with longer donor

DNAs, we repeated the experiments by synthesizing 200 nt-long ssODN oligos containing both LoxP sequences (Figure 59).

In our second strategy, which employed a single, longer donor containing both LoxP sites, our expectations were focused on the exclusive generation of double-LoxP-containing alleles. To our surprise, we observed the formation of numerous single-LoxP-containing alleles, as well as deletion alleles. Subsequent analysis revealed that the presence of a single LoxP sequence could result from recombination of the region located between the two LoxP sites (Figure 59).

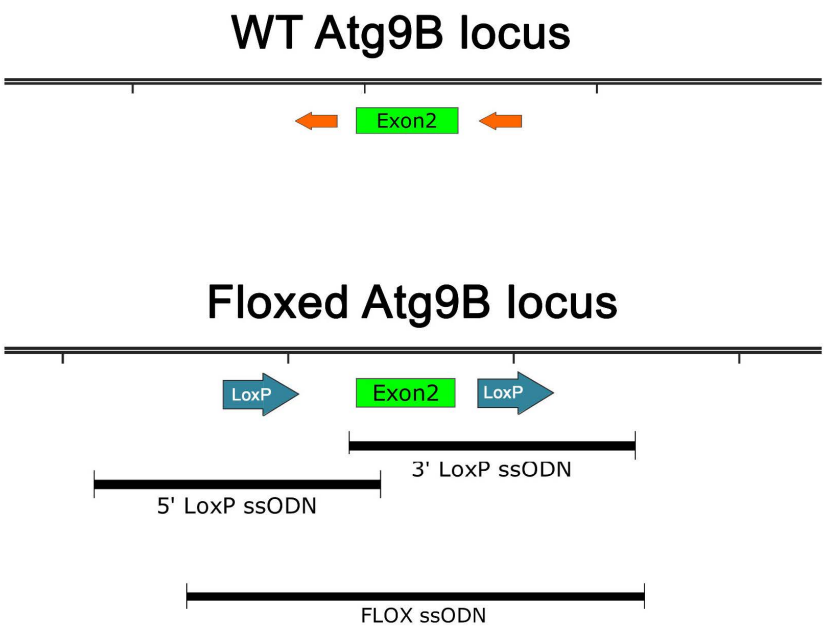

Figure 59. FLOX Editing Strategy. We adopted two different HDR editing strategy integrating LoxP sequences with one ssODN covering the entire sequence, and 2 different ssODNs for 5' and 3' LoxP sequences.

We developed a screening strategy by designing primers that encompassed the LoxP sites. Despite our efforts and initial success on the embryos, the sequenced embryo had a small deletion within the 5' LoxP sequence (Figure 60).

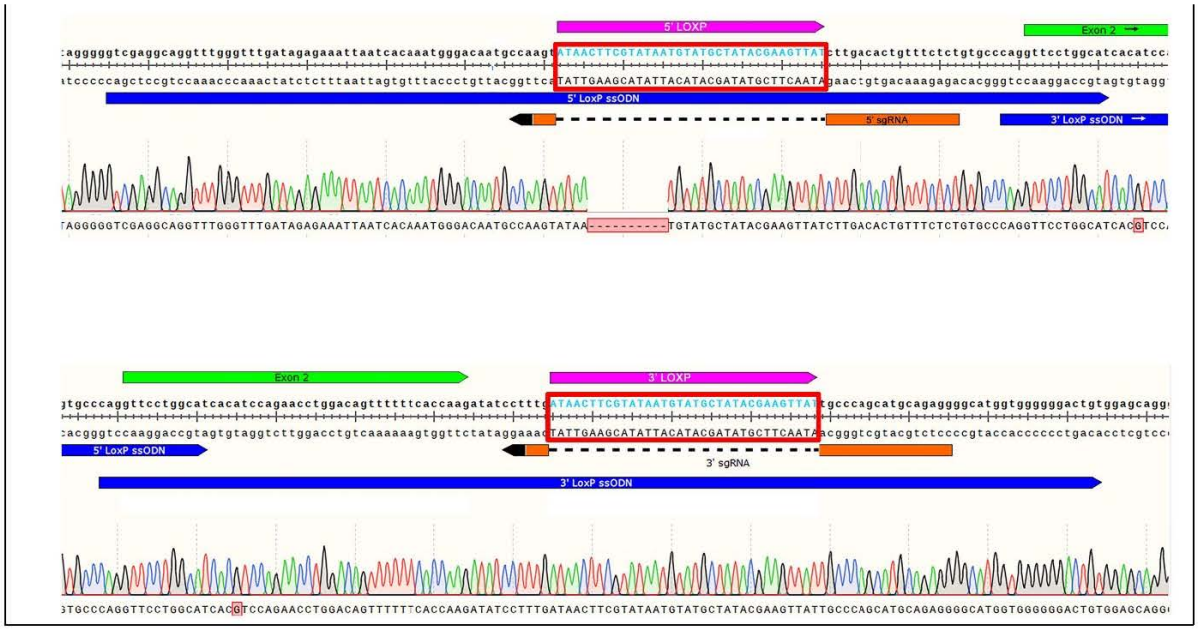

Figure 60. Sanger sequencing of double LoxP embryo. The addition of double LoxP was successful although there was a deletion in 5' flox sequence that was inserted through 5' HDR.

While some founders born of the implantation of subsequent electroporation, such as FLOX-168 and FLOX-171, displayed double LoxP additions the allele was not inherited by the next generation. Furthermore, there were deletions that were identified in FLOX-171 and FLOX-172, which had the potential to result in an Atg9b knock-out mice. Consequently, we initiated breeding with these founders carrying deletion mutations, using WT B6 females to establish an F1 exon 2-deleted knock-out strain (Figure 61).

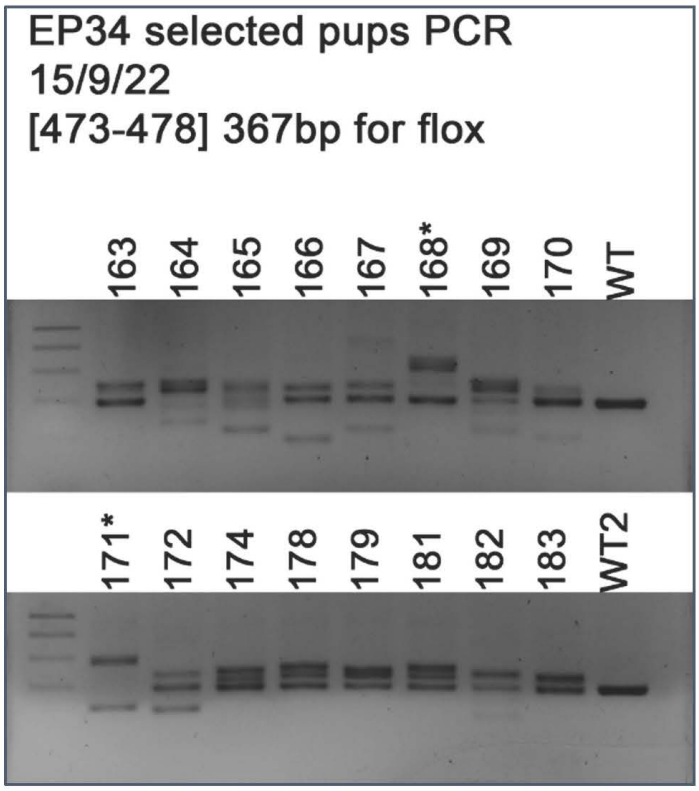

Figure 61. Double Flox screening. We designed and optimized primers, KD_473 and KD_478 were used for screening. Atg-168 and Atg-171 founders were presenting double flox bands and Atg-171 and 172 had deletion alleles.

4.4.4.6. Atg9b Knock-out Model (DEL3-DEL4)

Deletion mutations occurred in exon 2 as a result of our efforts to generate double LoxP additions. These deletions were specifically targeted at exon 2 of a 14-exon protein and resulted in a frameshift of the gene, effectively leading to a complete knockout of Atg9b. We mated heterozygous mice to obtain homozygous DEL-3 and DEL-4 mice (Figure 62). It is worth noting that both female and male Atg9b homozygous knock-out mice were phenotypically healthy, reached adulthood, and were fertile despite our initial reservations of the knockout might lead to fatality. Consequently, after successfully establishing this strain and confirming the viability of the mice, we decided to discontinue the conditional knock-out aspect of the project, as it proved unproductive and unnecessary.

Figure 62. The genotyping of heterozygous and homozygous Atg9b knock-out mice. Founder DEL3 and DEL4 mice were mated with WT mice and heterozygous mice were inbred to obtain homozygous knock-out mice ("*" indicates the parents of these littermates).

The deletions of exon 2, DEL3, and DEL4 were verified by Sanger sequencing, ultimately producing the Atg9b knock-out mouse model (Figure 63).

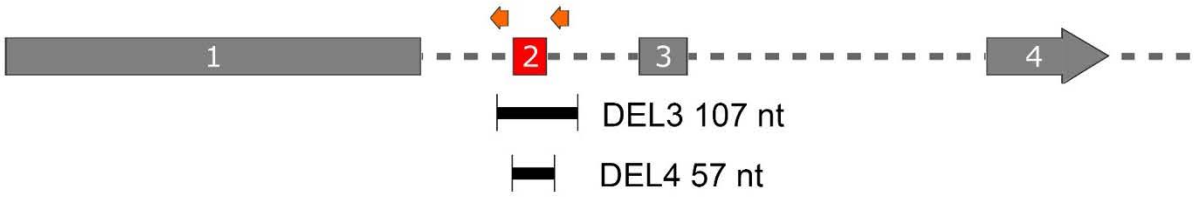

Figure 63. Atg9b Knock-out model confirmation by DEL-3 and DEL-4 sequencing.

In response to our observation of increased neonatal and maternal mortality in Atg9b DEL-1/DEL-2 mice, we performed breedings involving WT/DEL-3 and WT/DEL-4 heterozygous males paired with heterozygous and homozygous DEL3 and DEL4 females.

The initial crosses yielded limited data due to a small sample size. Two WT/DEL4 heterozygous females successfully gave birth and stayed alive, but one of them died 10 days post-delivery while still nursing, resulting in neonatal deaths. The other mother, also heterozygous, survived after giving birth to five litters, and all of her offspring are currently thriving at four weeks of age.

In the case of DEL-3, one homozygous DEL-3/DEL-3 female delivered seven neonates but died 12 days after giving birth. The neonates survived by placing than with another nursing mother.

We are presently genotyping these offsprings to elucidate the genotype composition of both surviving and deceased mothers. These observations may illuminate at potential health effects on mothers due to the collective toxicity of multiple conceptuses. Nevertheless, it is essential to emphasize that these findings remain speculative, and additional controlled mating experiments with a larger sample size are required to establish a causal link.

4.4.5. Molecular and Histologic Characterization of Knock-in Mice

In this section, our primary focus will be dedicated to the investigation of functional aspects of Atg9b and the novel *Atg9b* mutation that we have identified by knock-in the rare genetic disease mouse model, FLAG-Atg9b and Atg9b knock-out models, developed for our study.

4.4.5.1. ATG9B Expression and Histologic Assessments of Atg9b Knock-in Disease Model

The functional studies conducted for the rare genetic disease model were histological examinations, molecular assessments, and behavioral studies, to gain insight to the pathophysiological mechanisms underlying the human disease.

Both heterozygous and homozygous Atg9b knock-in mice were phenotypically healthy, seamlessly progressing into adulthood. Both female and male mice were fertile and contributed to the next generations.

In the F2 generation, the homozygous mice, born of the mating between mouse 34 and 38, as well as the 42 and 47 pairs both of which were heterozygous for the knock-in as demonstrated by Sanger sequencing (Figure 53). The genetic alteration followed an autosomal inheritance pattern, mirroring the same inheritance pattern observed within the family, with Mendelian-like distribution (Table 11).

Table 11. The pattern of inheritance of Atg9b genetic disease knock-in model. Mendelian-like distribution was observed in litters.

	WT	WT/KIN	KIN/KIN
Percentage	29,6	42,3	28,2

Continuing the investigation into the knock-in models, we turned our focus to the elevated expression of Atg9b within the placental tissue in RNA levels compared to the other tissues. It is worth noting that the placenta undergoes dynamic changes during development, with a fully functional placenta first developing at 12.5 dpc, labyrinth volume reaching its apex at 14.5 dpc, and subsequently undergoing decidual tissue regression between 15.5 and 17.5 dpc. (107) (Table 12). We opted to investigate the expression level of Atg9b in different stages of placental development.

Table 12. The timeline of mouse placental development. The table shows the stages starting with fully functional placenta (97).

Gestational Time	**Important Processes and Key Structures**
E12.5-E13.5	Processes: Definitive Placenta Becomes Fully Functioning Key Structures: Labyrinth (L), Junctional Zone (JZ), Decidua (D), Chorionic Plate (C) • Uterine natural killer (uNK) cell numbers plateau in the decidua by E12.5 • The ST cells of the JZ move from a mass to a more sheet-like configuration by E12.5
E14.5	Processes: Definitive Placenta Maximizes Maternal/Embryonic Blood Exchange Key Structures: Labyrinth (L), Junctional Zone (JZ), Decidua (D), Chorionic Plate (C) • The labyrinth contains solely non-nucleated RBCs of maternal and embryonic origin by E14.5 • The labyrinth has peaked in size and comprises approximately half the total placental weight
E15.5-E17.5	Processes: Degradation of Decidual Tissue Key Structures: Labyrinth (L), Junctional Zone (JZ), Decidua (D), Chorionic Plate (C) • Numbers of uNK cells begin to decline in the decidua • Decidual tissue begins to deteriorate in preparation for birth
E18.5	Processes: Preparation for Birth Key Structures: Labyrinth (L), Junctional Zone (JZ), Decidua (D), Chorionic Plate (C) • The quantity of GC in the JZ have increased 250-fold by E18.5 from the time of their differentiation around E9.5

A timed breeding was conducted using heterozygous males and homozygous females to assess developmental abnormalities in the 13.5 dpc. The breeding was monitored by the presence of copulation plugs, with 0.5 dpc marked upon plug detection. Following the sacrifice of pregnant females 13.5 dpc, their abdominal cavities were opened, and the uteri were extracted. Given that one breeding could yield between 3 to 10 conceptuses, which are handled and genotyped individually. The process of placenta and embryo isolation were depicted in Figure 64.

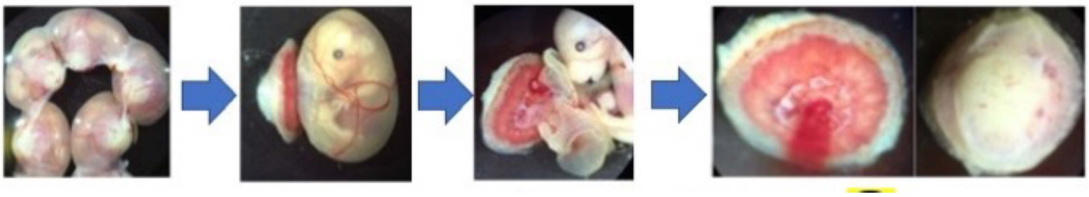

Figure 64. The method of placenta isolation. The site anterior to the embryo is rich with trophoblasts and blood vessels while the posterior site is metrial gland and decidua.

To assess embryonic development, stereomicroscopic images of homozygous and heterozygous embryos were acquired. There was no substantial developmental delay, fetal growth retardation observed in homozygous double knock-in embryos at 13.5 dpc. Given that complete Atg9b knockout has been correlated with anophthalmia and ocular abnormalities, we focused on the eye morphology, no major abnormality was observed (108). The representative images of the anterior aspects of two embryos from each phenotype were presented (Figure 65).

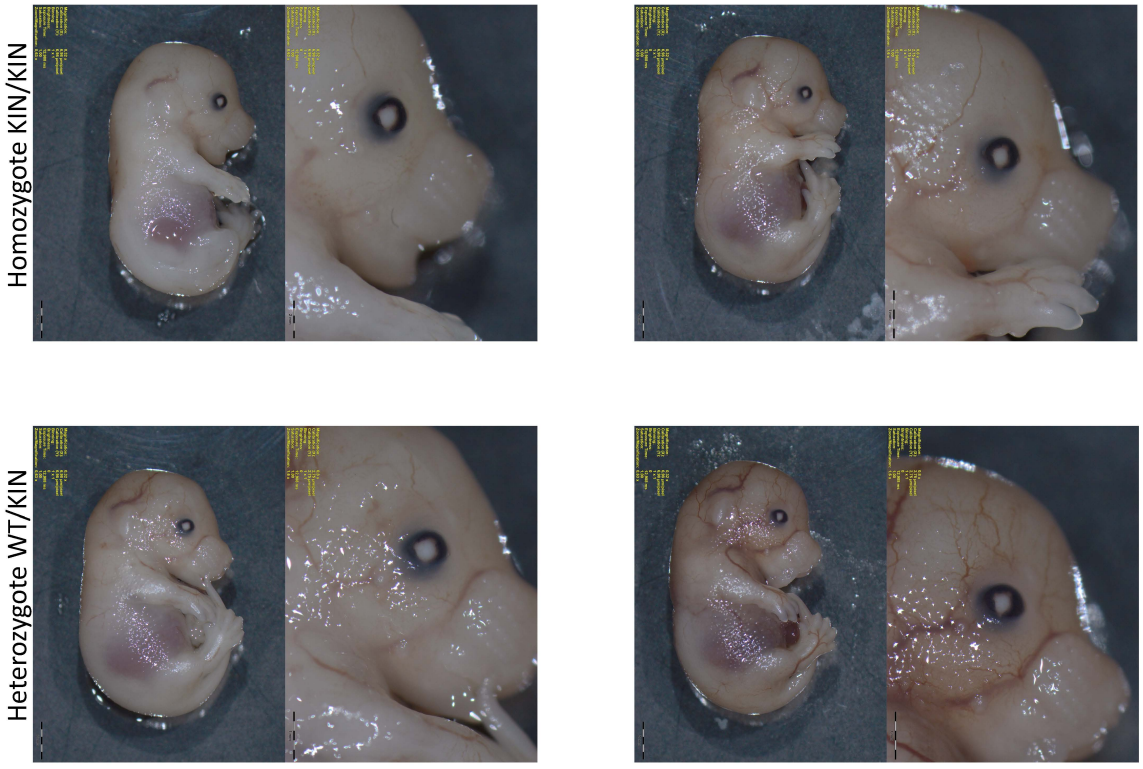

Figure 65. The morphology of 13.5 dpc homozygote and heterozygote embryos. 2 embryos of each genotype were presented. We observed no major morphological differences that may indicate developmental delay.

We opted to investigate the expression level of Atg9b in different stages of placental development. We crossed heterozygous WT/KIN (KIN: knock-in) female and homozygous KIN/KIN male and sacrificed pregnant females in 13.5 dpc and 17.5 dpc. Tissue samples were obtained from embryos for genotyping, and placentas were immediately submerged in liquid nitrogen and stored at -80 C for later the immunoblotting with commercial anti-ATG9B antibodies. In either stage Atg9b expression could not be detected. The expression of the B3 clone of HeLa cells stably overexpressing human ATG9B was observed using a C-terminal commercial Anti-ATG9B antibody. Notably, this C-terminal antibody failed to detect the Atg9b expression in either heterozygous WT/KIN or KIN/KIN genotypes or the positive control B3 cells (Figure 66). Consequently, pursued our aim of the development of a rabbit polyclonal ATG9B antibody.

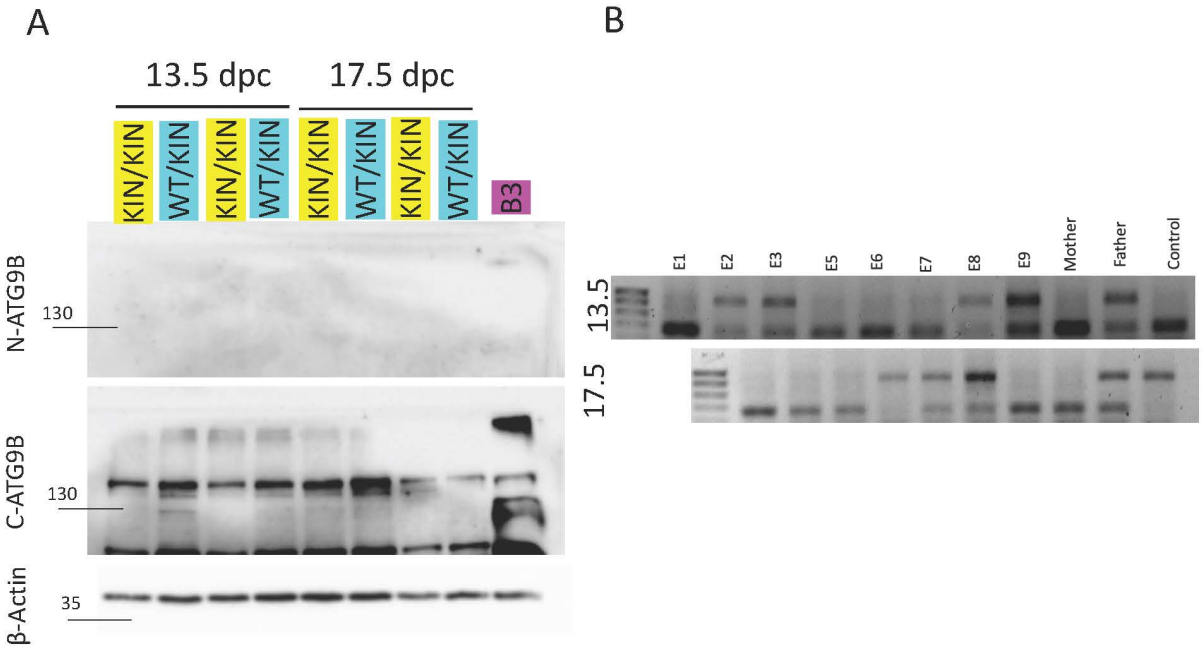

Figure 66. Atg9b expression in heterozygote and homozygote knock-in placenta tissues at 13.5 and 17.5 dpc. A) N-terminal and C-terminal commercial anti-ATG9B antibodies failed to detect endogenous Atg9b expression. B) Genotyping of 13.5 and 17.5 dpc embryo samples with EcoRI digestion. β-actin was used as a loading control (housekeeping gene).

To investigate potential morphological variations in placental development resulting from genetic mutations, we conducted hematoxylin eosin staining and examination of mature 18.5 dpc placentas. We aimed to display potential morphological abnormalities of knock-in

placentas compared to the WT. For this purpose, mature 18.5 dpc placentas were dissected and subsequently fixed using a 3.7% formaldehyde and 1% methanol solution (formalin). Simultaneously, genotyping was conducted on the embryos via EcoRI digestion. Following fixation in formalin, the tissues were embedded in paraffin, and sections were prepared for hematoxylin-eosin staining. The sections were specifically derived from the mid-section of the placenta identified by the presence of the umbilical cord. At 18.5 dpc, the decidua and junctional zone where the spongiotrophoblasts are dominant undergoes regression, marking the preparation of the placenta for birth (107). In a related study on *Atg7* conditional knockout mice, the spongiotrophoblast layer (junctional zone) was observed to be smaller than in WT mice (91). We did not observe major abnormalities in the knock-in placenta. Our initial observations indicated the overall size of the placenta may be enlarged, suggesting potential underdevelopment at this stage of pregnancy. Nonetheless, these were preliminary observations, and we refrained from making any conclusions without histomorphometry analysis (Figure 67).

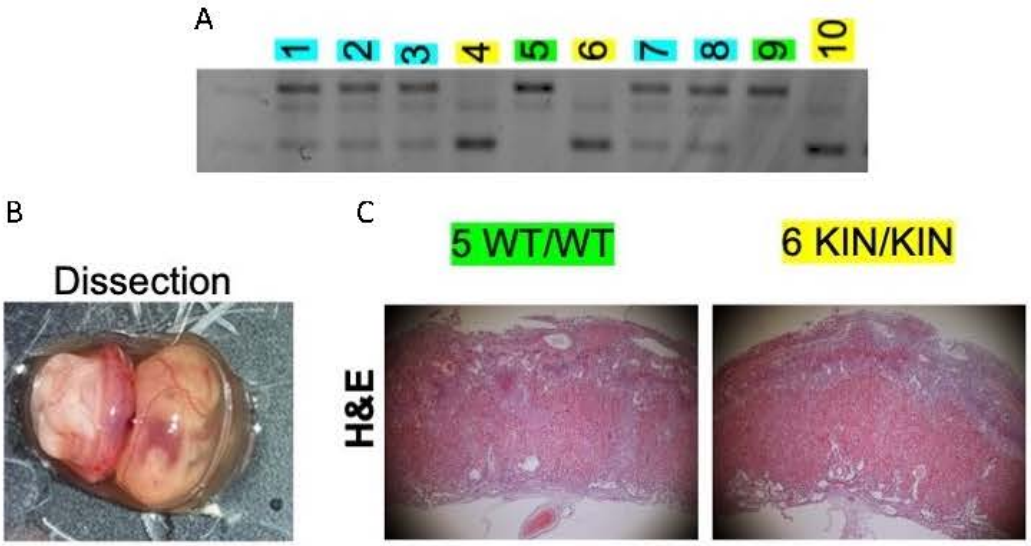

Figure 67. The histology of WT and knock-in placenta. A) Genotyping of the embryos. Blue represents heterozygous knock-in, yellow homozygous knock-in, green WT embryos. B) Representative image of placenta and embryo dissection C) Hematoxylin eosin staining of WT and homozygous knock-in placenta. The upper side is maternal, lower side is the fetal side of the placenta. The umbilical cord is visible on the lower side of the picture.

Subsequently, initial histomorphometry evaluations were obtained with the placenta sections of the WT, homozygous, and heterozygous knock-in genotypes in the developmental

stage of 18.5 dpc. The area of decidua was significantly larger in the homozygous knock-in placenta in comparison to WT. The other zones of the placenta did not display any significant difference (Figure 68). Decidua is the site that is responsible for physical protection, nutrient supply, hormone regulation (such as prolactin), and harboring immune cells to protect the embryo from maternal immune cells (109). It is important to stress that the decidua regresses at this developmental stage in preparation for the birth. Although, homozygous knock-in decidua were larger than WT, when heterozygous samples, which contain a copy of the WT *Atg9B* gene, were included in the WT set, the difference became statistically insignificant (data not shown).

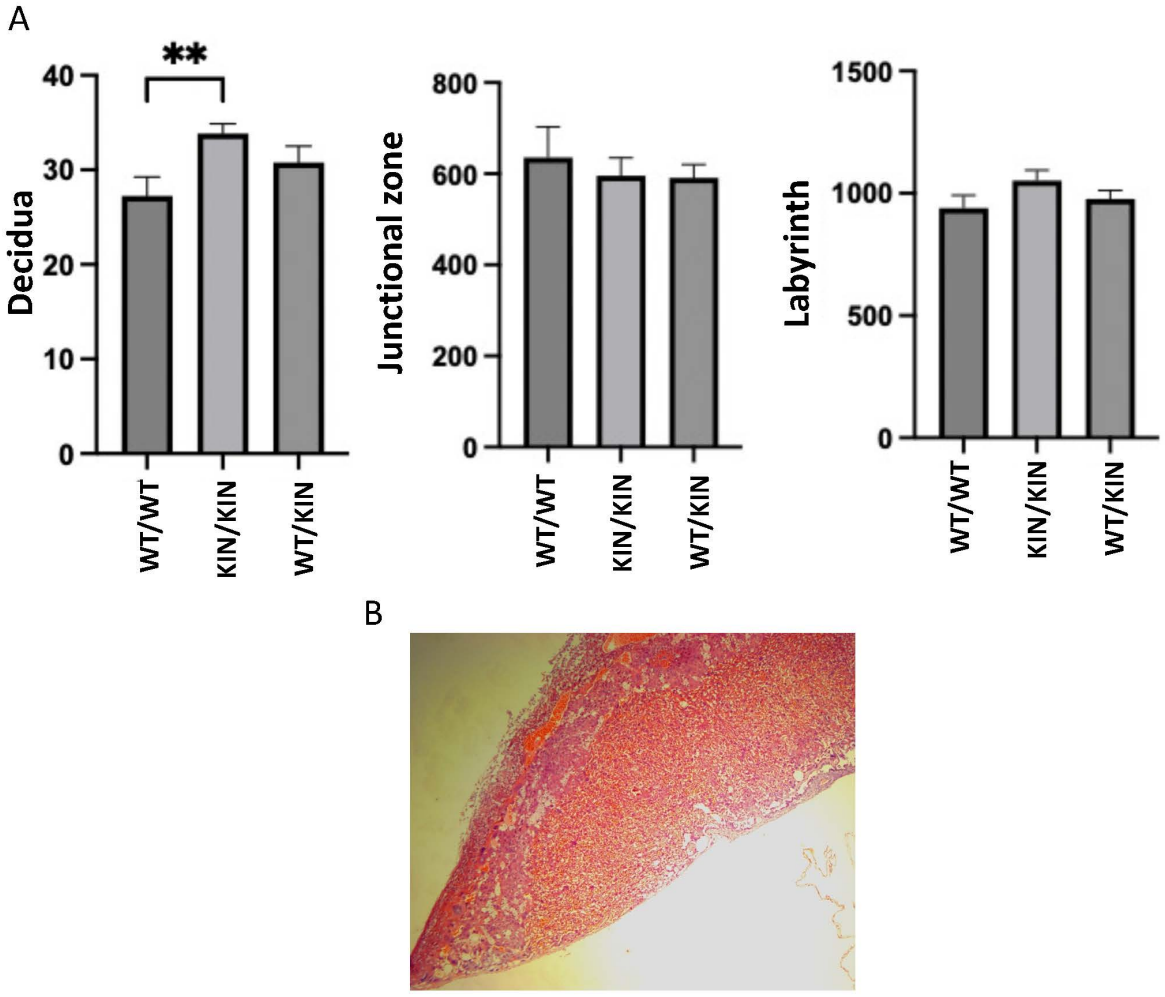

Figure 68. Histomorphometric analysis of the placenta in *Atg9b* knockin mice. A) The widths (μm) of major placental zones compared between WT and the knock-in disease model. B) The representative image of placenta sections stained with hematoxylin eosin staining that were employed for this study.

4.4.5.2. Behavioral Experiments with Atg9b Knock-in Disease Model

The major clinical finding of the patients was mental retardation. Cognitive tests are very well-established for mouse models (110,111). Having obtained the rare genetic disease model, we wanted to apply the behavioral tests for WT and homozygote knock-in litter mate 6-8-week-old male mice. We mated heterozygous knock-in male and female mice and offsprings were born within the same 2-week period. Newborn females were sacrificed immediately after birth. Male litters were genotyped when they were 3-week-old. 15 WT and 15 homozygote KIN male mice were transferred to Hacettepe University where our project partners performed cognitive tests after 2-week adjustment period. They performed a series of tests involving perinatal cortex-related new object recognition test, hippocampus-related novel object recognition and social novelty test, amygdala and hippocampus-related passive avoidance test. They additionally performed anxiety-related tests such as social interaction, ball embedding test, social preference test, and open field test or anxiety-like behavior were measured (112,113).

The locomotor activity test was performed by placing the mice in 22.5x22.5x30 cm cages and recording their movement for 10 minutes. Total displacements were measured for each group, and their movement was found similar (Figure 69).

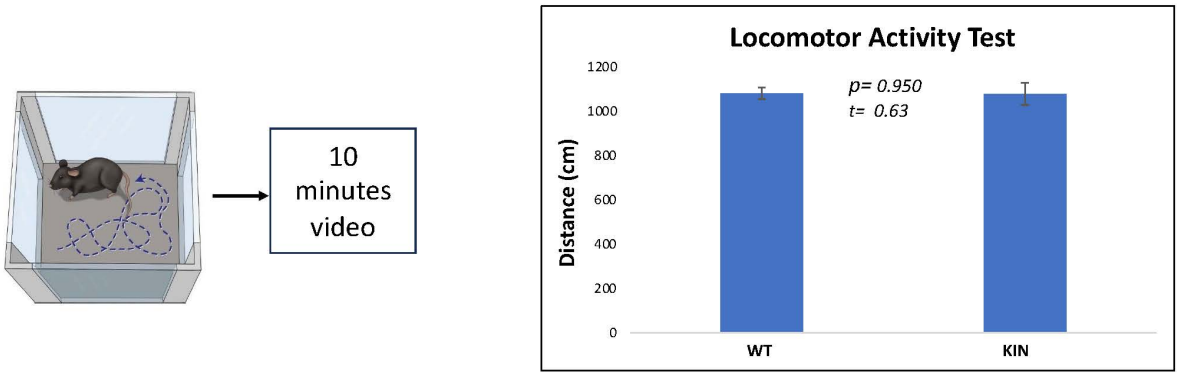

Figure 69. The locomotor activity test. The test was performed for placing mice in box and measuring their movement for 10 minutes. The results were similar in both groups.

The ball embedding test was performed by placing mice in clean, 3-4 cm sawdust-containing cages having 15 balls on 3 columns, 5 rows. After 20 minutes the ¾ of balls embedded were counted. The test was performed with an individual mouse at a time. There was not a statistically significant difference between the groups (Figure 70).

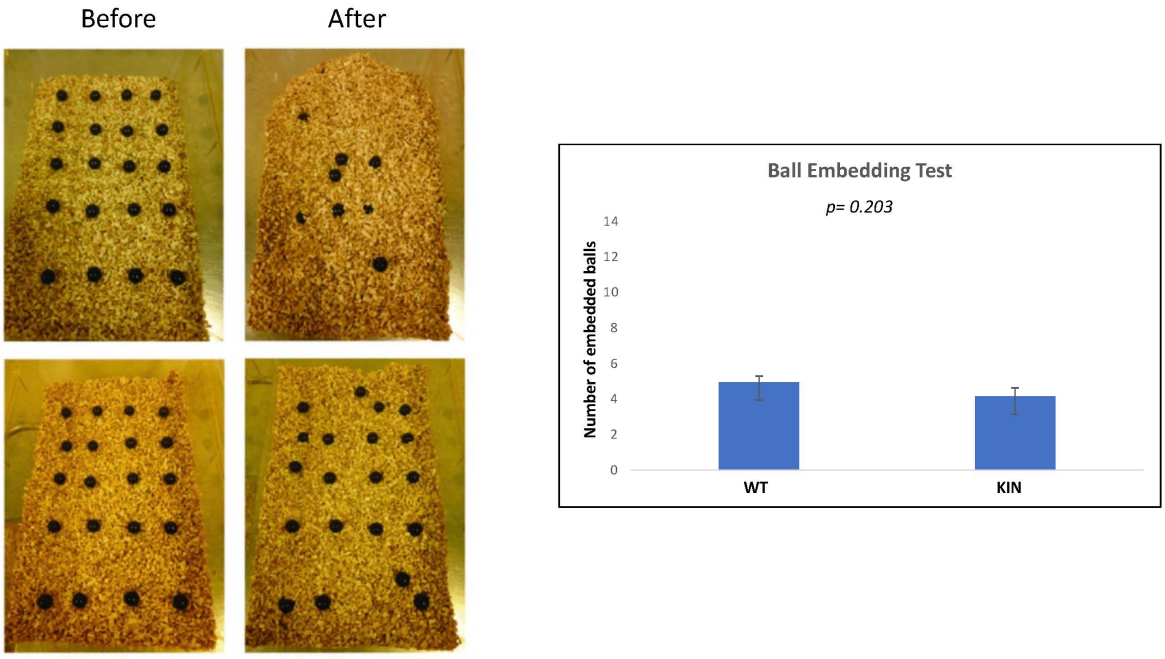

Figure 70. The ball embedding test. The setup of the experiment is shown on the left. WT and homozygote KIN animals showed similar performance.

The open field test was performed for the assessment of the anxiety. The box used in the locomotor activity test was used to measure the first time mice entered the open area of the box, the latency, and the total time they spent in the open area were measured. The tests were performed individually for the mice. The results were not statistically different between WT and homozygote KIN mice (Figure 71).

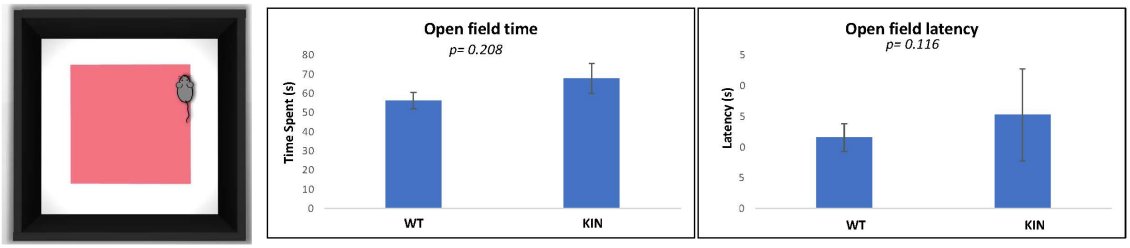

Figure 71. The open field test. The time spent on the middle zone and the time they first entered to the zone (latency) were measured. The results were statistically insignificant.

In the social preference test, a three-compartment box was utilized with a toy mouse in a cage placed in one of the compartments opposite to the living mice (social target). The experiment was started by placing the mice subjected to the experiment in the middle

compartment, restricting its movement to the right and left areas for the first 5 minutes. After this period, the barriers separating the compartments were removed, allowing the mice to move freely between the compartments for 10 minutes. The time (in seconds) spent around the social target and the toy was measured. The results demonstrated that the ratio of the time spent with the social target compared to the total time spent around both cages was similar between the groups (Figure 72).

The subsequent day, the social novelty test was performed, involving the placement of one familiar mouse (a cage mate) in one compartment and one unfamiliar in the other. Over the course of 10 minutes, the time spent with the familiar and unfamiliar mouse was recorded. In both tests, the results exhibited similarity between the WT and homozygote knock-in mice (Figure 72).

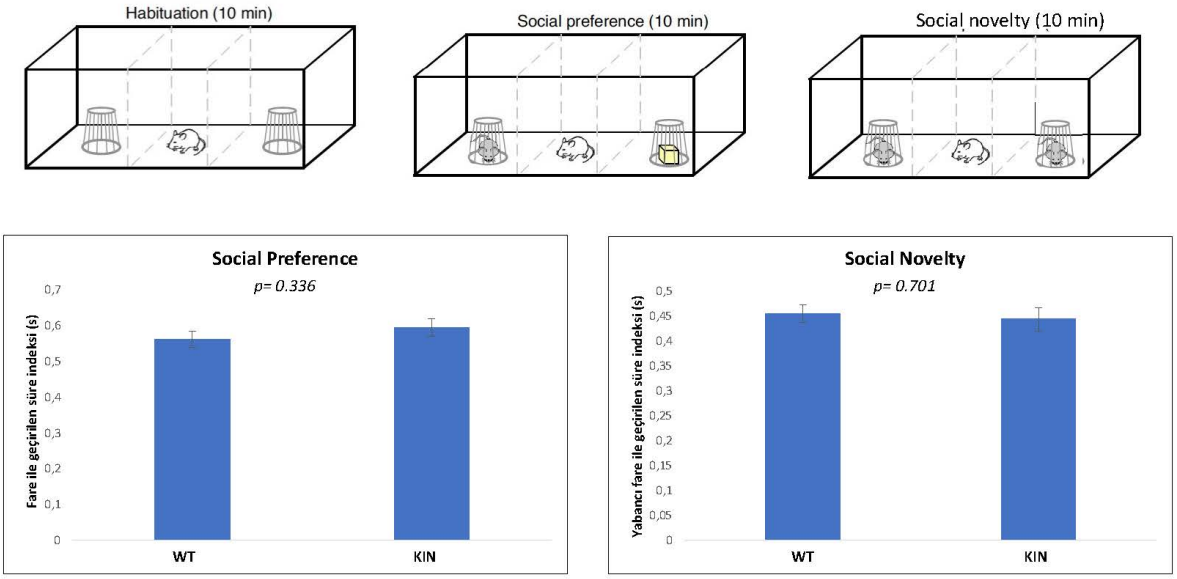

Figure 72. The social preference test. Time spent around the familiar and novel mice have been measured.

Memory Tests:

The novel object recognition test, which is regulated by the hippocampus, assesses behavior associated with memory. It is anticipated that mice will spend more time to exploring unfamiliar objects while spending less time with familiar ones.

The test was conducted in two phases: in the training phase, a 22.5x22.5x30 cm box with the same object on either side was placed to allow the mouse to get familiar with the objects over a period of 10 minutes.

In the short-term memory test, performed one hour after the training phase, one of the objects was replaced with an unfamiliar one, and the mice were recorded for 10 minutes. The time spent around the unfamiliar and familiar objects was analyzed (Short-term memory).

The long-term memory test, conducted 24 hours after the training phase, featured the replacement of one of the objects with another novel object, and the test was executed similarly (Long-term memory).

The results of both short-term and long-term memory tests did not reveal a significant difference between WT and knock-in mice (Figure 73).

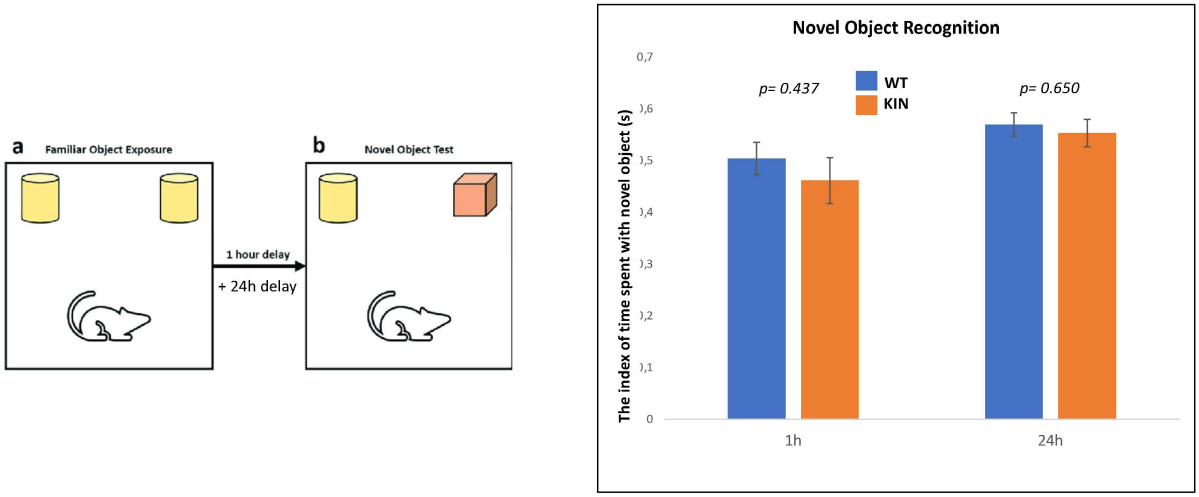

Figure 73. The novel object recognition test. A) Training phase: The mouse is trained for 1 hour to get familiar with objects. B) Test phase: Novel object placement with one of the familiar objects.

The spatial object recognition test is also a hippocampus-related experiment. Two identical objects were placed in the same box used in the novel-object recognition test. The mouse was trained for 10 minutes in the training phase. One hour later the position of one of the objects was changed and the time spent around the replaced object was measured for the assessment of short-term memory. 24 hours later the test was repeated for long-term memory. Mice should spend more time with the replaced object longer. Between the groups, there was not a statistically significant difference (Figure 74).

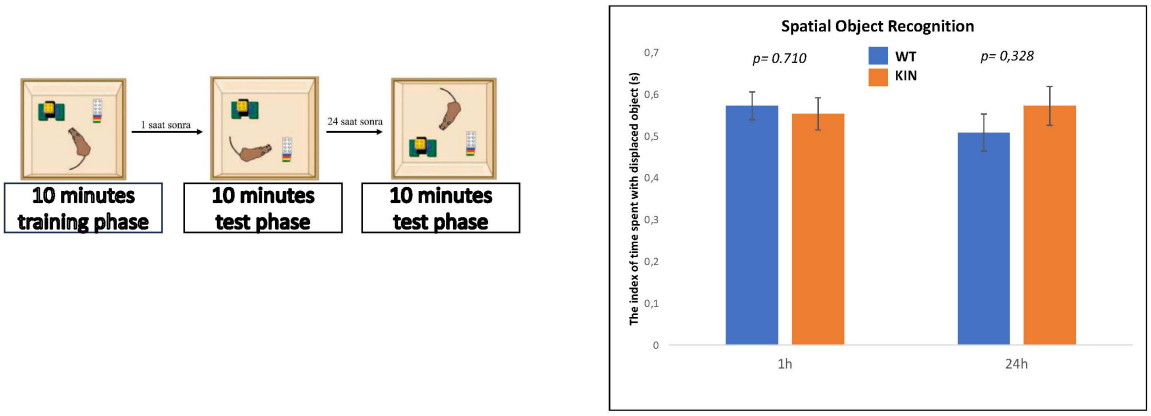

Figure 74. The spatial object recognition test. The test did not reveal statistically significant difference between WT and knock-in mice.

The passive avoidance test is designed to assess fear memory a response involving both hippocampus and amygdala (114). Mice naturally gravitate towards darker environments. A partitioned box with a door separator was used in this test. The mouse was initially placed in a well-lit area. As the door opens, the mouse tends to move towards the darker section. In the dark section, the mouse was subjected to a 0.9 mA electric shock for 2 seconds, followed by a 10-second interval to acclimatize to the environment in which the shock was administered.

One hour later, the same procedure was repeated, and the latency time required for the mouse to move to the dark section is recorded. Mice that did not enter to the dark area within 5 minutes were returned to their cages, and their latency was recorded as 300 seconds. Notably, homozygous knock-in mice displayed a higher inclination to move towards the dark area in comparison to the WT mice. The results approached to the statistical significance, indicating that homozygote knock-in animals exhibited reduced fear memory (Figure 75).

A

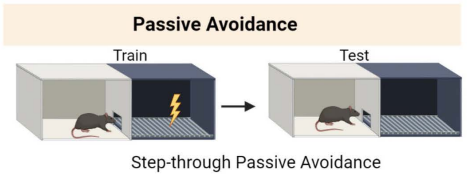

Step-through Passive Avoidance

B

Overall Comparisons			
	Chi-Square	df	Sig.
Log Rank (Mantel-Cox)	3,072	1	,080
Breslow (Generalized Wilcoxon)	3,195	1	,074
Tarone-Ware	3,136	1	,077

Test of equality of survival distributions for WT and KIN animals

C

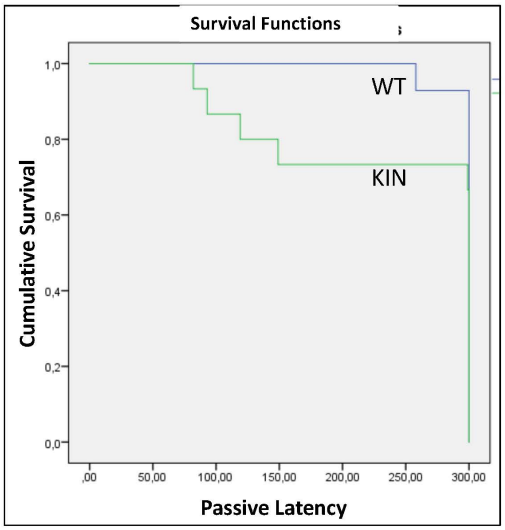

Figure 75. The passive avoidance test. A) The setup of the test. One well-lit and one dark section separated by a door. Dark side is where the electric shock is administered to the mouse. In test phase the latency of mouse passing through to the dark side were measured. B) The test scores of tested mice. C) Cumulative survival graph of the mice. Knock- mice had a tendency to move to the dark side more where electrocution was administered.

In summary, the truncation of Atg9b did not appear to have a significant impact on anxiety levels, or on cognition, dependent on the hippocampus and perirenal cortex. However, cognitive functions associated with the hippocampus and amygdala, particularly affecting fear memory displayed a decline in the knock-in mice.

4.4.6. Expressional and Histological Studies in Transgenic Mouse Tissues

In pursuit of a comprehensive assessment of Atg9b expression within the placental tissue at different developmental stages and among the other tissues, we decided to combine our efforts with the mouse models and anti-ATG9B serum.

Initially, we initiated a timed breeding strategy involving WT females and FLAG male founders. Given the founders' sequencing revealed homozygous status (Figure 57-B), the resulting placenta and embryos were expected to have heterozygous FLAG/WT genotype. Notably, the Atg9b gene is considered to be WT, with FLAG addition prior the Atg9b sequence. We conducted the sacrifice of two mothers at 13.5 and 15.5 dpc, to examine Atg9b expression by immunofluorescence experiment of the frozen, OCT embedded placenta sections. We

utilized a commercial polyclonal anti-FLAG antibody produced in rabbits, which was unlikely to exhibit cross-reactivity with mouse tissues. Unlike previous attempts using commercial anti-ATG9B antibodies with WT and knock-in mice, which did not display a specific staining (Data not shown), we explored various fixatives and experimental protocols for immunofluorescence experiments. Ultimately, we opted for Bouin's fixative and subjected the section to a 15-minute hydrogen peroxide treatment to facilitate decolorization (Figure 76). We employed both green and red fluorescent secondary antibodies to validate the specificity of the staining. Our findings revealed the expression of Atg9b at 15.5 dpc, predominantly within the spongiotrophoblast layer.

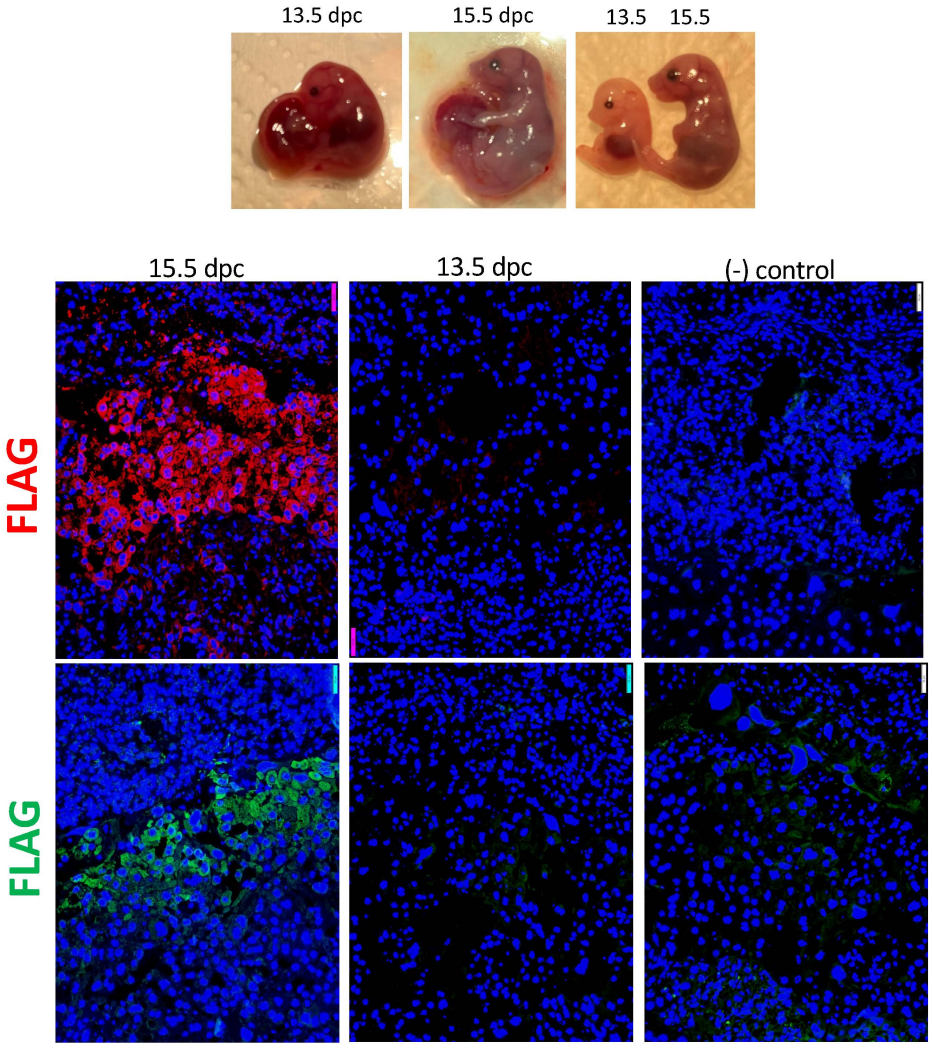

Figure 76. Immunofluorescence staining of mouse placenta sections with anti-FLAG antibody. Immunofluorescence displayed that Atg9b is expressed in the spongiotrophoblast layer, junctional zone at 15.5 dpc placenta.

Subsequently, we repeated the experiment and extended our examination to include placenta sections at 12.5, 15.5, and 18.5 dpc to further elucidate Atg9b expression. We observed conflicting staining patterns with the presented sections on different stages of placentas. We obtained false-positive signal so that we were unsure about the efficiency of the anti-FLAG antibody efficiency of the immunofluorescence protocol, and subsequently we refocused our efforts on generating home-made anti-ATG9B antibody and decided to progress to immunohistochemistry methods.

We performed immunofluorescence experiments with home-made anti-ATG9B serum with fresh-frozen placenta tissue sections with WT and knock-in genotype but failed obtain a specific signal. To amplify the signal and preserve the tissue we decided conduct immunohistochemistry experiments with our project partners with established reagents and technique.

In parallel, we performed immunoblotting with placenta tissues at these stages with the placenta samples frozen in liquid nitrogen with FLAG/WT heterozygous, FLAG/FLAG homozygous also with WT and knock-in placenta samples, with both FLAG M2 monoclonal antibody as well as FLAG polyclonal antibody, later our home-made ATG9B antibody without receiving a specific Atg9b band (Data not shown).

To address the Atg9b expression at the RNA level, we performed RT-PCR with the placenta samples from 12.5, 15.5, and 18.5 dpc developmental stages. The RNA samples were isolated from FLAG/WT placenta samples representing the WT Atg9b gene. For each developmental stage, two different placenta samples were randomly selected for the analysis. As a reference housekeeping gene, Gapdh was employed.

Notably, our RT-PCR results aligned with the findings from our initial immunofluorescence study (Figure76), indicating that Atg9b expression became evident at the 15.5 dpc developmental stage of the placenta. We also observed expression of Atg9b in testis, although to a lesser extent than in the placenta, further supporting the Protein Atlas data. Liver tissue was utilized as a negative control, no Atg9b expression being expected supporting the Protein Atlas data (Figure 9). This result represents the first comparative analysis of Atg9b expression at different stages of placental development (Figure 77).

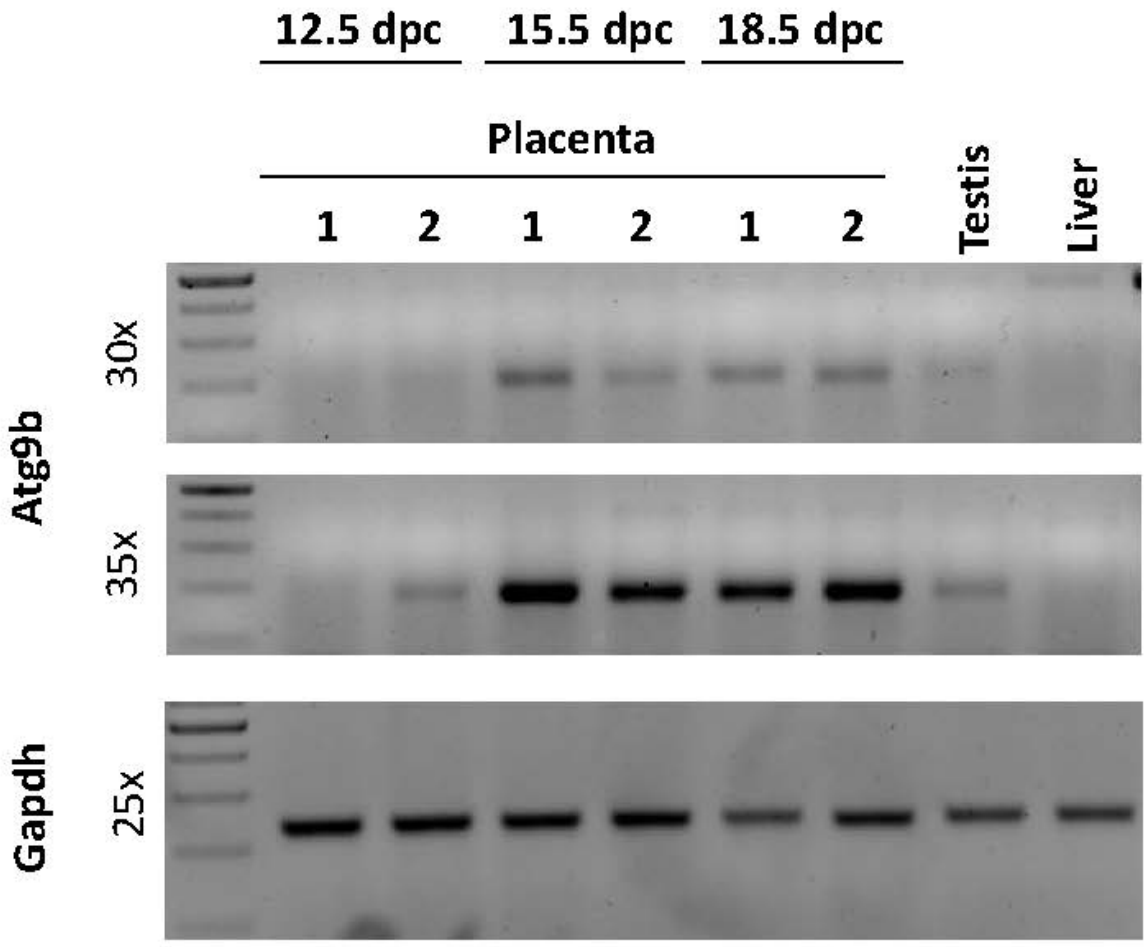

Figure 77. Atg9b expression during placental development in RNA level. Semi-quantitative RT-PCR was performed for placenta tissues. Atg9b expression was evident starting at 15.5 dpc placenta among the stages studied.

In parallel to the studies presented, we generated homozygous knock-out Atg9b mice from DEL-3 and DEL-4 to further investigate Atg9b expression patterns. Given that we established anti-ATG9B serum in our laboratory and tested with HeLa B3 cells, our goal was to perform immunoblotting using tissues from WT and Atg9b knock-out mice. The presence of an Atg9b band in WT samples and its absence in knock-out samples would provide a reliable model for the study of Atg9b expression assuming the antibody is effective in the detection of mouse Atg9b. We extended our analysis to a range of tissues, including negative controls such as the spleen and liver. The muscle tissue was considered to potentially express Atg9b due to the presence of multinucleated cells similar to those in placenta syncytiotrophoblast cells. The placenta exhibits the highest Atg9b expression, followed by the esophagus and testis according to Protein Atlas (Figure 9). However, we observed high molecular weight bands in both WT,

heterozygous, and homozygous knock-out samples. The HeLa B3 cells line was used as a positive control, and ATG9B band was detected, confirming the effectiveness of the experiment and that ineffectiveness of anti-Atg9b serum against mouse tissues. The bands that were detected proved to be nonspecific for mouse Atg9b (Figure 78).

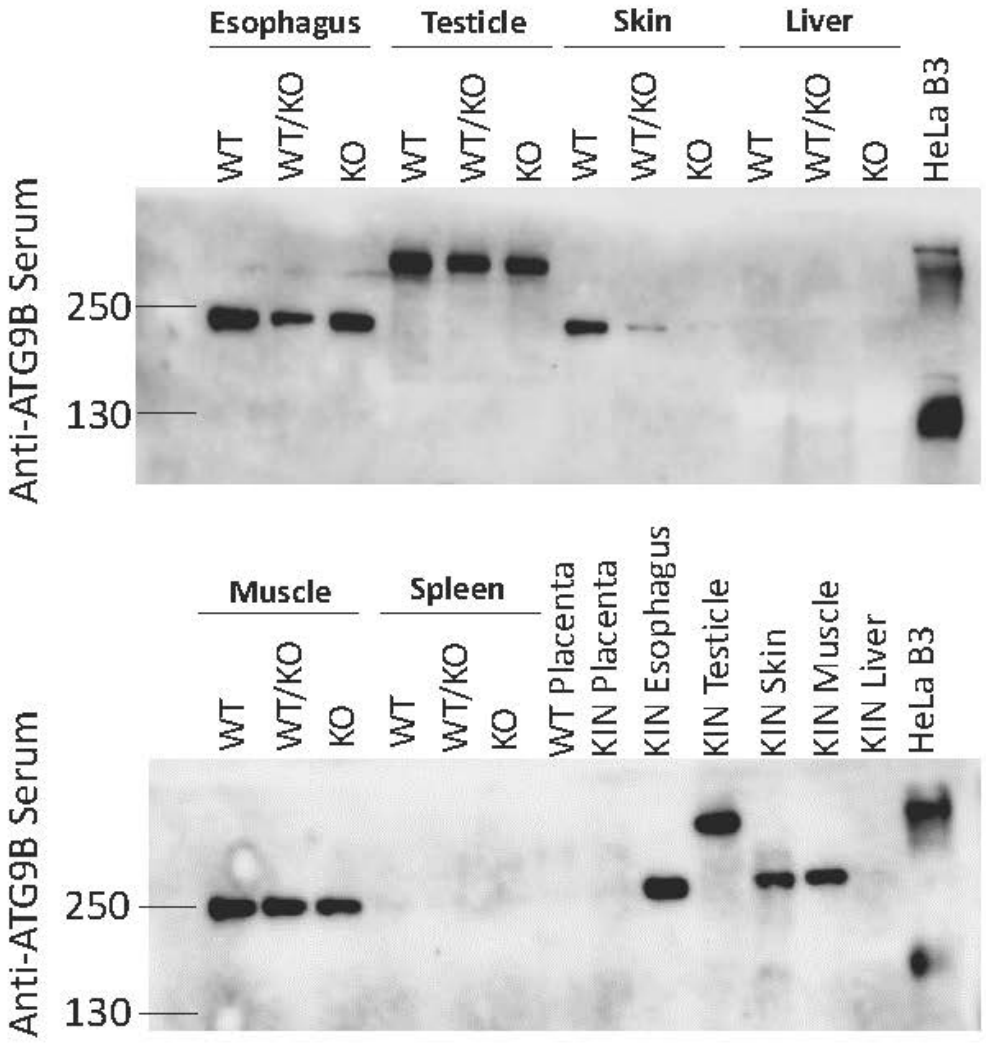

Figure 78. Atg9b expression in protein level for WT, knock-out and knock-in mouse tissues. With our knock-out model, the absence of a band that is prominent in WT tissues should indicate unequivocal evidence for expression. Only non-specific bands were observed for the mouse tissues despite the evident expression observed in HeLa B3.

We could not detect Atg9B expression at protein level through immunoblotting experiments. The most likely explanation was that anti-ATG9B antibody was ineffective in mouse tissues for the immunoblotting. The expression of the Atg9b specific to subsets of cells

such as syncytiotrophoblasts might not be sufficient for detection by immunoblotting. Yet, the antibody could work efficiently for the immunohistochemistry experiments and specifically detect the cells expressing Atg9b. Therefore, we took advantage of the Atg9b knock-out and knock-in models to investigate the tissues with the highest Atg9b expression. However, we did not observe specific ATG9B expression by immunohistochemistry, using our homemade anti-ATG9B serum (Figure 79).

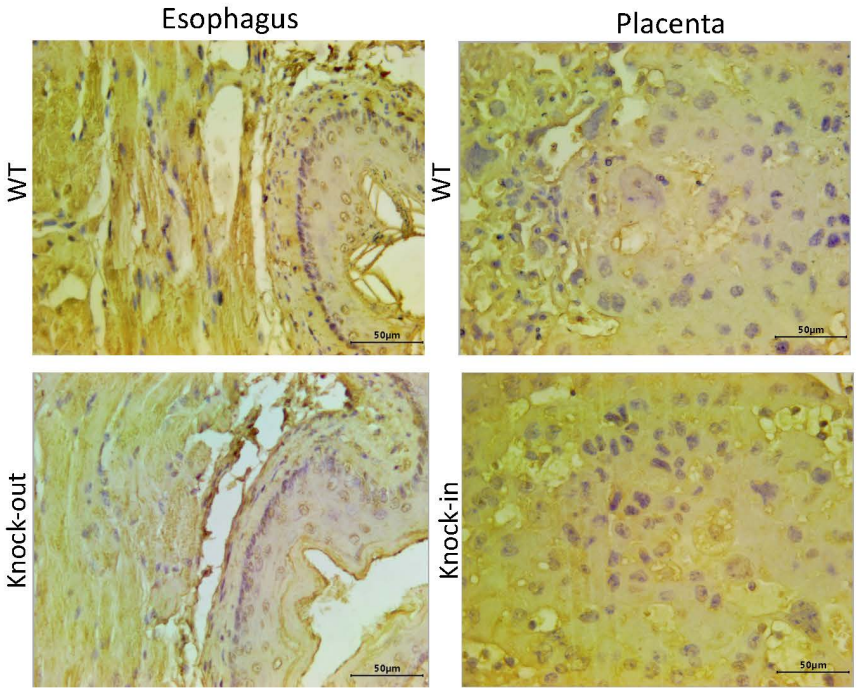

Figure 79. Immunohistochemistry staining employing anti-ATG9B serum developed in our laboratory. The staining patterns were not specific for the tissues that are stained.

As a final point, we recently focused on the Atg9b expression in the blastocysts at 3.5 dpc. Trophectoderm vs. inner cell mass decision is the first differentiation event during embryonic development specifying the cells later giving rise to the placenta (trophectoderm) and embryo (inner cell mass). Placenta trophoblast cells are differentiated from the trophectoderm (115). Therefore, we decided to investigate Atg9b expression in the blastocyst stage by anti-Atg9b serum to determine whether trophectoderm cells, encompassing the inner cell mass on the edge of the blastocyst, express Atg9b. We isolated blastocyst stage embryos after breeding WT C57BL/6 mice to determine Atg9b expression and localization by immunofluorescence microscopy. Our initial observations suggested that the trophectoderm layer specifically expresses Atg9b (Figure 80).

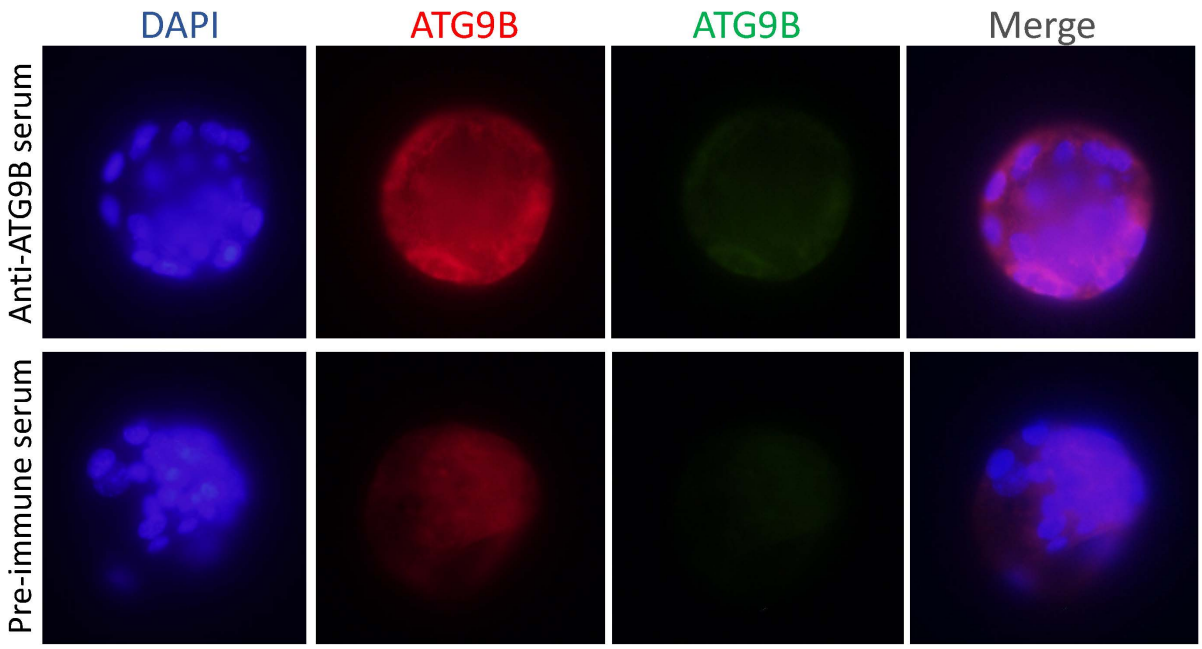

Figure 80. Atg9b protein expression in trophectoderm cells. Blastocysts were stained with homemade Atg9B antibodies. Pre-immune serum was used as a negative control and revealed no specific signal. ATG9B signal was evident in the outer trophectoderm cells of the blastocyst. Goat anti-rabbit Alexa-488 and Alexa-594 secondary antibodies were used together to detect Atg9b on both channels.

5. DISCUSSION

In this dissertation, we focused on the identification and functional validation of genetic diseases. Rare diseases, although each affecting a small fraction of the population, collectively the number of affected individuals is substantially high. Moreover, rare diseases predominantly manifest in pediatric patients and usually have a genetic background. Notably, only 15% of rare diseases currently have FDA-approved treatments. Because of the financial considerations of the drug industry, drug development efforts for rare disease have been overlooked until recently (17). The availability and affordability of whole exome sequencing techniques dramatically increased the identification of previously unknown rare genetic diseases (21).

Our research investigated three distinct families with neurodevelopmentally challenged children born to consanguineous parents, who themselves were asymptomatic.

WDR62: The first family presented a pediatric patient with microcephaly, motor-mental retardation in the proband, and lissencephaly combined with motor-mental retardation in the sibling. A novel genetic mutation, a deletion in the *WDR62* mutation was identified and validated by Sanger sequencing. The novel mutation followed the autosomal recessive inheritance pattern. The single nucleotide deletion leads to a frameshift mutation in exon 1 and subsequent deletion of the entire coding sequence. *WDR62* was first identified as a microcephaly gene and 100 pathogenic and likely pathogenic mutations were identified in the *WDR62* gene that are causative for microcephaly, lissencephaly, and abnormalities in the brain (29).

VARS1: The second family exhibited similar symptoms in their children as above. A missense mutation in the *VARS1* gene was identified and the sequence was subsequently validated. The mutation was a missense mutation causing p.T1068M alteration in protein sequence. The mutation followed an autosomal recessive inheritance pattern, the parents were heterozygous, one sibling was heterozygous, and the other sibling did not inherit the mutated allele. Extensive research on the literature involving all cytoplasmic aminoacyl tRNA synthetases was performed, with a particular focus on VARS1. Notably, mutations observed in aminoacyl tRNA synthetases predominantly localize at the enzymatic site, and the mutations within *VARS1* are also majorly concentrated in this domain. Nevertheless, in the literature, three additional mutations within a 15-nucleotide stretch of the novel mutation were identified leading us to particularly focus on this cluster of mutations (6–8). Structural modeling and web-based prediction tools were employed to assess the conservation of these amino acids and the

potentially destabilizing effects of the mutations. The publicly available crystal structure of VARS1 homologue in *Thermus thermophilus* (PDB ID 1GAX, (42)) was used as a template for modeling of the human VARS1. Given the high homology observed in amino acid alignment between human and *T. thermophilus* VARS1, the crystal structure served as a reliable template for modeling. The mutation located four amino acids away was also modeled based on the same template, reinforcing our approach (6). These mutations were located within the anticodon binding domain, on the helix-turn-helix motif, and revealed a common trend: a reduction in hydrophobic interactions. Additionally, the novel mutation resulted in the loss of a hydrogen bond, which is integral for the helix-turn-helix motif stability (98). These disturbances were predicted to compromise the stability of the protein, potentially impacting its efficiency within cellular processes. To further elucidate the consequences of the p.T1068M alteration, we conducted molecular dynamics simulations. These simulations demonstrated disturbances in the Root Mean Square Deviation (RMSD) and the loss of critical hydrogen bonds in amino acid-nucleotide interactions. Collectively, these findings suggest potential effects on the enzyme's efficiency within cellular environments. However, these results while suggestive, did not offer conclusive evidence for integration into our research paper (101).

ATG9B: The proband and his sister who displayed mental retardation, were homozygous for an 11-nt deletion mutation in exon 9 of the *ATG9B* gene. This deletion mutation was the best candidate identified by WES analysis that could potentially explain the pathologies observed in the subjects. Therefore, we cannot exclude the possibility of other genomic alterations not identified by our strategy can cause the symptoms. The deletion mutation resulted in a frameshift and was inherited with autosomal recessive pattern (asymptomatic parents, symptomatic siblings). Given the lack of previously established genetic diseases associated with *ATG9B*, and ATG9B protein remained mainly uncharacterized our focus was directed towards the characterization of this mutation and ATG9B protein. The information on the expression of ATG9B is mainly on the RNA level. To investigate ATG9B expression, we employed the cell lines of placental origin and BeWo choriocarcinoma cell line expressed the ATG9B highest confirming the literature (Protein Atlas). We adopted BeWo as an *in vitro* syncytiotrophoblast model by forskolin treatment. Our findings revealed an increase in ATG9B expression upon forskolin treatment, concomitant with an increase in hCGβ expression, a marker for syncytiotrophoblasts. Given the lack of prior studies demonstrating ATG9B expression at the protein level, we assessed ATG9B expression comparatively to the

ubiquitously expressed ATG9A. As expected, ATG9A was found to be expressed in most human cell lines, while endogenous ATG9B expression remained undetected. Consequently, we adopted ectopic expression models for our studies.

Our original research objective was to explore the expression and localization of ATG9B, comparing wild-type and truncated proteins designed to mimic the mutated human protein. To this end, we employed a variety of strategies, including different tag sequences. Notably, we observed that truncated ATG9B displayed limited expression compared to the WT variant, suggesting that the truncated protein is not expressed efficiently despite the expression on the RNA level being evident, therefore it was not due to the experimental approach which was kept identical. We successfully generated HeLa, BeWo, Hep3B, and HepG2 cells expressing ATG9B WT through lentiviral transduction, leading to the production of a monoclonal HeLa clone B3 but stable expression for truncated ATG9B was proven improbable. Therefore, for comparative immunofluorescence studies regarding the localization of the truncated protein, we proceeded with transient transfection. Our investigations revealed that ATG9B WT exhibited perinuclear localization in trans-Golgi network and distributed around the cytosol as puncta, similar to the pattern of ATG9A (66). Notably, ATG9B did not co-localize with the LC3 under nutrient-rich or starvation conditions. On the other hand, the truncated form of ATG9B was observed exclusively in perinuclear sites, localized as large puncta. Despite attempts to inhibit proteasomal degradation the truncated expression was not observed despite an increased WT expression upon the treatment. ATG9B and ATG9A colocalized suggesting they have a similar function in cells. The colocalization of ATG9B TR to ATG9A and to TGN were observed. However, in both cases vesicular abnormalities were detected, ectopic expression of ATG9B TR may result in disturbances in vesicular organization.

Recent literature suggests that yeast Atg9, human ATG9A, and ATG9B protomer structures rely on the cytosolic domains (9,65,78). The protomer structure employs the C-terminal cytoplasmic site to form lateral and central openings for bidirectional lipid movement with a hydrophobic core (65,78). The C-terminal cytoplasmic part contributes to the arch domain essential for the function of the protein as depicted in yeast Atg9 (65). Individual protomers form a homotrimer and physically interact with ATG2A to receive membrane phospholipids and exert its scramblase activity (76). In line with this recent literature, we can discuss that C-terminal deletion causes structural abnormality and stability of the protein thereby inhibiting the functional lipid scramblase activity of ATG9B.

Additionally, ATG9A is a hydrophobic protein that aggregates when subjected to sample boiling for immunoblotting assays (79). Our investigation showed that ATG9B expression is best visualized through immunoblotting when samples are treated at room temperature without heat exposure.

To comprehensively study ATG9B, it was important to develop an N-terminal ATG9B antibody for examining ATG9B expression at endogenous levels in both human cells and mouse tissues. While FLAG tags proved to be useful for ectopic expression studies, commercial ATG9B antibodies failed to detect ATG9B expression in cells, mouse tissues, and even placental tissues that exhibit the highest ATG9B expression. Therefore, we successfully produced N-terminal ATG9B antibody and conducted comparative analyses with commercial FLAG antibodies in various cell lines.

We hypothesized that the mental retardation observed in patients might originate during placental development due to placental expression of ATG9B and a variety of neuro-psychiatric diseases were linked with placental origins (103). Consequently, we aimed to examine Atg9b expression patterns in mouse placenta and various other tissues. To investigate this, we generated a transgenic knock-in mouse model to simulate the C-terminal deletion mutation. Typically, by 18.5 dpc, the placenta gets smaller due to regression, in the process of preparation for birth (107). We observed initially that the volume of the homozygous placenta was higher indicating underdevelopment and maturation. Subsequent histomorphometric analysis indicated a significant enlargement of the maternal decidua in the homozygous placenta, although the difference was smaller when heterozygous samples were taken into consideration. Maternal decidua is responsible of the protection of the fetus physically and by immune cells against maternal infections and immune cell attacks, and contributes to nutrient exchange and hormone regulation (109).

Considering that patients exhibit mental retardation; we designed a series of cognitive tests to compare WT and *Atg9b* mutant mice. These tests revealed that knock-in mice exhibited reduced fear memory a response that involves both amygdala and hippocampus, and no abnormalities were detected in other tests measuring anxiety and memory (114).

To evaluate Atg9b expression in mouse placenta and other tissues, we employed FLAG-Atg9b transgenic animals and conducted immunoblotting and histological analyses using anti-FLAG polyclonal antibody. Our findings showed that Atg9b is expressed in the junctional zone harboring spongiotrophoblast cells of mature placenta at 15.5 dpc. This finding was

subsequently supported by RT-PCR data, which indicated Atg9b expression in 15.5 dpc and 18.5 dpc placenta tissues, albeit at lower levels, in testis. Despite our significant efforts to optimize immunofluorescence experiments in tissue sections we did not obtain reproducibility for our data, possibly due to the ineffectiveness of anti-FLAG antibody and expertise in histology. Recently we adopted to study the Atg9b expression in mouse blastocysts to assess the expression in trophectoderm cells that are the precursor for placental trophoblasts by immunofluorescence (115). Our initial observations suggest the expression specific to the trophectoderm layer. Autophagy is first observed in the fertilized egg and crucial for embryonic development since the knock-out of autophagy genes often result in embryonic death. Therefore, this experiment is an important observation and needs to be elucidated further on the early development.

The generation of the Atg9b knock-out mouse model provided an excellent model for characterizing Atg9b in mice. Having generated anti-ATG9B antibody, we decided to determine Atg9b expression in a variety of tissues from knock-in, knock-out, and WT mice. However, while Atg9b expression was expected to be completely absent due to exon 2 deletion in the knock-out model, immunoblotting experiments failed to reveal a specific Atg9b band with our antibody rendering the subsequent characterizations with immunoblotting unproductive.

It is important to state that the mouse models generated in this thesis were viable, successfully reached adulthood, and were fertile, with the ability to give rise to the next generation.

One challenge encountered during our investigation was the undetectability of ATG9B in the placenta. Given the challenges associated with detecting Atg9b expression through immunoblotting, we planned co-immunoprecipitation experiments employing the anti-ATG9B serum. This approach would allow us to concentrate the protein and facilitate a more comprehensive understanding of its interactions with other proteins and organelle markers. Another significant difficulty was the instability of the mutated protein, even upon ectopic experiments. The phenotypes in the mice models revealed milder effects than initially anticipated, even in the case of knock-out mice.

The studies conducted in this thesis extended beyond the identification of novel mutations, by structural and functional characterization of the effects of these mutations to evaluate their impacts on the observed clinical findings. Notably, our findings on ATG9B were

undertaken with limited information available in the literature. Thus, we aimed to enrich the literature on the function of ATG9B with the starting point of the human mutation. We demonstrated the C-terminal deletion likely caused protein instability and reduced ATG9B expression dramatically. The RNA level expression of ATG9B upon *in vitro* syncytialization model was increased. We demonstrated the differences between the WT and truncated ATG9B protein cellular trafficking by transient and stable cell models. By transgenic mouse models, we showed Atg9b expression on the placenta at different developmental stages in RNA level. Finally, we demonstrated behavioral abnormalities arising from the mutation. Therefore, we provide a comprehensive input to the literature by identification and characterization of a novel disease and on ATG9B by *in vivo* and *in vitro* studies.

6. CONCLUSION AND FUTURE PERSPECTIVES

The objectives investigated in this thesis have been successfully addressed, and the research presented by this work is characterized by its originality, lack of derivation, or repetition. This project unraveled two novel mutations of the genes (*WDR62, VARS1*) that are previously associated with the presented symptoms. Moreover, we have identified one novel mutation for a gene previously unlinked with genetic diseases for neurodevelopmental disorders (*ATG9B*). This work represents a novel contribution to the field of molecular biology, rare genetic disease, and genetically modified mouse model fields.

In the context of molecular biology and transgenic models, structural assessments regarding WT and truncated ATG9B should be pursued by cryo-electron microscopy and *in-silico* modeling studies. *In vitro* approaches of the mutation-derived C-terminal deletion on lipid scramblase activity should be studied. Additionally, co-immunoprecipitation experiments to elucidate the interaction of ATG9B with ATG2A and the effect of the truncation should be explored. The expression of Atg9b in early placenta and embryonic development should be elucidated. Reproducible and efficient histology protocols should be optimized to determine placental abnormalities and the effects of Atg9b expression, and the genetic disease in placenta should be characterized in more detail.

Notably, our research has demonstrated that Atg9b is not essential for mice in terms of survival, as the viability, growth, and fertility of the mice were unaffected in knock-in or knock-out models. Moreover, the observed phenotypic effects were milder than originally anticipated.

Although ATG9B was initially identified as an ATG9A homolog, recent studies have begun to suggest that ATG9B may have distinct functions within cells, particularly in the context of colorectal cancer, the effect on focal adhesions and invasion mechanisms. ATG9A and subsequently ATG9B have also been shown to function as lipid scramblases, a role that extends beyond autophagy to encompass lipid-related membrane trafficking within cells such as plasma membrane repair. From this perspective, it is becoming increasingly clear that the roles of both ATG9B and ATG9A are not confined to autophagy alone, and further exploration is needed in various cellular events, including membrane repair, viral defense mechanisms, blood coagulation, apoptosis, cell signaling processes in which lipid scramblases function.

In summary, we have delivered comprehensive research related to the rare genetic diseases, the development of transgenic mouse models, and the enrichment of the ATG9B literature. This work stands as an important and original contribution to the field of molecular biology.

7. REFERENCES

1. Lim NR, Yeap YYC, Zhao TT, Yip YY, Wong SC, Xu D, et al. Opposing roles for JNK and Aurora A in regulating the association of WDR62 with spindle microtubules. J Cell Sci [Internet]. 2015 Feb 1 [cited 2023 Aug 25];128(3):527–40. Available from: https://dx.doi.org/10.1242/jcs.157537
2. Xu D, Zhang F, Wang Y, Sun Y, Xu Z. Microcephaly-Associated Protein WDR62 Regulates Neurogenesis through JNK1 in the Developing Neocortex. Cell Rep. 2014 Jan 16;6(1):104–16.
3. Bolat H, Sağer SG, Türkyllmaz A, Çebi AH, Akln Y, Onay H, et al. Autosomal Recessive Primary Microcephaly (MCPH) and Novel Pathogenic Variants in ASPM and WDR62 Genes. Mol Syndromol. 2022;363–9.
4. Pang L, Weeks SD, Van Aerschot A. Aminoacyl-tRNA Synthetases as Valuable Targets for Antimicrobial Drug Discovery. Int J Mol Sci 2021, Vol 22, Page 1750 [Internet]. 2021 Feb 10 [cited 2023 Aug 27];22(4):1750. Available from: https://www.mdpi.com/1422-0067/22/4/1750/htm
5. Antonellis A, Green ED. The role of aminoacyl-tRNA synthetases in genetic diseases. Annu Rev Genomics Hum Genet. 2008;9:87–107.
6. Stephen J, Nampoothiri S, Banerjee A, Tolman NJ, Penninger JM, Elling U, et al. Loss of function mutations in VARS encoding cytoplasmic valyl-tRNA synthetase cause microcephaly, seizures, and progressive cerebral atrophy. Hum Genet [Internet]. 2018 Apr 1 [cited 2023 Aug 29];137(4):293–303. Available from: /pmc/articles/PMC7251970/
7. Siekierska A, Stamberger H, Deconinck T, Oprescu SN, Partoens M, Zhang Y, et al. Biallelic VARS variants cause developmental encephalopathy with microcephaly that is recapitulated in vars knockout zebrafish. Nat Commun [Internet]. 2019 Dec 1 [cited 2023 Aug 29];10(1). Available from: https://pubmed.ncbi.nlm.nih.gov/30755616/
8. Karaca E, Harel T, Pehlivan D, Jhangiani SN, Gambin T, Coban Akdemir Z, et al. Genes that Affect Brain Structure and Function Identified by Rare Variant Analyses of Mendelian Neurologic Disease. Neuron [Internet]. 2015 Nov 4 [cited 2023 Aug 29];88(3):499–513. Available from: http://www.cell.com/article/S0896627315008375/fulltext
9. Chiduza GN, Garza-Garcia A, Almacellas E, De Tito S, Pye VE, van Vliet AR, et al.

ATG9B is a tissue-specific homotrimeric lipid scramblase that can compensate for ATG9A. Autophagy [Internet]. 2023 Nov 8 [cited 2023 Nov 14]; Available from: https://www.tandfonline.com/doi/full/10.1080/15548627.2023.2275905

10. Yamada T, Carson AR, Caniggia I, Umebayashi K, Yoshimori T, Nakabayashi K, et al. Endothelial Nitric-oxide Synthase Antisense (*NOS3AS*) Gene Encodes an Autophagy-related Protein (APG9-like2) Highly Expressed in Trophoblast. J Biol Chem [Internet]. 2005 May 6 [cited 2020 Apr 18];280(18):18283–90. Available from: http://www.jbc.org/lookup/doi/10.1074/jbc.M413957200
11. Parzych KR, Klionsky DJ. An Overview of Autophagy: Morphology, Mechanism, and Regulation. Antioxid Redox Signal [Internet]. 2014 Jan 1 [cited 2023 Nov 12];20(3):460. Available from: /pmc/articles/PMC3894687/
12. Sawa-Makarska J, Baumann V, Coudevylle N, von Bülow S, Nogellova V, Abert C, et al. Reconstitution of autophagosome nucleation defines Atg9 vesicles as seeds for membrane formation. Science (80-) [Internet]. 2020 Sep 4 [cited 2022 Apr 17];369(6508). Available from: https://www.science.org/doi/abs/10.1126/science.aaz7714
13. Maeda S, Yamamoto H, Kinch LN, Garza CM, Takahashi S, Otomo C, et al. Structure, lipid scrambling activity and role in autophagosome formation of ATG9A. Nat Struct Mol Biol 2020 2712 [Internet]. 2020 Oct 26 [cited 2023 Nov 12];27(12):1194–201. Available from: https://www.nature.com/articles/s41594-020-00520-2
14. Mehrabi Pour M, Nasiri M, Kamfiroozie H, Zibaeenezhad MJ. Association of the ATG9B gene polymorphisms with coronary artery disease susceptibility: A case-control study. J Cardiovasc Thorac Res [Internet]. 2019 Jun 25 [cited 2020 Nov 12];11(2):109–15. Available from: https://pubmed.ncbi.nlm.nih.gov/31384404/
15. Kang MR, Kim MS, Oh JE, Kim YR, Song SY, Kim SS, et al. Frameshift mutations of autophagy-related genes ATG2B, ATG5, ATG9B and ATGI2 in gastric and colorectal cancers with microsatellite instability. J Pathol [Internet]. 2009 Apr [cited 2020 Nov 12];217(5):702–6. Available from: https://pubmed.ncbi.nlm.nih.gov/19197948/
16. Koçkaya G, Atalay S, Oğuzhan G, Kurnaz M, Ökçün S, Sar Gedik Ç, et al. Analysis of patient access to orphan drugs in Turkey. Orphanet J Rare Dis [Internet]. 2021 Dec 1 [cited 2023 Aug 16];16(1):1–8. Available from: https://ojrd.biomedcentral.com/articles/10.1186/s13023-021-01718-3

17. Nguengang Wakap S, Lambert DM, Olry A, Rodwell C, Gueydan C, Lanneau V, et al. Estimating cumulative point prevalence of rare diseases: analysis of the Orphanet database. Eur J Hum Genet [Internet]. 2020 [cited 2023 Aug 16];28:165–73. Available from: https://doi.org/10.1038/s41431-019-0508-0
18. Deniz PAK GÜRE M, İnce Ö. Examining of Health Policy in Rare Diseases in Terms of Historical Perspective in Turkey. J Int Heal Sci Manag [Internet]. 2021 [cited 2023 Aug 17];7(14):62–71. Available from: https://10.0.187.249/jihsam.874683
19. P Mitchell AE, Mohammadian Khonsari N, Ozbek U, Ng HO, Dogan AO, Iseri US. Obstacles and expectations of rare disease patients and their families in Türkiye: ISTisNA project survey results.
20. Retterer K, Juusola J, Cho MT, Vitazka P, Millan F, Gibellini F, et al. Clinical application of whole-exome sequencing across clinical indications. Genet Med 2016 187 [Internet]. 2015 Dec 3 [cited 2023 Aug 20];18(7):696–704. Available from: https://www.nature.com/articles/gim2015148
21. Marwaha S, Knowles JW, Ashley EA. A guide for the diagnosis of rare and undiagnosed disease: beyond the exome. Genome Med 2022 141 [Internet]. 2022 Feb 28 [cited 2023 Aug 20];14(1):1–22. Available from: https://genomemedicine.biomedcentral.com/articles/10.1186/s13073-022-01026-w
22. Flicek P, Amode MR, Barrell D, Beal K, Billis K, Brent S, et al. Ensembl 2014. Nucleic Acids Res [Internet]. 2014 Jan 1 [cited 2023 Aug 23];42(D1):D749–55. Available from: https://dx.doi.org/10.1093/nar/gkt1196
23. Shohayeb B, Lim NR, Ho U, Xu Z, Dottori M, Quinn L, et al. The Role of WD40-Repeat Protein 62 (MCPH2) in Brain Growth: Diverse Molecular and Cellular Mechanisms Required for Cortical Development. Mol Neurobiol [Internet]. 2018 Jul 1 [cited 2023 Aug 22];55(7):5409–24. Available from: https://pubmed.ncbi.nlm.nih.gov/28940170/
24. Cohen-Katsenelson K, Wasserman T, Darlyuk-Saadon I, Rabner A, Glaser F, Aronheim A. Identification and Analysis of a Novel Dimerization Domain Shared by Various Members of c-Jun N-terminal Kinase (JNK) Scaffold Proteins. J Biol Chem [Internet]. 2013 Mar 3 [cited 2023 Aug 25];288(10):7294. Available from: /pmc/articles/PMC3591637/
25. Morrison DK. MAP Kinase Pathways. Cold Spring Harb Perspect Biol [Internet]. 2012

Nov 1 [cited 2023 Aug 25];4(11):a011254. Available from: http://cshperspectives.cshlp.org/content/4/11/a011254.full

26. Wasserman T, Katsenelson K, Daniliuc S, Hasin T, Choder M, Aronheim A. A novel c-Jun N-terminal kinase (JNK)-binding protein WDR62 is recruited to stress granules and mediates a nonclassical JNK activation. Mol Biol Cell [Internet]. 2010 Jan 1 [cited 2023 Aug 25];21(1):117–30. Available from: https://www.molbiolcell.org/doi/10.1091/mbc.e09-06-0512
27. Huang J, Liang Z, Guan C, Hua S, Jiang K. Wdr62 regulates spindle dynamics as an adaptor protein between tpx2/aurora a and katanin. J Cell Biol. 2021 Aug 2;220(8).
28. Guerreiro A, De Sousa F, Liaudet N, Ivanova D, Eskat A, Meraldi P. Wdr62 localizes katanin at spindle poles to ensure synchronous chromosome segregation. J Cell Biol. 2021 Aug 2;220(8).
29. Landrum MJ, Lee JM, Benson M, Brown GR, Chao C, Chitipiralla S, et al. ClinVar: improving access to variant interpretations and supporting evidence. Nucleic Acids Res [Internet]. 2018 Jan 4 [cited 2023 Aug 23];46(D1):D1062–7. Available from: https://dx.doi.org/10.1093/nar/gkx1153
30. Roberts E, Jackson AP, Carradice AC, Deeble VJ, Mannan J, Rashid Y, et al. The second locus for autosomal recessive primary microcephaly (MCPH2) maps to chromosome 19q13.1-13.2. Eur J Hum Genet [Internet]. 1999 Oct [cited 2023 Aug 23];7(7):815–20. Available from: https://pubmed.ncbi.nlm.nih.gov/10573015/
31. Bilgüvar K, Öztürk AK, Louvi A, Kwan KY, Choi M, Tatli B, et al. Whole-exome sequencing identifies recessive WDR62 mutations in severe brain malformations. Nature [Internet]. 2010 Sep 9 [cited 2023 Nov 14];467(7312):207–10. Available from: https://pubmed.ncbi.nlm.nih.gov/20729831/
32. Murdock DR, Clark GD, Bainbridge MN, Newsham I, Wu Y, Muzny DM, et al. Whole-Exome Sequencing Identifies Compound Heterozygous Mutations in WDR62 in Siblings With Recurrent Polymicrogyria. 2011;(August):2071–7.
33. Yu TW, Mochida GH, Tischfield DJ, Sgaier SK, Flores-sarnat L, Sergi CM, et al. Mutations in WDR62 , encoding a centrosome-associated protein , cause microcephaly with simplified gyri and abnormal cortical architecture. Nat Publ Gr [Internet]. 2010;42(11):1015–20. Available from: http://dx.doi.org/10.1038/ng.683
34. Sergi C, Zoubaa S, Schiesser M. Norman-Roberts syndrome: Prenatal diagnosis and

autopsy findings. Prenat Diagn. 2000;20(6):505–9.

35. Bhat V, Girimaji S, Mohan G, Arvinda H, Singhmar P, Duvvari M, et al. Mutations in WDR62, encoding a centrosomal and nuclear protein, in Indian primary microcephaly families with cortical malformations. Clin Genet. 2011;80(6):532–40.

36. Nicholas AK, Khurshid M, Désir J, Carvalho OP, Cox JJ, Thornton G, et al. WDR62 is associated with the spindle pole and is mutated in human microcephaly. Nat Publ Gr [Internet]. 2010;42(11):1010–4. Available from: http://dx.doi.org/10.1038/ng.682

37. Xu D, Zhi Y, Liu X, Guan L, Yu J, Zhang D, et al. WDR62-deficiency Causes Autism-like Behaviors Independent of Microcephaly in Mice. Neurosci Bull [Internet]. 2022;(0123456789). Available from: https://doi.org/10.1007/s12264-022-00997-5

38. Hao L, Ma J, Wu F, Ma X, Qian M, Sheng W, et al. WDR62 variants contribute to congenital heart disease by inhibiting cardiomyocyte proliferation. Clin Transl Med [Internet]. 2022 Jul [cited 2023 Aug 25];12(7). Available from: /pmc/articles/PMC9270576/

39. Wu J, Yu P, Jin X, Xu X, Li J, Li Z, et al. Genomic landscapes of Chinese sporadic autism spectrum disorders revealed by whole-genome sequencing. J Genet Genomics [Internet]. 2018 Oct 20 [cited 2023 Aug 25];45(10):527–38. Available from: https://pubmed.ncbi.nlm.nih.gov/30392784/

40. Gomez MAR, Ibba M. Aminoacyl-tRNA synthetases. RNA [Internet]. 2020 Aug 1 [cited 2023 Aug 27];26(8):910–36. Available from: http://rnajournal.cshlp.org/content/26/8/910.full

41. Nureki O, Yokoyama S. Valyl-tRNA Synthetases. 2013 [cited 2023 Aug 29]; Available from: https://www.ncbi.nlm.nih.gov/books/NBK6028/

42. Fukai S, Nureki O, Sekine S ichi, Shimada A, Tao J, Vassylyev DG, et al. Structural basis for double-sieve discrimination of L-valine from L-isoleucine and L-threonine by the complex of tRNA(Val) and valyl-tRNA synthetase. Cell [Internet]. 2000 Nov 22 [cited 2023 Sep 5];103(5):793–803. Available from: http://www.cell.com/article/S0092867400001823/fulltext

43. Orenstein N, Weiss K, Oprescu SN, Shapira R, Kidron D, Vanagaite-Basel L, et al. Bi-allelic IARS mutations in a child with intra-uterine growth retardation, neonatal cholestasis, and mild developmental delay. Clin Genet. 2017 Jun 1;91(6):913–7.

44. Kopajtich R, Murayama K, Janecke AR, Haack TB, Breuer M, Knisely AS, et al.

Biallelic IARS Mutations Cause Growth Retardation with Prenatal Onset, Intellectual Disability, Muscular Hypotonia, and Infantile Hepatopathy. Am J Hum Genet. 2016 Aug 4;99(2):414–22.

45. Smigiel R, Biela M, Biernacka A, Stembalska A, Sasiadek M, Kosinska J, et al. New evidence for association of recessive IARS gene mutations with hepatopathy, hypotonia, intellectual disability and growth retardation. Clin Genet. 2017 Dec 1;92(6):671–3.
46. Watanabe M, Shishido K, Kanehira N, Hiura K, Nakano K, Okamura T, et al. Molecular and Pathological Analyses of IARS1-Deficient Mice: An IARS Disorder Model. Int J Mol Sci. 2023 Apr 1;24(8).
47. Simons C, Griffin LB, Helman G, Golas G, Pizzino A, Bloom M, et al. Loss-of-function alanyl-tRNA synthetase mutations cause an autosomal-recessive early-onset epileptic encephalopathy with persistent myelination defect. Am J Hum Genet. 2015 Apr 2;96(4):675–81.
48. Nakayama T, Wu J, Galvin-Parton P, Weiss J, Andriola MR, Hill RS, et al. Deficient activity of alanyl-tRNA synthetase underlies an autosomal recessive syndrome of progressive microcephaly, hypomyelination, and epileptic encephalopathy. Hum Mutat. 2017 Oct 1;38(10):1348–54.
49. McLaughlin HM, Sakaguchi R, Giblin W, Wilson TE, Biesecker L, Lupski JR, et al. A recurrent loss-of-function alanyl-tRNA synthetase (AARS) mutation in patients with charcot-marie-tooth disease type 2N (CMT2N). Hum Mutat. 2012 Jan;33(1):244–53.
50. Friedman J, Smith DE, Issa MY, Stanley V, Wang R, Mendes MI, et al. Biallelic mutations in valyl-tRNA synthetase gene VARS are associated with a progressive neurodevelopmental epileptic encephalopathy. Nat Commun 2019 101 [Internet]. 2019 Feb 12 [cited 2023 Aug 29];10(1):1–10. Available from: https://www.nature.com/articles/s41467-018-07067-3
51. Shibutani ST, Saitoh T, Nowag H, Münz C, Yoshimori T. Autophagy and autophagy-related proteins in the immune system. Nat Immunol. 2015;16(10):1014–24.
52. Oral O, Yedier O, Kilic S, Gozuacik D. Involvement of autophagy in T cell biology. Histol Histopathol [Internet]. 2017 Jan 1 [cited 2020 Nov 8];32(1):11–20. Available from: https://pubmed.ncbi.nlm.nih.gov/27225864/
53. Nakatogawa H. Two ubiquitin-like conjugation systems that mediate membrane

formation during autophagy. Essays Biochem [Internet]. 2013 Sep 27 [cited 2020 Dec 14];55(1):39–50. Available from: /essaysbiochem/article/doi/10.1042/bse0550039/78221/Two-ubiquitin-like-conjugation-systems-that

54. Nair U, Klionsky DJ. Autophagosome biogenesis requires SNAREs. Autophagy [Internet]. 2011 Dec 28 [cited 2020 Apr 19];7(12):1570–2. Available from: http://www.tandfonline.com/doi/abs/10.4161/auto.7.12.18001

55. Noda T, Kim J, Huang WP, Baba M, Tokunaga C, Ohsumi Y, et al. Apg9p/Cvt7p is an integral membrane protein required for transport vesicle formation in the Cvt and autophagy pathways. J Cell Biol. 2000 Feb 7;148(3):465–79.

56. Reggiori F, Shintani T, Nair U, Klionsky DJ. Atg9 cycles between mitochondria and the pre-autophagosomal structure in yeasts. Autophagy [Internet]. 2005 Jul 5 [cited 2020 Apr 18];1(2):101–9. Available from: http://www.tandfonline.com/doi/abs/10.4161/auto.1.2.1840

57. Bialik S, Pietrokovski S, Kimchi A. Myosin drives autophagy in a pathway linking Atg1 to Atg9. EMBO J [Internet]. 2011 Feb 16 [cited 2020 Apr 19];30(4):629–30. Available from: http://emboj.embopress.org/cgi/doi/10.1038/emboj.2011.8

58. Reggiori F, Tucker KA, Stromhaug PE, Klionsky DJ. The Atg1-Atg13 Complex Regulates Atg9 and Atg23 Retrieval Transport from the Pre-Autophagosomal Structure sequestration of the cargo by a cytosolic double-mem-brane vesicle that delivers it into the lysosome/vacuole interior for destruction (Ogier-Denis a. Vol. 6, Developmental Cell. 2004.

59. Reggiori F, Klionsky DJ. Atg9 sorting from mitochondria is impaired in early secretion and VFT-complex mutants in Saccharomyces cerevisiae. J Cell Sci. 2006 Jul 15;119(14):2903–11.

60. Yamamoto H, Kakuta S, Watanabe TM, Kitamura A, Sekito T, Kondo-Kakuta C, et al. Atg9 vesicles are an important membrane source during early steps of autophagosome formation. J Cell Biol. 2012 Jul 23;198(2):219–33.

61. Kakuta S, Yamamoto H, Negishi L, Kondo-Kakuta C, Hayashi N, Ohsumi Y. Atg9 vesicles recruit vesicle-tethering proteins Trs85 and Ypt1 to the autophagosome formation site. J Biol Chem. 2012 Dec 28;287(53):44261–9.

62. He C, Baba M, Cao Y, Klionsky DJ. Self-interaction is critical for Atg9 transport and

function at the phagophore assembly site during autophagy. Mol Biol Cell. 2008 Dec 1;19(12):5506–16.

63. Wang K, Yang Z, Liu X, Mao K, Nair U, Klionsky DJ. Phosphatidylinositol 4-kinases are required for autophagic membrane trafficking. J Biol Chem [Internet]. 2012 Nov 2 [cited 2020 Apr 20];287(45):37964–72. Available from: http://www.ncbi.nlm.nih.gov/pubmed/22977244

64. Papinski D, Schuschnig M, Reiter W, Wilhelm L, Barnes CA, Maiolica A, et al. Early Steps in Autophagy Depend on Direct Phosphorylation of Atg9 by the Atg1 Kinase. Mol Cell. 2014 Feb 6;53(3):471–83.

65. Matoba K, Kotani T, Tsutsumi A, Tsuji T, Mori T, Noshiro D, et al. Atg9 is a lipid scramblase that mediates autophagosomal membrane expansion. Nat Struct Mol Biol 2020 2712 [Internet]. 2020 Oct 26 [cited 2023 Nov 12];27(12):1185–93. Available from: https://www.nature.com/articles/s41594-020-00518-w

66. Young ARJ, Chan EYW, Hu XW, Köchl R, Crawshaw SG, High S, et al. Starvation and ULK1-dependent cycling of mammalian Atg9 between the TGN and endosomes. J Cell Sci. 2006 Sep 15;119(18):3888–900.

67. Webber JL, Tooze SA. Coordinated regulation of autophagy by p38α MAPK through mAtg9 and p38IP. EMBO J [Internet]. 2010 Jan 6 [cited 2020 Apr 19];29(1):27–40. Available from: http://emboj.embopress.org/cgi/doi/10.1038/emboj.2009.321

68. De Pace R, Skirzewski M, Damme M, Mattera R, Mercurio J, Foster AM, et al. Altered distribution of ATG9A and accumulation of axonal aggregates in neurons from a mouse model of AP-4 deficiency syndrome. PLoS Genet [Internet]. 2018 Apr 1 [cited 2020 Oct 1];14(4). Available from: https://pubmed.ncbi.nlm.nih.gov/29698489/

69. Takahashi Y, Meyerkord CL, Wang HG. BARgaining membranes for autophagosome formation: Regulation of autophagy and tumorigenesis by Bif-1/Endophilin B1. Autophagy. 2008 Jan 1;4(1):121–4.

70. De Tito S, Hervás JH, Van Vliet AR, Tooze SA. The Golgi as an Assembly Line to the Autophagosome. Trends Biochem Sci [Internet]. 2020 [cited 2020 Nov 14];45:484–96. Available from: https://doi.org/10.1016/j.tibs.2020.03.010

71. Weerasekara VK, Panek DJ, Broadbent DG, Mortenson JB, Mathis AD, Logan GN, et al. Metabolic-Stress-Induced Rearrangement of the 14-3-3 Interactome Promotes Autophagy via a ULK1- and AMPK-Regulated 14-3-3 Interaction with

Phosphorylated Atg9. Mol Cell Biol. 2014 Dec 15;34(24):4379–88.

72. Judith D, Jefferies HBJ, Boeing S, Frith D, Snijders AP, Tooze SA. ATG9A shapes the forming autophagosome through Arfaptin 2 and phosphatidylinositol 4-kinase IIIβ. J Cell Biol. 2019 May 1;218(5):1634–52.

73. Orsi A, Razi M, Dooley HC, Robinson D, Weston AE, Collinson LM, et al. Dynamic and transient interactions of Atg9 with autophagosomes, but not membrane integration, are required for autophagy. Mol Biol Cell. 2012 May 15;23(10):1860–73.

74. Guardia CM, Christenson ET, Zhou W, Tan X-F, Lian T, Faraldo-Gómez JD, et al. The structure of human ATG9A and its interplay with the lipid bilayer. Autophagy [Internet]. 2020 Dec 1 [cited 2023 Aug 30];16(12):2292–3. Available from: https://www.tandfonline.com/action/journalInformation?journalCode=kaup20

75. Guardia CM, Tan XF, Lian T, Rana MS, Zhou W, Christenson ET, et al. Structure of Human ATG9A, the Only Transmembrane Protein of the Core Autophagy Machinery. Cell Rep [Internet]. 2020 Jun 30 [cited 2023 Nov 13];31(13):107837. Available from: http://www.cell.com/article/S2211124720308184/fulltext

76. van Vliet AR, Chiduza GN, Maslen SL, Pye VE, Joshi D, De Tito S, et al. ATG9A and ATG2A form a heteromeric complex essential for autophagosome formation. Mol Cell [Internet]. 2022 Nov 17 [cited 2023 Aug 30];82(22):4324-4339.e8. Available from: http://www.cell.com/article/S1097276522010176/fulltext

77. Claude-Taupin A, Jia J, Bhujabal Z, Garfa-Traoré M, Kumar S, da Silva GPD, et al. ATG9A protects the plasma membrane from programmed and incidental permeabilization. Nat Cell Biol [Internet]. 2021 Jul 12 [cited 2023 Aug 30];23(8):846–58. Available from: https://www.nature.com/articles/s41556-021-00706-w

78. Mailler E, Guardia CM, Bai X, Jarnik M, Williamson CD, Li Y, et al. The autophagy protein ATG9A enables lipid mobilization from lipid droplets. Nat Commun 2021 121 [Internet]. 2021 Nov 19 [cited 2023 Aug 30];12(1):1–19. Available from: https://www.nature.com/articles/s41467-021-26999-x

79. van Vliet AR, De Tito S, Almacellas E, Tooze SA. Imaging ATG9A, a Multi-Spanning Membrane Protein. J Vis Exp [Internet]. 2023 Jun 16 [cited 2023 Sep 11];(196). Available from: https://www.crick.ac.uk/research/publications/imaging-atg9a-a-multi-spanning-membrane-protein

80. Luo Q, Liu Q, Cheng H, Wang J, Zhao T, Zhang J, et al. Nondegradable ubiquitinated

ATG9A organizes Golgi integrity and dynamics upon stresses. Cell Rep [Internet]. 2022 Aug 16 [cited 2023 Aug 30];40(7). Available from: http://www.cell.com/article/S2211124722010129/fulltext

81. Zhong Y, Long T, Gu CS, Tang JY, Gao LF, Zhu JX, et al. MYH9-dependent polarization of ATG9B promotes colorectal cancer metastasis by accelerating focal adhesion assembly. Cell Death Differ [Internet]. 2021 Jun 15 [cited 2023 Aug 30];28(12):3251–69. Available from: https://www.nature.com/articles/s41418-021-00813-z
82. Mizushima N, Levine B. Autophagy in mammalian development and differentiation. Vol. 12, Nature Cell Biology. Nature Publishing Group; 2010. p. 823–30.
83. Kuma A, Komatsu M, Mizushima N. Autophagy-monitoring and autophagy-deficient mice. Vol. 13, Autophagy. Taylor and Francis Inc.; 2017. p. 1619–28.
84. Benirschke K, Kaufmann P. Pathology of the human placenta. 2000 [cited 2023 Oct 17];947. Available from: https://books.google.com/books/about/Pathology_of_the_Human_Placenta.html?id=NR1Pcv4Dxs4C
85. Moore KL, Persaud TVN, Torchia MG. The developing human : clinically oriented embryology. 2008 [cited 2023 Oct 17];522. Available from: https://books.google.com/books/about/The_Developing_Human.html?id=TQcpAQAAMAAJ
86. Cole LA. Implantation and Pregnancy Failure. Biol Life. 2016;157–61.
87. Baschat AA. Neurodevelopment following fetal growth restriction and its relationship with antepartum parameters of placental dysfunction. Ultrasound Obstet Gynecol [Internet]. 2011 May [cited 2023 Oct 17];37(5):501–14. Available from: https://pubmed.ncbi.nlm.nih.gov/21520312/
88. Nardozza LMM, Caetano ACR, Zamarian ACP, Mazzola JB, Silva CP, Marçal VMG, et al. Fetal growth restriction: current knowledge. Arch Gynecol Obstet [Internet]. 2017 May 1 [cited 2023 Oct 17];295(5):1061–77. Available from: https://pubmed.ncbi.nlm.nih.gov/28285426/
89. Saito S, Nakashima A. Review: The role of autophagy in extravillous trophoblast function under hypoxia. Placenta [Internet]. 2013;34(SUPPL):S79–84. Available from: http://dx.doi.org/10.1016/j.placenta.2012.11.026

90. Komatsu M, Waguri S, Ueno T, Iwata J, Murata S, Tanida I, et al. Impairment of starvation-induced and constitutive autophagy in Atg7-deficient mice. J Cell Biol [Internet]. 2005 May 9 [cited 2020 Oct 25];169(3):425–34. Available from: https://pubmed.ncbi.nlm.nih.gov/15866887/
91. Aoki A, Nakashima A, Kusabiraki T, Ono Y, Yoshino O, Muto M, et al. Trophoblast-Specific Conditional Atg7 Knockout Mice Develop Gestational Hypertension. Am J Pathol [Internet]. 2018 Nov 1 [cited 2022 Nov 14];188(11):2474–86. Available from: http://ajp.amjpathol.org/article/S0002944018303663/fulltext
92. Wang N, Tan HY, Li S, Feng Y. Atg9b deficiency suppresses autophagy and potentiates endoplasmic reticulum stress-associated hepatocyte apoptosis in hepatocarcinogenesis. Theranostics [Internet]. 2017 [cited 2020 Sep 28];7(8):2325–38. Available from: https://pubmed.ncbi.nlm.nih.gov/28740555/
93. Tingting C, Shizhou Y, Songfa Z, Junfen X, Weiguo L, Xiaodong C, et al. Human papillomavirus 16E6/E7 activates autophagy via Atg9B and LAMP1 in cervical cancer cells. Cancer Med [Internet]. 2019 [cited 2020 Nov 12];8(9):4404–16. Available from: https://pubmed.ncbi.nlm.nih.gov/31215164/
94. Ma Z, Qi Z, Shan Z, Li J, Yang J, Xu Z. The role of CRP and ATG9B expression in clear cell renal cell carcinoma. Biosci Rep [Internet]. 2017 Dec 22 [cited 2020 Nov 12];37(6). Available from: https://pubmed.ncbi.nlm.nih.gov/28923830/
95. Zhang X, Li C, Wang D, Chen Q, Li CL, Li HJ. Aberrant methylation of ATG2B, ATG4D, ATG9A and ATG9B CpG island promoter is associated with decreased mRNA expression in sporadic breast carcinoma. Gene [Internet]. 2016 Sep 30 [cited 2020 Nov 12];590(2):285–92. Available from: https://pubmed.ncbi.nlm.nih.gov/27265029/
96. Modzelewski AJ, Chen S, Willis BJ, Lloyd KCK, Wood JA, He L. Efficient mouse genome engineering by CRISPR-EZ technology. Nat Protoc [Internet]. 2018 Jun 1 [cited 2021 Apr 28];13(6):1253–74. Available from: https://pubmed.ncbi.nlm.nih.gov/29748649/
97. Truett GE, Heeger P, Mynatt RL, Truett AA, Walker JA, Warman ML. Preparation of PCR-quality mouse genomic DNA with hot sodium hydroxide and tris (HotSHOT). Biotechniques [Internet]. 2000 [cited 2023 Nov 4];29(1):52–4. Available from: https://pubmed.ncbi.nlm.nih.gov/10907076/

98. Aravind L, Anantharaman V, Balaji S, Babu MM, Iyer LM. The many faces of the helix-turn-helix domain: transcription regulation and beyond. FEMS Microbiol Rev [Internet]. 2005 [cited 2023 Nov 16];29(2):231–62. Available from: https://pubmed.ncbi.nlm.nih.gov/15808743/
99. Matthews BW. Hydrophobic Interactions in Proteins. 2001 [cited 2023 Nov 16]; Available from: www.els.net
100. Nakamura H. Roles of electrostatic interaction in proteins. Q Rev Biophys [Internet]. 1996 [cited 2023 Nov 16];29(1):1–90. Available from: https://www.cambridge.org/core/journals/quarterly-reviews-of-biophysics/article/abs/roles-of-electrostatic-interaction-in-proteins/BF318EFD89A89F88009EE6CD4D77AFB6
101. Hiz S, Kiliç S, Bademci G, Karakulak T, Erdoğan A, Özden B, et al. VARS1 Mutations Associated with Neurodevelopmental Disorder Are Located on A Short Amino Acid Stretch of The Anticodon-Binding Domain. Turkish J Biol [Internet]. 2022 Jan 1 [cited 2023 Aug 27];46(6):458–64. Available from: https://journals.tubitak.gov.tr/biology/vol46/iss6/3
102. Babu MM. The contribution of intrinsically disordered regions to protein function, cellular complexity, and human disease [Internet]. Vol. 44, Biochemical Society Transactions. Portland Press Ltd; 2016 [cited 2020 Dec 12]. p. 1185–200. Available from: /pmc/articles/PMC5095923/?report=abstract
103. Rosenfeld CS. The placenta-brain-axis. J Neurosci Res [Internet]. 2021 Jan 1 [cited 2023 Sep 7];99(1):271–83. Available from: https://onlinelibrary.wiley.com/doi/full/10.1002/jnr.24603
104. Orendi K, Gauster M, Moser G, Meiri H, Huppertz B. The choriocarcinoma cell line BeWo: Syncytial fusion and expression of syncytium-specific proteins. Reproduction [Internet]. 2010 Nov 1 [cited 2021 Apr 19];140(5):759–66. Available from: www.reproduction-online.org
105. Richardson CD, Ray GJ, DeWitt MA, Curie GL, Corn JE. Enhancing homology-directed genome editing by catalytically active and inactive CRISPR-Cas9 using asymmetric donor DNA. Nat Biotechnol [Internet]. 2016 Mar 1 [cited 2023 Sep 21];34(3):339–44. Available from: https://pubmed.ncbi.nlm.nih.gov/26789497/
106. Bhattacharya D, Van Meir EG. A simple genotyping method to detect small CRISPR-

Cas9 induced indels by agarose gel electrophoresis. Sci Reports 2019 91 [Internet]. 2019 Mar 14 [cited 2023 Oct 4];9(1):1–7. Available from: https://www.nature.com/articles/s41598-019-39950-4

107. Elmore SA, Cochran RZ, Bolon B, Lubeck B, Mahler B, Sabio D, et al. Histology Atlas of the Developing Mouse Placenta. Toxicol Pathol. 2022;50(1):60–117.
108. Groza T, Gomez Lopez FL, Mashhadi HH, Muñoz-Fuentes V, Gunes O, Wilson R, et al. The International Mouse Phenotyping Consortium: comprehensive knockout phenotyping underpinning the study of human disease. Nucleic Acids Res [Internet]. 2023 Jan 6 [cited 2023 Nov 18];51(D1):D1038–45. Available from: https://dx.doi.org/10.1093/nar/gkac972
109. Mori M, Bogdan A, Balassa T, Csabai T, Szekeres-Bartho J. The decidua—the maternal bed embracing the embryo—maintains the pregnancy. Semin Immunopathol [Internet]. 2016 Nov 1 [cited 2023 Nov 18];38(6):635. Available from: /pmc/articles/PMC5065593/
110. Wolf A, Bauer B, Abner EL, Ashkenazy-Frolinger T, Hartz AMS. A Comprehensive Behavioral Test Battery to Assess Learning and Memory in 129S6/Tg2576 Mice. PLoS One [Internet]. 2016 Jan 1 [cited 2023 Nov 17];11(1):e0147733. Available from: https://journals.plos.org/plosone/article?id=10.1371/journal.pone.0147733
111. Himanshu, Dharmila, Sarkar D, Nutan. A Review of Behavioral Tests to Evaluate Different Types of Anxiety and Anti-anxiety Effects. Clin Psychopharmacol Neurosci [Internet]. 2020 Aug 8 [cited 2023 Nov 17];18(3):341. Available from: /pmc/articles/PMC7382999/
112. Learning and Memory | Principles of Neural Science, Fifth Edition | AccessNeurology | McGraw Hill Medical [Internet]. [cited 2023 Oct 1]. Available from: https://neurology.mhmedical.com/content.aspx?bookid=1049&sectionid=59138701
113. Cellular Mechanisms of Implicit Memory Storage and the Biological Basis of Individuality | Principles of Neural Science, Fifth Edition | AccessNeurology | McGraw Hill Medical [Internet]. [cited 2023 Oct 1]. Available from: https://neurology.mhmedical.com/content.aspx?bookid=1049&sectionid=59138702
114. Ögren SO, Stiedl O. Passive Avoidance. Encycl Psychopharmacol [Internet]. 2013 [cited 2023 Nov 18];1–10. Available from: https://link.springer.com/referenceworkentry/10.1007/978-3-642-27772-6_160-2

115. Cockburn K, Rossant J. Making the blastocyst: lessons from the mouse. J Clin Invest [Internet]. 2010 Apr 4 [cited 2023 Nov 18];120(4):995. Available from: /pmc/articles/PMC2846056/

8. ATTACHMENTS

Attachment 1: Informed consent form sample

BİLGİLENDİRİLMİŞ GÖNÜLLÜ OLUR FORMU

LÜTFEN DİKKATLİCE OKUYUNUZ !!!

Bu çalışmaya katılmak üzere davet edilmiş bulunmaktasınız. Bu çalışmada yer almayı kabul etmeden önce çalışmanın ne amaçla yapılmak istendiğini anlamanız ve kararınızı bu bilgilendirme sonrası özgürce vermeniz gerekmektedir. Size özel hazırlanmış bu bilgilendirmeyi lütfen dikkatlice okuyunuz, sorularınıza açık yanıtlar isteyiniz.

Araştırmanın adı: "Uyarılmış Pluripotent Kök Hücrelerde MaviGen Projesi Kapsamında Yeni Tanımlanan Kalıtsal Hastalık Gen Adaylarının İşlevsel Validasyonu"

Değerli Anne/Baba,

Toplumda nadir olarak görülen gelişimsel gerilik, epilepsi, kanser, metabolik nörometabolik hastalıklar ve beyin malformasyonları gibi hastalıklar toplum sağlığı açısından önemli olan, rutin taramalarla tanı koymanın güç olduğu, aile içinde çok sayıda bireyi etkileyen ve tanımlanmış mutasyonlarla açıklanabilmesi zor olan ciddi durumlardır. Siz, çocuğunuz ve geniş aileniz ile birlikte daha önce yukarıda adı geçen hastalıklardan birine sahip olduğunuz ya da ailenizden birinde bu hastalıklardan biri bulunduğu için, başka çalışmalara katılmıştınız. Bu çalışmalarda söz konusu hastalıklara neden olabilecek gen ve/veya mutasyonları saptamayı amaçlamıştık. Bu projeler kapsamında sizin aileniz dahil olmak üzere, 30 kadar farklı aile için bir ya da daha fazla sayıda aday gen belirlenmiştir. Bunlardan bazılarının hastalıkla ilişkisi iyi bilinmektedir. Ancak bazılarında saptanan bu genetik bozukluğun ne şekilde hastalığa yol açtığı henüz bilinmemektedir. Sizin çocuğunuzda saptadığımız genetik bozukluk için de bu durum söz konusudur. Biz, bundan sonraki aşamada saptanan bu genetik bozuklukların ne şekilde hastalığa yol açtığını araştırmak istiyoruz. Bu araştırmalar hastalığın hücresel düzeydeki temellerinin anlaşılmasını sağlayacak, bu bilgiler de tedavi yöntemlerinin geliştirilmesi amacına yönelik çalışmaların önünü açacaktır. Sizi de çocuğunuz ve ailenizin diğer bireyleri ile birlikte bu çalışmaya katılmaya davet ediyoruz.

Çalışma toplam 3 yıl sürecektir. Bu çalışmada, çocuğunuzdan ve gerek olursa ailenizin diğer bazı bireylerinden deri biyopsisi alınacaktır. **Biyopsi işlemi çocuğunuza ait genetik verilerin incelenmesi tamamlandıktan sonra, hastane koşullarında gerekli gerekli sterilizasyon önlemleri alındıktan sonra gerçekleştirilecektir. İşlem sırasındaki ağrıyı**

azaltmak için biyopsi alınacak yer deri altından uyuşturulacak ve kol iç yüzünden 1-3 milimetrelik bir deri parçası alınacaktır. Biyopsi alınma işlemi sonrasında hastanıza uygulanacak herhangi bir ek işlem bulunmamaktadır. Deri biyopsisi alınmasından sonra ciltte hafif bir ağrı ya da morarma olabilir. Bu durum çocuğunuz için ciddi bir risk oluşturmayacak ve kendiliğinden gerileyecektir. Bunun dışında çocuğunuzun araştırmaya bağlı herhangi bir zarar görmesi söz konusu değildir. **Alınan deri biyopsisinden çeşitli laboratuvar yöntemleri kullanılarak hastalığınıza neden olan hücreler üretilecek ve bunlarda hastalığın nedenini anlamak için çeşitli çalışmalar yapılacaktır.** Herhangi bir sorunuzun olması halinde bilgi almak için doktorunuz ile iletişim kurabilirsiniz. Çocuğunuzun doku örnekleri çalışma sonunda imha edilecektir.

Sizinle birlikte yaklaşık 30 ailenin çalışmaya dahil edilmesi planlanmaktadır. Bu çalışmaya katılmayı reddetme ya da araştırma başladıktan sonra devam etmeme hakkına sahipsiniz. Bu çalışmaya katılmanız veya başladıktan sonra herhangi bir safhasında ayrılmanız daha sonraki tıbbi bakımınızı etkilemeyecektir. Araştırmacı da gönüllünün kendi rızasına bakmadan, olguyu araştırma dışı bırakabilir. **Bu çalışma sırasında size veya güvencesi altında bulunduğunuz resmi ya da özel hiçbir kurum veya kuruluşa hiçbir ücret ödetilmeyecektir.**

Bu çalışmada yer aldığınız süre içerisinde kayıtlarınızın yanı sıra ilişkili sağlık kayıtlarınız kesinlikle gizli kalacaktır. Bununla birlikte kayıtlarınız kurumun yerel etik kurul komitesine ve Sağlık Bakanlığı'na açık olacaktır. Hassas olabileceğiniz kişisel bilgileriniz yalnızca araştırma amacıyla toplanacak ve işlenecektir. Çalışma verileri herhangi bir yayın ve raporda kullanılırken bu yayında isminiz kullanılmayacak ve veriler izlenerek size ulaşılamayacaktır.

Yukarıdaki bilgileri okudum. Bunlar hakkında bana yazılı ve sözlü açıklamalar yapıldı. Bu koşullarla söz konusu klinik araştırmaya kendi rızamla, hiçbir baskı ve zorlama olmaksızın katılmayı kabul ediyorum.

Gönüllünün (veli/vasi)

Adı- soyadı: **Telefon:**

Adres: **İmzası:**

Proje Koordinatörünün

Adı- Soyadı: Prof. Dr. Semra Hız

İmzası:

Açıklamaları yapan araştırmacının

Adı- soyadı: Prof. Dr. Semra Hız **Telefon:**

İmzası:

Adı- soyadı: Prof. Dr. Uluç Yiş **Telefon:**

İmzası:

Adı- soyadı: Prof. Dr. Nur Arslan **Telefon:**

İmzası:

Adı- soyadı: Prof. Dr. Görsev Yener **Telefon:**

İmzası:

Adı- soyadı: Prof. Dr. Barış Akıncı **Telefon:**

İmzası:

Adı- soyadı: Prof. Dr. Çiğdem Eresen Yazıcıoğlu **Telefon:**

İmzası:

Adı- soyadı: Prof. Dr. Şermin Genç **Telefon:**

İmzası:

* Bu kısımda ilgili araştırmacılar hastalarına gerekli açıklamaları yapıp onay alacaktır, proje koordinatörü ve ilgili araştırmacılar imzalayacaktır.

**Bu form çalışmaya katılmaya gönüllü, hasta, 18 yaşından küçük çocuklar için (veli/vasi) hazırlanmıştır.

Rıza alma işlemine başından sonuna kadar tanıklık eden kuruluş görevlisinin

Adı-soyadı: **Görevi:**

İmzası:

Tarih: ...../...../.....

Attachment 2: Ethics committee approvals

KLİNİK ARAŞTIRMALAR ETİK KURULU KARAR FORMU

ARAŞTIRMANIN AÇIK ADI	**Uyarılmış Pluripotent Kök Hücrelerde MaviGen Projesi Kapsamında Yeni Tanımlanan Kalıtsal Hastalık Gen Adaylarının İşlevsel Validasyonu**
VARSA ARAŞTIRMANIN PROTOKOL KODU	-
ETİK KURUL PROTOKOL NUMARASI	446-SBKAEK

KARAR BİLGİLERİ	**Karar No:2018/13-02**	**Tarih:12.07.2018**
	Yukarıda bilgileri verilen başvuru dosyası ile ilgili belgeler araştırmanın/çalışmanın gerekçe, amaç, yaklaşım ve yöntemleri dikkate alınarak incelenmiş aşağıdaki eksikliklerin tamamlanmasından sonra Kurul'umuzda tekrar görüşülmesine karar verilmiştir. -Araştırma başvuru formu, protokol ve bütçe formu ve başvuru formu arasındaki katılan merkezler ve destekleyici ile ilgili tutarsızlıkların giderilmesi, -Araştırma bütçe formunda harcama kalemlerinin detaylandırılarak sunulması.	

Etik Kurul Başkanının
Unvanı/Adı/Soyadı: Prof.Dr.Ayşegül Yıldız
İmza:

Not: Etik kurul başkanı, imzasının yer almadığı her sayfaya imza atmalıdır.

İZMİR BİYOTIP VE GENOM MERKEZİ
HAYVAN DENEYLERİ YEREL ETİK KURULU (İBG-HADYEK)
KARARI

Toplantı Tarihi	: 08/04/2020	**Toplantı Günü**	: Çarşamba
Toplantı Sayısı	: 6	**Toplantı Saati**	: 15:30

Sayın Doç Dr. Kasım DIRIL,

2020-017 Protokol No'lu; yürütücüsü olduğunuz "Transgenik fare modellerinin yerel üretimi için yöntem geliştirilmesi" başlıklı projenin uygulanmasında etik açıdan sakınca olmadığına oy birliği ile karar verilmiştir.

Bilgilerinizi ve gereğini rica ederiz.

Doç. Dr. Güneş ÖZHAN BAYKAN **Başkan**	(Projede Araştırmacı) **Vet. Hek. Kerem ESMEN** **Başkan Yardımcısı**
(Onayladı) **Prof. Dr. H. Alper BAĞRIYANIK** **Üye**	(Onayladı) **Prof. Dr. Ensari GÜNELİ** **Üye**
(Projede Araştırmacı) **Doç. Dr. Kasım DİRİL** **Üye**	**Dr. Öğr. Üyesi Ayşe Banu DEMİR** **Üye** (Katılmadı)
(Onayladı) **Dr. Gülçin ÇAKAN AKDOĞAN** **Üye**	(Onayladı) **Vet. Hek. Umur KELEŞ** **Üye**
(Onayladı) **H. Muammer KARAGÖZ** **Üye**	

İZMİR BİYOTIP VE GENOM MERKEZİ
HAYVAN DENEYLERİ YEREL ETİK KURULU (İBG-HADYEK)
KARARI

Toplantı Tarihi	: 09/06/2021	**Toplantı Günü**	: Çarşamba
Toplantı Sayısı	: 8	**Toplantı Saati**	: 15:30

Sayın Doktora öğrencisi Seval KILIÇ,

2021-013 Protokol No'lu; yürütücüsü olduğunuz "ATG9B çerçeve kayması mutasyonunun işlevsel karakterizasyonu" başlıklı projenin uygulanmasında etik açıdan sakınca olmadığına oy birliği ile karar verilmiştir.

Bilgilerinizi ve gereğini rica ederiz.

Doç. Dr. Güneş ÖZHAN **Başkan**	(Projede Araştırmacı) **Vet. Hek. Kerem ESMEN** **Başkan Yardımcısı**
Prof. Dr. Ensari GÜNELİ **Üye**	(Projede Araştırmacı) **Doç. Dr. Kasım DİRİL** **Üye**
Dr. Öğr. Üyesi Ayşe Banu DEMİR **Üye** (Katılmadı)	**Dr. Gülçin ÇAKAN AKDOĞAN** **Üye** (Katılmadı)
Vet. Hek. Umur KELEŞ **Üye**	**Vet. Hek. Ceren ÜLKER** **Üye**
Vet. Hek. Gizem ARALAN **Üye**	**İrem KARADAŞ** **Üye** (Katılmadı)

İZMİR BİYOTIP VE GENOM MERKEZİ
HAYVAN DENEYLERİ YEREL ETİK KURULU (İBG-HADYEK)
KARARI

Toplantı Tarihi	: 16/02/2022	**Toplantı Günü**	: Çarşamba
Toplantı Sayısı	: 4	**Toplantı Saati**	: 15:30

Sayın Doç. Dr. Muhammed Kasım DIRIL,

2022-005 Protokol No'lu; yürütücüsü olduğunuz "Nörogelişimsel bir nadir genetik hastalık için transgenik fare modeli geliştirilmesi ve fenotipik karakterizasyonu: ATG9B mutasyonu" başlıklı projenin uygulanmasında etik açıdan sakınca olmadığına oy birliği ile karar verilmiştir.

Bilgilerinizi ve gereğini rica ederiz.

Dr. Gülçin ÇAKAN AKDOĞAN **Başkan**	(Projede Araştırmacı) **Vet. Hek. Kerem ESMEN** **Başkan Yardımcısı**
Prof. Dr. Ensari GÜNELİ **Üye**	**Doç. Dr. Güneş ÖZHAN** **Üye**
(Proje Yürütücüsü) **Doç. Dr. Kasım DİRİL** **Üye**	**Dr. Yavuz DOĞAN** **Üye**
Vet. Hek. Umur KELEŞ **Üye**	**Vet. Hek. Ceren ÜLKER** **Üye**
Vet. Hek. Gizem ARALAN **Üye**	**İrem KARADAŞ** **Üye**

T.C.
HACETTEPE ÜNİVERSİTESİ
Hayvan Deneyleri Yerel Etik Kurulu

Sayı : 52338575-06

HAYVAN DENEYLERİ ETİK KURUL KARARI

TOPLANTI TARİHİ	:	24.01.2023 (SALI)
TOPLANTI SAYISI	:	2023/01
DOSYA KAYIT NUMARASI	:	2023/02
KARAR NUMARASI	:	2023/01– 02
ONAY BİTİŞ TARİHİ		24.01.2028
ARAŞTIRMA YÜRÜTÜCÜSÜ	:	Doç. Dr. Muhammed Kasım DİRİL
HAYVAN DENEYLERİNDE GÖREVLİ ARAŞTIRMACILAR	:	Dr. Melike Sever BAHÇEKAPILI, Prof. Dr. Emine Eren KOÇAK, Tansu Bilge KÖSE
DİĞER YARDIMCI ARAŞTIRMACILAR	:	Prof. Dr. Abdullah YALÇIN, Vet. Hek. Kerem ESMEN, Prof. Dr. Hüsnü Alper BAĞRIYANIK, Doç. Dr. Şerif ŞENTÜRK
ONAYLANAN HAYVAN TÜRÜ ve SAYISI	:	***30 Adet (15 Adet Wild Type, 15 Adet ATG9B Homozigot Mutant) C57BL6/J Fare (20-25 gram)***

İzmir Dokuz Eylül Üniversitesi Biyotıp ve Genom Merkezi öğretim üyelerinden Doç. Dr. Muhammed Kasım DİRİL'in araştırma yürütücüsü olduğu 2023/02 kayıt numaralı ***"Nörogelişimsel Bir Nadir Genetik Hastalık İçin Transgenik Fare Modeli Geliştirilmesi ve Fenotipik Karakterizasyonu: ATG9B Mutasyonu"*** isimli çalışma Hayvan Deneyleri Yerel Etik Kurulu Yönergesi'ne göre uygun bulunarak oy birliği ile onaylanmasına karar verilmiştir.

Araştırma yürütücüsü en geç, onay bitiş tarihinden sonraki 1 ay içerisinde proje sonuç raporunu Kurulumuza teslım etmekle yükümlüdür.

Prof. Dr. Sema ÇALIŞ
Etik Kurul Başkanı

Hacettepe Üniversitesi Hayvan Deneyleri Yerel Etik Kurulu 06100 Sıhhiye-Ankara
Telefon: 0 (312) 305 1090-1082 • Faks: 0 (312) 310 0580
www.etikkurul.hacettepe.edu.tr/index_hdk.php
Ayrıntılı Bilgi için:

İZMİR BİYOTIP VE GENOM MERKEZİ
HAYVAN DENEYLERİ YEREL ETİK KURULU (İBG-HADYEK)
KARARI

Toplantı Tarihi	: 04/10/2022	**Toplantı Günü**	: Salı
Toplantı Sayısı	: 15	**Toplantı Saati**	: 13:00

Sayın Doç.Dr. Muhammed Kasım DIRIL,

2022-031 Protokol No'lu; yürütücüsü olduğunuz "FLAG epitop etiketli ATG9B fare hatları oluşturulması" başlıklı projenin uygulanmasında etik açıdan sakınca olmadığına oy birliği ile karar verilmiştir.

Bilgilerinizi ve gereğini rica ederiz.

Dr. Gülçin ÇAKAN AKDOĞAN **Başkan**	(Projede Araştırmacı) **Vet. Hek. Kerem ESMEN** **Başkan Yardımcısı**
Prof. Dr. Ensari GÜNELİ **Üye**	**Doç. Dr. Güneş ÖZHAN** **Üye**
(Proje Yürütücüsü) **Doç. Dr. Kasım DİRİL** **Üye**	**Dr. Yavuz DOĞAN** **Üye**
Vet. Hek. Ceren ÜLKER **Üye** (Katılmadı)	**Vet. Hek. Gizem ARALAN** **Üye** (Katılmadı)
Sevinç YAĞAN **Üye**	

Attachment 3: Resume

SEVAL KILIÇ

Personal Information

Contact Information

Contact Address	Dokuz Eylül Üniversitesi Inciraltı Yerleşkesi, 35340 Izmir
Telephone	
Email	sevalkilic01@gmail.com
Web Page	

Education Information

07 September 2017 - Now (6 Year 4 Month)
Doktora, Doktora, DOKUZ EYLÜL ÜNİVERSİTESİ, TÜRKİYE
İZMİR ULUSLARARASI BİYOTIP VE GENOM ENSTİTÜSÜ, MOLEKÜLER BİYOLOJİ VE GENETİK (DR) (İNGİLİZCE)
Diploma Number: -
Cumulative Grade Point Average: 3.8 / 4.0

01 September 2015 - 01 August 2017 (2 Year)
Yüksek Lisans, Tezli Program, SABANCI ÜNİVERSİTESİ, TÜRKİYE
FEN BİLİMLERİ ENSTİTÜSÜ, MOLEKÜLER BİYOLOJİ-GENETİK VE BİYOMÜHENDİSLİK (YL) (TEZLİ)
Thesis Title: The role of atypical and classical protein kinase C isozymes in autophagy and modulation of lysosomal pH by vacuolar ATPase as an alternative treatment approach for Gaucher disease
Thesis Subject: Autophagy is conserved degradation mechanism for long-lived proteins and organelle maintaining cellular homeostasis in eukaryotes. Protein Kinase C family isozymes are Serine/Threonine kinases involved in many crucial cellular and disease related pathways. According to their activation mechanism they are categorized to three subgroups: classical, novel and atypical PKC's. In this thesis, roles of atypical isozyme PKCzeta and classical isozyme PKCßII on autophagy were investigated. It was shown that autophagy is upregulated by PKCzeta.
We identified that lysosomal pH of fibroblast cells isolated from Gaucher patients were more basic than control cells. In lysosomes, V-ATPase is the main proton pump to maintain acidic pH. Therefore, we aimed to reacidify the lysosomes in patient cells by overexpressing H subunit of catalytic domain of V-ATPase. Upon reacidification, ß-glucocerebrosidase enzyme activity increased and the number of accumulated lipid droplets was diminished.
Date: 2017
Thesis Advisor: DEVRİM GÖZÜAÇIK
Thesis Co-Advisor: ÖZLEM KUTLU
Cumulative Grade Point Average: 3.87 / 4.0

01 October 2010 - 01 July 2015 (4 Year 10 Month)
Lisans, Anadal/Normal Öğretim, İZMİR YÜKSEK TEKNOLOJİ ENSTİTÜSÜ, TÜRKİYE
FEN FAKÜLTESİ, MOLEKÜLER BİYOLOJİ VE GENETİK BÖLÜMÜ
Diploma Number: 2860
Cumulative Grade Point Average: 3.01 / 4.0

01 September 2005 - 01 June 2009 (3 Year 10 Month)
İZMİR ATATÜRK LİSESİ, TÜRKİYE
Diploma Number: 24286
Cumulative Grade Point Average: 80.66 / 100.0

01 September 1997 - 01 June 2005 (7 Year 10 Month)
MİLLİ EĞİTİM BAKANLIĞI İL MİLLİ EĞİTİM MÜDÜRLÜKLERİ VE OKULLAR İZMİR İLİNDEKİ OKULLAR BUCA İLÇESİNDEKİ OKULLAR SAADET EMİR İLKÖĞRETİM OKULU, TÜRKİYE
Cumulative Grade Point Average: 5.0 / 5.0

Experience Information

01 September 2017 - Now (6 Year 4 Month) (Tam Zamanlı)
ARAŞTIRMACI, DOKTORA ÖĞRENCİSİ, İZMİR BİYOTIP VE GENOM MERKEZİ

01 September 2017 - Now (6 Year 4 Month) (Tam Zamanlı)
ARAŞTIRMACI, DOKTORA ÖĞRENCİSİ, İZMİR BİYOTIP VE GENOM ENSTİTÜSÜ

01 September 2015 - 01 August 2017 (2 Year) (Tam Zamanlı)
ARAŞTIRMACI, YÜKSEK LİSANS ÖĞRENCİSİ, SABANCI ÜNİVERSİTESİ FEN BİLİMLERİ ENSTİTÜSÜ

01 July 2014 - 01 September 2014 (3 Month) (Tam Zamanlı)
ARAŞTIRMACI, SOUTHAMPTON UNIVERSITY

Foreign Language Information

İNGİLİZCE (Reading: İyi, Writing: İyi, Speaking: İyi)

Scientific Technological Activity Fields

Scientific Technological Activity Field Information

Temel Bilimler -- Yaşam Bilimleri -- Moleküler Biyoloji ve Genetik -- Genetik Bozuklukların Moleküler Biyolojisi

Temel Bilimler -- Yaşam Bilimleri -- Nörobiyoloji -- Nörofizyoloji

Sağlık Bilimleri -- Tıp -- Temel Tıp Bilimleri -- Tıbbi Biyoloji

Temel Bilimler -- Yaşam Bilimleri -- Moleküler Biyoloji ve Genetik -- Genetik Mühendisliği

Temel Bilimler -- Yaşam Bilimleri -- Moleküler Biyoloji ve Genetik -- Hayvan Moleküler Genetiği

Temel Bilimler -- Yaşam Bilimleri -- Biyoinformatik -- Biyoenformasyon

Temel Bilimler -- Yaşam Bilimleri -- Moleküler Biyoloji ve Genetik -- Genomiks

Keywords

Otofaji

Nadir Genetik Hastalıklar

Nörogelişimsel Bozukluklar

R&D Competency

Articles

H. E. YİLMAZ, E. ISCAN, O. OZ, T. BATUR, A. ERDOGAN, S. KİLİÇ, Z. MUTLU, M. YİLMAZ & K. J. SPRİNG, Considerations for the selection of tests for SARS-CoV-2 molecular diagnostics, MOLECULAR BIOLOGY REPORTS, 2022, 0301-4851.

M. ERGUVEN, S. KİLİÇ, E. KARACA & M. K. DİRİL, Genetic complementation screening and molecular docking give new insight on phosphorylation-dependent Mastl kinase activation, JOURNAL OF BIOMOLECULAR STRUCTURE & DYNAMICS, 2022, 0739-1102.

S. HİZ, S. KİLİC, G. BADEMC, T. KARAKULAK, A. ERDOGAN, B. OZDEN, C. ERESEN, E. ERDAL, U. YİS, M. TEKİN, G. KARAKUELAH, E. KARACA & M. OZTURK, VARS1 mutations associated with neurodevelopmental disorder are located on a short amino acid stretch of the anticodon-binding domain, TURKISH JOURNAL OF BIOLOGY, 2022, 1300-0152, 46, 6, 458-+.

R. SREEKUMAR, H. AL-SAİHATİ, M. EMADUDDİN, K. MOUTASİM, M. MELLONE, A. PATEL, S. KİLİC, M. CETİN, S. ERDEMİR, M. S. NAVİO, M. A. LOPEZ, N. CURTİS, T. YAGCİ, J. N. PRİMROSE, B. D. PRİCE, G. BERX, G. J. THOMAS, E. TULCHİNSKY, A. MİRNEZAMİ & A. E. SAYAN, The ZEB2-dependent EMT transcriptional programme drives therapy resistance by activating nucleotide excision repair genes ERCC1 and ERCC4 in colorectal cancer, MOLECULAR ONCOLOGY, 2021, 1574-7891, 15, 8, 2065-2083.

Ö. KUTLU, Ö. YEDİER BAYRAM, S. KILIÇ & D. GÖZÜAÇIK, Involvement Of Autophagy In T Cell Biology, HISTOLOGY AND HISTOPATHOLOGY, 2017, 0213-3911, Vol.32, 1, 11-21.

Conference Papers

S. KILIÇ, A. S. HIZ, K. ESMEN, G. KARAKÜLAH, M. ÖZTÜRK & M. K. DİRİL, Generation and phenotypic characterization of a transgenic mouse model for a neurodevelopmental rare genetic disorder, Poster Sunumu, YSF 2023 and the 47th FEBS Congress, 06 July 2023, 12 July 2023, 2211-5463, FEBS Open Bio 13 (Suppl.2) (2023), 246 - null.

S. KILIÇ, T. KARAKULAK, A. ERDOĞAN ATAY, A. S. HIZ, G. KARAKÜLAH, G. BADEMCİ, Ç. ERESEN YAZICIOĞLU, Ş. E. ERDAL BAĞRIYANIK, U. YİŞ, M. TEKİN, E. KARACA EREK & M. ÖZTÜRK, Nörolojik Hastalıklarda VARS T1068M Mutasyonunun İlişkilendirilmesi ve Antikodon Bağlanma Domaininde Kümelenen Mutasyonların Önemi, Sözlü Sunum, XVI. Tıbbi Biyoloji ve Genetik Kongresi, 27 October 2019, 30 October 2019.

H. N. KALELİ, V. O. KAYA, Ö. YEDİER BAYRAM, S. KILIÇ, G. ÖNAL, A. YÜCE, S. DÖKMECİ, D. GÖZÜAÇIK & Ö. KUTLU, Reverse Activation of Defective Autophagy Mechanism Might Be an Alternative Approach for Gaucher Disease Therapy, Poster Sunumu, 13th European Working Group on Gaucher Disease Congress (EWGGD 2019), 04 July 2019, 06 July 2019.

H. N. KALELİ, E. ÖZER, Ö. YEDİER BAYRAM, S. KILIÇ, S. DÖKMECİ, D. GÖZÜAÇIK & Ö. KUTLU, Identification Of Novel Targets For The Role Of Pkc Isozymes On The Regulation Of Autophagy, Poster Sunumu, 6th International Congress Of The Molecular Biology Association Of Turkey, 05 September 2018, 08 September 2018.

Ö. YEDİER BAYRAM, H. N. KALELİ, E. ÖZER, S. KILIÇ, S. DÖKMECİ, D. GÖZÜAÇIK & Ö. KUTLU, Identification of Novel Targets for The Role of PKC Isozymes on The Regulation of Autophagy, Poster Sunumu, 6th International Congress of the Molecular Biology Association of Turkey, 05 September 2018, 08 September 2018, 175 - 175.

S. KILIÇ, Ö. YEDİER BAYRAM, D. GÖZÜAÇIK & Ö. KUTLU, Identification Of A Serine-threonine Kinase As A Novel Autophagic Regulator, Poster Sunumu, Vi. International Congress Of Molecular Medicine, 22 May 2017, 25 May 2017, 2149-0627.

Ö. YEDİER BAYRAM, S. KILIÇ, D. GÖZÜAÇIK & Ö. KUTLU, Pma Functions As An Inhibitor Through Activation Of Serine/threonine Kinase, Poster Sunumu, Vi. International Congress Of Molecular Medicine, 22 May 2017, 25 May 2017, 21, 113 - null.

Ö. KUTLU, S. KILIÇ, Ö. YEDİER BAYRAM, S. DÖKMECİ & D. GÖZÜAÇIK, Effect Of Serine/threonine Kinases On Autophagy Mechanism, Sözlü Sunum, Icracb 2016 : 18th International Conference On Regulators Of Autophagy And Cell Biology, 10 October 2016, 11 October 2016.

Projects

KURUMSAL (BAP V.B.), ARAŞTIRMACI, Nörogelişimsel Hastalıklarlarla İlişkilendirilen Aday Genlerin İşlevsel Validasyonu, Enforcing Institution: İZMİR BİYOTIP VE GENOM MERKEZİ, Sponsor Institution: İBG (Sistemde kayıtlı olmayan kuruluş) (Yurt İçi) (Still continues) .

TEMEL ARAŞTIRMA, BURSİYER, Aktif Protein Kinaz C İzozimlerinin Otofaji Mekanizması Üzerine Etkilerinin Belirlenmesi Ve Otofaji Ile Iliskili Hedef Gen/proteinlerinin Arastırılması, Enforcing Institution: MOLEKÜLER BİYOLOJİ-GENETİK VE BİYOMÜHENDİSLİK (YL) (TEZLİ), 01 May 2015, 01 August 2017.

TÜBİTAK, ARAŞTIRMACI, Sema6d, Sema3c, Slpi, Edn1, Cyr61 Ve Hmga2 Genlerinin Metastatik Olan Ve Olmayan Meme Kanseri Hücre Hatlarında Ifade Edilme Seviyelerinin Belirlenmesi, Enforcing Institution: MOLEKÜLER BİYOLOJİ VE GENETİK ANABİLİM DALI, Sponsor Institution: TÜBİTAK BİLİM KURULU (Yurt İçi) , 01 January 2015, 01 May 2015.

TÜBİTAK Scholarships and Fundings

Project Info

122Z025, Nörogelişimsel Bir Nadir Genetik Hastalık İçin Transgenik Fare Modeli Geliştirilmesi Ve Fenotipik Karakterizasyonu: Atg9b Mutasyonu, Burslu, Yürürlükte, KBAG - Kimya Biyoloji Araştırma Destek Grubu, 1001 - Araştırma, ARDEB, Project Participation/Leave Dates: 10/2/23 - Devam ediyor, Project Start/End Dates: 7/15/22 - 7/15/24..
122Z025, Nörogelişimsel Bir Nadir Genetik Hastalık İçin Transgenik Fare Modeli Geliştirilmesi Ve Fenotipik Karakterizasyonu: Atg9b Mutasyonu, BİDEB Burslusu, Yürürlükte, KBAG - Kimya Biyoloji Araştırma Destek Grubu, 1001 - Araştırma, ARDEB, Project Participation/Leave Dates: 8/2/22 - 10/1/23, Project Start/End Dates: 7/15/22 - 7/15/24.
121S347, ATG9B Çerçeve Kayması Mutasyonunun İşlevsel Karakterizasyonu, Yürütücü, Sonuçlandı, SBAG - Sağlık Bilimleri Araştırma Destek Grubu, 1002 - Hızlı Destek, ARDEB, Project Participation/Leave Dates: 9/1/21 - Devam ediyor, Project Start/End Dates: 9/1/21 - 9/1/22.
115G073, Kanser Ve Osteoporoz Tedavisi İçin Monoklonal Antikor Etkin Maddeli Biyobenzer İlaç Geliştirilmesi Ve Üretilmesi, Burslu, Yürürlükte, KAMAG - Kamu Araştırmaları Destek Grubu, 1007 - Kamu / Üniversite, ARDEB, Project Participation/Leave Dates: 6/16/19 - 6/4/20, Project Start/End Dates: 11/15/16 - 1/1/22.
114Z836, Aktif Protein Kinaz C İzozimlerinin Otofaji Mekanizması Üzerine Etkilerinin Belirlenmesi ve Otofaji ile ilişkili Hedef Gen/Proteinlerinin Araştırılması , Burslu, Sonuçlandı, KBAG - Kimya Biyoloji Araştırma Destek Grubu, 1001 - Araştırma, ARDEB, Project Participation/Leave Dates: 9/1/15 - 8/31/17, Project Start/End Dates: 5/1/15 - 5/1/18.

BIDEB Supports

SEVAL KILIÇ, Etkinlik Destekleri ve Eğitim Bursları Müdürlüğü, 2250-Lisansüstü Bursları Performans Programı, Destek Sona Erdi, 2022 - 1.
SEVAL KILIÇ, Etkinlik Destekleri ve Eğitim Bursları Müdürlüğü, 2250-Lisansüstü Bursları Performans Programı, Destek Sona Erdi, 2023 - 1.
SEVAL KILIÇ, Etkinlik Destekleri ve Eğitim Bursları Müdürlüğü, 2250-Lisansüstü Bursları Performans Programı, Destek Sona Erdi, 2023 - 2.
SEVAL KILIÇ, Araştırma Burs ve Destekleri Müdürlüğü, 2247-C Stajyer Araştırmacı Burs Programı (STAIR)- Star Lisans, Destek Sona Erdi, 2020 - 1, 6/1/20 - 1/31/21.
SEVAL KILIÇ, Etkinlik Destekleri ve Eğitim Bursları Müdürlüğü, 2211-A Genel Yurt İçi Doktora Burs Programı, Başvurusu Reddedildi, 2017 - 2, 10/1/17 - 9/30/21.
SEVAL KILIÇ, Etkinlik Destekleri ve Eğitim Bursları Müdürlüğü, 2211-A Genel Yurt

İçi Doktora Burs Programı, Başvurusu Reddedildi, 2018 - 2, 6/1/18 - 5/31/22.

SEVAL KILIÇ, Etkinlik Destekleri ve Eğitim Bursları Müdürlüğü, 2211-A Genel Yurt İçi Doktora Burs Programı, Başvurusu Reddedildi, 2019 - 1, 3/1/19 - 2/28/23.
SEVAL KILIÇ, Etkinlik Destekleri ve Eğitim Bursları Müdürlüğü, 2211-A Genel Yurt İçi Doktora Burs Programı, Bursu Kesildi, 2020 - 1, 3/1/20 - 9/30/23.

Number of Panelist/Observer/Reporter Jobs

Refereeing/Panelist/Outer Consultant Count	ARDEB/BİDEB 0	TEYDEB 0	Total 0
Number of Observer/Consultant Jobs	ARDEB/BİDEB 0	TEYDEB 0	Total 0
Number of Reporter Jobs	ARDEB/BİDEB 0	TEYDEB 0	Total 0

Attachment 4: Research Article

Turkish Journal of Biology

Volume 46 | Number 6 Article 3

1-1-2022

VARS1 Mutations Associated with Neurodevelopmental Disorder Are Located on A Short Amino Acid Stretch of The Anticodon-Binding Domain

AYŞE SEMRA HIZ

SEVAL KILIÇ

GÜNEY BADEMCİ

TÜLAY KARAKULAK

AYBİKE ERDOĞAN

See next page for additional authors

Follow this and additional works at: https://journals.tubitak.gov.tr/biology

Part of the Biology Commons

Recommended Citation

HIZ, AYŞE SEMRA; KILIÇ, SEVAL; BADEMCİ, GÜNEY; KARAKULAK, TÜLAY; ERDOĞAN, AYBİKE; YÜCEL, BURCU ÖZDEN; YAZICIOĞLU, ÇİĞDEM ERESEN; BAĞRIYANIK, ŞERİFE ESRA ERDAL; YİŞ, ULUÇ; TEKİN, MUSTAFA; KARAKÜLAH, GÖKHAN; EREK, EZGİ KARACA; and ÖZTÜRK, MEHMET (2022) "VARS1 Mutations Associated with Neurodevelopmental Disorder Are Located on A Short Amino Acid Stretch of The Anticodon-Binding Domain," *Turkish Journal of Biology*: Vol. 46: No. 6, Article 3. https://doi.org/10.55730/1300-0152.2631

Available at: https://journals.tubitak.gov.tr/biology/vol46/iss6/3

This Article is brought to you for free and open access by TÜBİTAK Academic Journals. It has been accepted for inclusion in Turkish Journal of Biology by an authorized editor of TÜBİTAK Academic Journals. For more information, please contact academic.publications@tubitak.gov.tr.

VARS1 Mutations Associated with Neurodevelopmental Disorder Are Located on A Short Amino Acid Stretch of The Anticodon-Binding Domain

Authors

AYŞE SEMRA HIZ, SEVAL KILIÇ, GÜNEY BADEMCİ, TÜLAY KARAKULAK, AYBİKE ERDOĞAN, BURCU ÖZDEN YÜCEL, ÇİĞDEM ERESEN YAZICIOĞLU, ŞERİFE ESRA ERDAL BAĞRIYANIK, ULUÇ YİŞ, MUSTAFA TEKİN, GÖKHAN KARAKÜLAH, EZGİ KARACA EREK, and MEHMET ÖZTÜRK

This article is available in Turkish Journal of Biology: https://journals.tubitak.gov.tr/biology/vol46/iss6/3

TÜBİTAK

Turkish Journal of Biology

http://journals.tubitak.gov.tr/biology/

Research Article

Turk J Biol
(2022) 46: 458-464
© TÜBİTAK
doi:10.55730/1300-0152.2631

VARS1 mutations associated with neurodevelopmental disorder are located on a short amino acid stretch of the anticodon-binding domain

Semra HIZ[1,2,3], Seval KILIÇ[1,3], Güney BADEMCİ[4], Tülay KARAKULAK[1,3], Aybike ERDOĞAN[1,3], Burcu ÖZDEN[1,3], Çiğdem ERESEN[5], Esra ERDAL[1,3,5], Uluç YİŞ[2], Mustafa TEKİN[4], Gökhan KARAKÜLAH[1,3,*,], Ezgi KARACA[1,3,*,**], Mehmet ÖZTÜRK[1,3]**

[1]İzmir Biomedicine and Genome Center, İzmir, Turkey
[2]Department of Pediatrics, Faculty of Medicine, Dokuz Eylül University, İzmir, Turkey
[3]Dokuz Eylül University, İzmir International Biomedicine and Genome Institute, İzmir, Turkey
[4]John P. Hussman Institute for Human Genomics and Dr. John T. Macdonald Foundation Department of Human Genetics, University of Miami Miller School of Medicine, Miami, USA
[5]Department of Medical Biology and Genetics, Faculty of Medicine, Dokuz Eylül University, İzmir, Turkey

Received: 19.01.2022 • **Accepted/Published Online:** 05.12.2022 • **Final Version:** 19.12.2022

Abstract: Majority of 37 human aminoacyl tRNA synthetases have been incriminated in diverse, mostly recessive, genetic diseases. In accordance with this, we uncovered a novel homozygous valyl-tRNA synthetase 1 (*VARS1*) gene variant, leading to p.T1068M mutation. As in the previously reported *VARS1* mutations, the affected individual harboring p.T1068M was experiencing a neurodevelopmental disorder with intractable seizures, psychomotor retardation, and microcephaly. To link this phenotypic outcome with the observed genotype, we structurally modeled human *VARS1* and interpreted p.T1068M within the spatial distribution of previously reported *VARS1* variants. As a result, we uncovered that p.T1068M is clustered with three other pathogenic mutations in a 15 amino acid long stretch of the VARS1 anticodon-binding domain. While forming a helix-turn-helix motif within the anticodon-binding domain, this stretch harbors one-fourth of the reported *VARS1* mutations. Here, we propose that these clustered mutations can destabilize the interactions between the anticodon-binding and the tRNA synthetase domains and thus hindering the optimal enzymatic activity of *VARS1*. We expect that the depiction of this mutation cluster will pave the way for the development of drugs, capable of alleviating the functional impact of these mutations.

Key words: VARS1, whole exome sequencing, protein stability, structural modeling, mutation modeling, psychomotor retardation

1. Introduction

Aminoacyl tRNA synthetases (ARSs) are ancient housekeeping genes. ARSs are ubiquitously expressed in all cells to catalyze the esterification of amino acids with their specific tRNA. Such specific tRNAs carry an appropriate anticodon sequence, which will be translated to messenger RNAs for the high fidelity production of proteins (Schimmel, 2018). There are 37 different human ARSs encoded by different genes. Majority of these ARSs are located either in the cytoplasm or in the mitochondria (except three functioning in both compartments) (Antonellis and Green, 2008). As reviewed in 2017, 31 ARS genes have been incriminated in different, mostly recessive, genetic diseases (Meyer-Schuman and Antonellis, 2017). Most of these profiled mutations show loss-of-function effects, leading to serious problems during protein translation. There are also examples where the ARS mutations can be tolerated, showing that such disease-causing missense variants may retain some residual activity (Meyer-Schuman and Antonellis, 2017).

Among the ARS genes, two homozygous Valine ARS (*VARS1*) variants were first identified in two individuals affected by neurological disorders (Karaca et al., 2015). Both individuals had severe developmental delay, microcephaly, seizures, and cortical atrophy. Expanding on this study, we screened a small set of Turkish families composed of consanguineous couples with children having neurological disorders. Through whole exome sequencing (WES), we detected a novel homozygous *VARS1* variant i.e. p.T1068M, in an affected individual who was experiencing microcephaly, developmental delay, and drug-resistant seizures. The p.T1068M, *VARS1* variant is located in close vicinity of the pathogenic p.R1058Q (Karaca et al., 2015), as well pathogenic p.M1064I and

* Correspondence: ezgi.karaca@ibg.edu.tr
** Equally contributing corresponding authors

This work is licensed under a Creative Commons Attribution 4.0 International License.

p.F1072L mutations (Okur et al., 2018; Stephen et al., 2018). All these mutations are all localized in a helix-turn-helix motif of the anticodon-binding domain, suggesting a functionally critical region for this enzyme. To interpret the effect of these mutations on the function of *VARS1*, we structurally modeled human p.R1058Q; p.M1064I; p.T1068M; p.F1072L *VARS1* bound to their tRNA by using *Thermus thermophilus VARS* as a template. As a result, we observed that these clustered mutations could lead to the destabilization of the interactions between anticodon-binding and catalytic tRNA synthetase domains, thus to a potential loss-of-function.

2. Methods

2.1. Ethics statement

The ethics committee approval for this study was granted by the Dokuz Eylül University Ethics Committee (document id: 446-SBKAEK). We also took a written consent from the parents of the affected individual.

2.2. Next generation whole exome sequencing

The genomic DNA isolation from blood was performed with Invitrogen PureLink Genomic DNA kit (Cat #: K1820-01) according to the manufacturer's protocol. Isolated DNA of the proband, one sister, mother, and father were randomly chopped into smaller fragments by sonication, then electrophoresed on 1% agarose gel. Fragments with 400–500 bp length were selected. The fragments corresponding to protein-coding exons were purified with Agilent SureSelect kit. Libraries for Illumina platform were prepared, the optimized barcode sequences were added. By this, four to five libraries could be sequenced in one sequencing lane. The sequencing was carried out in Illumina HiSeq2500 platform at TÜBİTAK Marmara Research Center DNA Services Facility (Gebze, Turkey) where the relevant FASTQ files were obtained. Sequencing reads were aligned to GRCh37/hg19 human reference genome with BWA (v.0.7.16a) (Li and Durbin, 2010). The variant calling step was performed with HaplotypeCaller of Genome Analysis Tool Kit (GATK; v.3.6.0) (DePristo et al., 2011). SnpEff package (v.4.1) was used for variant annotation (Cingolani et al., 2012). The variants with low depth of coverage (<7) and quality score (<30) were not considered for the downstream analysis. For the filtering, the variants that were homozygous in the proband and heterozygous in each parent were considered. Homozygous variants in the unaffected sibling were removed. The minor allele frequency (MAF) was chosen to be <0.005 in the global allele frequency of the Genome Aggregation Database (gnomAD; http://gnomad.broadinstitute.org/). The remaining variants were then prioritized according to their mammalian conservation (GERP and PhyloP), predicted deleteriousness (SIFT, PolyPhen2 and MutationTaster) and putative impact (high, moderate, or low).

2.3. Sanger validation and segregation analysis by restriction enzyme analysis

The genomic location of candidate variant detected by the next generation WES was amplified by polymerase chain reaction (PCR) via appropriate primers for Sanger validation and restriction digestion. For confirming the WES results, primers covering the mutation site were designed to amplify 488 bp DNA fragment by PCR using high fidelity Phusion polymerase. The amplified fragment of proband was sent to Sanger Sequencing (TRiOGEN) for forward and reverse reading. The sequences were investigated with FinchTV 1.4.0 program. The variant site is a recognition site for the *Tsp*45I digestion enzyme (New England Biolabs ref no: R0583S), which stalled the digestion of the proband DNA. Therefore, the parental and other two sisters' DNA restriction digestion was used for confirmation. For the restriction reaction, the conditions were set with 10× CutSmart buffer (New England Biolabs #B7204S), in 20 mL, which was incubated at 65 °C 1 h according to manufacturer's directions. One percent agarose gel electrophoresis was performed to detect the segregated DNA bands.

2.4. Structural modeling of p.R1058Q, p.M1064I, p.T1068M, and p.F1072L *VARS1*

The best structural template to model human *VARS1* was the *Thermus thermophilus* valyl-tRNA Synthetase (pdb id: 1IVS (Fukai et al., 2003), with 52.9% of sequence similarity. By using 1IVS as the template, *VARS1* structural model was constructed with MODELLER (Webb and Sali, 2014). As 1IVS did not contain any structural information on 879-916 amino acid range, this region was excluded during model building. Here, we used standard homology modeling, as AlphaFold2 could not produce a model compatible with RNA binding (Supplementary Figure 1A).

MODELLER was run through the MPI Bioinformatics Toolkit web service (https://toolkit.tuebingen.mpg.de/#/) (Alva et al., 2016). Modeled human *VARS1* was aligned on top of 1IVS with the "align" command of PyMOL (Schrödinger LLC, 2015). The *Thermus thermophilus* tRNA-Val was isolated together with human *VARS1* model. The human VARS1-tRNA complex was refined with HADDOCK 2.2 (Van Zundert et al., 2016). p.R1058Q, p.M1064I, p.T1068M, p.F1072L *VARS1* mutations were imposed one at a time by using the HADDOCK as described at https://www.bonvinlab.org/software/haddock2.4/faq/#what-about-point-mutations.

2.5. Measuring the impact of the mutation cluster on *VARS1* stability

The structural impact of the clustered mutations (p.R1058Q, p.M1064I, p.T1068M, p.F1072L) was assessed based on their interdomain contact changes (between the anticodon-binding and tRNA synthetase domains). The contacts were calculated with the PRODIGY web server (Xue et al., 2016). The specific interactions were calculated

with Protein Interactions Calculator web server (Tina et al., 2007). The impact of novel p.T1068M and previously reported p.R1058Q, p.M1064I, p.F1072L mutations on the anticodon-binding domain's stability were calculated with the MAESTROWeb (Laimer et al., 2015). We also used mutfunc web-server to check whether the mutations would lead to loss-of-function (http://www.mutfunc.com).

3. Results

3.1. Affected individual

A 45-day-old infant presented with migrating myoclonic seizures that had been lasting for three days. The seizures were apparent both during sleep and activity. She had focal tonic and clonic seizures. The infant was delivered to a 39-year-old mother with gestational diabetes without any complication at the 38th week of gestation via caesarean section. Upon her birth, she was weighing 3300 g. She was the third child of healthy parents who were first cousins. Before having her, the parents had two healthy daughters.

The affected individual's past medical history included two hospitalizations. She was hospitalized the first time when she was three days old due to dehydration and hypernatremia. She was then hospitalized when she was 15 days old due to urinary tract infection with indications of microcephaly, left renal agenesis, and patent foramen ovale. Her physical examination demonstrated that she had microcephaly, bifrontal narrowing, and high palate. She had mild axial hypotonia with slightly increased deep tendon reflexes, bilateral clonus without Babinski sign. She also had mild upper limb spasticity. Her ocular and hearing examinations were normal. Her laboratory examinations were normal with regard to complete blood count, and biochemistry tests (i.e. blood glucose, creatine kinase, lactate, ammonia, hepatic and renal function tests, lipid profile, vitamin B12, thyroid hormones, metabolic screening including urine organic acids, very long chain fatty acids, acylcarnitines, plasma and urine amino acids, lysosomal enzymes, serum lactate and pyruvate, biotinidase activity, cerebrospinal fluid (CSF) amino acid analysis, CSF/serum glycine and glucose ratios, urine sulfite screening). The electroencephalography showed multifocal epileptic activity. The brain magnetic resonance (MR) imaging revealed diffuse T2 hyperintensity in cerebral white matter. The MR spectroscopy indicated minimally increased lactate peak. Skeletal X-ray was normal. Her follow-up examinations at three months of age revealed that her clinical presentation progressed leading to axial hypotonia with increased deep tendon reflexes, clonus, and spasticity. She had severe global developmental delay without head control, eye contact, or tracking too. She had epileptic encephalopathy with drug (clobazam, clonazepam, levetiracetam, phenobarbital, potassium bromide, pyridoxine, topiramate, and ketogenic diet) resistant seizures. She died at the age of 11 months due to complications caused by an upper respiratory infection.

3.2. The whole exome sequencing identifies a homozygous missense *VARS1* variant

The WES analysis of the affected individual's proband revealed eight homozygous variants (Supplementary Table 1). Among these, only the variants observed in *VARS1*, *LAMC2*, and *USP24* genes occurred at conserved positions (for *VARS1*, please see Supplementary Figure 2A). The fact that the previously reported *VARS1* mutations were associated with microcephaly and epilepsy made us focus on the *VARS1* variant. The *VARS1* gene variant is located at the 31747470th nucleotide of chromosome 6 (6:31747470 (GRCh37), NC_000006.11:g.31747470G>A), leading to a p.Thr1068Met (p.T1068M, rsID: rs777665186) substitution (Figure 1A). This variant has previously been observed with 0.00002 worldwide frequency, but it has never been linked to a clinical condition. It was determined to be homozygous in the proband and heterozygous in other family members (see Section 2). Sanger sequencing confirmed proband's homozygous c.3203G>A variation (Figure 1A). To further validate the genotype of the family concerning the identified mutation, *VARS1* gene around the mutation site was PCR amplified and subjected to *Tsp*45I digestion. The c.3203G>A site prevents the proband's DNA cleavage by *Tsp*45I, as it coincides with the restriction site of the enzyme (Figure 1B). On the other hand, the parents' and one unaffected sister's DNA indicated a pattern compatible with heterozygous mutation, while the other sister contained two healthy alleles (Figures 1C and 1D). Considering the clinical outcome of the previously reported *VARS1* variants (MIM: 617802, phenotype: neurodevelopmental disorder with microcephaly, seizures, and cortical atrophy), together with the condition of our affected individual suggested further exploration of the autosomal recessive p.T1068M *VARS1* mutation.

3.3. Anticodon-binding domain of *VARS1* is a mutational hotspot

VARS1 is composed of glutathione S-transferase C-terminal, tRNA synthetase class 1, anticodon-binding and coiled coil domains (Supplementary Figure 1B). So far, including the one we report here, 19 *VARS1* mutations have been described (Figure 2A). Interestingly, 17 of these mutations occurred as homozygous or heterozygous missense mutations, mostly localized on the tRNA synthetase and anticodon-binding domains. A 15 amino acid long stretch of the anticodon-binding domain (encoded by the exon 27 of 207 bp length) harbors our described p.T1068M mutation, as well as the previously reported pathogenic p.R1058Q (recurrent), p.M1064I, and p.F1072L mutations. To observe the spatial distribution of these mutations, we modeled human *VARS1* in complex

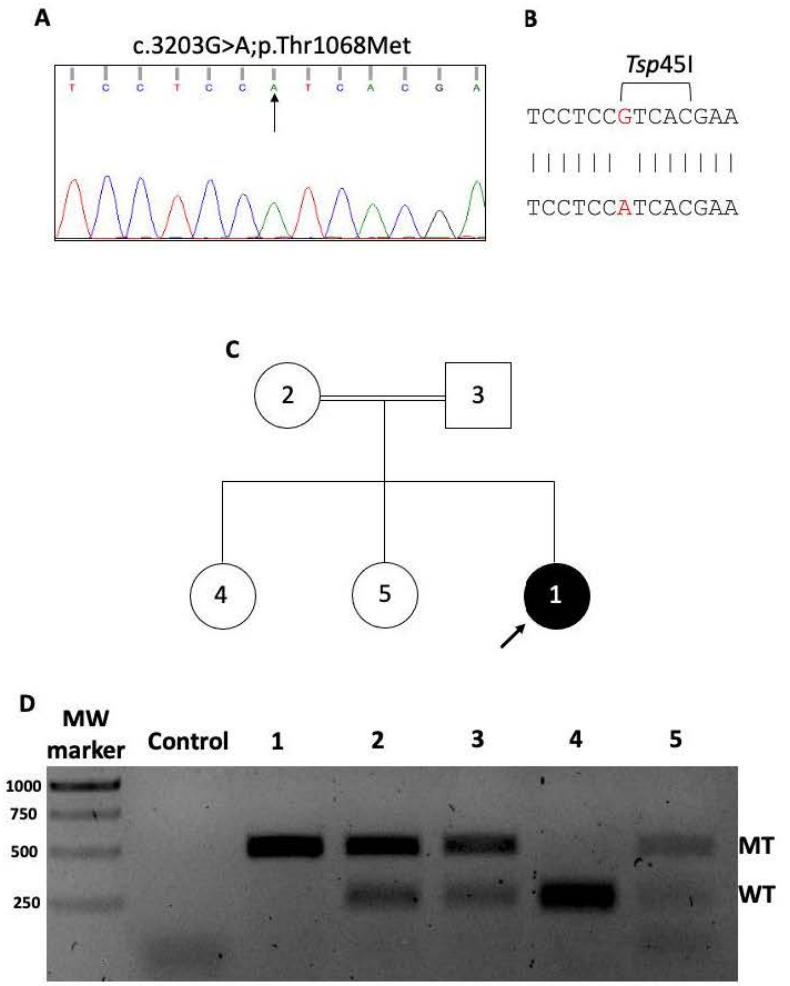

Figure 1. Sanger validation and segregation analysis of *VARS1* variant identified in. A: Sanger sequencing of the blood DNA from the proband confirmed homozygous c.3203G>A mutation identified by WES. **B:** The c.3203G>A mutation occurred in a recognition and cutting site by *Tsp*45I restriction enzyme. **C:** The proband (black circled), her parents (2 and 3) and her two unaffected siblings (4 and 5) studied during the segregation analysis by using *Tsp*45I digestion. **D:** Agarose electrophoresis demonstrating homozygous mutation in the proband (MT 488bp), heterozygous mutations in parents and one sister (WT 257/231, MT 488 bp), and wild-type status (WT 257/231) in the other sister.

with its tRNA, by using the valyl-tRNA Synthetase (ValRS) from *Thermus thermophilus* as a template (see Section 2; Supplementary Figure 1B). As a result, we found out that p.R1058Q, p.M1064I, p.T1068M, p.F1072L mutations are clustered within a helix-turn-helix (HTH) motif, running between Q1047-L1075 (Figures 2B and 2C). This HTH motif is located across the anticodon-binding and tRNA synthetase domain interface (Supplementary Figure 1B, Figure 2B). We also explicitly modeled p.R1058Q, p.M1064I, p.T1068M, p.F1072L *VARS1* point mutations (see Section 2). The structural analysis of the mutant *VARS1* structures revealed that each of these four mutations has the potential to reduce the number of (anticodon-binding and tRNA synthetase) domain-domain contacts by 10% (see Section 2; Supplementary Table 2). This reduction is triggered by the loss of interhelical hydrophobic (for p.M1064I and p.F1072M) and electrostatics interactions (for p.R1058Q and p.T1068M). Specifically, in the case of p.T1068M, residue 1068 is unable to make a stabilizing hydrogen bond with p.S1061 located on a reciprocal helix (Figure 2D). These observations were further supported by the MAESTROWeb and mutfunc web-servers, which

predicted all of these mutations to be destabilizing/deleterious (Supplementary Table 3, Supplementary Figure 2B).

4. Discussion

Karaca et al. (2015) was the first group reporting two homozygous, *VARS1* gene variants (p.R1058Q and p.L885F, respectively) in two families of consanguineous couples. Three children coming from these families experienced microcephaly, intellectual disability, seizures, and cortical atrophy. Alsemari et al. (2017a, 2017b) then described a homozygous p.R1217H *VARS1* mutation in a boy with severe mental retardation, ataxia, speech impairment, epilepsy, short stature, microcephaly, hypogonadism, and growth hormone deficiency. Stephen et al. (2018) also reported two siblings with severe early-onset neurological manifestations including microcephaly, intellectual disability, seizures, and cortical atrophy. The affected individuals demonstrated some dysmorphic facial features. WES analysis of these affected individuals detected two mutations in *VARS1*: a missense p.M1064I mutation in one allele and a splice site mutation resulting in a truncation in the other allele. Okur et al. (2018) reported two male siblings aged 15- and 10-year-old who had an intellectual deficiency, developmental delay, severe speech impairment, microcephaly, and prematurity. Both affected individuals were compound heterozygous with p.A22D and p.F1072L mutation in *VARS1* gene. Recently, two further studies were published reporting new *VARS1* variants. Siekierska et al. (2019) described ten affected individuals from seven families with biallelic variants in *VARS1*. All affected individuals demonstrated global developmental

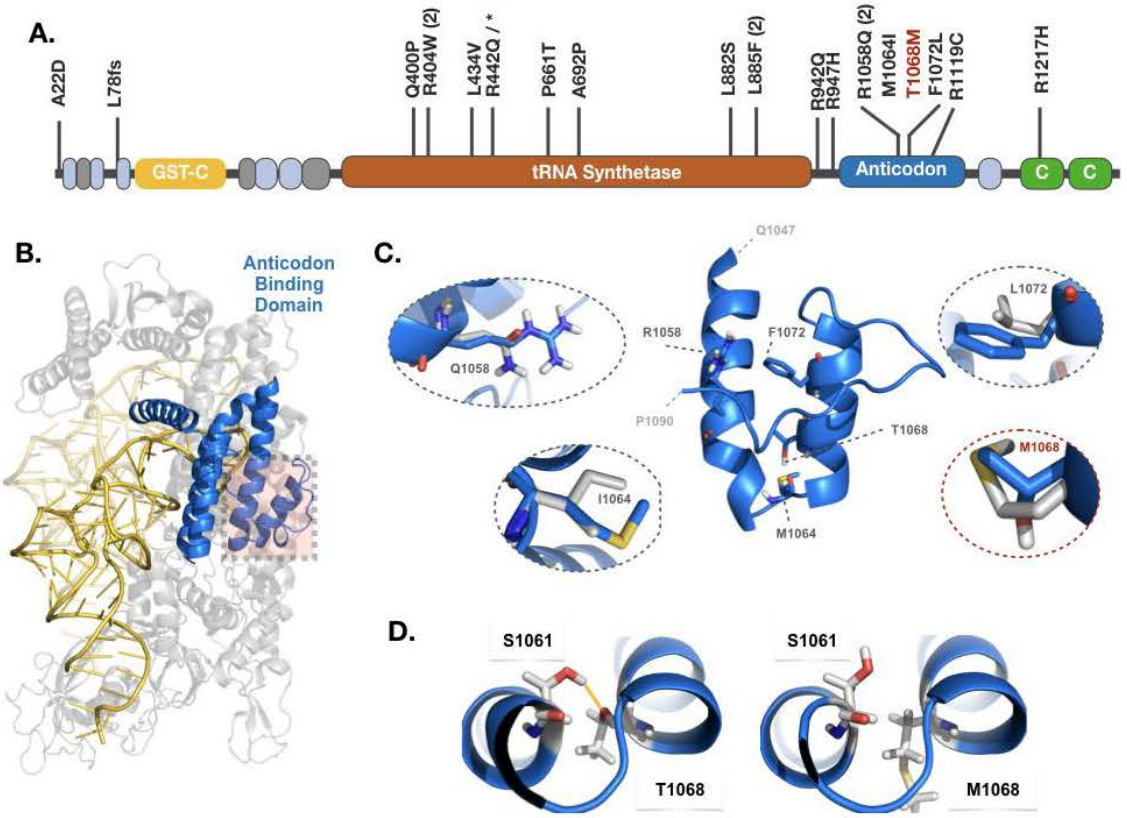

Figure 2. Structural mapping of the pathogenic *VARS1* mutation cluster. A: Domain organization of *VARS1* (yellow: glutathione S-transferase, orange: tRNA synthetase, blue: anticodon-binding, green: coiled coil) together with the localization of the reported pathogenic mutations. Light blue and gray boxes correspond to the low complexity regions, as annotated by Pfam (El-Gebali et al., 2019). The novel p.T1068M mutation is depicted in salmon. **B:** The structural model of *VARS1* anticodon-binding domain harboring pathogenic mutations. The color coding follows the one given in panel A. **C:** The structural motif belonging to the wild type anticodon-binding domain (running between amino acids Q1047 and P1090) is located in the middle. The wild type motif is surrounded by the close-up of each observed mutation position. In each oval, the conformation of the mutant amino acid (gray) is compared to its wild type counterpart. **D:** In the wild type *VARS1*, S1061 is making a stabilizing interhelical polar contact with T1068 (depicted by Pymol (Schrödinger LLC, 2015)). This interaction is lost in the case of p.T1068M substitution.

delay, microcephaly, and intellectual disability. Eight out of ten affected individuals had epileptic seizures and cerebral atrophy. Friedman et al. (2019) reported seven affected individuals from five unrelated families with five different biallelic missense *VARS1* variants. Subjects presented with global developmental delay, epileptic encephalopathy, primary or progressive microcephaly, and cortical atrophy. While the mutations reported by Siekierska et al. (2019), Friedman et al. (2019), and Stephen et al. (2018) are heterozygous together with a missense mutation, all other known mutations of *VARS1* are biallelic missense mutations (Figure 2A). The lack of affected individuals with a total loss of intact protein strongly suggests that *VARS1* is a vital protein. Thus, missense variants of *VARS1* are probably sufficient to maintain the vital functions, except for the normal development and/or function of the brain tissue. Our affected individual presenting the homozygous p.T1068M *VARS1* mutation has some common features with the abovedescribed affected individuals, including microcephaly, developmental delay, and intractable seizures. Though, she did not have cortical atrophy. In the reports of Okur et al. (2018) and Siekierska et al. (2019), some of the affected individuals did not demonstrate cortical atrophy too. This indicates that cortical atrophy is either not a persistent outcome of *VARS1* mutations or is acquired with time.

When compared with the affected individuals presented in the literature, it can be claimed that the neurological signs and symptoms of our case were more severe. She had axial hypotonia without head control and pyramidal symptoms including increased deep tendon reflexes with bilateral clonus and upper limb spasticity. She had no eye contact, and her microcephaly was prominent. She also had epileptic encephalopathy with refractory myoclonic seizures. Despite the use of many antiseizure drugs and ketogenic diet, her seizures continued. Her death due to an intervening respiratory infection was probably due to problems associated with severe neuromotor retardation and refractory epileptic encephalopathy. Affected individuals living up to 10 years of age have been reported in the literature, but our case died before reaching the age of one. Therefore, we cannot comment on whether symptoms such as cortical atrophy described in older children in the literature will also develop in our patient. One distinctive clinical feature of our affected individual was her left renal agenesis. This finding was not described in any of the affected individual with VARS1 mutation reported in the literature. Since parents of the case were consanguineous as first cousins, the finding of left renal agenesis may be associated with a genetic defect other than VARS1. However, we think that it is important to consider this finding in our case and to report it to the literature. The interpretation of whether this finding is related to VARS1 mutation or an incidental finding can be made when more VARS1 related affected individuals are reported in the literature.

To further explore the impact of the detected mutation, we structurally modeled human *VARS1* and interpreted p.T1068M within the spatial distribution of previously reported VARS1 variants. As a result, we uncovered that p.T1068M is clustered with three other pathogenic mutations (p.R1058Q, p.M1064I, p.T1068M, and p.F1072L) in a 15 amino acid long stretch of the anticodon-binding domain. Further, we showed that all these four mutations lead to the reduction in the number of anticodon-binding and catalytic tRNA synthetase domain-domain interactions by using computational approaches. We supply our models together with this paper as supplementary material to aid the drug design approaches targeting these *VARS1* mutations.

5. Conclusion

In this work, we screened a small set of consanguineous Turkish families with children suffering from different diseases, mostly neurological disorders by using whole exome sequencing. This study allowed us to identify a novel *VARS1* variant leading to a p.T1068M mutation. This mutation is located very close to previously reported pathogenic p.R1058Q. Here, we show that a helix-turn-helix motif on the anticodon-binding domain of *VARS1* not only harbors p.T1068M, but also three other pathogenic *VARS1* mutations. We demonstrate that all these mutations are potentially capable of destabilizing anticodon-binding and catalytic tRNA synthetase domain-domain interactions. It is highly likely that such destabilization hinders the optimal enzymatic activity of *VARS1* without compromising vital function. We expect that this realization will pave the way for the development of drugs, capable of enhancing mutant *VARS1* stability.

Conflict of interest

All authors declare lack of conflict of interest in relation to this report.

Data availability

The atomic coordinates of our models and original gel images are provided as Supporting Information.

Acknowledgments

We thank all participating patient families to this study. This project was supported by the Department of Scientific Research Projects of Dokuz Eylül University as numbered as 2014.KB.SAG.054 and İzmir Biomedicine and Genome Center.

References

Alsemari A, Al-Younes B, Goljan E, Jaroudi D, BinHumaid F et al. (2017a). Correction to: Recessive VARS2 mutation underlies a novel syndrome with epilepsy, mental retardation, short stature, growth hormone deficiency, and hypogonadism. Human Genomics 11 (1): 33. https://doi.org/10.1186/s40246-017-0130-6

Alsemari A, Al-Younes B, Goljan E, Jaroudi D, BinHumaid F et al. (2017b). Recessive VARS2 mutation underlies a novel syndrome with epilepsy, mental retardation, short stature, growth hormone deficiency, and hypogonadism. Human Genomics 11 (1): 28. https://doi.org/10.1186/s40246-017-0124-4

Alva V, Nam SZ, Soding J, Lupas AN (2016). The MPI bioinformatics Toolkit as an integrative platform for advanced protein sequence and structure analysis. Nucleic Acids Research 44 (W1): W410-415. https://doi.org/10.1093/nar/gkw348

Antonellis A, Green ED (2008). The role of aminoacyl-tRNA synthetases in genetic diseases. Annual Review of Genomics and Human Genetics 9: 87-107. https://doi.org/10.1146/annurev.genom.9.081307.164204

Auton A, Abecasis GR, Altshuler DM, Durbin RM, Abecasis GR et al. (2015). A Global Reference for Human Genetic Variation. Nature 526 (7571): 68–74. https://doi.org/10.1038/nature15393.

Cingolani P, Platts A, Wang le L, Coon M, Nguyen T et al. (2012). A program for annotating and predicting the effects of single nucleotide polymorphisms, SnpEff: SNPs in the genome of Drosophila melanogaster strain w1118; iso-2; iso-3. Fly (Austin) 6 (2): 80-92. https://doi.org/10.4161/fly.19695

DePristo MA, Banks E, Poplin R, Garimella KV, Maguire JR et al. (2011). A framework for variation discovery and genotyping using next-generation DNA sequencing data. Nature Genetics 43 (5): 491-498. https://doi.org/10.1038/ng.806

El-Gebali S, Mistry J, Bateman A, Eddy SR, Luciani A et al. (2019). The Pfam protein families database in 2019. Nucleic Acids Research 47 (D1): D427-D432. https://doi.org/10.1093/nar/gky995

Friedman J, Smith DE, Issa MY, Stanley V, Wang R et al. (2019). Biallelic mutations in valyl-tRNA synthetase gene VARS are associated with a progressive neurodevelopmental epileptic encephalopathy. Nature Communications 10 (1): 707. https://doi.org/10.1038/s41467-018-07067-3

Fukai S, Nureki O, Sekine S, Shimada A, Vassylyev DG et al. (2003). Mechanism of molecular interactions for tRNA (Val) recognition by valyl-tRNA synthetase. RNA 9 (1): 100-111. https://doi.org/ 10.1261/rna.2760703

Karaca E, Harel T, Pehlivan D, Jhangiani SN, Gambin T et al. (2015). Genes that Affect Brain Structure and Function Identified by Rare Variant Analyses of Mendelian Neurologic Disease Neuron 88 (3): 499-513. https://doi.org/10.1016/j.neuron.2015.09.048

Laimer J, Hofer H, Fritz M, Wegenkittl S, Lackner P (2015). MAESTRO--multi agent stability prediction upon point mutations. BMC Bioinformatics 16: 116. https://doi.org/10.1186/s12859-015-0548-6

Li H, Durbin R (2010). Fast and accurate long-read alignment with Burrows-Wheeler transform. Bioinformatics 26 (5): 589-595. https://doi.org/10.1093/bioinformatics/btp698

Meyer-Schuman R, Antonellis A (2017). Emerging mechanisms of aminoacyl-tRNA synthetase mutations in recessive and dominant human disease. Human Molecular Genetics 26 (R2): R114-R127. https://doi.org/10.1093/hmg/ddx231

Okur V, Ganapathi M, Wilson A, Chung WK (2018). Biallelic variants in VARS in a family with two siblings with intellectual disability and microcephaly: case report and review of the literature. Cold Spring Harbor Molecular Case Studies 4 (5). https://doi.org/10.1101/mcs.a003301

Schimmel P (2018). The emerging complexity of the tRNA world: mammalian tRNAs beyond protein synthesis. Nature Reviews Molecular Cell Biology 19 (1): 45-58. https://doi.org/10.1038/nrm.2017.77

Schrödinger LLC (2015). The PyMOL Molecular Graphics System, Version 1.8.6.2 Schrödinger, LLC.

Siekierska A, Stamberger H, Deconinck T, Oprescu SN, Partoens M et al. (2019). Biallelic VARS variants cause developmental encephalopathy with microcephaly that is recapitulated in vars knockout zebrafish. Nature Communications 10 (1): 708. https://doi.org/10.1038/s41467-018-07953-w

Stephen J, Nampoothiri S, Banerjee A, Tolman NJ, Penninger JM et al. (2018). Loss of function mutations in VARS encoding cytoplasmic valyl-tRNA synthetase cause microcephaly, seizures, and progressive cerebral atrophy. Human Genetics 137 (4): 293-303. https://doi.org/10.1007/s00439-018-1882-3

Tina KG, Bhadra R, Srinivasan N (2007). PIC: Protein Interactions Calculator. Nucleic Acids Research 35 (2): W473-476. https://doi.org/10.1093/nar/gkm423

Van Zundert GCP, Rodrigues J, Trellet M, Schmitz C, Kastritis PL et al. (2016). The HADDOCK2.2 Web Server: User-Friendly Integrative Modeling of Biomolecular Complexes. Journal of Molecular Biology 428 (4): 720-725. https://doi.org/10.1016/j.jmb.2015.09.014

Webb B, Sali A (2014). Protein structure modeling with MODELLER. Methods in Molecular Biology 1137: 1-15. https://doi.org/10.1007/978-1-4939-0366-5_1

Xue LC, Rodrigues JP, Kastritis PL, Bonvin AM, Vangone A (2016). PRODIGY: a web server for predicting the binding affinity of protein-protein complexes. Bioinformatics 32 (23): 3676-3678. https://doi.org/10.1093/bioinformatics/btw514

Supporting Information

VARS1 Mutations Associated with Neurodevelopmental Disorder Are Located on A Short Amino Acid Stretch of The Anticodon-Binding Domain

Semra HIZ[1,2,3], Seval KILIÇ[1,3], Güney BADEMCİ[4], Tülay KARAKULAK[1,3], Aybike ERDOĞAN[1,3], Burcu ÖZDEN[1,3], Çiğdem ERESEN[5], Esra ERDAL[1,3,5], Uluç YİŞ[2], Mustafa TEKİN[4], Gökhan KARAKÜLAH[1,3,*,], Ezgi KARACA[1,3,*,**], Mehmet ÖZTÜRK[1,3]**

[1]İzmir Biomedicine and Genome Center, İzmir, Turkey
[2]Department of Pediatrics, Faculty of Medicine, Dokuz Eylül University, İzmir, Turkey
[3]Dokuz Eylül University, İzmir International Biomedicine and Genome Institute, İzmir, Turkey
[4]John P. Hussman Institute for Human Genomics and Dr. John T. Macdonald Foundation Department of Human Genetics, University of Miami Miller School of Medicine, Miami, USA
[5]Department of Medical Biology and Genetics, Faculty of Medicine, Dokuz Eylül University, İzmir, Turkey

*Equally Contributing Corresponding Authors: ezgi.karaca@ibg.edu.tr; gokhan.karakulah@ibg.edu.tr

Supporting Figures

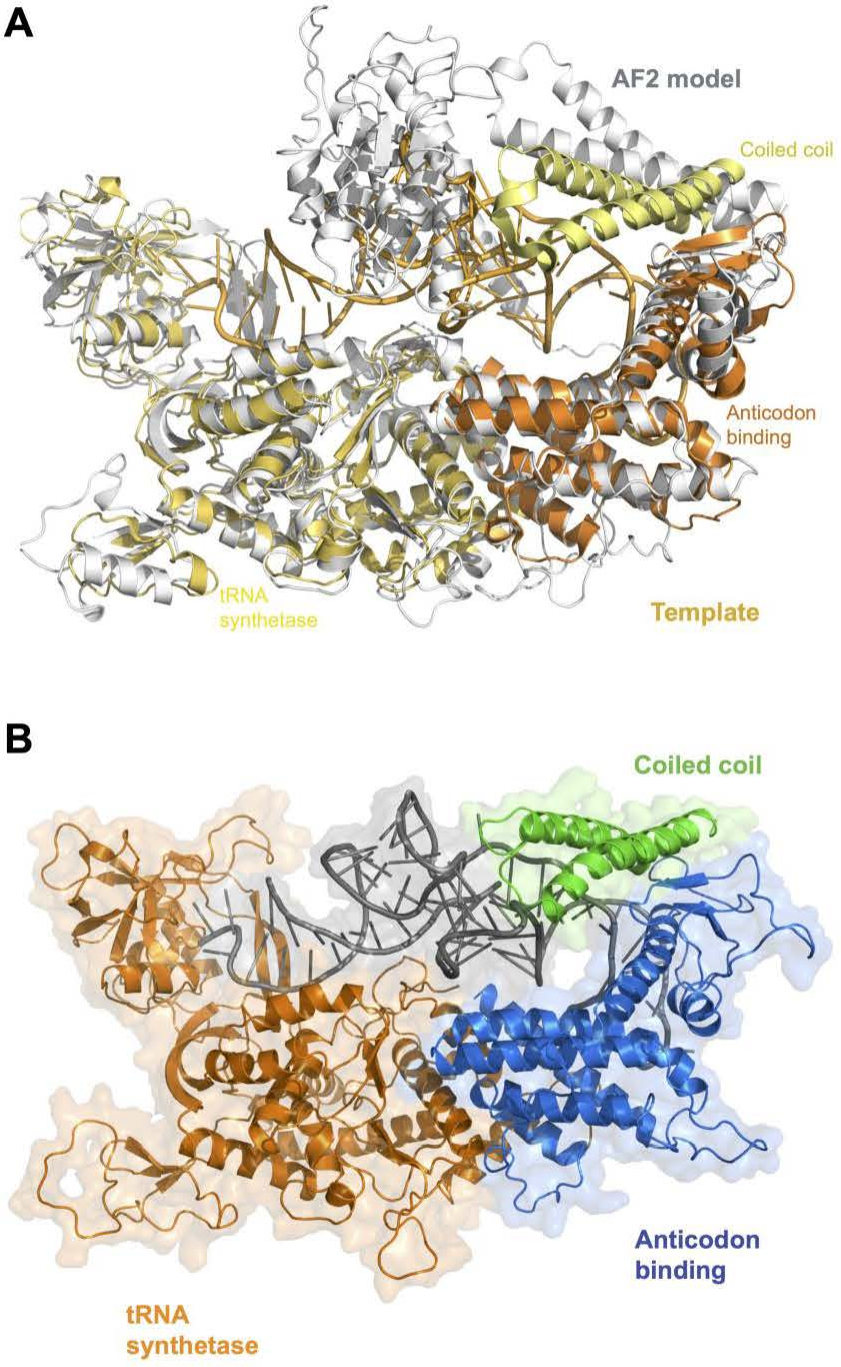

Supplementary Figure 1. (**A**) AlphaFold2 model (white) is aligned with *Thermus thermophilus* valyl-tRNA Synthetase (pdb id: 1IVS, yellow) as the best structural template to homology model *VARS1*. (**B**) The structural model of the human *VARS1* (all depicted in cartoon). The domain coloring follows the scheme reported in Figure 2. tRNA is colored in gray.

Supplementary Figure 2. A. T1068 is conserved across different organisms. **B.** Mutfunc webserver (http://www.mutfunc.com) predicts the amino acids substitutions occurring in the mutation cluster to be impactful due to the conserved positions of these substitutions.

Supporting Tables

Supplementary Table 1. The list of homozygous variants identified in the proband.

Chromosome	Chr Start	Chr End	Var. Type	Ref Seq	Var Seq	rsid List	Genes List	Gene Component List	Prot Impact List	aa Change	Global Allele Freq.	Mammalian Conservation
1	53108597	53108597	SNP (X2)	C	G	rs200885042	FAM159A	CDS	MISSENSE	A-82-G	0.01	no
1	183189995	183189995	SNP (x2)	A	C		LAMC2	CDS	MISSENSE	N-180-T	0	Yes (5.4)
4	68384019	68384019	SNP (x2)	C	A		CENPC	CDS	MISSENSE	D-229-y	0	no
6	31747470	31747470	SNP (x2)	G	A	rs777665186	VARS	CDS	MISSENSE	T-1068-M	0.01	Yes (5 .3)
12	95927026	95927026	SNP (x2)	T	A		USP44	CDS	MISSENSE	E-336-V	0	Yes (4.9)
12	101777396	101777396	SNP (x2)	A	G	rs139767850	UTP20	CDS	MISSENSE	M-2669-V	0.02	no
12	104054522	104054522	SNP (x2)	A	T		STAB2	CDS	MISSENSE	Q-617-L	0	no
12	108961059	108961059	SNP (x2)	T	G		ISCU	INTBQN; CDS	MISSENSE	S-14 5-A	0	no

Supplementary Table 2: Number of contacts calculated by PRODIGY between the anticodon-binding and tRNA synthetase domains, in the case of mutant and wild-type VARS1 (Xue et al., 2016).

Contact types	WT	p.R1058Q	p.M1064I	p.T1068M	p.F1072L
charged-charged:	4	3	4	3	3
charged-polar:	13	12	12	12	12
charged-apolar:	48	46	47	47	44
polar-polar:	2	2	2	2	2
polar-apolar:	28	29	23	29	24
apolar-apolar:	75	73	70	74	78
Total	170	165	158	167	163

Supplementary Table 3: Stability Predictions calculated by the MaestroWeb web-server for the anticodon-binding domain mutations (Laimer et al., 2015).

Mutation	MaestroWeb (arbitrary units)
p.T1068M	0.49 (Destabilizing)
p.R1058Q	1.83 (Destabilizing)
p.M1064I	0.84 (Destabilizing)
p.F1072L	1.76 (Destabilizing)

Appendix

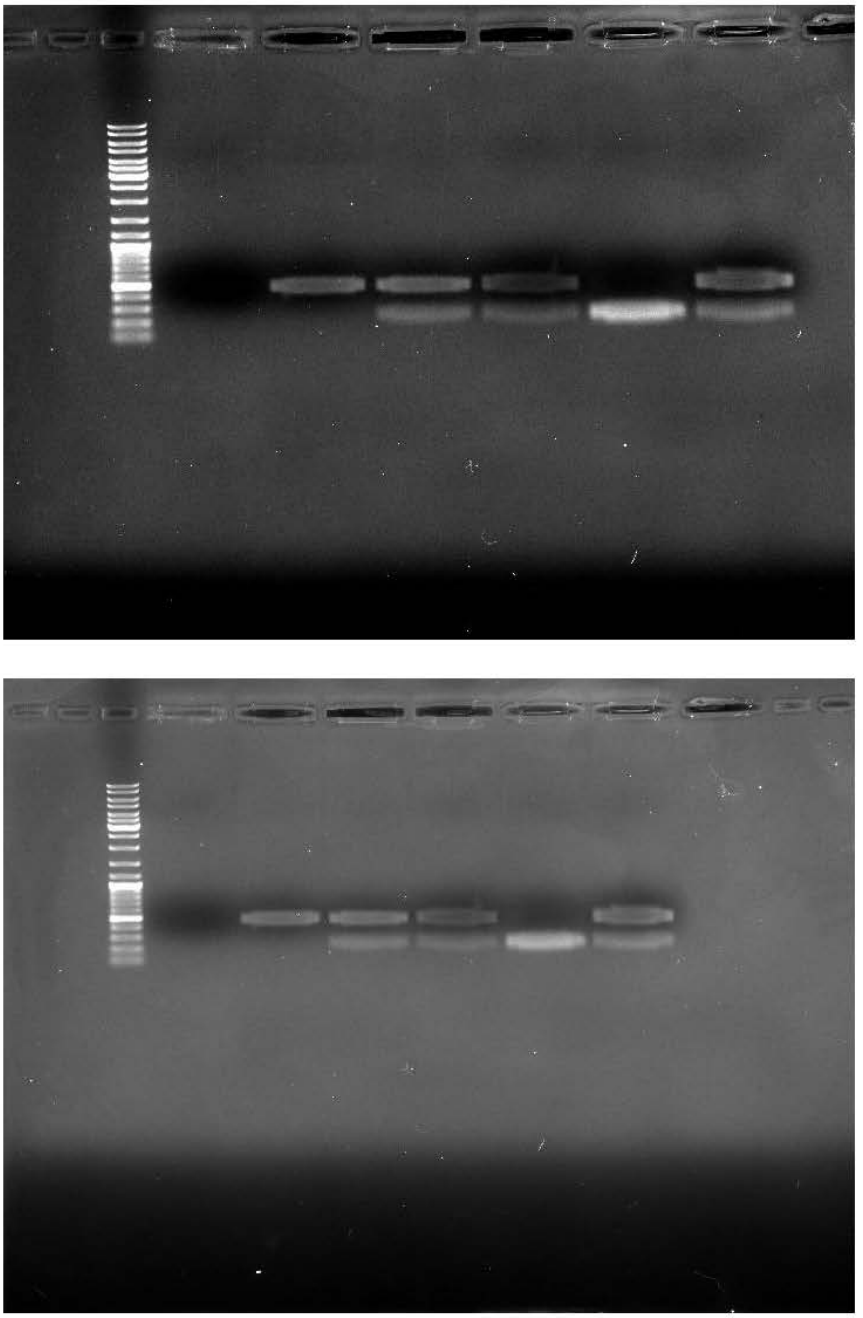

Figure 1D – original gel images: